Electrochemical Characterization of Environmental Electron Transfer Mediators

by

Ania S. Pavitt

A DISSERTATION

presented to the Division of Environmental Science & Engineering
and the Oregon Health & Science University
School of Medicine
in partial fulfillment of
the requirements for the degree of

Doctor of Philosophy
in
Environmental Science and Engineering

September 2020

For my mom and dad

Table of Contents

List of Tables

List of Figures

There is nothing more wonderful than being a scientist, nowhere I would rather be than in my lab, staining up my clothes and getting paid to play.

Marie Skłodowska Curie

Acknowledgements

I will always remember coming into the lab one day to find five books on comma usage on my desk. This is just one example of how my advisor, Dr. Paul G. Tratnyek, humorously, but effectively lets you know you need to improve. Looking back, this one gesture, besides always making me laugh, always makes me mind my commas. I sincerely appreciate him for trying to make me a better, writer, researcher, more effective communicator, and for being available to listen to my ideas. I will be eternally grateful for being allowed this tremendous opportunity. This has no doubt been the greatest accomplishment of my life.

It seems appropriate somehow to follow this with how hard it has been, but it was quite enjoyable, and dare I say easy. However, I think I owe this to the extremely helpful people I came across in my time at OHSU. Specifically, Dr. Richard L. Johnson for being available to help in many capacities, from proofreading my presentations to making me a special cap for my electrochemistry cell. I would like to thank my committee members, Drs. Paul G. Tratnyek, Richard L. Johnson, Joseph A. Needoba, W. Paige Hall, and Tawnya D. Peterson for their time, effort, and support. I am also very grateful to my summer interns, David Panfilov, Eric Sauer, Nick Slenning, and Nancy Nguyen, who helped collect and organize some of my very large datasets. Lastly, the staff and the professors at OHSU have all been approachable, helpful, encouraging, and a pleasure to work with.

On a personal level, I could not have done any of this without my amazing parents. It was them believing in me, guiding me, being there for me even when I failed, that showed me anything is possible. In addition to being blessed with an amazing family, I have been blessed with wonderful friends and for all of these things, I feel extremely lucky. And a special thank you to Graham, all of our fun trips, outings, and food adventures have been icing on the cake.

Abstract

Electrochemical Characterization of Environmental Electron Transfer Mediators

Ania S. Pavitt

Doctor of Philosophy

Division of Environmental Science & Engineering

School of Medicine

Oregon Health & Science University

September 2020

Thesis Advisor: Paul G. Tratnyek

Reduction-oxidation (redox) reactions are central to environmental chemical processes. Many redox reactions occur as sequences (e.g., photosystem II, which provide electrons for photosynthesis), with the intermediate species referred to as electron transfer mediators (ETMs). ETMs can be any molecule that helps transfer electrons from one chemical moiety to another. In the laboratory, ETMs are more specific, such as species that are well characterized, and undergo fast electron transfer in both oxidation and reduction reactions (reversible). Here, various electrochemical methods were used to characterize environmentally relevant ETMs, such as phenols and anilines, natural organic matter, and various iron oxides.

Phenol and aniline oxidation potentials are a major determinant of their behavior, but with numerous substituents are either too tedious to study using only experimental methods, or are not widely available (e.g., insensitive munition compounds). To address this, quantitative structure-activity relationships (QSARs) are developed to study the relationship between reactivity and chemical structure. To verify the descriptors that would provide the most accurate QSARs, a correlation analysis was performed between experimental and theoretical oxidation potentials of phenols and anilines to the kinetics of phenol and aniline oxidation by MnO_2.

We obtained experimental values using staircase cyclic (SCV), and square wave voltammetry (SWV), theoretical numbers were computed using density functional theory. The former gave more accurate correlations, while the latter was faster, allowing a much wider range of compounds to be studied. Correlations between theoretical oxidation potentials and kinetics of phenol and aniline oxidation by MnO_2 gave more diverse results than the correlation between experimental oxidation potentials and kinetics of oxidation by MnO_2. The correlation between the computed vs. kinetic vales had to be split into two datasets (phenols and anilines) to give statistically similar results as the experimental vs. the kinetic correlation. Direct comparisons between theoretical and experimental values varied widely. The best results were obtained by calibrating the theoretical values to experimentally acquired values, indicating that when using numbers calculated from theory, experimental calibration is required for accuracy.

Electrochemical methods used above were expanded to characterize a diverse suite of natural organic matter (NOM) samples and model compounds. NOM is an environmentally important, redox-active structure, similar in complexity to a protein. This complexity makes it hard to characterize, but its importance in many disciplines (e.g., medicine, biogeochemical cycles) makes it widely studied. To address its complexity, NOM has been fractionated into components based on solubility in acids and bases. We characterized 54 of these fractions using SCV and SWV, along with various model compounds for comparison, in an aprotic solvent.

The majority of the NOM fractions redox potentials behaved similarly. This behavior could be due to the extraction process during NOM fractionation, or the accessible redox groups being limited by the solvent used during the experiments. Most NOM fractions had a current response whose width (potential value where the current started and ended) spanned more than double the width of the model compounds, indicating the presence of possible multiple redox-active groups. There was no correlation between the various fractions and electrochemical behavior. To translate the NOM potentials to more environmentally relevant conditions, experiments on model compounds were performed in water and in an aprotic solvent (DMSO). The model compound peak potentials were plotted in water vs. DMSO, which resulted in two lines for the two peak potential values. The slopes of the lines were set to 1, and their intercepts were used to determine the average redox potentials of NOM in water. The estimated redox potentials for NOM in water were -0.128, -0.613, and -0.0930 V vs. SHE for E_{pa1}, E_{pc1}, and E_{p1} respectively.

Lastly, the electrochemical method suitable for in-situ temporal redox characterization was improved upon from previous work. Zero current chronopotentiometry (CP) was used to examine the effects on pH and redox potential when aqueous Fe(II) was added to various iron oxides. Iron oxides are crystalline structures made up of Fe(III), and/or Fe(II) and oxides, hydroxides, or oxyhydroxides. Iron oxides are abundant in the environment and have been shown to be more redox-active when coupled to aqueous Fe(II) (which occurs naturally under various conditions), forming reactive mineral intermediates (RMIs). Due to iron oxide abundance and increased reactivity in the presence of aqueous Fe(II), there is significant interest in characterizing their dynamic redox properties.

Six iron oxides were characterized using CP in a buffered solution, followed by three representative (Fe(III), Fe(II)/Fe(III), Fe(II) containing) iron oxides in unbuffered solutions. We monitored pH, and open circuit potential (E_{OC}) over several hours, while adding various components (e.g., iron oxide to electrolyte, Fe(II) aqueous to iron oxides). The E_{OC} of the iron oxides behaved predictably, with Fe(III) containing iron oxides (e.g., goethite) having the most positive, and Fe(II) containing minerals (e.g., siderite) having the least positive E_{OC} values respectively. Upon addition of aqueous Fe(II), all iron oxides converged to similar E_{OC} values, of approximately -400 mV vs. Ag/AgCl. Another similarity between the iron oxides studied was the first addition of Fe(II) resulting in the steepest E_{OC} decline. E_{OC} response with second and third additions of aqueous Fe(II) was significantly less. When the first addition of Fe(II) concentration was reduced seventeen-fold, the E_{OC} response did not decline proportionately. These findings suggest that *(i)* surface site availability is not a major factor in Fe(II) adsorption and the resulting E_{OC}, *(ii)* aqueous Fe(II) adsorption is dependent on structural Fe(III), *(iii)* and the first addition of Fe(II) causes the steepest decreases in E_{OC} indicating that the formation of RMIs is instantaneous and additional perturbations have much less of an effect.

Next, we plotted E_{OC} vs. pH of the experimental data and theoretical values using Fe(II) alone and three representative minerals (goethite, magnetite, and siderite) with Fe(II) included. Experimental values for aqueous Fe(II) matched the theoretical data for the formation of $Fe(OH)_3$. Goethite (GT) experimental values fell in between the values calculated for the redox couples GT/Fe(II) and GT/$FeCl_2$. Magnetite (MT) was slightly above the redox couples MT/$FeCl_2$ and MT/GT, and siderite (ST) fell in between ST/$Fe(OH)_3$ and ST/GT, ST/HT, ST/MT. Magnetite experimental data was anomalous, in that its EOC was more positive than that of the theoretical values. This was expected, as the theoretical data assumes stoichiometric magnetite (Fe(II)/Fe(III) = 0.5) in the calculation and our experimental values were obtained using a slightly oxidized magnetite (as shown previously by our lab), which would have a higher E_{OC} value.

Chapter 1. Introduction

1.1. Electron Transfer Mediators

Reduction, oxidation reactions are some of the most important processes in the environment, from electron transport systems of aerobic respiration and photosynthesis to element cycling. Electron transfer mediators (ETMs) are a central part of these reactions. ETMs are intermediate species that facilitate electron transfer in species that cannot directly and/or easily exchange electrons between themselves. For example, ETMs can shuttle electrons from humic substances to contaminants present in the environment, from insoluble minerals to microorganisms (*1*) and in nitrogen fuel cells to reduce N_2 to NH_3 (*2*).

In the laboratory, ETMs can be any reversible redox couple that aids in the transfer of electrons between non- or quasi-reversible couples and the electrode. ETMs have been used in the laboratory for over a century in many capacities, from speeding up electron transfer between the hard to access redox centers in proteins and a working electrode (*3*) or to help obtain potentials (amount of work needed to move charge V=J/C) for irreversible couples such as As(V)/As(III) (*4*). Ideally, a mediator should be fully reversible, meaning fast electron transfer with no side reactions, have a well-known redox potential, and react with known proton and electron stoichiometry. For a one-electron reaction, ETMs mediate over approximately ±120 mV, per the Nernst equation (log of reduced/oxidized (r/o) activities), and the assumption that mediators are effective between ratios of r/o = 100/1:1/100 (*5*). If a wide potential window is needed, multiple mediators need to be employed, and verification is needed to ensure that the mediator's potentials do not change when grouped due to side chemical reactions as shown in **Figure 1.1**.

Most environmentally relevant ETMs fall into four classes: flavins, porphyrins, siderophores, and quinones. In this study, we focused mostly on quinones, because they are ubiquitous in the environment. Quinones are oxidized forms of aromatic molecules, such as phenols and catechols (Section 1.2). Quinones serve in electron transport during photosynthesis and aerobic respiration and are thought to make up the redox-active group in natural organic matter (NOM) (Section 1.3). Because quinones are widespread, how they interact with other species is important. You can use redox potentials of quinones to help predict redox properties, and/or reaction kinetics of other species, whose potentials are not widely available or cannot be obtained for one reason or another. Relationships between oxidation rate constants and electrochemical potentials will be discussed in **Chapter 2**, along with the value of using both experimental and computed numbers in these types of correlations.

Formal potentials (experimental) can be more indicative of true redox behavior than standard (computed) potentials (*6*), as they are a direct measurement. For example, the difference between the formal and standard potential for a well-known reversible couple Fe(II)/Fe(III) can vary 100 mV, or more depending on the experimental conditions. This value is not insignificant when trying to predict the behaviors of other less-known species. Experimental potentials are easily and quickly obtained using electrochemistry, which will be discussed in more detail as it pertains to our work in Section 1.5.

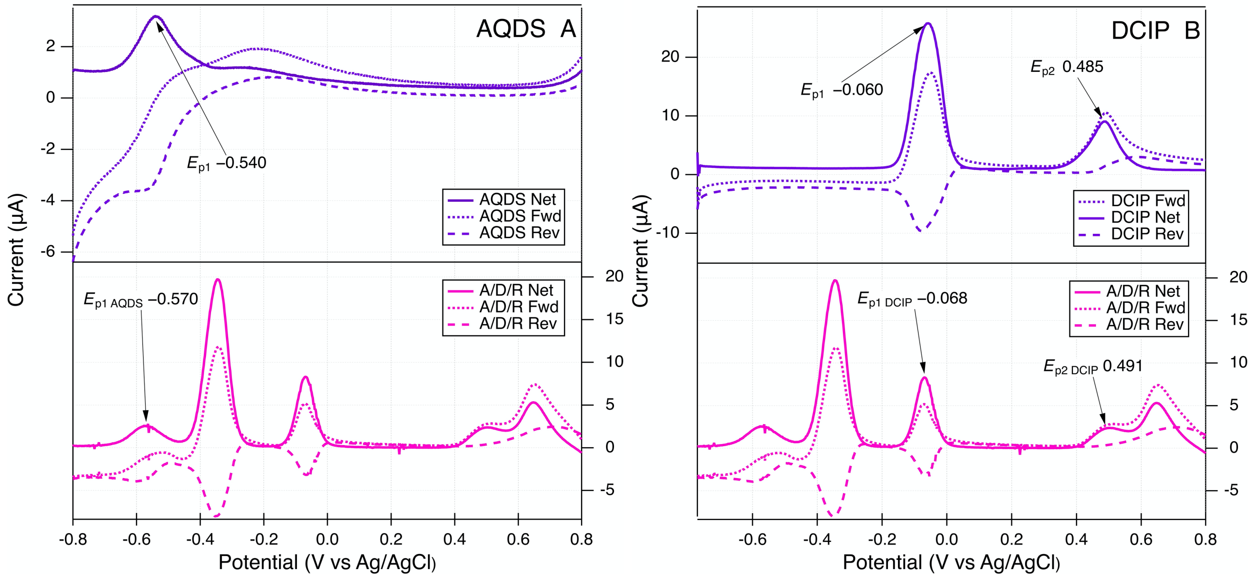

Figure 1.1. SWV of (A) 9,10-Anthraquinone-2,6-disulfonic acid disodium salt (AQDS) and (B) 2,6-dichloroindophenol sodium salt (DCIP). Top (purple) is the forward, reverse, and net current response of the individual compound, and below (pink) is the combined forward, reverse, and net current of three mediators, AQDS, DCIP, and resorufin (individual scan for resorufin not shown). Conditions: 10 mM NaCl, 10 mM HEPES, 1 mM mediator, 3 mm glassy carbon working electrode, 3.0 M KCl Ag/AgCl reference electrode encased in a fritted bridge tube filled with 10 mM NaCl and 10 mM HEPES, Pt coil reference electrode, scan rate 25 mV s^{-1}, step size 2 mV, amplitude 25 mV. Reprinted from Pavitt et al., see Appendix C for more details.

1.2. Phenols and Anilines

Phenols and anilines are aromatic hydrocarbons with a hydroxyl group (phenol), or amino group (aniline) bonded to a benzene ring. Both phenols and anilines are prevalent in the environment (phenols more than anilines). Anilines are primarily synthesized and used industrially, including in herbicides, dyes, and drugs. Phenols are both natural (synthesized by plants and microorganisms) and synthesized industrially for use in pesticides, pharmaceuticals, resins, and plastics. In addition to phenols and anilines persistence in the environment as contaminants, phenols play an important role in natural systems—from their antioxidant properties (*7*), oxygenic photosynthesis (*8, 9*), as mediators in redox reaction chains, and presence in natural organic matter (*10*) (Section 1.3). Phenols and anilines have a variety of substituents **Figure 1.2**, with each substituent altering the reactivity of its parent compound.

Due to the broad range of phenols and anilines, it would be daunting to experimentally characterize each one. An alternate approach is to obtain experimental potentials for a set of environmentally relevant phenols and anilines and correlate their reactivities to their structures (e.g., quantitative structure-activity relationships (QSARs)). To this end, we measured oxidation potentials of 38 phenols and 18 anilines and used these potentials (along with computed values) to perform correlation analysis between experimental, theoretical, and rate constants for oxidation by manganese oxides to verify the most precise descriptors for QSARs, of which the details can be found in **Chapter 2**.

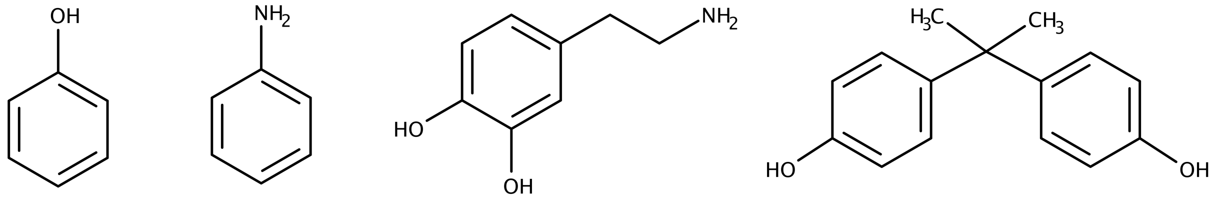

Phenol Aniline Dopamine Bisphenol A

Figure 1.2. Structures for phenol, aniline, dopamine, and bisphenol A.

1.3. Natural Organic Matter

Another type of ETM present in abundance in the environment is natural organic matter (NOM). NOM is the product of decaying plants and microorganisms. It is a complex structure composed of various quinone monomers bonded through hydrogen atoms (*11, 12*). NOM is redox-active and is therefore immensely important in environmental processes, and global biogeochemical cycles (*13-15*). NOM has been associated with contaminant degradation (*16-19*), waste water treatment (*20*), cancer research (*21, 22*), and trace element mobility (*23-25*).

Due to its importance NOM has been studied extensively, with the most recent and best efforts of characterization of NOM coming from Fourier-transform ion cyclotron resonance mass spectrometry (FTICR-MS) studies (*26-28*). Electrochemical characterization of NOM is probably the most important but has faced difficulty due to a lack of electrode response between NOM and various working electrode materials. This lack of electrode response could be due to NOMs structure.

NOM structure is not unlike a protein, whose redox-active centers are hidden and unavailable to macro-scale electrodes. There are several ways to address this issue (*i*) immobilize the analyte onto the electrode (e.g., protein film voltammetry), (*ii*) use an ETM to communicate between the analyte and the working electrode, (*iii*) use an aprotic solvent to allow hydrophobic structures to unwind due to the absence of water and thereby allow access to hidden redox centers. In our work, we performed electrochemistry in an aprotic solvent to characterize 54 NOM fractions, 7 model compounds and 2 fresh plant extracts **Figure 1.3**, the details of which can be found in **Chapter 3**.

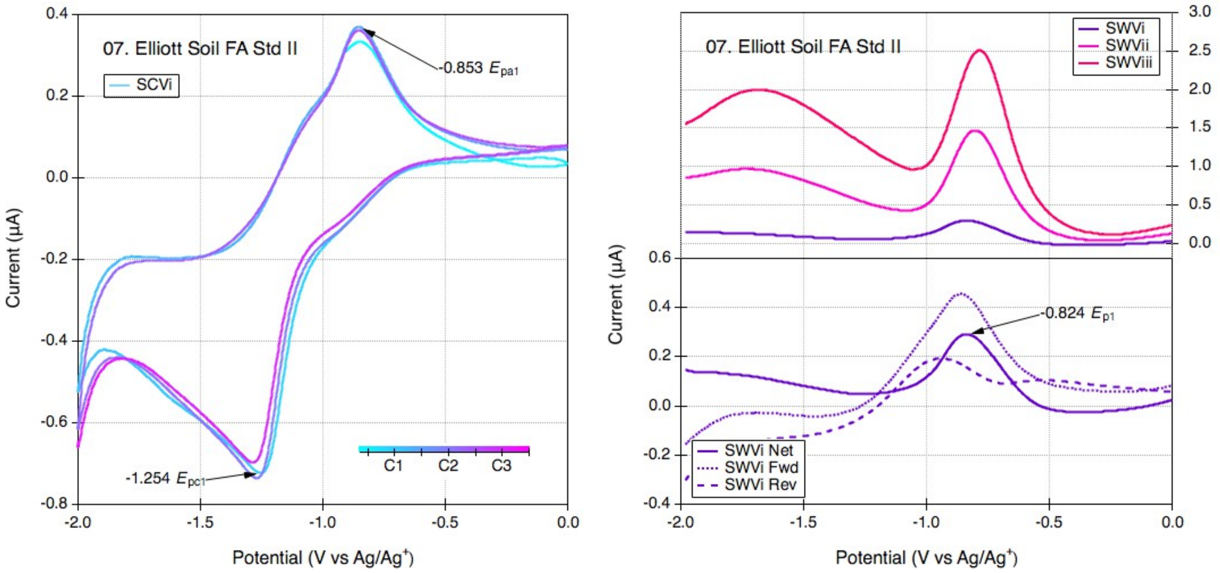

Figure 1.3. Staircase cyclic voltammogram (left) and square-wave voltammogram (right) of Elliott soil fulvic acid (#7 of 54). The square-wave voltammogram features the use of (top) three different scan rates and (bottom) one scan rate showing the forward, reverse, and net currents.

Conditions: 1.0 mg/mL of analyte in 0.1 M TBAFP in DMSO, 1.6 mm Pt working electrode, Pt coil counter electrode, Ag/Ag+ reference electrode filled with 0.1 M TBAFP and 0.005 M $AgNO_3$ in DMSO. Scan rate: SWV*i* and SCV*i* 25 mV s^{-1}, SWV*ii* 125 mV s^{-1}, SWV*iii* 225 mV s^{-1}. Step size 2 mV, amplitude 25 mV. Reprinted from Pavitt et al., see Appendix B for more details.

Because NOM is large and complex, studies of NOM are usually performed on fractions. NOM can be divided into non-humic (insoluble) and humic (soluble) substances. The humic substances are further divided into humic and fulvic acids, dependent on whether they precipitate out of a basic solution upon acidification (humic acid), or not (fulvic acid). Other operational definitions include dissolved organic matter (DOM), which consists of aquatic NOM (mostly derived from terrestrial NOM) after passing through a 0.45 µm filter, particulate organic matter (POM) does not pass through the filter, hydrophobic acid (HPOA) and transphilic acid (TPIA) which correspond to resin extracted fractions XAD-8 and XAD-4 respectively.

1.4. Iron Oxides

Iron oxides are a suite of inorganic compounds that are prevalent in the environment, are redox-active, studied extensively due to their importance in many areas from contaminant degradation (*29*) to medical applications (*30*), and are hard to study electrochemically due to sluggish electrode response. On the other hand, Fe(II) forms a reversible couple with Fe(III) and therefore is very easy to characterize, and by definition can be added to an irreversible couple to act as an ETM. Aqueous Fe(II) and iron oxides existing together in the environment are very common (e.g., weathering of Fe(II) rocks, areas of microbial respiration, upwelling of anoxic waters, etc.).

When aqueous Fe(II) is added to iron oxides, Fe(II) adsorbs and the adsorbed Fe(II) donates an electron that travels through the crystal (conduction) and reduces an Fe(III) in the iron oxide structure (*31*). In this way, iron oxides with adsorbed Fe(II) can be thought of as doped semiconductors. They are semiconductors because energy is needed to transfer an electron from one orbital (highest occupied molecular orbital, HOMO) to another (lowest unoccupied molecular orbital, LUMO), and doped because we introduced an element (Fe(II)) to lower the difference between the two energy levels. This lowering of the band gap (the region between HOMO and LUMO) enables electrons to flow with less external energy. It is feasible that a lower band gap could make the electrons more available to interact with other species nearby, such as contaminants. It has been shown in many studies that iron oxides doped with Fe(II) can reduce species that Fe(II), or iron oxides alone cannot (*32-34*). This is one of the primary reasons there has been so much interest in studying iron oxides associated with aqueous Fe(II).

There are sixteen iron oxides and they are composed of Fe (either Fe(II), or Fe(III)) with oxides (O), hydroxides (OH), or oxide hydroxides (OOH). For simplicity, they will be referred to collectively as iron oxides. In our study, we focused on five iron oxides (goethite, hematite, magnetite, lepidocrocite, wustite) and one iron carbonate (siderite). Goethite, hematite, and lepidocrocite contain Fe(III). Goethite can be found in soils and sediments and is one of the most thermodynamically stable iron oxides (*35*). Hematite is common in rocks and soils (large deposits in banded iron formations), is the oldest known iron oxide, is very stable, and as a result often the end species after transformations (*35*). Lepidocrocite is formed from the weathering of iron minerals and iron ore deposits, it is the oxidation product of Fe(II) in soils, biota, and rust. Magnetite contains both Fe(II) and Fe(III), it occurs in almost all igneous and metamorphic rocks and is responsible for the magnetic properties of rocks. Magnetite can also be found in bacteria and animals, including humans. Wustite and siderite contain Fe(II). Wustite is usually deficient in oxygen (non-stoichiometric), and is an important intermediate in the reduction of iron ores. For example, in a highly reducing environment magnetite is converted to wustite by reduction of all of its Fe(III) ions. However, such strongly reducing environments are rare in nature. Siderite is a common mineral and can be found in carbonate sediments and rocks. Large concentrations of siderite have been found in some salt marshes. Almost all of the iron oxides are crystalline with the degree of crystallization depending on the conditions during formation (*35*).

1.5. Electrochemical Methods

Electrochemistry is a suite of versatile techniques that have been used in many different capacities: in synthesizing and characterizing electroactive films (*36*), in water treatment technologies (*37*), in medicine (tumors, and drug design (*38*)), and energy storage and battery research (*39*). They represent one of the few methods that can be used to synthesize a species, such as a short-lived radical, and characterize its redox properties in one experiment. Electrochemistry can be divided into two sections, controlling either current or potential as both cannot be varied at the same time. Methods where current is varied (or kept constant) potential or current is measured vs. time. Methods where potential is varied (or held constant) current is measured vs. time or potential. Primarily, we will discuss the methods used in the subsequent chapters. These methods involve varying the potential and measuring current vs. potential, which include the sweep methods, staircase cyclic voltammetry (SCV), and square wave voltammetry (SWV), or keeping the current constant and measuring potential vs. time, which includes zero-current chronopotentiometry (CP).

Voltammetric methods (applying a potential excitation signal) take place in a three-electrode cell. The working electrode (WE) is where the potential is applied and where the analysis is focused. In SCV and SWV, the potential changes with respect to the reference electrode (RE) as the scan proceeds. The RE potential remains fixed and the WE potential is read vs. the RE. Eventually, at a characteristic potential, an analyte will lose an electron (for an oxidation reaction) to the WE. The electron will flow from the WE through the potentiostat (also where signals are generated) to the counter electrode (CE) where the analyte gains an electron. The reverse happens for a reduction reaction, where the analyte gains an electron from the working electrode. This electron flow is current, formally defined as charge (Q) passing with time (t) (Q/t). Since we are only focused on what happens at the working electrode, oxidation/reduction reactions are loss/gain of electrons from/to the analyte in solution to/from the working electrode respectively.

Staircase cyclic voltammetry (SCV) involves stepping the potential from point A to point B (switching potential) and back to A (one scan). The user chooses the step size, the number of scans, and the speed at which the scan progresses. Varying these parameters is informative of what is happening in the electrochemical cell. For example, an electron transfer reaction (E) followed by a chemical reaction (C) that produces an electroactive species will manifest in a voltammogram with a new peak potential in the second scan that was not present in the first scan **Figure 1.4**. In addition to the importance of performing multiple scans, varying the scan rate can be indicative of an EC reaction mechanism. If the scan is performed at a faster rate than the following chemical reaction a new peak will not form because the chemical reaction will not have had time to occur during the time course of the experiment. Varying the scan rate is one way to diagnose the reversibility of a system. Fast reversible electron transfer reactions in SCV fulfill the following criteria *(i)* the anodic and cathodic peak potentials are 0.059 mV apart for a one-electron reaction as per the Nernst equation, *(ii)* ratio of the peak currents is 1, *(iii)* square root of the scan vs. current is linear, *(iv)* increase in scan rate increases current but does not change the potential.

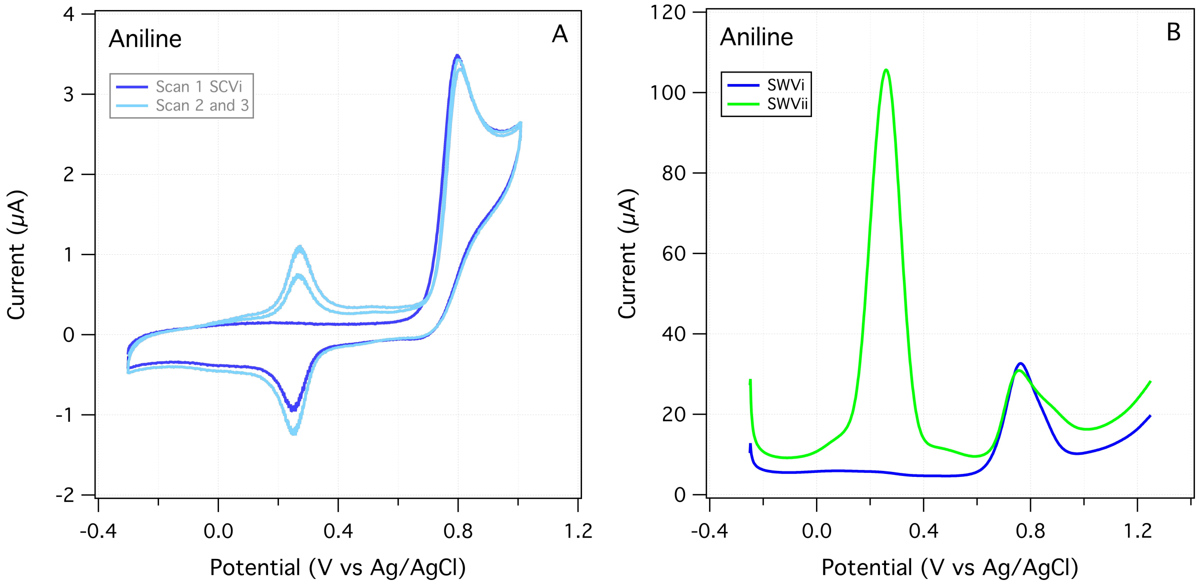

Figure 1.4. (A) SCV and (B) SWV of Aniline. In the first scan (dark blue) of the SCV and the first SWV (SWV*i*) there is no oxidation peak (positive current) at ~ 350 mV. In SCV, a reduction peak (negative current) appears on the first scan and both oxidation and reduction peaks are present for scans two and three. In SWV*ii* (the second scan) a new peak appears. Both the SCV and SWV indicate that an electrochemically reversible species formed after the first anodic scan. Conditions: 2.5 x 10^{-4} M analyte, pH 5.1, in 25% IPA/ 0.5 M acetic acid and sodium acetate buffer, GC working electrode, Ag/AgCl 3 M KCl reference electrode, 0.5 mm Pt wire counter electrode. Scan rate: SCV 25 mV s^{-1}, SWV*i* 60 mV s^{-1}, SWV*ii* 60 mV s^{-1}, step size 2 mV, amplitude: SWV*i* 50 mV, SWV*ii* 75 mV. Reprinted from Pavitt et al., see Appendix A for more details.

SCV can be very informative concerning qualitative analysis, especially in complex systems. It is important to note that due to the nature of the potential scan, SCV is not well suited for quantitative analysis. This is exemplified in **Figure 1.5**, where cyclic and square-wave voltammograms are overlaid, and the square-wave voltammogram shows a smaller net current response than the cyclic voltammogram for the same experiment. In electrochemical experiments, faradaic processes and non-faradaic processes are occurring at the same time. Faradaic processes are ones in which electron transfer is taking place between the analyte in solution and the electrode. In non-faradaic processes, the charge that is passed is not due to redox processes. As you scan the potential in SCV, you build up a charge. However, because there is no way to quantify how much charge is built up as the scan proceeds, it is difficult to use this method for quantitative analysis. A better method for quantitative evaluation is square wave voltammetry.

In SWV, the scan is pulsed in a forward and reverse fixed value (user-chosen step size), incrementally stepping up in voltage (or down if scanning cathodically). The result is voltage vs. net current. The net current response is a subtraction of the forward and reverse current response, and as evidenced by **Figure 1.5** is smaller than the current response in the SCV method. The nature of the pulse in SWV keeps the charging current to a minimum allowing for more quantitative analysis. SWV also allows separation of the net current into forward and reverse components which can be used to diagnose processes at the working electrode **Figure 1.5**. Much like with SCV, you can determine the reversibility of a redox reaction by examining the forward and reverse components of the current. A fast, reversible reaction will have *(i)* the forward and reverse peak potentials at the same potential, *(ii)* the forward and reverse current ratio is 1, *(iii)* increase in scan rate increases current but does not change potential, *(iv)* square root of the scan rate vs current is linear. Deviations from these criteria indicate irreversibility.

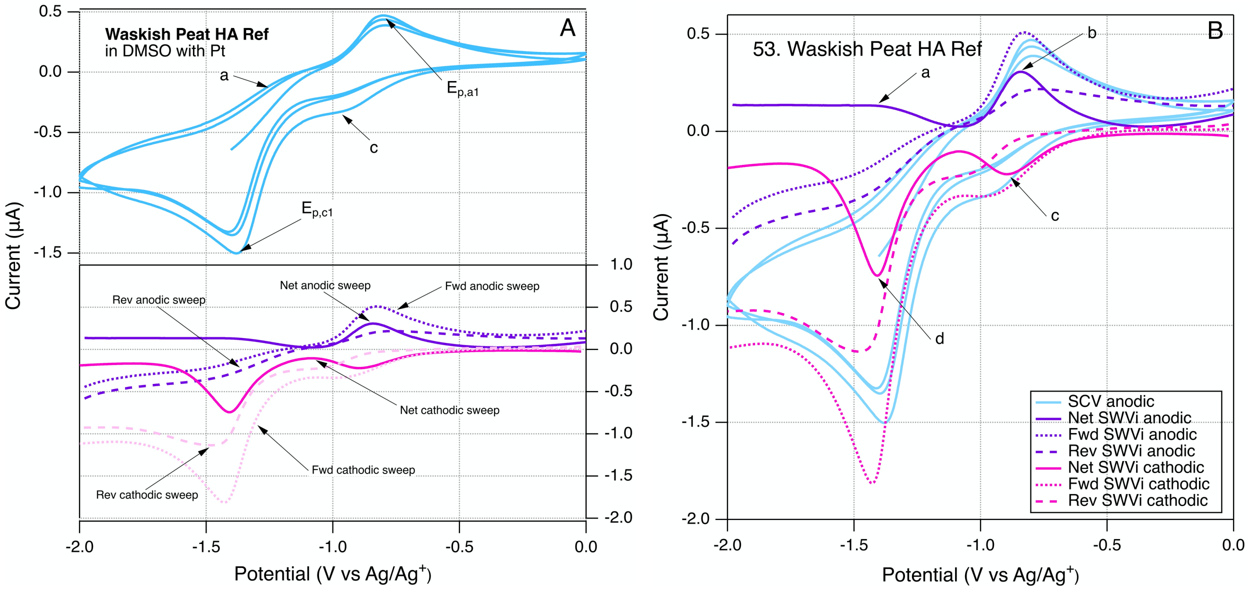

Figure 1.5. SCV (blue) and SWV anodic (purple) cathodic (pink) sweeps for Waskish Peat HA. Conditions: 1.0 mg/mL of analyte in 0.1 M TBAFP in DMSO, 1.6 mm Pt working electrode, Pt coil counter electrode, Ag/Ag+ reference electrode filled with 0.1 M TBAFP and 0.005 M AgNO$_3$ in DMSO. Scan rate: SWV*i* and SCV 25 mV s^{-1}, step size 2 mV, amplitude 25 mV. Reprinted from Pavitt et al., see Chapter 3 for more details.

To help describe the characteristic shape of SCVs, **Figure 1.6** shows a voltammogram of a model quinone. The oxidation and reduction reactions are a two-electron process, hence the two peaks in the positive and in the negative ordinate. In the oxidation reaction, the hydroquinone gets oxidized, loses one electron to form a semi-quinone, followed by another electron to form a quinone. The reduction reaction is the reverse, where the quinone gets reduced (gains an electron) to the semi-quinone, followed by reduction to the hydroquinone.

Moving from left to right in the abscissa, as the potential is scanned to a more positive value the energy of the working electrode (WE) is lowered. At a specific energy level (characteristic of the analyte), when the lowest unoccupied molecular orbital (LUMO) of the electrons in the WE is lower than the highest occupied molecular orbital (HOMO) of the electrons in the molecule, the electrons will transfer to the WE to maintain a lower energy level. The transfer of electrons results in current response. At the working electrode, as the electrons are being removed from species in solution, the charge becomes more positive with respect to the bulk solution. To maintain charge balance, species diffuse to the working electrode (ions migrate and help the analyte diffuse) when the analyte arrives it is oxidized, resulting in more current flow. Eventually, a point is reached when species cannot diffuse any faster. As the diffusion layer grows, diffusion slows and the current starts declining. The peak grows and decays following diffusion and the Nernst equation, as potential changes, so do the concentrations of reduced to oxidized ratios. The Nernst equation describes the ratio of the activities of the reduced to oxidized species at a particular potential away from the standard potential. Scanning in the negative direction (cathodically), reduction currents flow as a result of the transfer of electrons from the WE to the analyte.

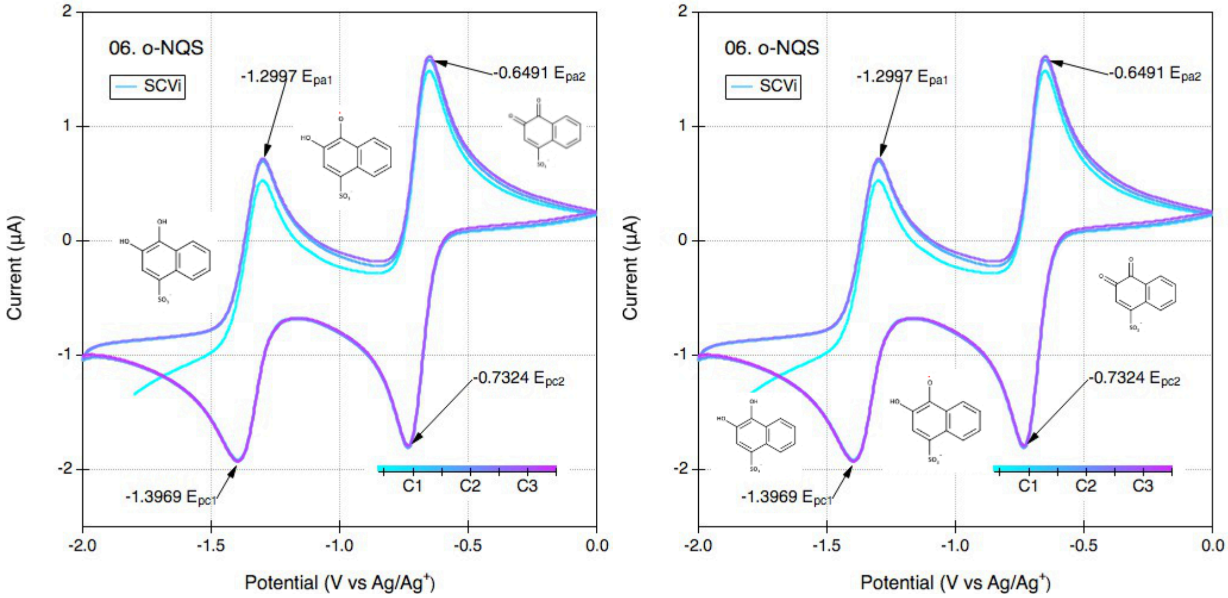

Figure 1.6. SCV of model quinone, 1,2-naphthoquinone-4-sulfonic acid disodium salt (o-NQS). Scanning from -2.0 to 0 V, E_{pa1} corresponds to hydroquinone (*40*) gaining an electron to form semi-quinone (SQ), E_{pa2} semiquinone gains an electron to become a quinone (Q). Scanning from 0 to -2 V E_{pc2} is Q to SQ, E_{pc1} is SQ to HQ. Conditions: 1.5 mM of analyte in 0.1 M TBAFP in DMSO, 1.6 mm Pt working electrode, Ag/Ag+ reference electrode filled with 0.1 M TBAFP and 0.005 M $AgNO_3$ in DMSO, Pt coil counter electrode. Scan rate 25 mV s^{-1}, step size 2 mV. Adapted from Pavitt et.al., see Chapter 3 for more details.

Each redox-active species will have a characteristic potential where electron transfer occurs, depending on the energy levels of its molecular orbitals. The potential determines where the current flows, while the magnitude of the current is determined by the rate of the redox reaction. The rate is controlled by transport to and from the WE, and the rate at which electrons pass between species in solution and the WE. Transport can come from diffusion, convection, or migration. To simplify modeling this behavior, one or more contributions, such as convection (non-stirred solutions), or migration (movement of ions) can be eliminated. The latter can be minimized by having at least two orders of magnitude higher electrolyte concentration than analyte concentration.

Unlike the last two methods, where the measurements were active, zero current chronopotentiometry (CP) is a passive measurement (potential is measured with respect to time without any external perturbations). Passive measurements are useful for sensitive samples that otherwise might be altered irreversibly by applying a large potential. CP employs two electrodes, the WE and the RE, and is one of the simplest measurements to make. CP is very powerful for the qualitative determination of in-situ redox characterization of dynamic systems. For example, this technique is applied here to study in real-time what happens when aqueous Fe(II) is added to various iron oxides (**Chapter 4**).

Here we have shown how three electrochemical methods can be used to determine numerous processes. Varying the electrochemical parameters is useful for diagnosing electron transfer and chemical reaction mechanisms, reversibility of redox reactions, adherence of species to the electrode, and formation of electroactive species. Electrochemical methods can be combined with ease to thoroughly study complex systems, such as NOM, and be used to verify redox processes that might otherwise be misdiagnosed. Electrochemistry measurements are simple to make, accessible to most laboratories as they are less costly than most analytical instruments, and can be performed anywhere (potentiostats are available in the size of smartphones), including in a glove box or at a field site. In **Figure 1.7** several of these aforementioned categories were summed and used to compared to other analytical methods. Electrochemistry has been underutilized but has been gaining popularity in various fields, as it can be used for numerous purposes other than characterizing redox reactions, such as synthesis and analysis of organic molecules (i.e., pharmaceuticals), battery research and energy storage, corrosion protection, and medical technologies and devices.

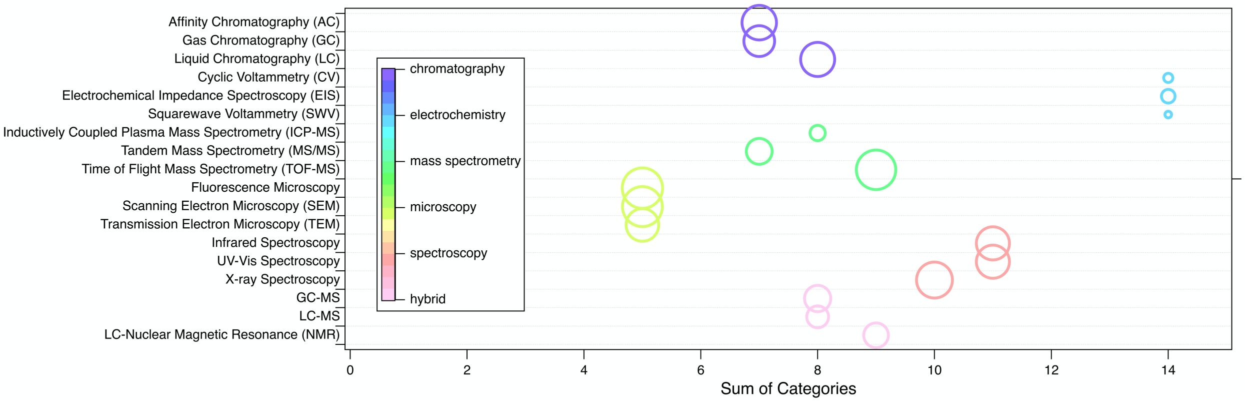

Figure 1.7. Types of analytical methods (colors) vs. sum of categories. The size of the circles represents the number of Google Scholar results for that particular method. The categories include: ease of use (includes sample prep, and instrument maintenance), destructive or non-destructive method, portability, cost of instrument, and specificity of results. Each category was assigned a value of 1-3. The higher number represent the easiest to use, the least expensive,

etc. For example, electrochemistry plots as the easiest, least expensive, portable, but is underutilized as evidenced by the small circles.

1.6. Objectives

Objective 1—Develop and apply electrochemical methods to characterize the redox properties of a wide suite of environmentally relevant electron transfer mediators. Use experimental redox potentials to verify calculated potentials and use both in correlation analysis, with kinetic data to verify the most precise descriptors for QSARs. Verifying descriptors for QSARs will aid future studies to better relate experimental and/or calculated values to other significant descriptors (e.g., kinetics of contaminant degradation, toxicity values of hazardous chemicals, pathological factors in disease processes), and aid in improvements or corrections to calculation theories that are inexpensive and easily available.

Objective 2—Extend and validate electrochemical methods from Objective 1 to directly characterize more complex systems, such as natural organic matter (NOM). Improve electrode response between NOM and the working electrode by using an aprotic solvent, so that NOM potentials can be measured directly. Measuring NOM potentials directly is central for verification of potentials obtained using mediators. More importantly, NOM redox potentials can aid in the prediction of carbon sequestration which affects climate change, transport and distribution of contaminants, trace metals, and nutrients, which are responsible for eutrophication.

Objective 3—Develop and apply a non-destructive temporal electrochemical method for direct characterization of redox properties of in-situ formed reactive mineral intermediates (RMIs). RMIs are transient and very reactive, characterizing their redox properties as they form and how they change over time is key in developing predictions of their behavior in the environment. RMIs are important for contaminant degradation, the release of contaminants, or trace metals during mineral dissolution, biogeochemical cycling of elements, act as terminal electron acceptors in microbial respiration, and influence bioavailability of nutrients.

1.7. Thesis Organization

Chapter 1. Introduction

This chapter is a general discussion on the description, importance, and background of electron transfer mediators, phenols and anilines, natural organic matter, and iron oxides. Electrochemical methods used to study the redox properties of the aforementioned species are discussed, including staircase cyclic voltammetry, square-wave voltammetry, and zero current chronopotentiometry.

Chapter 2. Oxidation Potentials of Phenols and Anilines: Correlation Analysis of Electrochemical and Theoretical Values.

In this chapter, a broad range of phenols and anilines were characterized electrochemically using SCV and SWV. Theoretical redox potentials were calculated using density functional theory. The experimental potentials were cross-correlated with computed potentials and kinetics of phenol and aniline oxidation by manganese oxides. All of these parameters were used to verify descriptors for developing relationships between phenol and aniline structure and reactivity. The experimental values gave more accurate results, while the computed numbers were faster. Calibrating the calculated values using experimental numbers gave the best results when correlating with the kinetics of phenol and aniline oxidation by MnO_2. In conclusion, both calculated and experimental values are complementary, experimental data are needed to ensure the accuracy of computed results, while computed results are faster.

Chapter 3. Electrochemical Characterization of Natural Organic Matter by Direct Voltammetry in an Aprotic Solvent.

A wide suite of natural organic matter fractions, along with model compounds, were electrochemically characterized using SCV and SWV. Qualitatively, the SCVs showed a wide redox response (twice that of the model compounds), indicating possible multiple redox-active moieties per sample. The peak potentials were surprisingly similar, despite the numerous samples analyzed. The lack of diversity in the peak potentials was attributed to (*i*) the fractionation method of standard NOM samples, and/or solvent choice selectively concentrating, or allowing access to only a small group of redox-active moieties, (*ii*) NOMs are only redox-active within a certain potential range and that range is similar for all NOMs, which is why the peak would decay in the same area for most samples, (*iii*) the redox-active species in NOM may not be very diverse as has been shown for a wide variety of quinones.

Chapter 4. Electrochemical Characterization of Reactive Mineral Intermediates (RMIs) from Fe(II) Amended Iron Oxides.

Zero current chronopotentiometry was employed to characterize the temporal in-situ formation of reactive mineral intermediates. The reactive mineral intermediates were formed from iron oxides and titrated aqueous Fe(II). Six iron oxides were studied, hematite, goethite, lepidocrocite, magnetite, siderite, and wustite in buffered solutions, followed by three representative oxides (goethite, magnetite, siderite) in non-buffered solutions. The iron oxides had varying open-circuit potentials (E_{OC}), with Fe(III) oxides (goethite, hematite, and lepidocrocite) having the most positive E_{OC} and Fe(II) containing oxides (siderite and wustite) having the lowest E_{OC}. When aqueous Fe(II) was added, the E_{OC} values converged to within ~ 50 mV of each other, suggesting a common initial RMI phase regardless of the mineral substrate. The subsequent addition of aqueous Fe(II) resulted in small E_{OC} changes. This prompted us to decrease the concentration of aqueous Fe(II) (first addition), but this still resulted in a large E_{OC} decrease and smaller subsequent decreases even though the Fe(II) concentration was seventeen-fold less (first addition). Our E_{OC} and pH data (non-buffered) suggest that surface site availability is not a major factor in Fe(II) adsorption and the resulting $E_{\mathrm{OC},}$ that Fe(II) adsorption is dependent on structural Fe(III), and the formation of the initial RMI phase is instantaneous and additional perturbations have a small effect.

Chapter 5. Summary

Chapter 5 is a summary of the electrochemical characterization of environmental electron transfer mediators and the broad conclusions from the various moieties studied.

Chapter 2. Oxidation Potentials of Phenols and Anilines: Correlation Analysis of Electrochemical and Theoretical Values[1]

Ania S. Pavitt, Eric J. Bylaska and Paul G. Tratnyek

2.1. Abstract

Phenols and anilines have been studied extensively as reductants of environmental oxidants (such as manganese dioxide) and as reductates (e.g., model contaminants) that are transformed by environmental oxidants (ozone, triple organic matter, etc.). The thermodynamics and kinetics of these reactions have been interpreted using oxidation potentials for substituted phenols and anilines, often using a legacy experimental dataset that is of uncertain quality. Although there are many alternative oxidation potential data, there has been little systematic analysis of the relevance, reliability, and consistency of the data obtained by different methods. We have done this through an extensive correlation analysis of kinetic data for phenol or aniline oxidation by manganese oxide—compiled from multiple sources—and oxidation potentials obtained from (*i*) electrochemical measurements using cyclic and square wave voltammetry and (*ii*) theoretical calculations using density functional theory. Measured peak potentials (E_p) from different sources and experimental conditions correlate very strongly, with minimal root mean squared error (RMSE), slopes ≈ 1, and intercepts indicative of consistent absolute differences of 50-150 mV; whereas, one-electron oxidation potentials (E_1) from different sources and theoretical conditions exhibit large RMSE, slopes, and intercepts vs. measured oxidation potentials. Calibration of calculated E_1 data vs. measured E_p data gave corrected values of E_1 with satisfactory accuracy. For oxidation by manganese dioxide, normalization of rate constants (to the 4-chloro congener) allowed correlation of phenol and aniline data from multiple sources to give one, unified quantitative structure-activity relationship (QSAR). Comparison among these QSARs illustrates the principle of matching the observational vs. mechanistic character of the response and descriptor variables.

---

[1] Reprint with permission from A. S. Pavitt, E. J. Bylaska, P. G. Tratnyek, Oxidation potentials of phenols and anilines: correlation analysis of electrochemical and theoretical values, Environ. Sci.: Proc. Impacts, 19, 339-349 (2017). Copyright 2017 The Royal Society of Chemistry.

2.2. Introduction

Phenol and aniline moieties are ubiquitous in the environment, biology, and commerce. They are characteristic components of many important organic compounds—including pesticides, pharmaceuticals, antioxidants, and various natural products—as well as polymeric materials, such as natural organic matter (NOM), lignin, and some resins and plastics. The most significant pathway for transformation of these compounds is often the oxidation of the phenol or aniline moieties, so this chemistry has been studied extensively. Many of these studies compare the reactivity of multiple substituted phenols and/or anilines, which has made them prototypical families of congeners for analysis of correlations between chemical structure and reactivity. The resulting abundance of data, and quantitative structure-activity relationships (QSARs) for correlations among these data, has led to a variety of cross-correlation and meta analyses and reviews thereof (*41-43*). This large body of work makes phenols and anilines good systems for illustrating or exploring general concepts regarding the development and application of correlation analysis.

With respect to the oxidation of phenols and/or anilines, most correlation analyses are structured as relations between rate constants for oxidation of multiple substituted phenols/anilines (by a single oxidant) and one or more descriptor variables that are either measured from electrochemical experiments or calculated from molecular structure theory. Other work has emphasized the development of theoretical methods for calculation of phenol/aniline redox properties, in part using correlations to experimental data for validation and/or calibration. In both cases, the most commonly used experimental descriptor data is the set of electrochemically-measured half-wave oxidation potentials ($E_{1/2}$) reported by Suatoni et al. in 1961 (*44*). This dataset is attractive for correlation analysis because it is accessible and relatively large (including 41 phenols and 32 anilines), was obtained under a consistent set of conditions that are compatible with biological and environmental science, and has accumulated a legacy as a useful descriptor dataset in studies of reactivity of various environmental oxidants.

The first studies to make prominent use of the $E_{1/2}$ data from Suatoni et al. in correlation analysis were focused on oxidation by manganese dioxide (MnO_2). These studies reported that measured rates (or rate constants) for oxidation by MnO_2 correlate well with $E_{1/2}$ for mono substituted phenols (*45*) and anilines (*46, 47*). Klausen et al. (*47*) showed that these correlations become superimposable when based on relative rate constants (k_{rel}), obtained by normalizing measured rate constants (usually k_{obs}) to rate constants for a common reference compound (they used the 4-Cl congener). In a recent study, we showed that correlations based on k_{rel} for aniline oxidation by MnO_2 were suffficently comparable to justify fitting QSARs using kinetic data from multiple sources (*48*). In **Figure 2.1A**, all of these data—including both phenols and anilines—are summarized, showing that the combined dataset for k_{rel} correlate sufficiently well to $E_{1/2}$ from Suatoni et al. to fit a single QSAR. As a meta statistical analysis, the correlation in **Figure 2.1A** is remarkably successful, but its theoretical interpretability is limited by the heterogeneous nature of the oxidant. Other correlation analyses that utilitize $E_{1/2}$ from Suatoni et al. involve oxidation of phenols by homogeneous solution-phase oxidants singlet oxygen (*42, 49, 50*), chlorine dioxide (*41, 50-52*) persulfate (*50*), and chromate (*50*)). Among these oxidants, chlorine dioxide is the most likely to produce kinetics controlled by simple outer-sphere one-electron transfer, and this made it possible to describe the kinetics using a model based on Marcus theory (*52*). For that analysis, free energies of oxidation for phenols by chlorine dioxide were calculated using the $E_{1/2}$ data from Suatoni et al., assuming—and then supporting—their claim that these $E_{1/2}$'s are the one-electron oxidation potentials for phenols. The data by Suatoni et al. also are included in a compilation by Meities and Zuman (*53*), which has been cited as the source of oxidation potentials for correlation analysis of rate constants for anilines with carbonate radical (*54*) and borate radical (*55*).

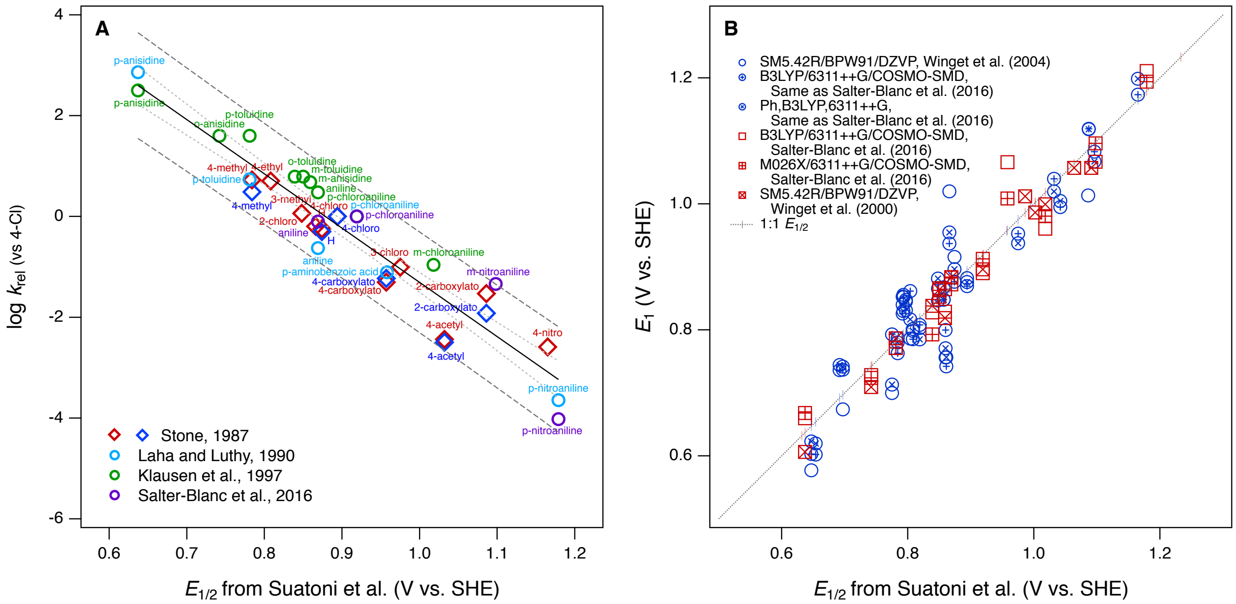

Figure 2.1. Examples of correlation analyses performed using $E_{1/2}$ for phenols and anilines from Suatoni et al. as the descriptor variable. (**A**) Rate constants (k_{rel}) for oxidation by manganese oxides; (**B**) One-electron oxidation potentials (E_1) calculated from theory.

The other most significant use of the $E_{1/2}$ dataset from Suatoni et al.—in the development of theoretical methods for calculation of phenol/aniline redox properties—assumes that the accuracy of the measured potentials is sufficient for them to be useful in validation of redox potentials calculated from chemical structure theory (*56, 57*). The primary example of this is work by Winget et al. where they found that their calculated one-electron oxidation potentials (E_1) for anilines (*58, 59*) and phenols (*60*) differed significantly from Suatoni's measured values of $E_{1/2}$ and these differences vary significantly with the level of theory used in the calculations. They discussed various possible sources of "error" in the theoretical calculations, and suggested that some of this error could be corrected by using the expected value of E_1 (here E_{1c}, for corrected by calibration), calculated from a regression of E_1 on $E_{1/2}$. The results of this calculation are shown in **Figure 2.1B** for selected sets of E_1 calculated by Winget et al. (*58-60*) and Salter-Blanc et al. (*48*). A linear regression (not shown) performed on all the data in this correlation does not differ significantly from the 1:1 line included in the figure, but the residuals are highly variable, within as well as between compounds, and therefore hard to rationalize as due to any one particular source of error.

The results in **Figure 2.1B** illustrate some of the general concerns that arise from the use of correlation analysis with computational electrochemistry. The first is that the absolute precision and accuracy required to make modeling results statisically satisfactory becomes relatively less severe as the calibration and application range of the model increases. This is evident in the contrast between **Figure 2.1B**, which suggests significant need for improvement in the residuals, versus studies such as Moens et al. (*61*) that aim to model a much wider range of compound structures—with a much wider range of potentials—and therefore find that the residuals that arise from utilizing $E_{1/2}$ data from Suatoni to be insignificant. Another general issue is that the overall fitness of correlation models increases when the variables included are consistent with each other—and with the intended applications of the model—with respect to their observational vs. mechanistic character. In this respect, a correlation such as in **Figure 2.1A**, which is between two properties measured in solution for one class of reactions, is a favorable formulation for describing the observed kinetics of phenol/aniline oxidation. In contrast, a calibration such as in **Figure 2.1B** is less favorable because it is based on correlation between two less consistent (less well "matched") variables: one that is a property measured in solution and another that is calculated from theory assuming an elementary reaction step that may, or may not, dominate the solution chemistry.

From a fundamental, mechanistic perspective, the mismatch implicit in calibrating theoretically calculated E_1's by correlation to electrochemically measured potentials, as in **Figure 2.1B**, should have significant disadvantages (*62, 63*). This has led recent studies to calibrate E_1's using potentials measured by methods such as pulse radiolysis (*63-67*), which should provide a more accurate estimate of potentials for reversible, one-electron oxidation of phenols/anilines. However, these data are less common, more complex to measure, and not necessarily more closely matched to the processes that are controlling solution-phase oxidation kinetics. Therefore, they may not provide the most useful, or even the most accurate, structure-activity relationships for oxidation reactions of environmental interest. To explore this hypothesis, a correlation analysis was performed with new and previously published data for kinetics of phenol/aniline oxidation by MnO_2, oxidation peak potentials measured electrochemically, and one-electron oxidation potentials calculated theoretically. Overall, the results show that correlations between these three properties are statistically similar, so the main factors that distinguish the results are (*i*) a small number and variable mixture of compounds that are significant outliers, usually of uncertain origin, and (*ii*) the breadth of structures and potentials covered, which is greater for the calculated and measured potentials reported here than was available previously.

2.3. Experimental

2.3.1. Chemical Reagents

All of the substituted phenols and anilines used in experiments are summarized in Appendix A (**Tables A1 and A2**) with source and purity data. 2-Propanol (isopropyl alcohol, IPA), sodium acetate, and acetic acid were from Fisher Scientific. All chemicals were obtained analytical grade or higher and used as received.

Stock solutions of the phenols and anilines were dissolved in IPA and stored in amber bottles for a maximum of three days. The buffer-electrolyte was made with 0.5 M acetic acid and 0.5 M sodium acetate ($pK_a = 4.54$). Before use, the buffer-electrolyte was diluted with IPA in varying amounts, usually to 25% or 50% IPA (v/v) to buffer.

2.3.2. Electrochemical Methods

All square wave voltammograms (SWV) were performed with an Autolab PGSTAT30. SWV were performed at varying amplitudes of 50, 75, 100, and 125 mV, and varying scan rates of 30, 60, 120, 180, and 240 mV s^{-1}. Staircase cyclic voltammograms (SCV) were performed with a Pine AFCBP1 Bipotentiostat, or an Autolab PGSTAT30. SCV were performed at varying scan rates of 25, 75, 125, 175, and 225 mV s^{-1}. The step size was 2 mV for all runs. Most runs were performed in duplicate. The SCV and SWV peaks were fit using the peak search function in Nova 2.02 for the Autolab and Aftermath 1.4.7760 for the Pine instruments. The three-electrode cell consisted of a Pine Research Instrumentation low profile 3 mm glassy carbon working electrode, an Ag/AgCl 3 M KCl reference electrode (BASi), and a 0.5 mm diameter platinum wire (Alfa Aesar) counter electrode. All potentials measured in this work are corrected from the Ag/AgCl reference electrode to standard hydrogen electrode (SHE) by adding 209 mV (*68*). Note that the potentials measured by Suatoni et al. were reported vs. the saturated calomel electrode, so those data were converted to SHE by adding 241 mV (*68*) for use in this study.

Before each set of electrochemical measurements, the working electrode was polished using a 0.05 μm MicroPolish Alumina (Buehler), washed with 1% Micro90 (International Products Corp.) and water, rinsed several times with DI water, sonicated for 5 min, and rinsed again with DI water. The electrochemical cell was prepared by adding 10 mL of buffer-electrolyte-IPA solution and purging for 10 min with N_2 (ultra-high purity). After deaeration a background scan was performed, subsequently the solution was spiked with 1 mL of the compound of interest and purged for 2 min with N_2. A layer of N_2 was kept over the solution for the duration of the experiment. The initial concentration of all phenols and anilines in the cell was 2.5×10^{-4} M. The pH of the solution was measured using a glass combination electrode calibrated at pH 4.00 and 7.00. The measured pH (pH_{meas}) was 5.1 and 5.6 for 25% IPA and 50% IPA respectively.

2.3.3. Computational Methods

In previous work (*48*), we compared the performance of several electronic structure methods (functionals, basis sets, and solvation models) for computation of one-electron oxidation potentials for aromatic amines (E_1) from chemical structure theory, and a selection of those methods was used in this study, with minor modifications. Only oxidation of the neutral form of the parent compounds was considered ($ArOH \rightleftharpoons ArOH^{\bullet+} + e^-$ and $ArNH_2 \rightleftharpoons ArNH_2^{\bullet+} + e^-$). The electronic structure calculations were carried out using density functional theory (DFT) calculations (*59*) using the 6-311++G(2d,2p) basis set (*59, 61*) and the B3LYP (*62, 63*) and M06-2X23 exchange correlation functionals. Solvation energies for parent and oxidized compounds were approximated using both the COSMO and COSMO-SMD methods. Other recent studies have performed similar calculations (*58, 59, 61, 63-67*), and the calculations here, which make use of large triple zeta basis sets, are expected to be well converged. All of the calculations were done using NWChem.28. Additional details regarding the computation methods are given in Appendix A.

2.4. Results and Discussion

2.4.1. Electrochemical Method Optimization and Validation

The objectives of this study include reevaluating the $E_{1/2}$ dataset from Suatoni et al., but also establishing a new, expanded dataset of measured potentials using updated and refined methods. Therefore, we attempted to replicate Suatoni's methods as much as possible during preliminary investigation of operational variables that were likely to be significant, and only made changes where a substantial benefit was expected. Based on considerations presented in Appendix A, we chose solution chemical conditions that were nearly identical to those in Suatoni et al. ($C_0 = 2.5 \times 10^{-4}$ M phenols or anilines, 0.5 M NaAc/HAc buffer in 50/50 v/v% isopropanol/water ($\mathrm{pH}_{\mathrm{meas}} = 5.6$), ambient temperature = 23±2 °C). The only notable difference in solution conditions is that the experiments by Suatoni et al. were aerobic and ours were purged with N_2 to remove O_2. For our working electrode, we chose a commercial glassy carbon electrode, rather than trying to replicate the custom wax-impregnated electrode used by Suatoni et al. Preliminary experiments were performed on both a pyrolytic graphite edge electrode and a wax impregnated graphite electrode was used to simulate Suatoni et al. There was no difference in potentials between electrodes and since better results were obtained with the glassy carbon electrode only those results are presented.

Suatoni et al. performed anodic voltammetry by polarography, apparently measuring only linear, anodic potential sweeps (in duplicate). They reported half-wave potentials ($E_{1/2}$), but no raw data were shown, so the robustness of their calculations cannot be evaluated. In polarography, $E_{1/2}$ is obtained from the potential of half the peak current (*69*), and these potentials are directly related to the formal reduction potentials used in the Nernst equation (*70*). $\mathrm{E}_{1/2}$ can also be related to the half-peak potentials ($E_{p/2}$) obtained from cyclic voltammetry, because $E_{p/2} = E_{1/2} \pm 28.0$ mV/n (subtract for oxidation) (*69*). To acquire $E_{p/2}$ from CVs such as obtained in this study, we could use the mean value of the cathodic and anodic peak potentials, or the potential that corresponds to the current at half height. Because the majority of our data were irreversible voltammograms, we did not use $E_{1/2}$, or $E_{p/2}$, but instead we usually report peak potentials (E_p) obtained directly from the SCV data (exemplified with aniline in **Figure 2.2A**). For two compounds (dopamine and 4-aminophenol), E_p was calculated from SCV data using $(E_{pa} + E_{pc})/2$ because these compounds were reversible (*71*).

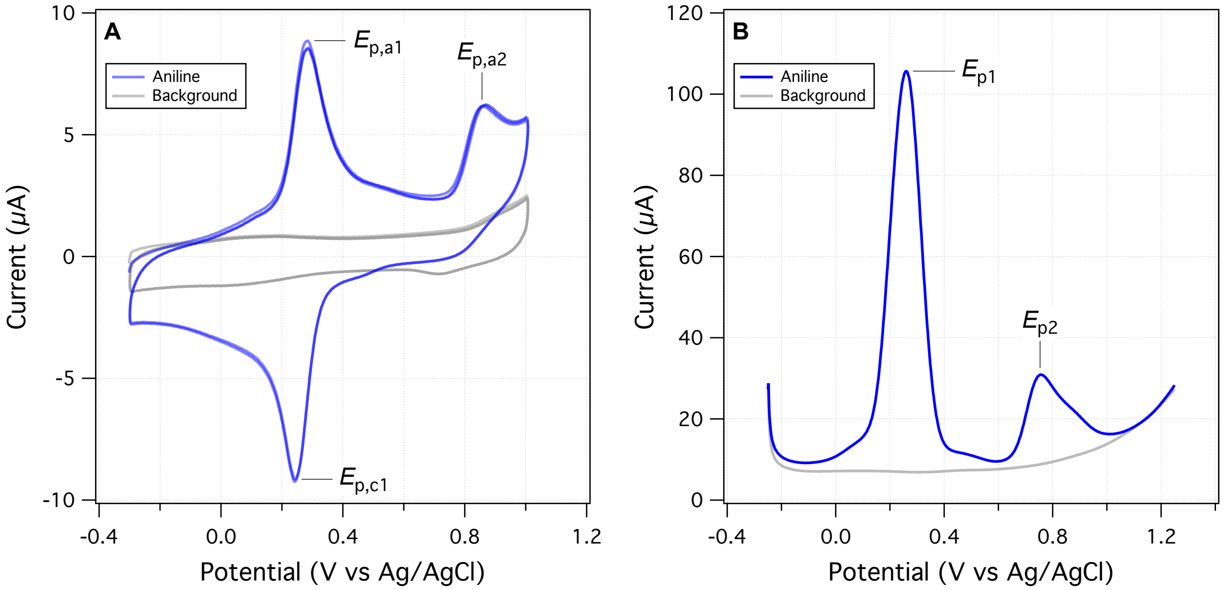

Figure 2.2. Electrochemical data from this study, using aniline as an example. (**A**) staircase cyclic voltammetry (SCV) at a scan rate of 125 mV s^{-1} and (**B**) square-wave voltammetry (SWV) at a scan rate of 60 mV s^{-1} and amplitude of 75 mV. Both for 0.25 mM aniline in 25% IPA/buffer, pH_{meas} 5.1 and step size 2 mV.

We also performed square-wave voltammetry (SWV) using the same solution conditions and working electrode as in SCV and obtained peak potentials from these data as illustrated in **Figure 2.2B**. In general, the SWV peaks are better resolved than those from SCV (because it uses the difference in current sample at the end of the forward potential pulse and the end of the reverse potential pulse, thereby eliminating most of the non-faradaic current), but the resulting peak potentials are not expected to differ at all from those determined by SCV (*71*). Whether obtained by SWV or SCV, E_p should be related to $E_{p/2}$ by $|E_p - E_{p/2}| = 56.5$ mV/n for reversible and 47.7/αn for irreversible reactions (where α is the transfer coefficient, and n is the number electrons) (*69*). Preliminary calculations suggest that this is approximately true for our data, but the results are not shown.

The shapes, and peak properties, of the SCVs and SWVs varied with the substituents on the various phenols and anilines, but also with experimental factors such as the scan rate and pH. Suatoni et al. measured only one scan, starting at 150 mV before the anodic peak and scanning at 2.4 mV s^{-1}, whereas we performed SCVs with a variety of switching potentials and a range of scan rates. In most experiments, we used 0 to +1 V, but varied the scan rate from 25 to

225 mV s^{-1}. The effect of scan rate on peak current or potential are among the criteria used to assess the reversibility of electrode reactions (*71*). With SWV, we varied the scan rate, as well as the potential step amplitude, because varying both of these parameters can provide insights into the electrode kinetics. The results and conclusions from varying these parameters, in both SCV and SWV, are discussed in Appendix A.

Despite differences due to experimental conditions, the SCVs for the various phenols and anilines have similar features, so they can be classified into four types. Most types (all except for Type IV), exhibited an irreversible anodic peak, which is due to initial electron transfer from the parent phenol or aniline (*72*). The E_p data from these peaks are compared to Suatoni's $E_{1/2}$ data below. For **Type I** SCVs, the primary anodic peak height ($i_{p,a}$) decreased slightly (some decreased significantly) with repeated scans. After the first scan, these compounds developed a reversible or quasi-reversible set of peaks shifted to less positive potentials. This secondary peak appears with almost all anilines (e.g., **Figure 2.2A**) and almost half of the phenols, seventeen in total. Secondary peaks were reported in Suatoni et al., for p-toluidine, p-ethylaniline, and 2,4-dimethylaniline, but our experimental data for p-toluidine showed one peak with a shoulder in both the SCV and SWV. Secondary peaks have been described and discussed in many more recent electrochemical studies of phenols and anilines (*72*). The main cause for these peaks is that radicals formed by the oxidation of anilines and some phenols couple to form dimers, which are still electro-active but at lower oxidation potentials (*73*). For this study, the secondary peak formation was not considered further, although it may have implications for the redox properties of natural matter during diagenesis (*74*).

Type II SCVs exhibit the primary oxidation peak, but no secondary peaks. The primary peak current decreases substantially with subsequent scans, resulting in no peaks by the fifth scan. This behavior is seen with fourteen phenols and two anilines. The disappearance of all peaks after multiple scans suggests passivation of the electrode, most likely due to adsorption. It has been previously documented that oxidation of phenols generates phenoxy radicals which dimerize and form a passivating film on solid electrodes (*75*). **Type III** CVs show the primary irreversible anodic peak whose current increases with the scan rate. Current is expected to increase with increasing scan rate because slow scan rates allow the diffusion layer to grow further from the electrode, thereby decreasing the flux to the electrode. As the scan rate speeds up the diffusion layer is smaller and the flux to the electrode is faster resulting in higher current.

This behavior is seen with several phenols and 4-methyl-3-nitroaniline. **Type IV** CVs show one set of reversible or quasi-reversible peaks, as seen with 4-aminophenol and dopamine. For 4-aminophenol the peak separation by exactly 60 mV suggests a one electron transfer reaction. The ratio of the peak currents averaged over five different scan rates is 1.075 and is also consistent with single electron transfer. The peak potentials shift 3-5 mV with the change in scan rate, but this small effect could be due variations in choosing peaks.

2.4.2. Quantitative Comparison of Peak Potentials

The primary data for E_p obtained for each substituted phenol or aniline, over the range of conditions tested, are summarized in Appendix A, **Figure A5**. The expected trends with respect to wave form, scan rate, etc. are evident in the figure, but the overall conclusion is that the range in primary potentials for individual compounds is about 100-200 mV. To select a representative value, we considered two options: the results from the first scan (for SCV this was 25 mV s^{-1} scan rate for SWV 30 mV s^{-1} scan rate, 50 mV amplitude and a step size of 2 mV), or the average of all scans (including scan rates and replicates). The main rationale for the former is that the first scan will be least affected by sorption and/or product formation during electrooxidation of the test compound; whereas the latter leverages more individual measurements and may be more representative of the range of conditions that are included in (meta) correlation analysis. These resulting four sets of E_p data (E_{pa}^{1st} and E_{pa}^{Avg} from SCV; E_{p1}^{1st} and E_{p1}^{Avg} from SWV) are summarized in Tables **A4** and **A5** for all of the phenols and anilines used in the experimental part of this study.

The data in **Tables A4 and A5** are the experimentally measured values, adjusted to SHE, but not corrected for any factors that require more complex justifications. One such factor is pH, which affects the oxidation potential of phenols and anilines mainly through (de)protonation of their hydroxyl or amino moieties. Assuming appropriate values for their pKa's, and a Nernstian relationship between potential and speciation of the hydroxyl or amino moieties, a variety of pH adjustments have been made (e.g., pH 5.6 to 0 (*52*), pH 7 to 0 (*67*)). For reversible reactions with Nernstian electrode response, a pH adjustment can be made by decreasing the oxidation potentials 59 mV per unit increase in pH. However, for this study, we decided not to make pH adjustments to our measured E_p data because (*i*) our buffer and pH conditions were identical to those used by Suatoni et al.; (*ii*) using the estimated pK_a's in **Tables A2 and A3** and pH's that we measured before each set of electrochemical measurements (pH_{app} = 5.4–5.6) showed that variation in degree of protonation had negligable effect on E_p for the anilines and was <30 (usually <15) mV for the phenols; and (*iii*) there are numerous potential secondary effects that would be difficult to fully evaluate. One such secondary effect might be the influence of IPA on the pKa's on phenols, anilines, and water and another might be the influence of buffer speciation on electrode kinetics (*76*).

Another factor that could merit corrections is the irreversibility of the primary anodic peaks used to obtain our E_p data. Recall from the discusion of SCV types (above and in Appendix A) that many of the phenols and anlines studied did not give ideal reversible electrochemical peaks. E_p data can be adjusted to approximate (theoretical) reversible potentials as has been done for SCV of phenols (*77*). However, for this study, we decided not apply this correction to our E_p data because (*i*) Suatoni et al. did not do it, (*ii*) SCV peak type did not correlate in any way with the E_p data, and (*iii*) this correction involves assumptions that were unnecessary to make.

Our four sets of E_p data (from **Tables A4 and A5**) are summarized by phenol or aniline in **Figure A6**, together with the $E_{1/2}$ data from Suatoni et al. and electrochemical oxidation potentials from three other studies of complementary scope. In general, the variability among the datasets appears to be smaller than the variability between the phenols/anilines, which can be seen more clearly in the correlation between all of our E_p and Suatoni's $E_{1/2}$, data, which is shown in **Figure 2.3**. All of our E_p datasets appear to correlate with the same slope and intercept, so they can be fitted globally, which give 0.99±0.02 and 0.13±0.03, respectively ($r^2 = 0.92$). The slope of 1 indicates all the measured E_p's have the same sensitivity to phenol/aniline structure, but the intercept suggests a well defined "offset" of about 130 mV (which is discussed further below).

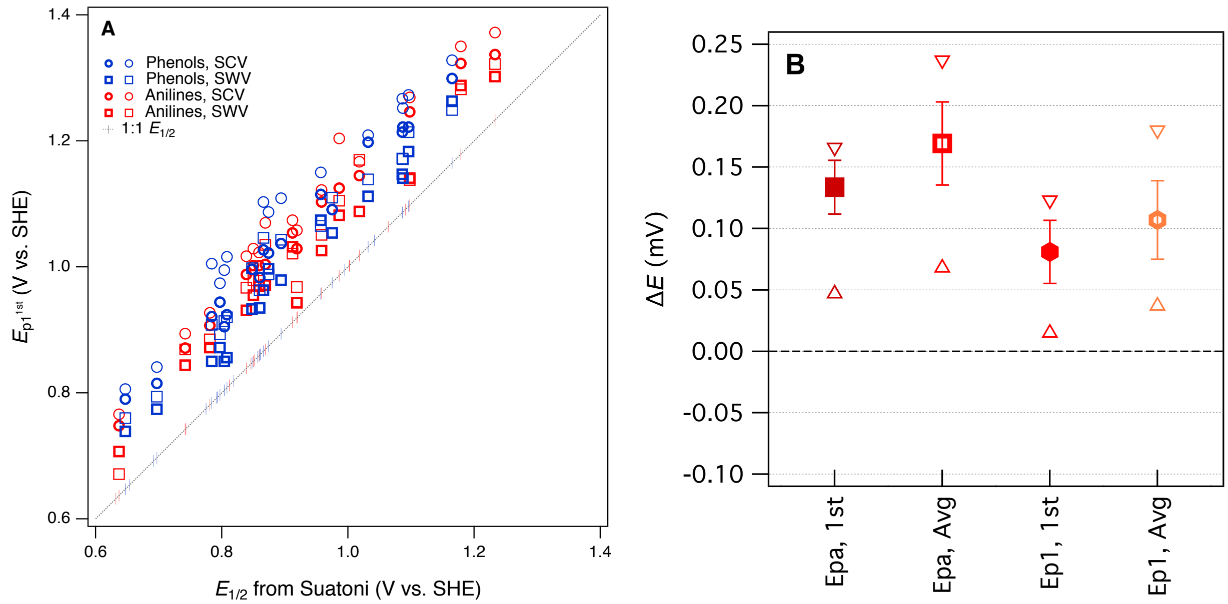

Figure 2.3. Comparisons between measured E_p from this study and $E_{1/2}$ from Suatoni et al. for phenols and anilines. (**A**) Direct comparison between measured potentials, (**B**) Statistical analysis of the difference between E_p and $E_{1/2}$ (Δ*E*). In (A), phenols and anilines are distinguished, but in (B) their data are combined.

To prioritize among the four sets of measured potentials, we considered three criteria: accuracy, precision, and relevance. Since our experiments were designed to match most of the conditions in the work by Suatoni et al., we calculated the difference between our values and Suatoni's (Δ*E*) and used this as one indicator of accuracy. Values of Δ*E* for each phenol or aniline are summarized in **Figure A6**. And the average, standard deviation, maximum, and minimum of these values are summarized in **Figure 2.3B**. Based on the results in **Figure 2.3B**, and the general considerations regarding the electrochemistry of phenols/anilines presented above, we chose to emphasize E_{p1}^{1st} (the potential of the first anodic peak from the first scan obtained by SWV) in most of the correlation analysis that follows.

One overall implication of the results summarized in **Figures 2.3 and A6** is that the new experimental data presented here are 100-150 mV more positive than those reported in Suatoni et al. Two contributors to this offset are certain: (*i*) in cyclic voltammetry $E_{1/2}$ should be ~28 mV less than E_p for peaks with typical shape (*69*), and (*ii*) the difference between Suatoni's scan rate (2.4 mV s^{-1}) and ours (25-330 mV s^{-1}), should make their potentials about 50-150 mV higher than their $E_{1/2}$'s (based on analysis in Appendix A). This reduces the unexplained Δ*E* to a range of −75 mV to +25 mV. One possible contributor to the remaining Δ*E* is differences in cell design

(Suatoni's cell volume and working electrode diameter were 2.5- and 2-fold greater than ours, respectively), which can influence electrode potential measurements in various ways, such as differenes in iR drop, non-Faradaic current, etc. (*70*). Another possible effect of electrode kinetics is that the slow scan rate used by Suatoni et al. could have resulted in conditions at the electrode boundary layer that were influenced by convection as well as diffusion, which would influence E_p by unpredictably affecting the current response (*68*). Finally, it is possible that Suatoni's electrode potentials were affected by the presence of dissolved oxygen in their system, which can generate reactive oxygen species during anodic voltammetry, and these species can react directly with the electrode or with the test compounds (*70*). Taken together, these considerations are sufficient to rationalize the roughly 100-150 mV offset between $E_{1/2}$ from Suatoni and $E_{p1}{}^{1st}$ from this study, and suggest that the absolute accuracy is likely greater for our $E_{p1}{}^{1st}$ dataset.

2.4.3. Computational Method Optimization and Validation

For this study, the theoretical calculations of E_1 were performed to serve three general purposes. First, to obtain a dataset with maximum overlap with the phenols and anilines for which there are electrochemical potentials from Suatoni et al. and/or the newly-measured values reported in this study, we included most of the phenols and anilines in **Tables A2 and A3**. Second, to represent the putative initial oxidation step for phenols and anilines (*78-80*) at the pH of Suatoni's work, E_1 was calculated for simple electron transfer from the neutral form of the phenols and anilines to the corresponding phenoxy or aryl amino radicals (i.e., $PhOH \rightleftharpoons PhOH^{\bullet+} + e^-$ and $ArNH_2 \rightleftharpoons ArNH_2^{\bullet+} + e^-$) assuming no atom transfers. Third, to provide an avenue for extending the coverage of substituent combinations in future work, we chose moderately-high, but accessible levels of theory, so calculations could be done for many compounds without special accommodations (such as for the larger or more flexible compounds). The range of computational conditions used was chosen to include those that proved most useful in our recent work (*48*), included one basis set (6-311++G(2d,2p)), two functionals (B3LYP and M062S) and two solvation models (COSMO and COSMO-SMD). The newly calculated values of E_1 are given in **Table A6** (phenols) and **Table A7** (anilines).

The newly calculated values of E_1 are summarized for each phenol in **Figure A7** and each aniline in **Figure A8**. For comparison, we have included in the plots: literature values of E_1

from prior studies that used Suatoni's $E_{1/2}$ for validation (*48, 60*), the $E_{1/2}$ data from Suatoni et al., and the E_p data from this study (**Table A4, A5**). It is evident from these figures that most of the range in E's is due to relatively consistent differences (i.e., offsets) between the E_1 datasets (~2-4 V), while the offset among the measured E_p's is much less (<0.5 V), and that the variability among the phenols and anilines within each dataset is intermediate in size (~1 V). The relatively large offsets between sets of calculated and measured oxidation potentials is an issue that has been addressed in prior work by using the expected values of E_1 (E_{1c}) calculated from regresssion of E_1 on experimental data (*56*). This approach has been used specifically with substituted phenols and/or anilines (*59, 67*), but the results and implications have not been fully explored.

For validation and calibration of the E_1 data obtained in this study, we compared our four sets of E_1's vs. two sets of measured potentials, $E_{1/2}$ from Suatoni et al. and E_p from this study. The direct plots and linear fits of each combination are shown in **Figure A9**, the fitting coefficients and goodness-of-fit statistics are given in **Table A8**, and a subset of these results is summarized below in **Figure 2.4A**. The major features of the calibration fitting results are (*i*) the slopes are similar in most cases, but (*ii*) the intercepts differ considerably, and (*iii*) the residual variance about the fitted lines is greater for phenols than anilines. To examine the residuals for trends or outliers, we calculated E_{1c} for combinations of E_1's and measured potentials (**Table A9-A10**) and plotted them versus the measured potential used for calibration in **Figure A10**. The most relevant subset of these results are shown in **Figure 2.4B**. By factoring out the differences in slope and intercept between the calibrations, **Figure 2.4B** shows that the residual variance E_{1c} for anilines is small and appears random. In contrast, the phenols exhibit significant scatter and clustering among the outliers that suggests systematic effects.

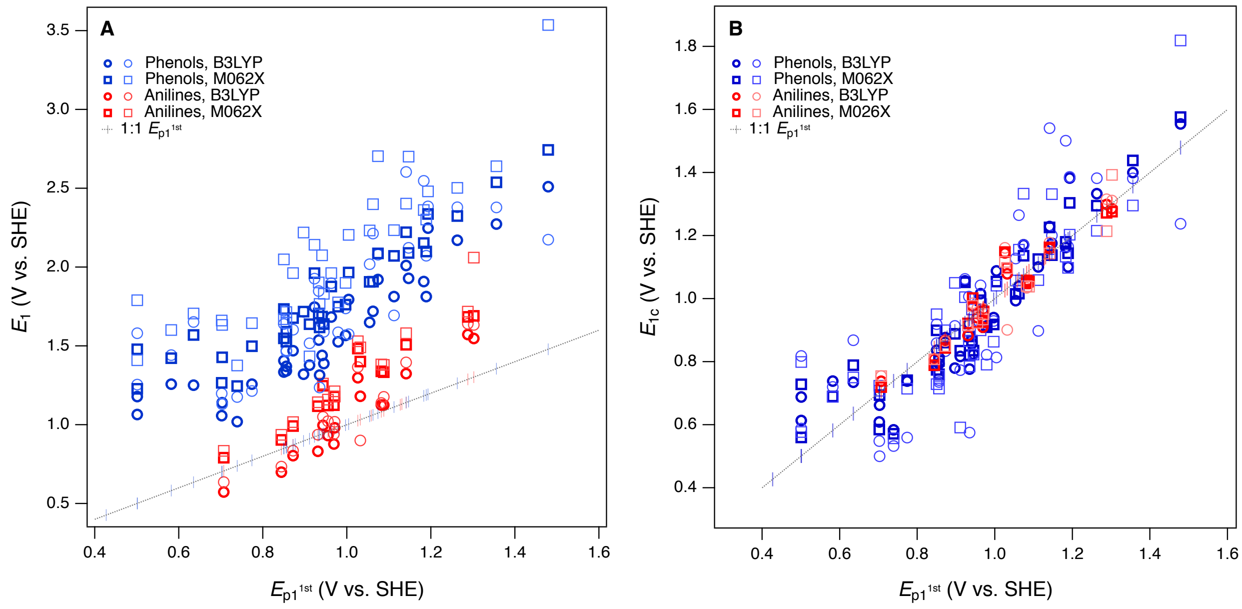

Figure 2.4. Comparisons between measured E_1 (without calibration) and E_{p1}^{1st} for phenols and anilines. (**A**) Direct comparison between measured potentials, (**B**) Statistical analysis of the calibration equations from regression of E_1 and E_{p1}^{1st} (shown in Figure A6). In (A) and (B), phenols and anilines are distinguished, not combined.

Overall, the two functionals used (B3LYP and M062X) performed equally well, so we emphasize M062X in the remaining discussion only because it was slightly preferred in our previous work (*48*). All of the most severe outliers in **Figure 2.4B** fit two criteria. The most general is the SMD solvated E_1's (lighter markers in **Figure 2.4B**), which account for all of the more extreme values of E_{1c} for each compound. Since the COSMO-SMD model has been extensively parameterized for compounds similar to the parent compounds in this study, these differences suggest that the parametrization of COSMO radii in the SMD model may need to be adjusted for the oxidized forms. The other notable group of outliers includes the three phenols with the lowest values of E_{p1} (2-hydroxyl, 4-hydroxyl, and 2,6-dimethoxy), which plot about 100 mV high relative the trends in **Figures 2.4A** and **B**. The absolute and relative values of E_{p1} for these compounds are quite consistent with previous electrochemical studies (*81*), which suggests that the calculated values of E_1 are too high. This anomoly might be rationalized in terms of their strongly electron donating substitutents, and these differences might be corrected by using higher levels of electronic structure theory, such CCSD(T) with large basis sets. However, these higher level calculations are very expensive and would only be accessible to researchers with access to very large supercomputers, and would be inconsistent with our overall approach of favoring lumping over splitting where ever possible.

2.4.4. Structure-Activity Relationships

The ultimate goal of the cross-correlation analysis of oxidation potentials presented above is to validate them for use as desciptor variables in relationships between phenol/aniline structure and reactivity (i.e., QSARs). However, that analysis suggests that most of the differences between the four major sets of oxidation potentials ($E_{1/2}$ from Suatoni et al. and E_p, E_1, and E_{1c} from this work) are due to compound-specific effects that may be dependent on operational factors. (For example, the dissociation or migration of protons in association with hydroxyl groups could be affected by the cosolvent (IPA) used in the electrochemical measurements or the basis set used in the modeling calculations.) This complexity means that the three sets of oxidation potentials may have complementary value as descriptors in correlation analysis with kinetic data. This complementarity is apparent when the correlation presented in **Figure 2.1A**—between log k_{rel} for phenol/aniline oxidation by MnO_2 and $E_{1/2}$ from Suatoni et al.—is compared with the correlations in **Figure 2.5**, obtained using E_p and E_1 as alternative descriptor variables.

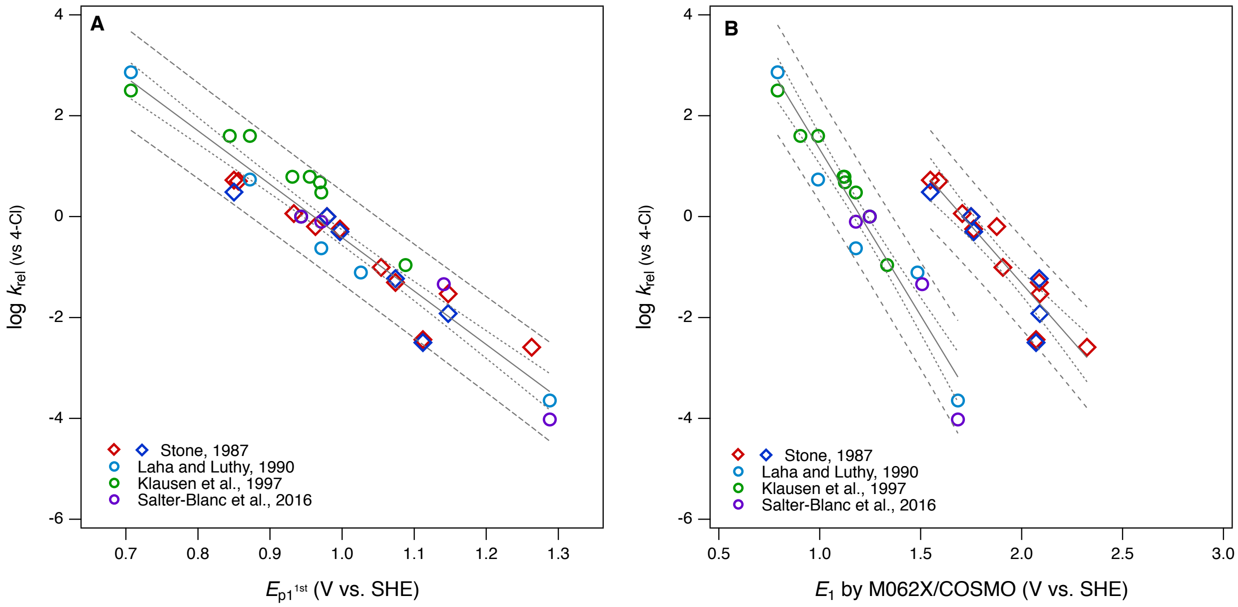

Figure 2.5. Correlations of rate constants for oxidation by manganese oxides (k_{rel}) and oxidation potentials of phenols and anilines: (**A**) log k_{rel} from compiled sources (Table A1) vs. E_{p1}^{1st} from this study (Table A4-A5); (**B**) log k_{rel} vs. E_1 without calibration, from this study (Table A6-A7).

The differences between the correlations to $E_{1/2}$ (**Figure 2.1A**) and E_{p1}^{1st} (**Figure 2.5A**) are subtle: mainly there is slightly different distribution of residuals, resulting in slightly better overall regression statistics with E_{p1}^{1st} (**Table A13**). Since the two sets of electrochemical oxidation potentials are strongly covariant (**Figure 2.3A**), the residuals in **Figures 2.1A and 2.5A** are likely arise from the same source. Certainly, one source could be experimental error in the original k_{rel} data, but another possibility is that it reflects compound-specific effects that influence the response and descriptor variables differently. In this case, a likely contributor to such effects is that the surface properties of MnO_2 and graphitic carbon are very different, which could result in significantly different surface interactions with the phenols/anilines with different combinations of substitutents.

Compared with the correlations between log k_{rel} and electrochemically determined oxidation potentials, the correlations to calculated E_1's give more diverse results. Using uncalibrated E_1's (**Figure 2.5B**) produces separate correlations for the phenols and anilines, both of which are statistically satisfactory, but the differences in slope and intercept are not consistent with the experimental potential data. Because of the latter, this appears to be a case where splitting lead to less chemically meaningful results. Calibration of E_1's to the experimental potentials ($E_{1/2}$ or E_{p1}^{1st}) normalizes the phenols and anilines to the same slope and intercept, so correlations between log k_{rel} and E_{1c} can be fit to one QSAR for all compounds (**Figure 2.6**). The fitting statistics for these correlations are very good and similar to those obtained with experimentally measured potentials (**Table A13**). Values of E_{1c} obtained using the B3LYP functional produce nearly identical correlations to log k_{rel} (not shown).

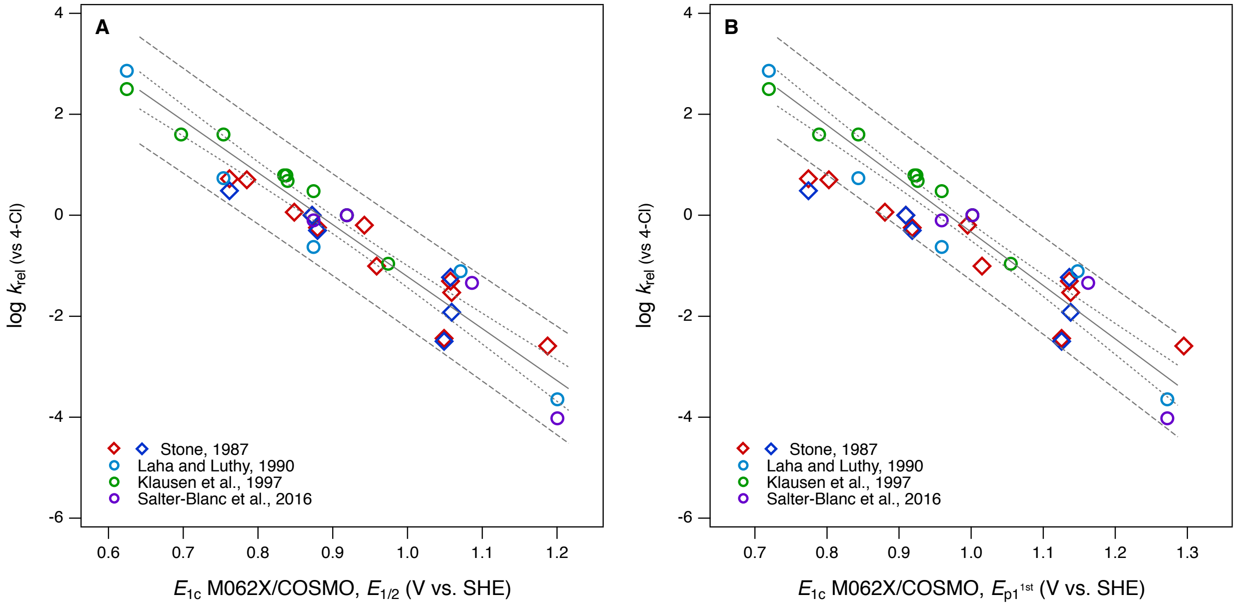

Figure 2.6. Correlations of rate constants for oxidation by manganese oxides (k_{rel}) and oxidation potentials of phenols and anilines: (**A**) log k_{rel} from compiled sources (Table A1) vs. E_1 without calibration (Table A6-A7); (**B**) log k_{rel} from compiled sources vs. E_1 with calibration using data for E_{p1}^{1st} (Table A9-A10).

In **Figure 2.6B**, the three points that fall outside the prediction interval are 2-hydroxy, 4-hydroxy, and 2,6-dimethoxy phenol. The substitutents on these compounds are likely to cause effects that require compound-specific modeling; e.g., a shift from one- to two-electron oxidation potentials corresonding to the formation of quinonoid products (*82*). In fact, these compounds are responsible for the three sets of anamolously high E_1's in the lower-left corner of their calibrations to E_{p1}^{1st} (**Figure A9B, A10B**), and it is the leverage these points exert on the calibration regression that causes these compounds to appear as outliers in **Figure 2.6B**. The $E_{1/2}$ dataset from Suatoni et al. does not extend to phenols with such low potentials, so the corresponding E_1's do not appear in **Figure A9A** or **A10A** and therefore do not have any effect on the correlation using E_{1c} calibrated to $E_{1/2}$ (**Figure 2.6A**).

Comparing the statistical quality of all the QSARs derived here with log k_{rel} (**Figures** 2.**1A, 2.5A, 2.6**, and **Table A13**) shows little difference between the descriptors $E_{1/2}$, E_{p1}, and E_{1c}. However, other, subjective differences are important. For example, while the original experimental dataset of $E_{1/2}$ by Suatoni et al. is large, it contains few compounds with challenging substitutents. The new set of E_{p}'s reported here includes more ionizable and polar functional groups, more substituents that are likely to cause proximity effects, more compounds with two or more substitutents, and more complex phenols and anilines of biological or environmental interest (e.g., dopamine and triclosan). These complications favor net substituent effects that are not easily modelled, which can contribute to greater residuals in correlation analysis. These residuals can be useful, however, such as for diagnosing specific substituent effects, selection among descriptor variable datasets, and identification of the limits of applicability of a QSAR model.

(In addition to diversity of substituents included,) Another subjective difference that distinguishes the QSARs obtained here using $E_{1/2}$, E_{p1}, and E_{1c} as descriptor variables is their suitability for use in prediction. For new phenols and anilines, Suatoni et al. concluded that values of $E_{1/2}$ can be estimated by assuming additivity of substituent effects or a Hammett correlation between $E_{1/2}$ and σ, and these approximations have proven useful in several subsequent studies (*49, 52*). However, they are likely to break down with more complex compounds. The new datasets of experimental E_{p1}'s reported in this study have the advantage of being extendable with new measurements using the modern methods documented and validated here. Interpolation of additional E_{p1}'s without new measurements should be possible using the same additivity and Hammett correlations approaches used by Suatoni et al., but this was not verified as part of this work.

In contrast to experimental or empirical approaches to obtaining descriptor data for new phenols or anilines, purely in silico calculation of E_1's from molecular structure theory could be very efficient (because the calculations can be programmed to run in batches). As demonstrated in this study, however, E_1 must be calibrated to experimental data to ensure the absolute and relative accuracy of the results. Even after calibration, values of E_{1c} for some compounds may not fully reflect the processes controlling oxidation in solution, which can cause unnecessary outliers when applied in QSARs (e.g., **Figure 2.6B**). Such outliers could be avoided with sufficiently detailed modeling calculations, but this would obviate the efficiency of the modeling approach to populating new descriptor data. Overall, the balance of considerations (statistical and subjective) favor the experimental and empirical approach obtaining descriptor data for predictive applications of QSARs.

In the end, the main advantage of correlation analysis performed using E_1 from molecular structure theory is clarity and precision regarding the mechanisms that are represented by the descriptor. This complements the relative ambiguity of k_{rel}, $E_{1/2}$, E_{p} regarding the mechanisms controlling these properties measured in solution. Correlation analysis between the two types of properties can provide insights into either, or both, as exemplified in this study for oxidation of phenols and anilines. Selection of one type of descriptor over another should be done with consideration of the principle of matching the observational vs. mechanistic character of descriptor variables. So, for the purpose of developing QSARs to predict rates of oxidation by MnO_2, the most effective descriptors will be those that reflect similar interfacial redox processes (e.g., $E_{1/2}$, E_{p}). For the purposes of testing hypotheses regarding the mechanism of electron transfer involving MnO_2 (or other oxidants), there may be greater diagnostic value to correlation analysis with descriptors that are calculated from molecular structure theory (e.g., E_1) and therefore mechanistically less ambigous.

The complementary advantages of measured and calculated descriptors are somewhat obscured by the calibration of calculated descriptors with measured descriptors, as was done to obtain $E_{1\mathrm{c}}$ in this study. We did this partly for the practical reasons that (*i*) we were interested in validating our newly measured values of E_{p} and (*ii*) experimental values of E_1 are much less abundant, or easily obtained. However, the results of this decision also serves to illustrate the overall theme of this work, that lumping works best when the response and descriptor variables are matched with respect to observational vs. mechanistic character.

2.5. Acknowledgements

This work was supported by the U.S. National Science Foundation, Environmental Chemical Sciences Program (NSF Grant # 1506744) and the U.S. Department of Defense, Strategic Environmental Research and Development Program (SERDP Grant #ER-1735). Some of the electrochemistry was performed by David Panfilov, while on an internship funded by the NSF Center for Coastal Margin Observation and Research. The modeling portion of this research was performed using the Institutional Computing facility (PIC) at the Pacific Northwest National

Laboratory (PNNL) and the Chinook, Barracuda, and Cascade computing resources at the Environmental Molecular Sciences Laboratory (EMSL). PNNL is operated by Battelle Memorial Institute for the U.S. Department of Energy (DOE). EMSL is a national scientific user facility, located at PNNL, and sponsored by the DOE's Office of Biological and Environmental Research (DE-AC06-76RLO 1830). We also acknowledge EMSL for supporting the development of NWChem. Structure database management and some property prediction was performed using Instant JChem (Instant JChem 16.12.5.0) ChemAxon [http://www.chemaxon.com]). This report has not been subject to review by any of the sponsors and therefore does not necessarily reflect their views and no official endorsement should be inferred.

Chapter 3. Electrochemical Characterization of Natural Organic Matter by Direct Voltammetry in an Aprotic Solvent[2]

Ania S. Pavitt and Paul G. Tratnyek

3.1. Abstract

The complex and indeterminant composition of NOM makes characterization of its redox properties challenging. Approaches that have been taken to address this challenge include chemical probe reactions, potentiometric titrations, chronocoulometry, and voltammetry. In this study, we revisit the use of direct voltammetric methods in aprotic solvents by applying an expanded and refined suite of methods to a large set of NOM samples and model compounds (54 NOM samples from 10 different sources, 7 NOM model compounds, and 2 fresh extracts of plant materials that are high in redox-active quinonoid model compounds (dissolved in DMSO). Refinements in the methods of fitting the data obtained by staircase cyclic voltammetry (SCV) provided improved definition of peaks, and square wave voltammetry (SWV), performed under the same conditions as SCV, provided even more reliable identification and quantitation of peaks. Further evidence is provided that DMSO improves the electrode response by unfolding some of the tertiary structure of NOM polymers, thereby allowing greater contact between redox-active functional groups and the electrode surface. We averaged experimental peak potentials for all NOM compounds and calculated potentials in water. Average values for E_{pa1}, E_{pc1}, and E_{p1} in DMSO were −0.866±0.069, −1.35±0.071, and −0.831± 0.051 V vs Ag/Ag$^+$, and -0.128, -0.613, and -0.0930 V vs SHE in water. In addition to peak potentials, the breadth of SCV peaks was quantified as a way to characterize the degree to which the redox activity of NOM is due to a continuum of contributing functional groups. The average breadth values were 1.63±0.24, 1.28±0.34, and 0.648±0.15 V for E_{pa1}, E_{pc1}, and E_{p1} respectively. Comparative analysis of the overall dataset—from SCV and SWV on all NOMs and model compounds—revealed that NOM redox properties vary over a narrower range than expected based on model compound properties. This lack of diversity in redox properties of NOM is similar to conclusions

---

[2] Reprint with permission from A. S. Pavitt and P. G. Tratnyek, Electrochemical Characterization of Natural Organic Matter by Direct Voltammetry in an Aprotic Solvent, *Environ. Sci.: Proc. Impacts,* **21**, 1664-1683 (2019). Copyright 2019 The Royal Society of Chemistry.

from other recent work on the molecular structure of NOM, all of which could be the result of selectivity in the common extraction methods used to obtain the materials.

3.2. Introduction

A defining characteristic of environmental science is that many of its grand challenges arise from the indeterminate composition of environmental materials. This is true of the mineralogical materials that comprise soils, sediments, and aquifers, but it is even more true of the natural organic matter (NOM) that is abundant in these compartments, as well as in surface waters, rain water, atmospheric aerosols, etc. Inevitably, the composition of NOM varies across these compartments, as well as spatially and temporally within compartments, due to variation in the source material and extent of diagenesis. This has led to a vast amount of research on the molecular structure and macromolecular composition of NOM (*11, 26-28, 83-97*), but quantitative characterization of the diversity of NOM is complicated by its indeterminant structure.

The indeterminant composition of NOM is often dealt with by (*i*) fractionation to decrease structural diversity and/or (*ii*) fingerprinting to encompass the whole range of NOM structural diversity. The various methods for fractionation of NOM have been optimized, standardized, compared, and criticized over many years of study (*88, 98-102*), and during this process they have become deeply embedded in the literature on all aspects of NOM. The methods used to fingerprint NOM have expanded with advancements in the availability of high-resolution instrumentation, beginning with Fourier transform infrared spectroscopy (FTIR) and nuclear magnetic resonance (NMR) (*84, 95, 103-111*), then excitation emission matrices (EEMs) (*112-116*), and most recently Fourier transform ion cyclotron resonance mass spectrometry (FTICR-MS) (*26-28, 87, 90, 98, 100, 102, 117-120*). The increasingly wholistic characterizations of NOM obtained from fingerprinting methods have renewed concerns over the representativeness NOM samples obtained by extraction methods (*88, 99, 102*), and growing recognition that sample preparation for fingerprinting can introduce biases due to fractionation (*28, 98-102, 121*).

The ultimate motivation for on-going work on the characterization of NOM structure and composition is to enable new insights into its fate and effects. Currently, the main focus of this work is on the bioavailability of carbon in NOM, because of its role in the global carbon cycle, and implications for climate change (*117, 122-128*). The other major applications of NOM characterization are to its role in biogechemistry (*13-15, 123, 129, 130*), and contaminant fate (*16-19, 131-143*). In both of these contexts, NOM participates in reactions as a ligand (*144-148*), electron donor/acceptor (*13, 130, 149-157*), electron shuttle (i.e., electron-transfer mediator) (*1, 158-164*), and/or catalyst (*161, 164*). Most of these are redox reactions, so the thermodynamics, kinetics, capacity, and mechanisms of redox reactions involving NOM have been studied extensively. The majority of this work has focused on probe reactions (usually involving model contaminants) (*18, 19*), but spectroscopies such as electron paramagnetic resonance (EPR) (*165*), X-ray absorption spectroscopy (XAS) (*166*), and electrochemical methods have also proven useful.

The earliest applications of electrochemical methods to the study of NOM extend back to the 1950's and include a surprisingly wide range of methods, but as late as the 1990's these methods were still not producing data that was amenable to quantitative analysis (*167*). Since then, two innovations have greatly improved the resolution and quantification of electrochemical data on NOM: the use of aprotic solvents (e.g., dimethyl sulfoxide (DMSO)) and the addition of electron-transfer mediators (ETMs or electron "shuttles"). In both approaches, the key innovation (the solvent or the shuttle) is believed to improve the electrode response to NOM by facilitating interaction between the working electrode surface and redox-active functional groups in the NOM (*167*). In the former approach, the solvent allows unfolding of the NOM's tertiary structure, thereby exposing protected functional groups to the electrode. In the latter approach, the size and mobility of the shuttle compounds allow it to diffuse between the protected functional groups and the electrode surface. These conceptual models are summarized in **Figure 3.1**, with representative data from cyclic voltammetry that is explained later.

Aprotic solvents have long been used in organic electrochemistry (*168-176*), and also have only recently been shown to be useful for characterization of NOM redox properties (*167, 177, 178*). This approach was rooted in recognition that NOM under aqueous conditions develops tertiary structure, that could result in protection of redox-active functional groups from direct interaction with electrodes. This effect might arise if the tertiary structure of NOM had micelle-like character, which was proposed for humic substances (HS) in 1978 (*179*), and has since been supported by results obtained by a variety of methods. For example, fluorescence spectroscopy using pyrene as a fluorescent probe molecule that should partition into the hydrophobic interior of a micelle and bromide as a flourescence quencher that should be excluded from the micelle (*180, 181*). Other evidence consistent with the micellar character of NOM include (*i*) the surface tension of water being lowered by HS and increasing solubility of organic compounds that are otherwise insoluble in water without HS present (*182*); and (*ii*) that addition of organic acids and observed structural changes suggested micelle type formation and hydrophobic bonding playing a key role in aggregation (*183*). Because NOM is complex it cannot be directly compared to a surfactant that would simply form micelles, but rather have many different associations with one molecule having varying effects of coiling and folding.

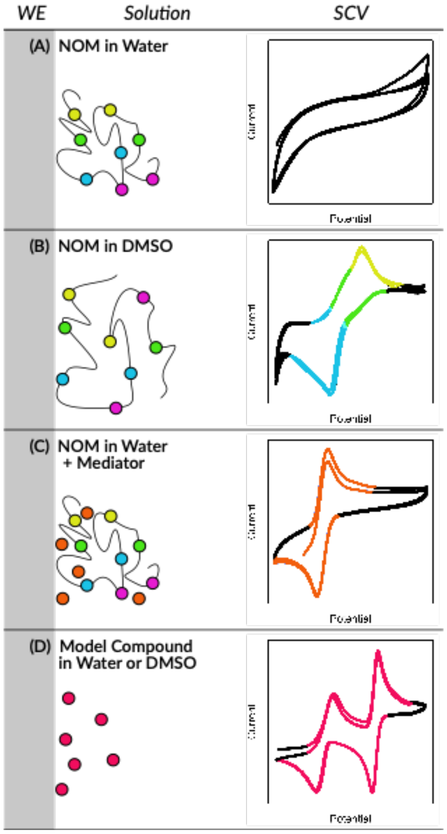

Figure 3.1. Conceptual model of interactions between NOM and a working electrode (WE), with colored circles representing different moieties of electroactive functional groups. (A) NOM in water where its tertiary structure protects redox-active groups from the electrode, (B) NOM in DMSO where unfolding allows direct contact of some groups, (C) NOM in water where soluble mediators (red circles) shuttle electrons between NOM and the electrode, and (D) model or shuttle compounds in DMSO, which stabilizes one-electron transfer products. In each case, an example voltammogram is shown (right column) with sections colored to match the specific functional group markers in the cartoon.

A better model for the tertiary struture of NOM—and how it influences electrode response—might be the self-assembly of biological molecules such as proteins, lipids, and DNA. This analogy is justified by the similarity in H-bonding interactions between moieties in these polyelectrolytes (*11, 12, 184*). Disassociation of H-bonds is favored by aprotic solvents like DMSO (*185*), so it has long been used as a solvent for polyelectrolytes like proteins and lignin (*186-188*). DMSO has also been used as a (co)solvent for NOM, where it has been found to increase the quantity of humin recovered by the standard alkaline extraction method (*108*), the diversity of organic matter obtained by alkaline extraction of soils and sediments (*189*), and the quantity of hydrophobic moieties detected during structural characterization of NOM by high resolution NMR (*185*). Analogous benefits from the solvency of DMSO have been reported in studies of proteins, including reducing binding affinites of proteins (*190*), protein unfolding (*191, 192*), DMSO affecting protein charge (*190*), and aiding in electron transfer (*193-195*).

While mediators and aprotic solvents can greatly improve the electrode response of polyelectrolytes like proteins and NOM, other advances in electrochemical methodology can also have significant benefits. One such opportunity for method refinement concerns the working electrode composition (e.g., various forms of carbon vs. noble metals) and configuration (e.g., micro vs. reticulated). Another such opportunity concerns methods of data acquisition (e.g., voltametric waveform) and analysis (various corrections and transforms). In our original work on NOM in DMSO (*178*), we gave limited attention to these opportunities, including only preliminary experiments with microelectrodes and square wave voltammetry (*167, 177*). Recently, we have done an extensive study of phenol redox properties (including common NOM model compounds) and demonstrated several advantages to using square wave voltammetry, and we have noted studies that have very successfully applied square wave voltammtery with analysis methods to the electrochemical characterization of the redox properties of proteins (*196*). Given the analogy (noted above) between the challenges to doing electrochemistry on proteins and NOM, we hypothesized that an optimized combination of these method developments might provide a significant improvement in direct electrochemical characterization of NOM redox properties.

The objectives of this work include development of optimized methods for direct electrochemical characterization of NOM, comparison of the most promising methods to clarify ways in which the methods are complementary, demonstration of the applicability of these methods to NOM samples from a wide ranges of sources, and analysis of the data for correlations that provide new insight into the redox activity of NOM. For comparison with the results obtained with 54 samples of NOM, the same suite of electrochemical methods were applied to 7 quinonoid model compounds and 2 fresh plant abstracts. A notable overall result was the general lack of diversity in measured redox properties of NOMs (compared with the model compounds), which is interpreted as evidence that the extraction methods used to obtain most samples of NOM favor a relatively narrow range of redox-active functional groups.

3.3. Experimental

3.3.1 Materials and Reagents

All of the NOM samples used in this study are listed in Appendix B in **Table B1**, together with the available meta data on each sample's source, composition, and key references. The model compounds selected for this study are listed in **Table B2**, and their molecular structures are given in **Figure B1**. The calculated values of pK_a's for each model compound in water and DMSO are given in **Table B3**. Additional model compounds used during method development—including 2,2'-azino-bis(3-ethylbenzothiazoline-6-sulphonic acid) diammonium salt (ABTS), 2,6-dichloroindophenol (DCIP), and resorufin (RSZ)—were all obtained from Sigma Aldrich. These and other chemical regents including—dimethyl sulfoxide (DMSO), tetrabutylammonium hexafluorophosphate (TBAFP), potassium chloride (KCl), mono and di-potassium phosphate—were ACS reagent grade and used as received without further purification.

Two different methods were used to prepare solutions of NOM for analysis: (*i*) if there was sufficient loose powder of the sample for subsampling, then, preweighed portions were dissolved in DMSO to form stock solutions that could be used over multiple experiments; (*ii*) if sample quantity was insufficient for this, all of the sample container contents were washed into the cell with two ~1 mL volumes of electrolyte from the background scan, and the difference in container before and after washing was used as the quantity of NOM. In general, the target final concentration of the NOM in the cell was 1 mg mL^{-1}, but the concentration was less for samples that did not fully dissolve or for which the total sample mass was limited. Stock solutions of NOM in DMSO were stored in amber bottles and used within three days (even though control experiments shown in **Figure B15** indicate there was not a significant effect of aging on the electrochemical results).

In a few cases, dry powders of plant material were purchased (Mountain Rose Herbs, Eugene, OR) and extracted using DMSO or H_2O. For these extractions, 500 mg of black walnut hull or pau d'arco bark (natural sources of juglone and lapachone, respectively) were dissolved in 5 mL of DMSO, or in 5 mL of ultrapure Millipore water, then left to mix for 24 h and centrifuged. The supernatant was removed and analyzed by SCV and SWV (**Figure B16**) as detailed below. For the aqueous samples, a second extraction was performed using DMSO after the powder was oven dried at ~200 °C for 24 h.

3.3.2. Electrochemical Methods

For the NOM samples, all square-wave voltammograms (SWVs) and staircase cyclic voltammograms (SCVs) were obtained with a Metrohm Autolab PGSTAT30. The model NOM compounds were characterized with a Princeton Applied Research VersaSTAT4, a Pine AFCBP1 Bipotentiostat, and the PGSTAT30. There were no significant differences between the data obtained using the three different potentiostats. All of the voltammograms were acquired at an amplitude of 25 mV (SWV) and with a step size of 2 mV (SWV and SCV), based on method optimizations that we performed in a previous study on the electrochemistry of phenols and anilines (*197*). The effect of SWV scan rate has greater diagnostic value, so it was performed at 25, 125, and 225 mV s^{-1} (which are designated SWVi, SWVii, and SWViii, respectively, in some figures). The SCV scan rate was always 25 mV s^{-1} and is labelled SCVi. Most runs were performed at least in duplicate.

The peak potentials summarized in **Tables B4-B5** were obtained from voltammetry data using both Nova 2.02 (Metrohm, Herisau Switzerland) and Igor Pro 7 (Wavemetrics, Lake Oswego, OR) software. For NOM samples, peak data were determined using cubic baseline and Gaussian fit functions in Igor's Multi-peak Fit module, with manual adjustment of peak start and stop positions only when necessary. For the model compounds, peak data were determined using either the manual or automatic peak selection/integration tools in Nova 2.02. The results obtained by these methods were compared on selected datasets and no significant differences were found. However, data analysis with Nova generally was faster (so preferred for well-defined peaks from the model compounds), and Igor gave greater control (needed for the less-well defined peaks from most NOM samples).

All measurements were made in a three-electrode cell with a low profile 1.6 mm diameter platinum working electrode (Pine Research Instrumentation), and a 0.5 mm diameter coiled platinum wire counter electrode, and a reference electrode. For aprotic conditions, the reference electrode was a Ag/Ag$^+$ reference electrode (BASi) filled with 0.1 M TBAFP and 0.010 M $AgNO_3$, whereas experiments in aqueous media were performed using a Ag/AgCl reference electrode (BASi) filled with 3.0 M KCl. The reference electrode for aprotic conditions had BASi's exchangeable CoralPor tip for the liquid junction, and required frequent changes (every 3 days) during continuous experiments in DMSO. For comparison, a low profile 3.0 mm glassy carbon working electrode (Pine Research Instrumentation) was used in some runs with NOM model compounds. All potentials measured in aprotic solvent are reported vs the Ag/Ag$^+$ reference electrode and those done in aqueous medium are reported vs the Ag/AgCl reference electrode.

Before each set of electrochemical measurements, the working electrode was polished using 0.05 μm MicroPolish Alumina (Buehler), rinsed with DI water, sonicated for 2 min, and rinsed again with DI water. The electrochemical cell was prepared by adding 5 mL of 0.1 M TBAFP in DMSO, or 5 mL of 0.1 M KCl and 0.1 M phosphate buffer (pH 7.0), and purging for 15 min with N_2 (ultra-high purity), purging of the cell headspace was continued during the experiments. After deareation, a background scan was performed and 0.5 mL of the analyte stock solution was added so the final concentration in the cell was 1.5 x 10^{-3} M for NOM model compounds (where possible, but not all of these compounds were completely soluble in either water or DMSO), or 1 mg mL^{-1} for NOM (for the 17 samples that fully dissolved, and less for the 37 that did not). For the DMSO extracts of plant material, the concentration was 2 mg mL^{-1}. Details on how the electrochemical measurements were performated are descibed below under Method Development.

3.4. Results and Discussion

3.4.1. Selection of Method Conditions

In preliminary experiments, various combinations of NOM and model compounds, solvents, and mediators were tested using four working electrodes: 1.6 mm platinum, 3.0 mm glassy carbon, 5.0 mm edge plane pyrolytic graphite (all macro electrodes from Pine), and a 10 μm platinum electrode (BASi). The 1.6 mm platinum electrode gave the most consistent and characteristic response (data not shown), so it was used for all subsequent experiments.

Additional preliminary experiments were done to test whether the combination of added mediators and SWV would give improved characterization of NOM under aqueous conditions. Using one type of NOM (NOM-GT) with three common ETMs (**Figure B2A**) and one mediator (ABTS) with several types of NOM (**Figure B2B**), both gave SWVs that appear to be dominated by the mediator response (**Figures B2C and B2D**). Based on these results, we decided not to include mediators in most experiments with NOM.

To confirm that direct voltammetry of NOM (without mediators) is best done in 100% DMSO, and that DMSO as a co-solvent in predominatly aqueous media is not as effective, we performed otherwise identical experiments on Georgetown NOM in water with and without added DMSO (**Figure B2A**), and in DMSO with and without added water (**Figure B2B**). When the primary solvent was water, the sample voltammograms contained no more well-defined features than the solvent-only control; but when DMSO was the main solvent, the sample voltammograms gave clear peaks with currents that were 2-3 times the size of any features in the control. Similar exploratory experiments with other solvents (isopropanol, acetonitrile, etc.) did not show the advantages of DMSO. Therefore, all subsequent experiments were done with 100% DMSO as the solvent. (Note that no effort was made to remove traces of water from the DMSO, as is often done in applications of organic electrochemistry that require rigorously aprotic media (*172-174*).

3.4.2. Method Validation using Model Quinones

The conditions and protocols selected for electrochemical characterization of NOM were first applied to a variety of model compounds, most of which are known to be well-behaved ETMs from prior studies of their electrochemistry (*5, 198-201*). Of the seven model compounds we tested (**Table B2** and **Figure B1**), six were derivatives of ortho- or para-naphthoquinones and one was a para-anthraquinone. These quinones were further distinguished by hydroxyl, alkyl, or sulfonate substituents. An example of the resulting SCV and SWV data (for AQDS) can be seen in **Figure 3.2A** and all of the model compound data are shown in **Figure B3**. In all cases, the model compounds gave SCVs and SWVs that are typical of reversible quinone-hydroquinone couples in aprotic solvents (*168, 172, 178, 202*). In such cases, SCVs typically exhibit anodic and cathodic peaks that differ by 59/n mV, where n is the number of electrons transferred in the reaction, and the ratio of anodic to cathodic peak currents should be ~1 (*71*). Also, the corresponding SWV peak potential should be the average of potentials of the anodic and cathodic SCV peaks (i.e., ($E_{pa} + E_{pc}$)/2). All of these conditions apply to the data obtained in this study for AQDS (**Figure 3.2A**) and most of the other quinone model compounds (**Figure B3**).

Comparing the voltammograms for the whole set of model compounds (**Figure B3**) reveals some differences that could shed light on their relevance to redox reactions of NOM. One such comparison is between the six quinones and sphagnum acid, which is a p-alkyl substituted phenol. Like most phenols (*197*), it oxidizes to a phenoxy radical, which is less stable than semiquinone radicals, resulting in irreversible peaks similar to those observed in NOM (as discussed below). Another comparison is between the quinones that give increasing current from the beginning of each anodic scan (AQDS, lawsone, menadione, and menaquinone-4) and those that show a delayed response and anodic peaks that begin only above about −1.5 mV (juglone and o-NQS). The difference between these two groups is most likely due to substituent effects. For example, sterically bulky susbtituents, like the one on menaquinone-4, will have a more negative redox potential than a quinone with a charged substituent, like o-NQS with its SO_3^- group (*203*). Depending on the microenvironment surrounding the redox-active groups in NOM, the onset and magnitude of potentials will shift accordingly. Lawsone is unique among the quinones studied in that the second peak on the anodic scan is shifted to higher potentials (~0 mV), which likely is due to H-bonding involving the hydroxy group ortho to the quinone/semiquinone (*10*).

Another consistent characteristic of the model quinone data is that the SCVs show deviation between the first anodic potential scan and the later cycles. This type of deviation is common and reflects a variety of processes needed to develop the conditions required for stable and reversible electrode response. Since these experiments were prepared using only pure quinones, the shape of the first anodic scan is determined partly by the reduction of that starting material at the beginning of the scan, the oxidation of which then causes the anodic peaks even in the first and subsequent cycles of the SCV. This was ensured by preceding each SCV with 5 s induction period, during which −2 V was applied at the working electrode.

3.4.3. Method Application to Natural Organic Matter

Preliminary characterization of the overall stability of the controlling reactions during electrochemical experiments with NOM was done by comparing SCVs obtained over a sequence of three scan cycles (*71*). In most of the SCV figures shown in this study (model compounds and NOMs), the progression of the scans is represented by a color gradient (teal to pink) and the cyles are labelled C1 to C3 in the corresponding legend (e.g., **Figure 3.2**). Qualitative changes in SCV shape over multiple cycles can indicate changes in the reactions controlling the electrode response. This is commonly observed during the first scan, as was discussed above for the SCVs for model quinones included in this study. Another well defined example of this effect that can be seen in our previous work on electrochemistry of phenols and anilines, which typically showed featureless first anodic scans because the subsequent cathodic scan is needed to produce the reduction products that give electrode response in the next anodic scan (*197*). In this study, the first anodic scan of SCVs with some NOMs also gave a different electrode response, but subsequent cycles were very similar for most NOMs, suggesting that the controlling interfacial reactions had stablized (e.g., **Figure 3.2B**).

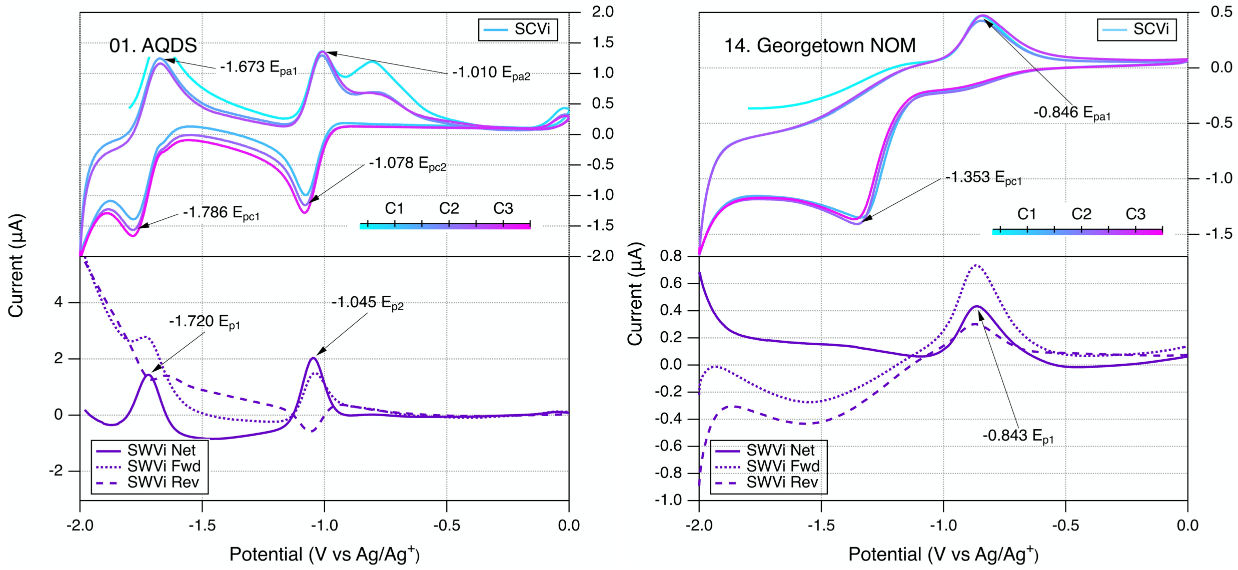

Figure 3.2. Comparison of SCV (top) and SWV (bottom) for (A) AQDS (B) Georgetown NOM. Only scan rate (i) is shown (25 mV s^{-1}), but others are given in Figures B3.01 and B4.14. The color gradient in the SCVs represents the potential sweep through cycles labelled C1, C2, and C3 in the legend. All runs in DMSO with a Pt working electrode.

In our original study of NOM electrochemistry in DMSO (*178*), the SCVs for most NOMs that we studied gave anodic and cathodic peaks at potentials that differed by a few hundred milivolts, which we interpreted as evidence of quasi-reversible redox couples. In the current study, the SCVs obtained with some NOM samples might also have been interpreted as containing quasi-reversible anodic-cathodic peak pairs (e.g., **Figures B4.11, 4.13, 4.14, and 4.16**), but the wide range of NOM types included in the scope resulted in relatively few SCVs that could be interpreted reliably in this way. A typical example of an NOM that does not appear to give reversible or quasi-reversible electrode response is Georgetown NOM (**Figure 3.2B**), where the dominant anodic and cathodic peaks are well defined but not close enough in potential to be interpreted as the result of one electroactive redox couple. In these cases, the forward and reverse currents in SWV confirm this by the prescence of two oxidation (or reduction) peaks in both the forward and reverse directions of the scan.

Another operational factor with diagnostic value in voltammetry is scan rate. The effects of scan rate on SCVs are confounded by multiple factors, so they were performed only at one, slow scan rate (25 mV s^{-1}, where time for decay of the capacitive current should provide more purely Faradaic electrode response (*71, 204*)). However, compared with SCV, the data obtained by SWV is less confounded with capacitive current and therefore the effect of scan rate on SWVs is better defined (*71*). To explore this, we measured SWVs at three scan rates for all NOMs and model compounds and all of these data are documented in **Figures B3 and B4**. In all cases, increasing scan rate increased the net SWV current, but had negligable effect on the potentials of the major anodic peak. Therefore, only one scan rate (the slowest) was used in the quantitative analysis of SWV peak potentials presented below.

To provide further insight into the robustness of our method for direct electrochemical characterization of NOM, we took the somewhat unusual step of running SCVs and SWVs by scanning potential in the cathodic, as well as anodic, direction. Because the SCVs were identical regardless which direction the scan was initiated, only SCVs intitiated in the anodic direction are reported. However, the SWVs gave different results when scanned in the anodic or cathodic direction, and these differences can be diagnostic of electrode processes (*205*). An example of these data is given in **Figure 3.3**, using Waskish Peat Reference Humic Acid because it was a good representation of the behavior of the majority of the NOM data. **Figure 3.3A** shows the SCV (top, initiated anodic, three cycles, without color gradient) and SWVs (bottom) performed by scanning potential in the cathodic (pink) and anodic (purple) directions. To facilitate quantitive comparisons, all of these data are superimposed in **Figure 3.3B**, and the SWV peaks are labeled: (*a*) and (*b*) for the anodic scan and (*c*) and (*d*) for the cathodic scan.

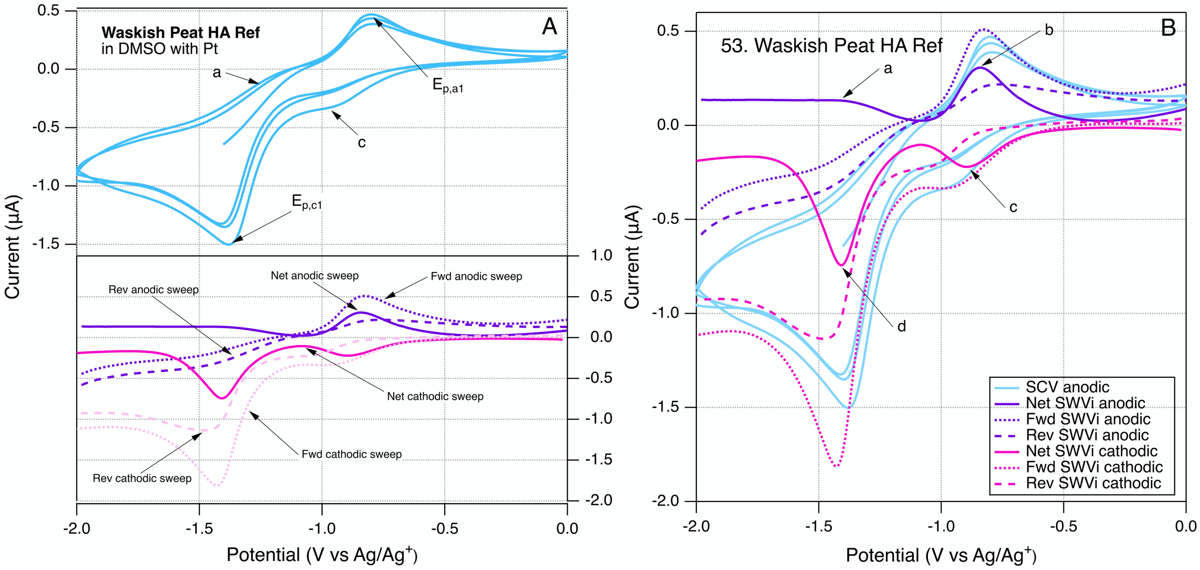

Figure 3.3. SCV (blue) and SWV anodic (purple) and cathodic (pink) sweeps for Waskish Peat HA. For SWV, forward, reverse, and net currents are shown with dashed and solid lines. (A) SCV and SWV separated and annotated to identify each component, a, c in the SCV show anodic and cathodic analogues discussed below. (B) SCV and SWV data are superimposed for comparison. All measurements made at scan rate of 25 mV s^{-1}, 2 mV step size, and 25 mV amplitude using a Pt working electrode.

3.4.4. Qualitative Comparison of NOM Voltammograms

The main features in **Figure 3.3A** are the two major peaks in the SCV (labelled $E_{p,a1}$ and $E_{p,c1}$) and the corresponding peaks (at the same potential) in the net current data for anodic and cathodic SWVs. The SCV also shows a shoulder that could be the cathodic analog to $E_{p,a1}$ and hump that could be the anodic analog to $E_{p,c1}$ (labelled *c*, and *a* respectively). Pairing the shoulder with $E_{p,a1}$ is supported by their alignment with the potentials of the peaks in the net anodic and cathodic SWV data (**Figure 3.3B**, peaks *b* and *c*). However, resolving the net anodic SWV data into forward and reverse components (dashed lines) shows they are roughly parallel, in constrast to the inverse relationship expected if peak *b* were due to a reversible electrode reaction (e.g., see E_{p2} for AQDS in the bottom of **Figure 3.2A** for AQDS). This evidence for irreversibility of the first anodic peak of NOM also can be seen in **Figure 3.2B**, for Georgetown

NOM, and most of the other NOMs studied (**Figure B4**). In contrast to the anodic results, the cathodic SWV for peak *c* shows net, forward, and reverse currents that are indicative of a quasi-reversible reduction reaction. The improved resolution of this feature in the SWV relative to the shoulder in the SCV could just be due to the higher sensitivity of SWV, but it could also arise because irreversible oxidation products formed during the forward scan of SCV interfere with the electrode response during that reverse scan (whereas the cathodic SWV is not preceeded by an anodic scan).

The other main feature in the SCV shown in **Figure 3.3A** is the large cathodic peak labelled $E_{\mathrm{p,c1}}$. In this case, the corresponding SWV feature is the peak in the cathodic scan that is labelled *d* in **Figure 3.3B**. As with peak *b*, the net current that defines peak *d* is the result of forward and reverse components (dashed lines) that are roughly parallel, and therefore indicative of an irreversible electrode reaction. The putative anodic analog to $E_{\mathrm{p,c1}}$ is the hump labelled *a* in **Figure 3.3A**, but inspection of the corresponding region of the SWV data shows no peak in oxidation current at the point labelled *a*, and signficant peak in reduction current labelled *d*, which is consistent with the electrode process that causes $E_{\mathrm{p,c1}}$ being fully irreversible. This analysis of electrode processes responsible for $E_{\mathrm{p,c1}}$, and above discussion regarding $E_{\mathrm{p,a1}}$, illustrates how SWV data can be used to clarify the interpreation of otherwise ambiguous features of SCV data on complex materials such as NOM. Similar interpretations apply to the data obtained with many of the NOMs included in this study (**Figure B4**).

In addition to the the four characteristic peaks and shoulders labelled (*a*, *b*, *c*, and *d*) in **Figure 3.3**, some of the SCVs for NOM had another distinctive characteristic: a sharp increase in current from the beginning of each anodic scan, an example of which can be seen in **Figure 3.2B**. In some cases, this feature is prominent enough to clearly define a new peak (e.g., Bemidji FA (**B4.02**), Kitty Hawk NOM (**B4.20**), Red Tussock NOM (**B4.35**), Rio Negro NOM (**B4.36**) and Suwannee River NOM (**B4.50**)), but in most cases it produces only a shoulder (**Figure B4**). The SCVs for model quinones do not show this feature (except possibly AQDS), but it is prominent in the SCV for the model phenol Sphagnum Acid **Figure B3.07**. This combination of results suggests that the sharp rise in current at the beginning of the anodic scan involves oxidation of species derived from phenolic moieites, which are more prevalent in NOM then quinonoid moieties. The feature is often absent from the first anodic sweep by SCV, which could indicate that it reflects oxidation of species formed during the previous cathodic scan, similar to the interpretation given in a study of analogous features in SCVs of nitrobenzene in DMSO (*206*). However, inspection of the SWV data obtained in this study shows that when NOMs gave an analogous peak in the net SWV data (at about −1.8 V), it was mainly due to increased current in the forward scan, and there generally was no change in the SWV reverse scan. Since the former is anodic, it confirms that the sharp rise during anodic scans in the SCV data was due to oxidation. Such an oxidation of phenolic moieties is likely to lead to products via autooxidation like reactions (*200, 207, 208*), which will tend to be irreversible, which is consistent with both the SCV and SWV data.

To codify and summarize the qualitative characteristics of the SCVs of NOM, we classified them into four types and by six features. The types include: (1) negligible response of features above background, (2) significant but somewhat featureless response, (3) sharp features similar to model compounds, and (4) combination of features characteristic of NOM. The feature characteristics of most NOM SCVs include: (*i*) the core, which creates "thickness" of the SCV on which other features are added, (*ii*) a rise in current immediately upon initiation of the anodic scan (IAR), (*iii*) a small inflection midway through the anodic scan (AI), (*iv*) the major peak during the anodic scan (MAP), (*v*) a small inflection near the beginnning of the cathodic sweep, which is analogous to *iii* (CI) (*vi*) the major peak during the cathodic peak, which is analogous to *iv* (MCP). **Figure B5** illustrates how these characteristics can generate the whole range of shapes of SCVs obtained with NOM. We scored each of the catgories and features (0 for absent; 1, 2, and 3 for weak, moderate, and strong, respectively), and calculated the sum as a measure of the overall "featurefullness" of the SCVs. That data for this accounting is given in **Table B6** and the results are summarized in **Figure 3.4**, with the NOMs sorted by increasing values of the sum of scores. The data in **Figure 3.4A** are also colorized by the sum of scores, to demonstrate that classification of the SCVs in this way gives a continuum of results with considerable range.

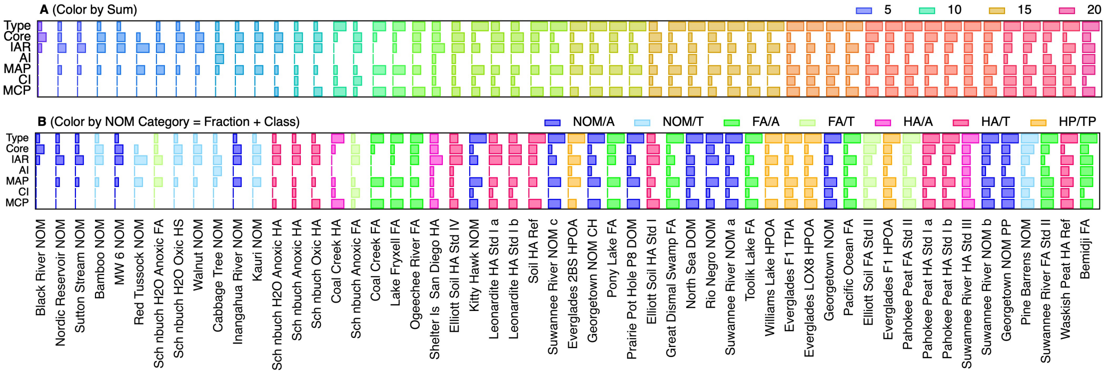

Figure 3.4. Comparison of scores that characterize features of the SCVs for all NOMs, ordered by increasing sum of all scores. (A) NOMs also colorized by sum of scores, and (B) NOMs colorized by category. Categories represent NOM class and fraction: e.g., aquatic fulvic acid, terrestrial humic acid, etc. Sums of scores and category assignments are given in Table B6 and the fraction and class data for each NOM are given in Table B1.

Figure 3.4B shows the same data as **Figure 3.4A**, but colorized by the NOM category, where category reflects both the fraction and class (**Table B1**). This presentation shows that nominally similar NOMs (i.e., similar category) give qualitatively similar SCVs (i.e., relatively similar feature score and therefore position on the x-axis). For example, whenever two samples of the same material were included (Leonardite HA, Pahokee Peat HA), the score obtained from their SCVs plot together (with the exception of Suwannee River NOM, which may be due to the very different age of these two samples, or because NOM being less fractionated is more diverse as opposed to HA which is more fractionated and less diverse owing to more similar SCV features). Comparing the color gradients for the six features shown in **Figure 3.4A** reveals that AI, MAP, CI, and MCP increase with overall featurefullness of the SCVs, but the Core and IAR scores appear to vary independently of the sum of scores.

To test the diagnostic value of the scoring and ordering of SCVs shown in **Figure 3.4A**, that result can be compared with **Figure 3.4B**, which shows the same data, but colorized by NOM category. In general, the low scores are dominated by terrestrial samples (light colors), and the high scores are mostly aquatic samples (dark colors). For example, all terrestrial NOMs except Pine Barrens have low scores (light blue) and all aquatic FAs have moderate to high scores (dark green). The most variable categories are aquatic NOM (dark blue), which are distributed about evenly across the whole range of scores, and both terrestrial (red) and aquatic humic acids (pink), which are mixed together in the middle of the range of scores. Other studies have reported a different trend in redox properties: electron accepting capacity (EAC) tends to be higher for humic acids than fulvic acids, and higher for terrestrial humic acids than aquatic humic acids (*150, 155*). However, EAC is more directly comparable to the cathodic peak potential breadths defined later in this study, and the trends in this aspect of our voltammetric data are more consistent with the trends in EAC. Comparison of **Figure 3.4B** to **Table B1** also reveals that most of the NOMs provided by D. Macalady scored low (with the exception of Rio Negro and Kitty Hawk) as did all of the Schönbuch Soil samples from A. Kappler, whereas most of the standard materials from IHHS gave high scores. This trend is not consistent with differences in the age of these samples, or what detail we have on differences in the extraction methods, but may be due to differences to the extent that the redox-active moieties were concentrated in the sample.

3.4.5. Fitting of Peaks in Voltammetry Data

In addition to the qualitative analysis of the SCV and SWV data presented above, we investigated several methods for *quantitative* determination of peak currents and potentials. On both the SCV and SWV data, the raw data with analyte was modified by subtracting background scans that were obtained without the analyte, but under otherwise identical conditions (solvent, electroyte, buffer, etc.). In principle, this approach should isolate the electrochemical response of the analyte from non-Faradaic effects, but we found that background subtraction produced distorted peaks in a few cases, usually where the sample signal was weak. Therefore, we used background subtraction to process the data for most materials, but when this gave problematic results, we used the raw analyte in further analysis, and include the background data for comparison. The latter group is identifiable in **Figure B4** by the presence of background scans shown in gray.

The next step on quantitative analysis was determination of peak position and size (position/height/area). To choose peak position and size: (*i*) a baseline was defined from the start to the end of the current response, (*ii*) a vertical line was drawn from the middle of this baseline to where the current response was largest. The potential at which this line crosses to the highest current response is defined as the peak potential. These values are summarized in **Tables B4 and B5** and used throughout the remainder of this study. Peak height is defined by the length of the vertical line described above and is defined as the peak current. Peak areas were quantified by integrating the area under the curve bordered by the peak and defined baseline. Peak current data are not tabulated because their significance was ambigous in many cases, for reasons elaborated below. But, we did use the better defined peak current data for a few samples to demonstrate the electrode response in our system showed the expected relationship to sample concentration. This is shown in **Figure 3.5** for a model ETM, AQDS, and Georgetown NOM. In both cases, peak currents show a roughly linear increased peak current with concentration (**Figure 3.5**, insets). The result with NOM is notable because it verifies that the peaks obtained by the method developed in this study are the direct result of an electrode reaction involving NOM.

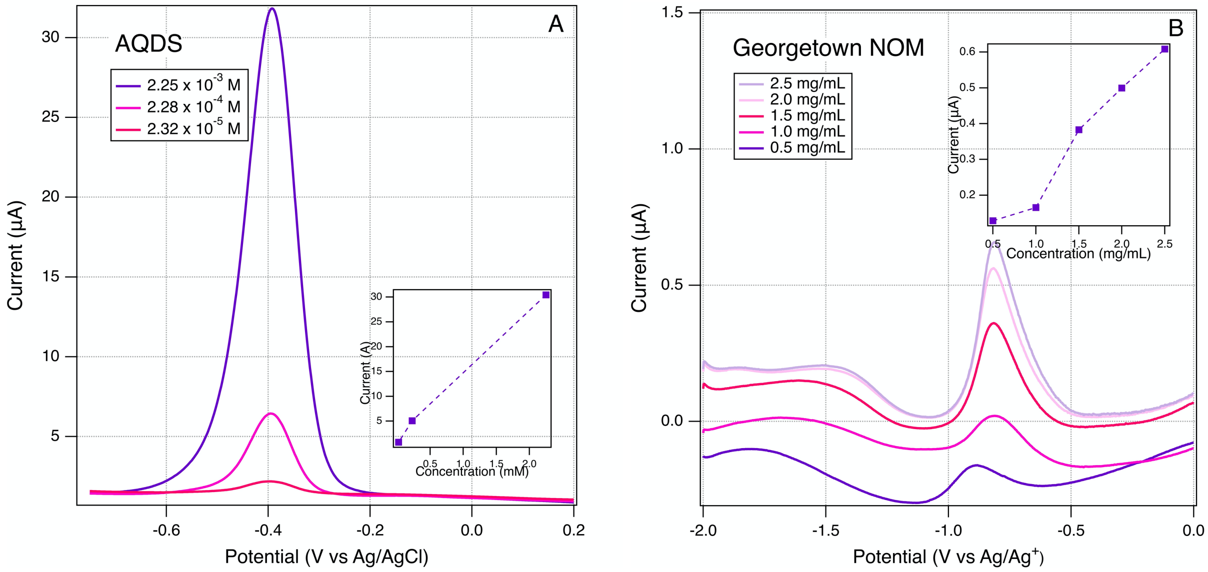

Figure 3.5. Effect of varying analyte concentration on SWVs: (A) AQDS in H2O (B) Georgetown NOM in DMSO. Scan rate of 25 mV s^{-1}, 2 mV step size, and 25 mV amplitude using a Pt working electrode.

After background subtraction, the SCVs and SWVs for the model quinones show roughly flat baselines (**Figures 3.2A** and **B3**), which made it straight-forward to define baselines for accurate measurement of peak size. However, most SCVs and SWVs for NOMs showed significantly uneven baselines, even after background subtraction (**Figures 3.2B** and **B4**). To overcome this, we investigated using the moving average baseline correction method (*196, 209*), which is the most common advanced method for defining the baseline of voltammograms with complex shape. The method is not easily applied to SCVs, but it gave nearly flat baselines for the SWVs of most NOMs (not shown). However, we chose not to use these results because the correction removed prominent features from the raw SWV data that might be indicative of electrochemical characteristics of NOM the could deserve further consideration. In particular, we noted that NOM usually gave SWVs with current that was significantly greater than expected background (capacitive) current over a much wider range of potentials than expected from specific peaks (e.g., compare **Figure 3.2A and 3.2B**). Elevated Faradaic current over wide potential ranges is sometimes attributed to redox reactions of species in the bulk solution that have not had time to diffuse to the electrode surface (*71*), or it could arise from the combined effect of multiple redox-active function groups (i.e., the "continuum" hypothesis described in the introduction). To allow us to explore the continuum hypothesis further in the analysis that follows, we did not apply baseline correction to the data. Instead, we adopted a novel set of criteria to define the broad regions of electrode response that extend beyond well defined peaks.

3.4.6. Quantitative Comparison of Characteristic Potentials

Using the peak identification and fitting methods described above, two anodic and cathodic pairs of peaks were assigned for most model quinones and one anodic and one cathodic peak (unpaired) were asssigned for the NOMs. These peaks are labelled (E_{pa1}, E_{pa2}, E_{p1}, etc.) in **Figures B3 and B4**, and the potential values are summarized in **Tables B4 and B5**. Direct correlation of peak potentials obtained by SWV with those obtained by SCV—for all peak types and samples—shows the two methods gave values that agree within ~50 mV (**Figure 3.6**). While the overall trend in **Figure 3.6** suggests a 1:1 correlation between the two types of potentials, this is mainly due to the distribution of data for model compounds and a relatively tight cluster for most NOMs. The NOM responses, like the model compounds make up two clusters within their respective groups. The two model compounds that form the smaller cluster are o-NQS and juglone, which as mentioned previously is most likely due to substituent effects. A quinone with a charged substituent (o-NQS) will have a more positive reduction potential. The NOM clustering is most likely to do with similar substituent effects. One implication of this result is that the quinones used as NOM model compounds have potentials that are substantially more negative than any of the NOM samples studied, which has been noted in other recent studies (*167*).

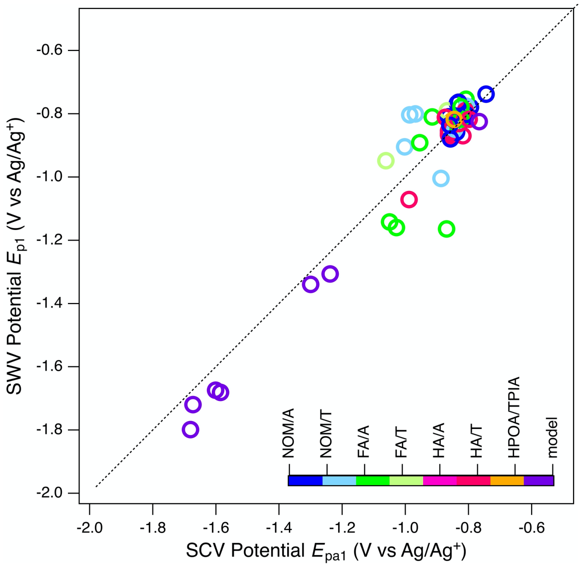

Figure 3.6. Comparison of potentials obtained by SWV (E_{p1}) and by SCV (E_{pa1}). Markers represent peak potentials (from Table B4) for each NOM sample. Colors and the legend refer to the NOM classification documented in Tables B1 and B6. Diagonal dashed line is 1:1.

The clustering of peak potentials for NOMs in **Figure 3.6**—and lack of a correlation between SCV and SWV potentials within that range of data—was surprising and led us to consider additional characteristics of the NOM voltammograms before further analysis for correlations within the peak potential data set. The main concern was that the features identified as peaks in the SCVs for NOM tend to be broader than the range of potentials expected for peaks from well-defined redox couples (which should be roughly ±120 mV about the peak (*71*), as seen with the model quinones shown in **Figure B3**). For many of the NOMs, large portions of the potential scan (often about 1 Volt) exhibit current that is elevated beyond what could be non-Faradaic background from the electrode or electrolyte (**Figures 3.2B, 3.3, and B4**). This result is expected if the sample is comprised of multiple electrode-active moieties with potentials that are too similar to be resolved by (conventional) SCV, such as for some quinones at high pH (*200*). Of particular interest is the possibility that the redox-active moieties in NOM are coupled through intramolecular conduction to a sufficient degree that the sample potential is a continuum, analogous to the band gap in semiconductor materials. The continuum hypothesis has been suggested previously (*130, 149, 150, 167, 210*), but not evaluated quantitatively.

As a first step toward quantitative characterization of the hypothesized continuum of NOM electrode response, we characterized the “breadth” of each major anodic and cathodic peak from SCV and SWV by determining beginning and end potentials that were chosen with more inclusive criteria than is used in conventional analysis of peak widths (*211, 212*). The criteria—which are summarized together with the data in **Table B7**—were necessarily subjective because the features that define the full extent of these peaks often were ambiguous, but comparison of the SCV and SWV data helped to ensure consistency. The results of this analysis are summarized in **Figures 3.7 and B6** (for SCV, and SWV respectively), with the peak potentials shown as black markers and the corresponding start and end potentials (colored markers) connected with a bar to represent breadth. When there was more than one anodic or cathodic peak (usually the model compounds), they are distinguished by marker shape. Note that this often resulted in overlapping breadths for SCV data, although not for SWV data. The samples (y-axis) are sorted and colorized by fraction and class (using the same category scheme defined in **Table B1** for **Figures 3.4 and 3.6**).

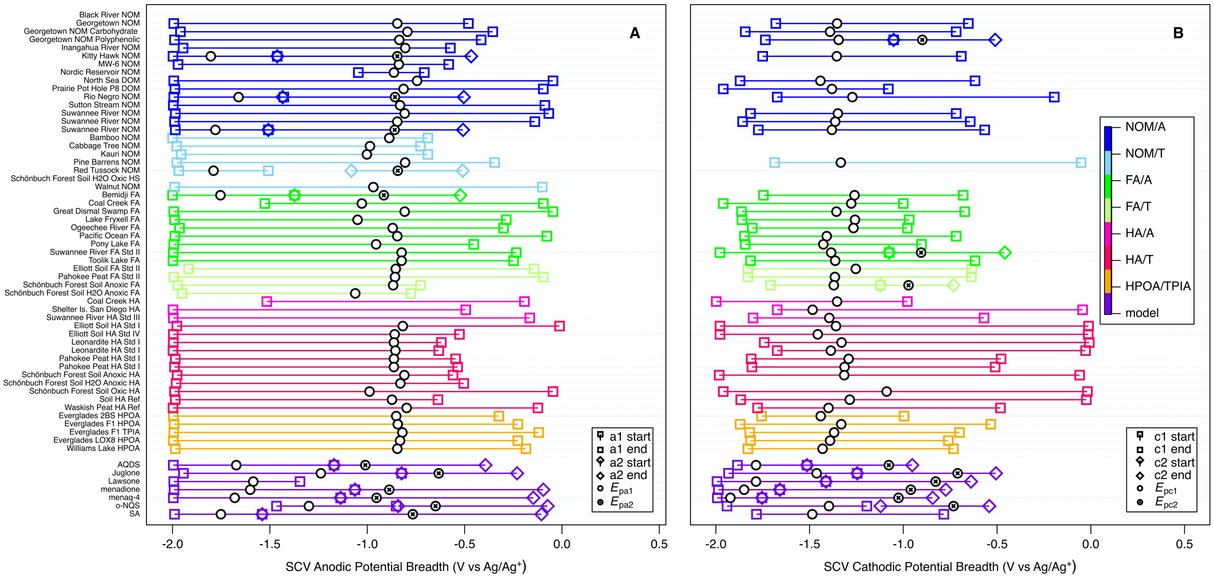

Figure 3.7. SCV anodic and cathodic potentials and peak breadths of all NOMs and model compounds. Squares indicate onset and end of current surrounding E_{pa1} or E_{pc1}, diamonds indicate onset and end of current surrounding E_{pa2} and E_{pc2}. Colors indicate type of NOM. For SWV breadths see Figure B6**.**

The main purpose of **Figures 3.7 and B6** is to provide a broad perspective on trends in the overall dataset. Starting with the peak potentials (black markers), the figure shows there is relatively little variation in the main anodic and cathodic peak potentials for NOMs, so we calculated the average and standard deviation of these values, which are −0.866±0.069 V vs

Ag/Ag$^+$ for E_{pa1} (**Fig. 3.7A**), −1.35±0.071 for E_{pc1} (**Fig. 3.7B**), and −0.831± 0.051 for E_{p1} (**Fig. B6**). The similarity between average values of E_{pa1} and E_{p1} is consisent with **Figure 3.6**. The low relative standard deviation on all three of these average potentials (5-8%) despite the very wide range of NOM types and sources included in the dataset, could be due to (*i*) selectivity in the methods used to extract NOM samples and/or (*ii*) a "central limit" that arises from continuum redox potentials. Both of these possiblities are discussed further in the sections that follow.

The peak breadth data (colored markers and bars in **Figures 3.7 and B6**), shows greater variability than the peak potentials, but some of this is likely to be due to ambiguity in the assignment of the start/end potentials, and there is no simple relationships between breadth and other factors. For example, while the breadth about E_{pc1} in **Figure 3.7B** appears to be greater for HA and less for FA and HPOA/TPIA, consistent with observations for electron accepting capacities (*150, 155*), this pattern does not extend to E_{pa1} or E_{p1} (**Figures 3.7A and B6**), but electron donating capacities have been shown to be affected by the molecular weight of NOMs (*213*). Therefore, we conclude that breadths, like potentials, are largely invariant with NOM category and source. The average values of breadth are 1.63±0.24 V for E_{pa1} (**Fig. 3.7A**), 1.28±0.34 for E_{pc1} (**Fig. 3.7B**), and 0.648±0.15 for E_{p1} (**Fig. B6**). These values are similar for E_{pa1} and for E_{pc1}, and about twice that of E_{p1}, which probably just reflects the greater resolution of SWV over SCV. The average values of breadth are much greater than the standard deviation in the peak potentials (about 3- and 5-fold for SWV and SCV, respectively), which is futher evidence for the continuum hypothesis.

Evidence for redox potentials ranging of a continuum of values has been seen in electrochemical characterization of iron minerals and in electron donating capacities of microbially reduced humic substances (*153, 214, 215*). Some of those studies modeled the larger than expected range over which electrons are accepted and donated with a Nernst equestion that contained a factor (β) to account for the non-ideal beahvior. When β is 1 behavior is Nernstian and when β is less than 1 the potential range is widened. This formulation originates from models developed to account for peak broadening and narrowing (non-ideal behavior) in electroactive polymer films (*216*). Even though we experienced this in our system, using the β factor did not apply in our case due to the complex and indeterminate nature of the analyte, and ascertaining fraction of reduced to oxidized moieties to obtain the β factor is something which we did not pursue.

Comparing the peak potentials and breadths in **Figures 3.7 and B6** reveals that the SCVs for NOMs are asymmetrical about the corresponding potentials and skewed opposite the direction of the scan (i.e., anodic scans are negatively skewed in **Figure 3.7A** and cathodic scans are positively skewed in **Figure 3.7B**). This trend is the reverse of prototypical SCV peak shape (which rises sharply when a characteristic potential is reached and then decays slowly as diffusion become limiting) (*71*) and the SCV peaks obtained with most model compounds (**Figure B3**). However, this comparison may be strong evidence for the continuum hyphothesis of NOM redox potentials, because that scenario should produce a gradual increase in current over an extended range of potentials. The SWV data (**Figure B6**) shows a modest positive skew for NOMs, which is slightly more consistent with the model compounds. This is expected because the breadths for the SWVs were chosen using the net potential, which subtracts the forward and reverse components, and this essentially subtracted out the effect of the rising current.

3.4.7. Relationship to Chemical Composition

The above analysis of characteristic potentials from the electrochemical measurements made in this study was interpreted mainly as evidence for the continuum hypothesis of NOM redox properties. However, this does not preclude the other possible explanation for the lack of significant trends in the peak potentials: that the methods used to obtain the samples (extraction, fraction, and concentration) were selective for some chemical components over others, thereby decreasing the diversity of chemical structure within the sample set. To investigate this possibility, it would be useful to compare the electrochemical data with chemical composition data for the whole set of test compounds. Unfortunately, the very limited quantities of some samples, and cost of performing larger numbers of structural characterizations by advanced methods (e.g., FTICR-MS) made it infeasible to fully implement this approach within the study. However, for 25 of the 54 NOM samples that we characterized electrochemically, chemical composition data were available from the suppliers, or their publications. These data were used to calculate ratios of H:C and O:C so that they could be summarized in a Van Krevelen diagram format (*28, 217*). Comparing the data (solid markers in **Figure 3.8**) to regions of typical composition for component types (dashed lines, from (*218*)), shows that all of the sample data fall in just two regions on the diagram: aquatic NOMs plot as tannins, most fulvic and humic acids plot as lignins, and HPOA/TPIA straddles the tannin and lignin regions.

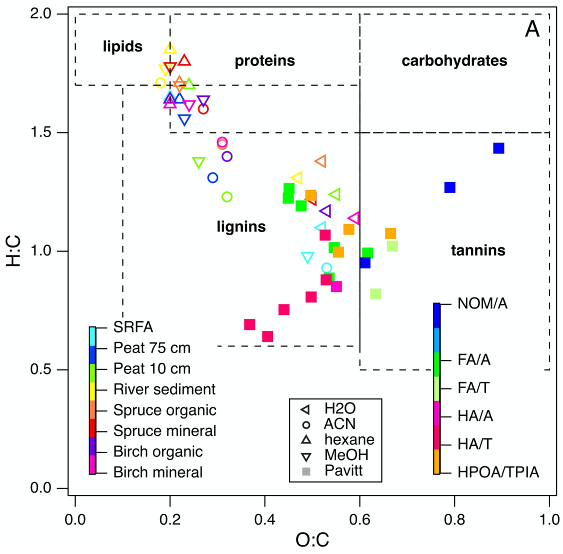

Figure 3.8. Van Krevelen diagram of 25 NOMs used in this study and recreated data from the following reference (*189*). Colors indicate different categories of NOM. The legend in the middle and left defines the open markers (recreated data), the legend on the right defines the filled in markers (data in this study). Elemental composition data obtained from IHSS, USGS, and Ref. (*84*).

To provide further context for interpretation of **Figure 3.8**, data are included (open markers) from a recent study on the chemical composition of organic matter obtained by different extraction methods (*189*). For these data, the source material is represented by color and the extraction method is represented by marker shape (left and middle legends, respectively). Most of the data distrubute along a trend with negative slope according to the extraction method (high H:C, low O:C ratio for hexane and methanol, intermediate H:C and O:C ratio for acetonitrile and water). In contrast, solvent extraction of SRFA (light blue markers) had little influence on H:C and O:C and the data all plot in the vicinity of other source materials that were extracted with water. Unlike the other source materials, SRFA was initially obtained by the conventional alkaline extraction step, and it was concluded that this step decreased the diversity in molecular structure that was otherwise evident in the NOMs that were obtained without alkaline extraction (*28*).

Many of the NOMs used in this study were alkaline extracted, so it is not surprising that they plot near the SRFA data in **Figure 3.8**. Therefore, the distribution of the chemical compostion of the samples used in this study is consistent with selectivity of the conventional (alkaline) extraction methods for similar redox-active moieities. Similar conclusions have been drawn from other types of evidence, such as near edge X-ray absorption fine structure (NEXAFS) spectra (*219*), collision induced dissociation coupled to FTICR MS (*220*), solid phase extractions and FTICR MS (*100*), fluorescence spectroscopy coupled to PARAFAC analysis (*221*), and statistical analysis of chemical composition data for hundreds of NOMs (*99, 106*). A few of the NOMs from this study distribute along a diagonal in **Figure 3.8** that is consistent with H:C/O:C ratio of ~2. This type of trend in a Van Krevelen diagram can aries from a homologous series of molecules that vary only by an exact mass of a certain functional group (*222*), which could arise from a consistent diagenetic history (*217*), but this interpretation is not likely to apply to the selection of NOMs sample used in this study.

For the relatively narrow range of peak potentials observed in this study to be due to the polyphenolic and quinoid moities associated with lignin and tannin, the redox-active moieites that are expected under these conditions should have peak potentials that are consistent with the peak potentials measured for NOM. A previously published survey of over one-hundred quinones shows that the potential window in DMSO for naphthoquinones and anthraquinones (~0.6 V) is smaller than the potential window of benzoquinones (~1.5 V) (*176*). Similarly, another study compared over seventeen hundred quinones, and found that the potentials for most of them fell in a window of ~0.6 V (*223*). The narrower potential range for the more conjugated quinone model compounds could be consistent with the relatively narrow range observed for NOM because NOM is thought to be a complex network of quinones and polyphenols.

3.4.8. Solvent Effects on Potential Measurements

The main benefit of using DMSO as the solvent for electrochemical characterization of NOM is the improved electrode response due to increased access to the redox-active moieties, as conceptualized in **Figure 3.1**. However, this effect also creates other challenges: for example, it will take further study to fully understand how the access to redox-active moieties created by unfolding the tertiary structure of NOM compares with the access gained by mediation with solution-phase ETMs. However, the primary issue is whether potentials measured in DMSO can be adjusted for direct, quantitative comparison with potentials measured in water or calculated from thermodynamic data. In previous work (*167*), we assumed this could be done by applying a constant correction factor, obtained by measuring the potential of a suitable redox couple (commonly ferrocene (*224*)) measured in both solvent systems. This calculation led to estimates of the redox potential of NOM in water that ranged from 0.4 to −0.3 Volts vs. SHE, which overlaps with other estimates of NOM redox potential and model quinones.

However, there are additional factors that complicate the comparison of potentials made in different solvents (e.g., solvation effects on activity coefficients) that are not as easily quantified (*225, 226*). To investigate this issue more thoroughly than we did in previous work, all seven of the model compounds used in this study (**Tables B2-B3**) were characterized by SCV and SWV in both DMSO and in water (**Figures B3** for DMSO, not shown for water). Not all of the model compounds were fully soluble in both solvents, so the two sets of data are not directly comparable in terms of current, but modest differences in the model compound concentration should not affect the peak potentials significantly. As discussed above, the model quinones in DMSO give two pairs of peaks representing (quasi)reversible one-electron transfer, but in water they give one pair of peaks representing a two-electron tranfser (*172-174, 198, 200, 203*). The potentials corresponding to these peaks are given in **Table B5** and SWV data are summarized in **Figure 3.9** by plotting both E_{p1} and E_{p2} obtained in DMSO versus E_{p1} obtained in water. The two correlations are roughly linear and parallel, so we fit the data as two lines with a common slope by global regression. The resulting intercepts were −1.26 and −0.533 V for E_{p1} and E_{p2} respectively. We then used the E_{p2} intercept to adjust our average peak potentials. We were able to disregard E_{p1} by assuming that its shift to resolve from a two wave (aprotic) to a one wave (water) response was minimal in comparison to the shift of E_{p2} (*174*). This value (0.533 V) is similar to the correction factor determined previously (0.472 V) using only ferrocene (*167*).

Assuming that the new correction factor more accurately reflects the whole range of factors that cause differences in potentials from DMSO and water, we used this new value to adjust the average peak potentials for E_{pa1}, E_{pc1}, and E_{p1} obtained from the data in **Figures 3.7 and B6**. The resulting estimates, for aqueous conditions vs. SHE, are −0.128, −0.613, and −0.0930 V, for E_{pa1}, E_{pc1}, and E_{p1}, respectively. The values for E_{pa1} are in excellent agreement with values for select humic acids that were calculated from MER/MEO data (*153*). It is important to note that these numbers should be considered a rough estimate, due to the difficulty in comparing potentials using two different reference electrodes, higher concentrations of electrolyte can alter potentials by several hundred milivolts (*227*), and a change of electrolyte type can alter the potential significantly (*174*).

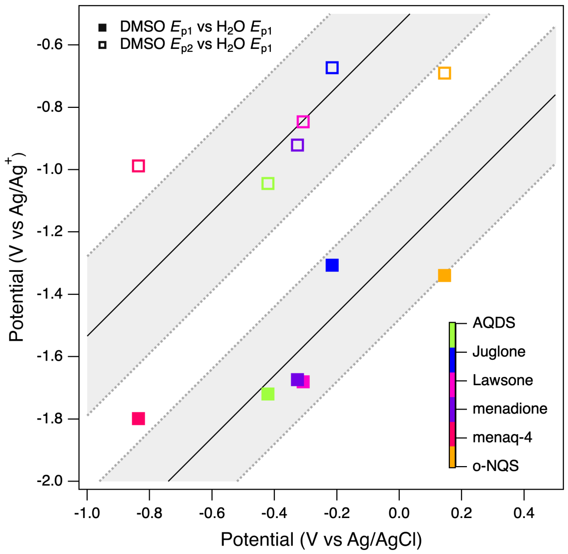

Figure 3.9. SWV potentials of model compounds in water vs DMSO. Conditions in water are, 0.1 M KCl, 0.1 M phosphate buffer (pH 7), Pt or GC WE, Ag/AgCl RE. Conditions in DMSO are, 0.1 M TBAFP, Pt WE, Ag/Ag$^+$ RE filled with 0.1 M TBAFP and 0.005 M $AgNO_3$. CE Pt coil for both DMSO and water. The slope for both lines were fixed at 1; the fitted intercepts are -1.26 ± 0.22 for E_{p1} and -0.533 ± 0.26 for E_{p2}. Dashed lines are the 95% confidence bands about the regression lines.

3.5. Conclusions

Characterization of the properties of NOM is greatly complicated by its complex, indeterminant, and presumably variable composition. This necessitates the use of multiple, complementary characterization methods, ranging from mass spectrometry to fluorescence spectroscopy and electrochemistry. Conventional electrochemical methods generally produce poor results due to poor contact between the redox-active moieties in NOM and the working electrode surface, but that can be overcome using soluble electron transfer mediators or aprotic solvents. The latter has been shown to produce promising voltammograms for a variety of NOM samples, and the approach was refined and extended to a large range of NOMs in the study.

A major refinement to the method used in this study was the sequential use of cyclic and square-wave voltammetry (SCV and SWV), which provided complimenatary information that greatly improved confidence in the interpretation of peaks and other features in terms of NOM redox processes. Most samples gave voltammograms that were dominated by one anodic and one cathodic peak, superimposed on a background of apparently Faradaic current over a wide range of potentials. The peak potentials and breadths were found to be similar across all types of NOM, which contradicts the expectation that the redox properties would vary significantly with NOM source, type, etc.

The lack of differentiation in electrochemical properties of NOM may be partly due to the extraction methods commonly used to obtain NOM samples, which may result in selection for some components of NOM structure over others. This hypothesis is supported by comparison with recent results using other structural characterization methods like FTICR-MS and PARFAC. However, the similarity in NOM redox properties may also be because the redox-active moieties in NOM are coupled through intramolecular conduction to a sufficient degree that the sample potential reflects a continuum of electrode response, which would result in voltammograms with more broad and average features. This conclusion is similar to the interpretation given to the redox properties of NOM determined in other studies using coulometry.

The continuum model of NOM redox properties has broad implications for the role of NOM in biogeochemistry and contaminant fate. In both contexts, NOM may act as an electron donor or acceptor with a wide range of other redox-active species, thereby mediating reactions among species with a range of redox potentials. Coupling between the redox-active moieties within NOM determines the aggregate potentials measured by voltammetry, as well as the electron donor/acceptor capacities measured by coulometry. Measurement of these properties is facilitated by dissolution in DMSO, which allows unfolding of the tertiary structure of NOM and, thereby, access of redox-active groups to the eletrode.

3.6 Acknowledgements

The study was initiated for a presentation by P. Tratnyek for a symposium in honor of George Aiken at the 253rd ACS National Meeting in San Francisco, CA, 2-6 April 2017. Initially, a goal of the study was to compare results obtained on samples of NOM acquired over several decades from George Aiken, Donald Macalady, Yo-Ping Chin, and Baohua Gu. The scope was expanded to include new NOM samples from Paul Bloom (IHSS), Joel Coates, Gordon Getzinger, Andreas Kappler, Boris Koch, Joseph Needoba, and Brett Poulin. We thank all of these colleagues for their contributions to this work. Some preliminary electrochemical experiments were performed by undergraduates Eric Sauer, Nancy Nguyen, and Nick Slenning. Nguyen and Slenning were funded by a Murdock Trust grant to Paige Osberg Hall (Univ. of Portland). This material is based upon the work supported by the National Science Foundation, Environmental Chemical Sciences Program under Grant # 1506744.

Chapter 4. Electrochemical Characterization of Reactive Mineral Intermediates (RMIs) from Fe(II) Amended Iron Oxides[3]

Ania S. Pavitt and Paul G. Tratnyek

4.1. Abstract

Iron oxides amended with Fe(II) exhibit enhanced reactivity towards contaminants, and as a result, there has been a vast amount of research in the use of these for the remediation of contaminated soils and sediments as well as in predicting their reactivity. Electrochemistry allows for the characterization of redox properties, which in turn could be used to correlate to degradation kinetics, it offers the ability to obtain in situ, temporal redox changes. Toward this end, we used zero current chronopotentiometry to obtain redox properties of six iron oxides, goethite, hematite, lepidocrocite, magnetite, siderite, and wustite amended with Fe(II) in unbuffered solutions. We obtained a range of potentials for the iron minerals alone, but once Fe(II) was added all potentials converged to similar values. This is in line with other work that has shown that the primary reactivity was not derived from the mineral substrate but from the result of iron addition. We plotted our data on Eh/pH diagrams and compared the experimental data to thermodynamically calculated values. The Fe(II) only system fell directly on the calculated Fe(II)/Fe(OH)$_3$ couple, while the mineral/Fe(II) systems fell in between several possible species, with slopes comparable to many of the expected species. Based on this and the similarity of our E_{OC} values, it is possible that the RMI phase starts (hours timescale) as a common phase and eventually shifts to varying phases that are then more dependent on the mineral substrate.

4.2. Introduction

The most stable and familiar forms of iron in the environment are the oxide minerals such as magnetite, hematite, and goethite (*30, 35*). These phases play important roles in a wide range of natural biogeochemical and engineered environmental remediation processes (*228-231*). The vast amount of research that has been, and continues to be, done on these processes includes many studies that treat the stable and familiar iron oxides as reactive species. Most of these

---

[3] To be submitted as A. S. Pavitt and P. G. Tratnyek, Electrochemical Characterization of Reactive Mineral Intermediates (RMIs) from Fe(II) Amended Iron Oxides, *In prep*.

studies, however, find that the reactivity of these minerals is highly variable, so understanding the source(s) of this variability has become a priority research objective.

A recent example of this evolution involves the remediation of contaminated soils and sediments by processes known collectively as abiotic natural attention (ANA) (*232*), or more broadly, in situ chemical reduction (ISCR) (*233*). Many studies using the stable/familiar iron oxides in laboratory batch and/or column experiments have reported significant rates of contaminant removal that appear to be due to abiotic processes. These studies include chlorinated solvents and other aliphatic organohalides (*234-237*), explosives and other nitroaromatic compounds(*32, 238-244*), cationic metals and metalloids (*245*), and transition metal or actinide oxyanions (*246-248*). However, the conditions of these studies were selected—at least in part—for efficient laboratory experimentation, so it is unclear how the results translate to in situ environmental conditions.

One factor that appears to be a major determinant of reactivity involving iron oxides under anaerobic conditions is the interaction of minerals with solution-phase Fe(II). For example, while $Fe(II)_{aq}$ or magnetite (Fe_3O_4) alone do not reduce perchloroethene or trichloroethene (PCE, TCE) at measurable rates, the combination of these species (Fe_3O_4/Fe(II)) can cause complete dechlorination with half-lives ($t_{1/2}$) of a few years in batch experiments under favorable conditions (*249*). Similarly, nitrobenzene undergoes negligible reduction over the timescale of a few hours to days, when using non-stoichiometric Fe_3O_4 (ratio of Fe(II)/Fe(III)<0.5), or Fe(II) alone, but is rapidly reduced using stoichiometric Fe_3O_4 (ratio of Fe(II)/Fe(III)=0.5), or when combined with $Fe(II)_{aq}$ regardless of stoichiometry (*33, 243*). Increases in reduction rates have also been observed upon the addition of $Fe(II)_{aq}$ to the Fe(III) oxides goethite, hematite, and lepidocrocite (*34, 243*).

Increased reduction rates in Fe(II) amended iron oxide systems have long been attributed to the lower reduction potential of adsorbed Fe(II) (*34, 247, 250*). However, recent studies have shown that adsorption of Fe(II) onto iron oxides leads to the delocalization of electrons into the solid, resulting in the reduction of structural Fe(III) to Fe(II) (*251*). This exchange has been demonstrated with hematite (*252-254*), goethite (*31, 255, 256*), and maghemite/magnetite (*33, 257*), using Mössbauer spectroscopy with isotope-labeled iron and verified by computational studies (*258-261*). A third way that sorption of Fe(II) can change the reactivity of iron oxides is by causing recrystallization and/or (co)precipitation, which can increase the surface area and/or reactivity of the phases exposed at the particle surface (*31, 256*). The idea that authigenic phases (e.g., in situ formed surface coatings composed of amorphous iron oxyhydroxides) can increase the reactivity of minerals has been invoked in many past studies of processes such as water treatment (*262*) weathering (*263*)and corrosion (*264*).

Several recent studies have provided additional evidence that authigenic iron oxyhydroxides could contribute significantly to the reactivity of iron oxides under conditions relevant to ANA and ISCR. These studies include (*i*) the reductive dechlorination of PCE and TCE by magnetite (*249*) and ferrogenous clays (*265*) upon addition of sufficient Fe(II) to exceed the solubility product of $Fe(OH)_2$ and (*ii*) the bimodal kinetics of H_2 formation from reduction of water by zerovalent iron (*266*). The results of these studies have been interpreted as evidence that reduction in these systems is mediated by highly *reactive mineral intermediate* (RMI) phases that form under in situ conditions and that react rapidly with any available oxidants, including contaminants. The transient, dynamic, and metastable character of RMIs makes them a likely source of variability in contaminant reduction rates that is otherwise difficult to explain.

Another consequence of the dynamic character that is expected of RMIs is that they will be difficult to sample and characterize. The initial evidence for RMI formation in the three studies noted above (*249, 265, 266*) was indirect and arose from the interpretation of kinetic data on contaminant reduction. Follow-up experiments—using Mössbauer spectroscopy and X-ray diffraction—provided direct evidence for formation of an authigenic phase similar to $Fe(OH)_2$, but it is not yet certain that this phase is responsible for the contaminant reduction attributed to the RMIs. Other, earlier studies provide additional direct characterization of authigenic (i.e., secondary) phases that might be similar to RMIs. For example, X-ray absorption spectroscopy (XAS) has been used to show there are temporal changes in the mineralogy of ferroginous clays upon addition of $Fe(II)_{aq}$ (*267*), Mossbauer has been used to show secondary mineral formation upon reduction of contaminants when coupled to XRD (*257*). Atom probe tomography has verified atom exchange between sorbed Fe(II) and structural iron (*31*), others have shown complete mineral recrystallization of iron oxides using Mossbauer coupled to TEM (*256*).

One limitation to all of the above methods is that they are not normally usable for real-time characterization of mineralogical conditions in situ, which is likely to be essential for unbiased and complete characterization of RMIs. Electrochemical methods, in contrast, are very well suited to real-time and in situ characterization of redox-active species, with temporal resolution that can range from seconds to weeks or more. A variety of electrochemical methods can be performed with similar equipment to obtain data on the potential, current, interfacial capacitance and impedance, and bulk electron acceptor/donor capacity of redox-active species at a working electrode. Typically, electrochemistry is performed either with an inert working electrode (e.g, Pt, or glassy carbon (*197, 268*)) interacting with redox-active species in solution or with a working electrode made from the redox-active species (e.g., iron metal (*269*), hematite (*253, 270*), or magnetite (*271, 272*)) in an inert electrolyte.

Most electrochemical methods can also be applied when the analyte is a particulate material, although this introduces a variety of additional operational and theoretical challenges. The main operational issue is the disposition of the particles vis-à-vis the working electrode, which can range from suspended in the electrolyte, to deposited as a thin-film, to packed into a cavity. Most environmental applications of the latter approach involve packed powder disk electrodes (PDEs) made with various nano- and micro-sized metallic iron and iron oxide powders (*273-279*), and the thin-film electrode approach has been used to characterize drop- or spin-coated environmentally-relevant particles, including metallic iron (*280*), iron oxides (*281-283*), green rusts (*284, 285*), ferrogenous clays (*286*), alumina and titania (*287*), and manganese oxides (*288*). An important advantage of these two approaches is that they involve direct electrical contact between analyte particles and the bulk working electrode.

The most frequently used approach to electrochemical characterization of environmental materials involves suspensions where contact between the analyte and the working electrode is intermittent and presumably outer-sphere (due to entrainment of particles in the boundary layer on the electrode interface) and/or indirect (if mediated by a soluble electron shuttle). The use of mediators in electrochemical studies of suspensions of minerals and other environmental colloids (e.g., various forms of particulate organic carbon) has been developed extensively in recent work (*29, 289-294*), but we determined that this approach was not well-suited to the goals of this study—for reasons elaborated later—and therefore made minimal use of it. Instead, we chose to focus on the former approach, which in this case involved freely-suspended iron oxides in an aqueous medium that served both as electrolyte and model for aquatic conditions. Although this approach is similar to traditional methods of measuring oxidation-reduction potential (ORP) on samples of soil and sediment (*295, 296*) several innovations were employed to obtain more precise, accurate, and meaningful results.

The approach taken here—including some of the methodological innovations and aspects of the conceptual model—is partly an extension of the work described in Shi et al. (*297, 298*). In that work, we set out to provide a basis for interpretation of ORP measurements on groundwater as an indicator of nano zerovalent iron (nZVI) transport, but many of the results are applicable to the interpretation of ORP measurements on suspensions of particles in general. For example, it was concluded that *direct* (inner and/or outer sphere) interactions between the working electrode and the suspended nanoparticles can contribute to the overall, mixed potential that is measured, but the significance of this effect relative to the electrode-response of dissolved redox-active species varies greatly with factors such as particle size and mixing intensity (*297, 298*). The primary mineral particles used in this study may be too large to contribute directly to the measured mixed potential, but we hypothesized that the RMI phases formed under the conditions of this study would have properties that could give a direct electrode response.

Several other issues explored in our prior work (*297, 298*) are applicable to this study. One involves the deposition of particles (or precipitates) onto the working electrode such that its response transitions from that of an inert metal to that of the thin-film of deposited material. The color of the film formed from nZVI suggested the material was partially oxidized (*297*), which presumably includes corrosion products similar to RMIs formed in the absence of ZVI. This connection to the current work is supported by evidence presented below. Another issue involves the influence of suspended (charged) colloids at the liquid junction between the sample suspension and the reference electrode. The suspension effect (SE) can be significant and varies with operational factors such as those that influence particle settling (*299, 300*), so it was characterized and controlled in this study using methods described in Appendix C.

One way that this study differs from most prior work on electrode potentials of minerals in suspension is that the medium was effectively titrated with acid, base, or (mainly) $Fe(II)_{aq}$ in order to explore the dynamics of RMI formation and its influence on the effective redox potential of the solids. This was done using zero-current single-electrode chronopotentiometry (CP) (*301*) on a rotating glassy carbon disk electrode in suspensions of six reagent-grade iron oxides: goethite (GT), hematite (HT), lepidocrocite (LC), magnetite (MT), siderite (ST), and wustite

(WT). The minerals were selected to include Fe(III) oxides (GT, HT, LC), Fe(II) oxides (ST, WT), and mixed Fe(II)/Fe(III) oxides (MT). The solution conditions were varied from below surface site availability of the iron oxides to concentrations of aqueous Fe(II) found in the environment. The open-circuit potential (E_{OC}), measured by CP, and pH (also measured in situ) were compared to calculation from equilibrium speciation models and thermodynamic data. The results suggest that most of the conditions yield similar limiting values of E_{OC}, which is consistent with the formation of a common RMI phase over time. Eventually, these results should help to define the relationship between RMI formation and rates of contaminant reduction, under laboratory and field conditions.

4.3. Experimental

4.3.1. Materials and Reagents

All of the iron oxide samples used in this study were obtained from Bayferrox (GT, HT, LC, MT)(99.4, 99.1, 99.4, 96.5%), Strem (ST)(technical grade), and Alfa Aesar for (WT)(99.5%). Relevant, previously reported properties of these materials are summarized in **Table C1**.

The electrolyte (NaCl) and aqueous Fe(II) ($FeCl_2$) were both ACS certified from Fisher. The buffer used during development was HEPES (99%) from Sigma, but it was not used for the majority of the experiments. Electron-transfer mediators tested included anthraquinone-2,6-disulfonic acid disodium salt (AQDS)(Combi-Blocks 98%), 2,6-dichloroindophenol sodium salt hydrate (DCIP)(Fluka 97%) and 7-hydroxy-3H-phenoxazin-3-one sodium salt (resorufin)(Sigma). Mediators and their SWVs can be found in Appendix C, **Table C2, Figure C1**. 5,5-indigodisulfonic acid sodium salt (TCI 95%) was used to test anoxic conditions in our electrochemical cell. NaOH and HCl (Fisher) were used to adjust the pH. Nitrobenzene (Aldrich)(99%) was used as a model contaminant. All reagents were used as received without further purification.

4.3.2. Electrochemical Methods

The primary electrochemical method used for characterization of in-situ RMI formation was zero current, single electrode potentiometry measured over time (i.e., chronopotentiometry, CP) CP measurements were made using a potentiostat (Metrohm Autolab PGSTAT30), or (Vernier Electrode Amplifier). For mediator compounds, we measured square-wave voltammograms (SWVs) and staircase cyclic voltammograms (SCVs) using the potentiostat (above). All of the voltammograms were acquired at an amplitude of 25 mV with a step size of 2 mV. Amplitude, step size, and scan rate were based on method optimizations that we performed in previous studies on the electrochemistry of phenols and anilines, and NOM (*197, 268*). The electrochemical methods developed specifically to this study will be discussed below.

All potentiometric experiments (CP) were performed using a two-electrode cell. Voltammetric experiments (SCV and SWV) were performed using a three-electrode cell (both Gamry Instruments, EuroCell). In both cells, the working electrode was a 3 mm diameter glassy carbon rotating disk electrode (Pine Research Instrumentation) rotated at 2000 rpm. The reference electrode was Ag/AgCl (BASi) filled with 3.0 M KCl encased in a fritted (porous glass) bridge tube filled with 10 mM NaCl (and 10 mM HEPES when used). The counter electrode used in the 3-electrode cell was a 0.5 mm diameter coiled platinum wire (Alfa Aesar). All potentials are reported vs. the Ag/AgCl reference electrode.

Before each set of electrochemical measurements, the working electrode was polished using 1.0, 0.3, and 0.05 μm MicroPolish Alumina (Buehler), rinsed with DI water in between each polish, then sonicated for 10 min and rinsed again with DI water. The electrochemical cell was prepared by adding 200 mL of 10 mM NaCl (and 10 mM HEPES when required), and purging for 60 min with N_2 (ultra-high purity) using a copper catalyst oxygen filter and PEEK tubing, purging of the cell headspace was continued during the experiments. Solution conditions were a dilute system to mimic environmental conditions and consisted of the following: 10 mM NaCl, 0.5, or 1.0 g/L of iron oxide, additions each of 0.25 mM Fe(II) (except in a few cases where we used site calculated Fe(II)) in the form of $FeCl_2$, and when used, 10 mM HEPES, and 10 μM electrochemical mediators. Additions of Fe(II) were done using dry $FeCl_2$ powder, this ensured a more accurate measurement of Fe(II) and prevented oxidation of the stock solution. A few times a stock solution was used and spectrophotometric measurements revealed an approximate 10% oxidation daily. The starting pH was 8 and was adjusted by titrating with NaOH and HCl. When the model contaminant nitrobenzene was used, its concentration was 100 μM.

After deaeration, the CP run was started and a background collected for 5 min, or a background scan was performed for SCV and SWV. This was followed by adding a 20 mL solution of iron oxide in 10 mM NaCl (and 10 mM HEPES when required) that had previously equilibrated in the glovebox ~ 24 hrs. After approximately 60-90 minutes doses of $FeCl_2$ were added every 20-30 minutes.

To ensure anoxic conditions the following procedures were maintained. All powders (iron oxides, $FeCl_2$), all solutions (DI water, electrolyte), and all dispensing equipment (syringes, needles, etc…) were stored in an anaerobic chamber (>0.1 ppm O_2) for a minimum of three days before use. Approximately 24 hours before an experiment was performed, 20 mL of electrolyte was added to the iron oxide and was left stirring on a mechanical roller. It was then transferred from the glove box to the benchtop electrochemical cell using a syringe. To ensure that no oxidation occurred during the transfer from the glove box to the benchtop and also for the duration of our CP runs, 5,5-indigodisulfonic acid sodium salt (indigo carmine) was used as a test solution. Indigo carmine undergoes a distinct color change upon oxidation. Oxidation of indigo carmine was noted well past the time frame of our experiments **Figure C2**.

4.4. Results and Discussion

4.4.1. Buffered vs. Non-buffered Conditions

In initial experiments, we used buffered and unequilibrated iron oxide solutions. For the latter, it was previously demonstrated (*290, 297*) that equilibrating iron oxides in their aqueous environment (~ 24 hours) gave more stable ORP readings, so this was used for all subsequent experiments. The former has been shown to significantly interfere with iron oxides (*302*), either by changing solution conditions due to the release of Fe(II) from the mineral, or by forming complexes with oxide bound Fe(II) (*303*). Buffers have been shown to enhance particle aggregation and dramatically change degradation rates of contaminants (*303, 304*).

In many systems, buffers are necessary, as pH changes interfere with experimental results more than the deleterious effects of the buffer, so the artifacts can usually be neglected. In our work, there was a greater benefit in using non-buffered solutions to highlight the pH changes concurrently with E_{OC}, which we found to be more diagnostic than E_{OC} alone. For example, in our work using HEPES the addition of Fe(II) caused the pH to instantaneously decrease followed by an immediate increase (albeit minor), contrary to the behavior in the unbuffered system where the pH decreased as expected **Figure C3**.

Fluctuations of pH can be diagnostic of the types of reactions occurring in the cell. Typically, pH increases are due to ligand exchange (possible effect of buffer interference), while pH decreases are due to metal binding (H^+ is released as OH^- associates with the iron oxide surface) (*35*). When iron oxides were added to a non-buffered electrolyte, there was an immediate drop in pH (**Figure 4.1**), typical of what is expected when hydroxides adsorb to the iron oxide surface and release protons. However, the pH decrease was not consistent across all iron oxides. In GT the pH decreased 1.76 units, MT 0.36 units, and ST no pH change occurred, **Figure 4.1**. As these minerals differ in the amount of Fe(III) present, this could be evidence for structural iron affecting the extent of hydrolysis (instead of surface area availability), similar to adsorption of Fe(II) being dependent on the amount of structural Fe(II) present (*33*).

Other causes of pH decrease are metal-binding and $Fe(OH)_2$ formation. For the former, the metal will complex to the oxygen bound to the iron oxide and release H^+, either in an inner or outer-sphere reaction (*35*), while the latter manifests itself as a rapid drop in pH (*305*). When $Fe(II)_{aq}$ was added to our unbuffered iron oxide solutions, the pH decreased immediately indicating the possibility of $Fe(OH)_2$ formation. GT and MT had the largest pH decrease of 1.7 and 1.9 pH units respectively, while ST decreased 0.73 units. Other work has shown, based on the solubility of $Fe(OH)_2$, that precipitation is likely under our conditions (*249, 306*). Furthermore, the smaller pH drop of ST is indicative of less Fe(II) adsorption, which as mentioned earlier, is possibly due to structural Fe(III) content (*33*). GT and MT were able to adsorb more Fe(II), due to its larger Fe(III) content, and because of this, they were able to produce more $Fe(OH)_2$. Recent work has shown adding $Fe(II)_{aq}$ to iron oxides results in, *(i)* added $Fe(II)_{aq}$ adhering to the mineral surface and becoming oxidized by structural Fe(III), *(ii)* followed by electron transfer through the mineral (conduction), and *(iii)* subsequent reduction of structural Fe(III) elsewhere, which then desorbs back into solution as a newly formed Fe(II) (*252, 254, 256, 307*). Upon desorption Fe(II) may associate with OH^-, releasing H^+, driving down the pH, and forming $Fe(OH)_2$. This is consistent with the pH changes in our electrochemical cell as iron oxides, and $Fe(II)_{aq}$ were added to our unbuffered solutions.

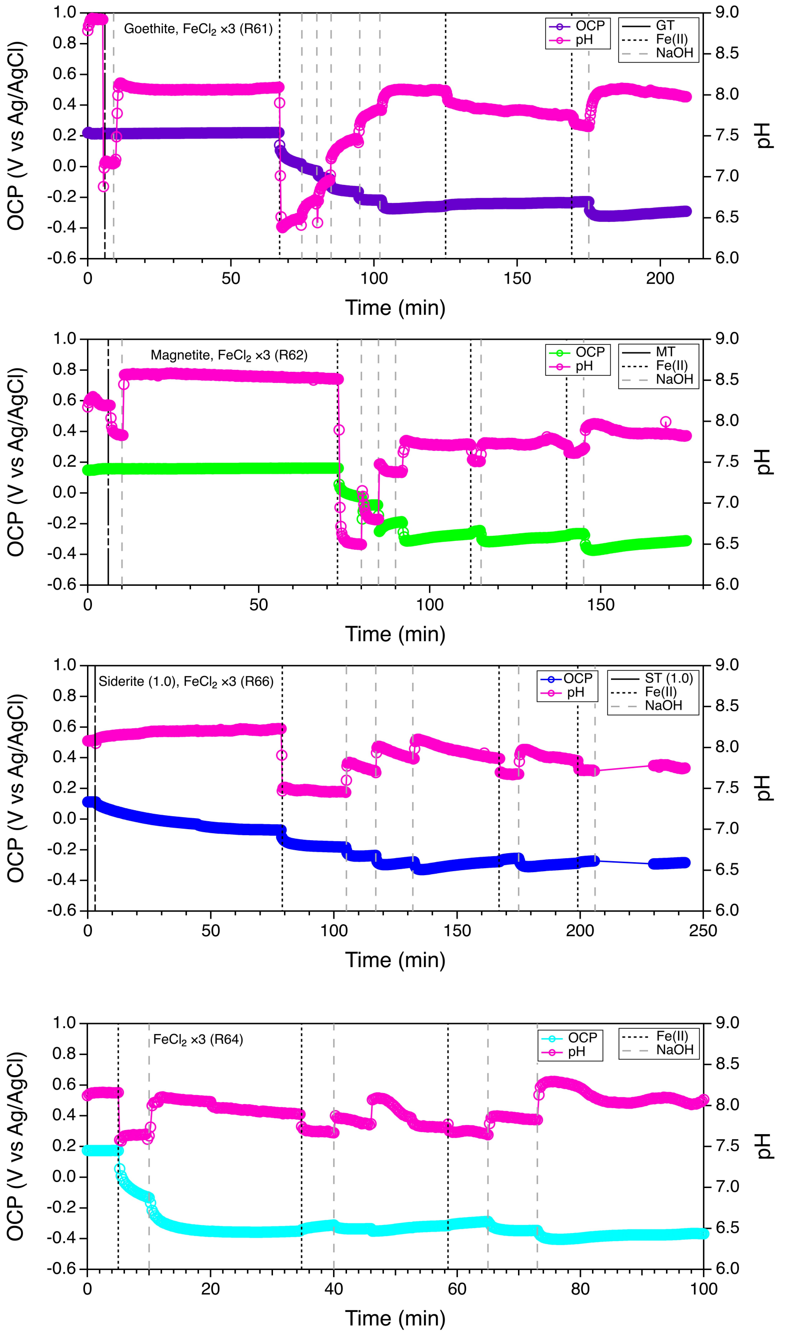

Figure 4.1. E_{OC} and pH vs. time for three representative iron oxides (GT, MT, ST) and Fe(II). Vertical lines indicate addition of Fe(II) or pH adjustments using NaOH. Conditions: 10 mM NaCl, 0.5 g/L iron oxide, 0.25 mM doses of Fe(II) x 3, 3 mm glassy carbon rotating disk electrode at 2000 rpm, 3.0 M KCl Ag/AgCl reference electrode encased in a fritted bridge tube filled with 10 mM NaCl.

Other effects to consider are H^+ adsorption by a mineral to neutralize negatively charged sites, ligand exchange, and ternary surface complexation. The former is caused by imperfections, broken bonds, or local charge balance effects (*308, 309*). Since pH increases only occurred in buffered solutions, we do not believe this applies here otherwise the effects would show up in both buffered and unbuffered systems. In ligand exchange, the ligand exchanges with OH^- releasing it and causing the pH to increase (*310*). It is likely that the pH increases in our buffered system were due to ligand exchange, which is consistent with literature observations of Good's buffers forming complexes with iron (*303, 304*). Ternary surface complexation which releases either H^+ or OH^- is very rare and can be ignored (*310*).

4.4.2. Selection of Method Conditions: Electron Transfer Mediators

Electron transfer mediators (ETMs) are a broad class of both inorganic and organic molecules that aid in the transfer of electrons between species whose electron transfer is otherwise hindered. In the laboratory ETMs are more specific but are utilized for the same purpose, to aid in communication and to speed up reactions on experimental time scales. There are three types of redox reactions to consider: *(i)* reversible, *(ii)* reversible, but hindered (energy barrier), *(iii)* and irreversible. Reversible reactions do not require a mediator to measure redox potentials. These reactions are fast, with the exchange of electrons between the working electrode and the species in solution easily captured on the time scale of a SWV scan as evidenced for select mediators in Appendix C **Figure C1**. To obtain potentials of irreversible couples, a reversible couple needs to be added to the system (*311*). The reason for this is that an irreversible couple's potential will drift, sometimes it can obtain a steady-state, but it will not obey Nernstian behavior (*311*) and cannot be easily modeled and used to predict reaction behaviors. Mediated studies allow for quick ascertaining of potentials for irreversible redox couples and the ability to model and predict these potentials using Nernstian behavior.

In our study, the goal was not to obtain potentials, but rather examine the dynamic changes in pH and potential over several hours during the formation of transient reactive mineral intermediates. In this sense, the use of a mediator was not required and could have obscured some important results. For example *(i)* forcing our system to be reversible, so we could match it to thermodynamic data would impede the development of a more sophisticated theory to explain the RMI system and its departure from thermodynamic data, *(ii)* an equilibrium may be achieved, but by more than one redox couple, *(iii)* we wanted to show the path of this dynamic system, not the endpoint, (*iv)* using thermodynamics to describe irreversible systems is rarely studied and can be of great value in natural systems, and *(v)* it is still unknown how mediated studies translate to natural conditions, in some cases, such as corrosion studies, mediators are not used due to their interference (*312*).

Even though the focus of our study did not include ETMs, we did some control experiments (along with other experiments, including aging and the absence of light) all of which can be found in Appendix C **Figure C4, C5** along with a table of mediators used in **Table C2** and their SWVs **Figure C1.** We used mediators in both buffered and unbuffered systems and, contrary to other studies where mediators lowered the E_{OC} of iron oxides by at least 100 mV (*290, 313*), we found no difference in E_{OC} using mediators as evidenced in **Figure 4.3, C4.**

4.4.3. Selection of Method Conditions: Suspension Effects

Working with suspended particles requires certain experimental effects to be taken into consideration. In previous work on nZVI (*297*) two types of effects were discussed. These effects were initially written as guidelines for obtaining pH measurements (*300*) in suspended soils, but have been recognized for some time (*314, 315*). The first type of effect, the liquid junction effect, is part of every electrochemical measurement and can be minimized by experimental design parameters, such as ensuring electrolyte concentration is one-hundred times greater than analyte concentration and that the reference electrode is as close as possible to the working electrode (*71*). The second effect is one that cannot be minimized and stems from interactions of the double layers of the working electrode and the suspended particles.

To address the suspension effects that were within our control, we used a double junction electrode to separate our reference electrode (details in Section 4.3.2). This was to serve two purposes, to ensure placement of the working and reference electrodes near each other and to keep the reference electrode clear of particles (as sometimes happened with our working electrode). We looked at the effects of using a double junction versus without on stirring rate **Figure C6** and mineral concentration (not shown) for two minerals, MT and ST. There was no difference in E_{OC} for mineral concentration with or without the double junction so we focused on stir rate only. The stir rate between 2000 and 1000 rpm did not make a significant difference, but at 0 rpm the E_{OC} for both MT and ST increased by ~ 10-15 mV while using the double junction. When not using the double junction the E_{OC} for ST at 0 rpm was very similar, while for MT the E_{OC} was lower (and approximately the same as without the double junction at 2000 and 1000 rpm). The difference between the two minerals could be due to settling rates, MT settled a lot faster than ST. Overall, using the double junction made the E_{OC} more sensitive to changes with stirring, whereas not using the double junction the E_{OC} approached the same values at all and zero stir rates. This could be attributed to the blocking of the reference electrode with the suspended particles, similar to forming a film on a working electrode and blocking access to electroactive species. In conclusion, using the double junction to encase the reference electrode did not make a significant difference in the E_{OC}, but it did aid in keeping the reference electrode free from being clogged up by particles and allowed for reproducible and closer positioning of the reference and working electrodes, so it was used for the remainder of our experiments. To briefly address electrolyte concentration, it became a matter of weighing the effects of suspensions being more stable at low ionic strength (stronger ionic strength promoting coagulation (*35*)) vs. the small double junction effect due to concentration ratio of electrolyte to analyte, we chose the former.

4.4.4. Addition Aqueous Fe(II) to Iron Oxides in Buffered Suspensions

Using chronopotentiometry we monitored E_{OC} over several hours for six different minerals (GT, HT, LC, MT, ST, WT), **Figure 4.2**. As expected, the E_{OC} for the three Fe(III) minerals (GT, HT, LC) were similar to one other and more positive than for the Fe(II) minerals (ST, WT), with MT (mixed Fe(II)/Fe(III)) values falling in the middle. When Fe(II) was added to the system (grey dots in **Figure 4.2**) E_{OC} decreased significantly. The E_{OC} decrease varied amongst the minerals but reached similar values. That is, ST had the smallest difference (~ 120 mV), while GT had the largest difference (~ 500 mV), but all the minerals decreased in value to approximately -330 to -370 mV. The second and third additions of Fe(II) resulted in much smaller potential decreases ~ 20-30 mV (each addition of Fe(II) was 0.25 mM).

To explore if smaller subsequent drops (second and third Fe(II) additions) occurred as a result of site saturation, we calculated the sites available per mineral (details of which can be found in Appendix C). Briefly, we made calculations using measurements made in our lab using Brunauer-Emmett-Teller (BET) theory to obtain the total surface area of four minerals (GT, HT, LC, MT), and literature values for estimated sites per unit area (*316, 317*). These calculations resulted in a high and low estimate for sites available per unit area of mineral. Using the low estimate (2 sites/nm^2), an appropriate amount of Fe(II) was added as our first dose, corresponding to ~ 50% coverage of the available low estimated sites. This Fe(II) concentration caused the ST to decrease ~ 87 mV while GT decreased ~380 mV **Figure 4.2B**. The decrease for ST resulted in a 33 mV difference in E_{OC} for a seventeen fold difference in Fe(II) molarity (0.25 to 0.015 mM). For GT, the E_{OC} decrease was 120 mV lower for a similar difference in molarity of Fe(II) (0.25 to 0.014 mM). These differences suggest that mineral surface site availability is not the only factor governing E_{OC}. The second and third dose of Fe(II) added was well over ~ 1.5 times the low and high estimate (22 sites/nm^2) respectively. The second and third Fe(II) additions resulted in decreases in E_{OC} ~ 100 mV for GT, and HT (one anomaly was LC, with a second E_{OC} decrease of ~ 10 mV, while the third E_{OC} decrease was similar to the other Fe(III) minerals, ~ 90 mV). MT and ST second and third Fe(II) doses resulted in E_{OC} decreases of ~ 50 and 90 mV and ~ 25 and 80 mV respectively.

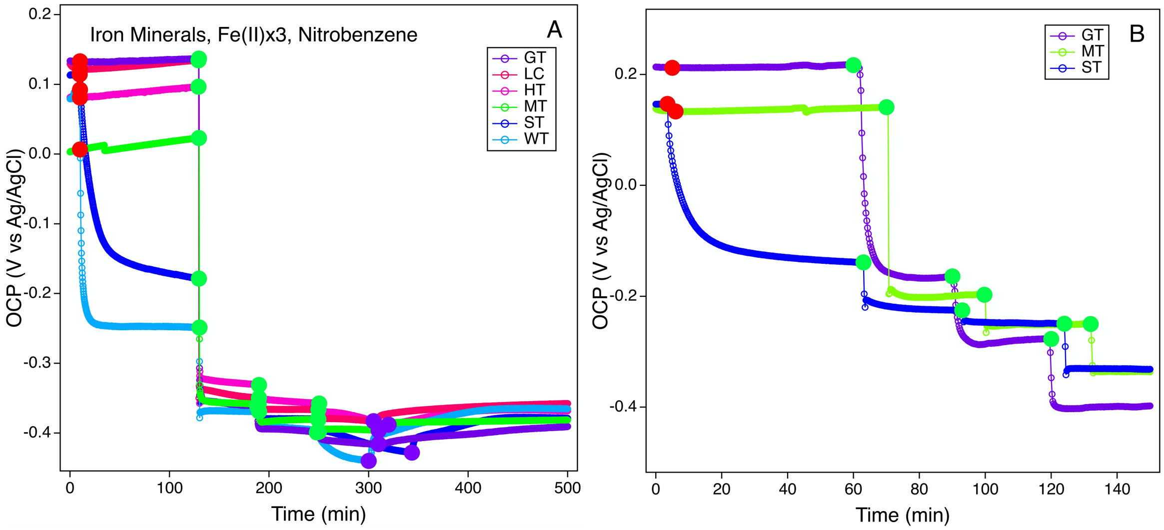

Figure 4.2. Open circuit potential vs. time of iron oxides and Fe(II) 0.25 mM (A) and by site availability of three representative minerals (B). Dots indicate addition of iron oxide (red), Fe(II) (green) and nitrobenzene (purple). Conditions: 10 mM NaCl,10 mM HEPES, 0.5 g/L iron oxide, 0.25 mM doses of Fe(II) x 3 (A), or by site availability (B), 3 mm glassy carbon rotating disk electrode at 2000 rpm, 3.0 M KCl Ag/AgCl reference electrode encased in a fritted bridge tube filled with 10 mM NaCl and 10 mM HEPES.

In summary, the minerals that did not have structural Fe(II) had significantly larger decreases in E_{OC} during the second aqueous Fe(II) addition, while the third and largest aqueous Fe(II) dose was similar amongst all minerals. More importantly, the difference in E_{OC} decreases between the first, second, and third additions of aqueous Fe(II) using surface site calculations was much larger than expected if the only controlling mechanism was surface site availability. This is further evidence that surface site availability does not explain Fe(II) adsorption. Classic surface complexation modeling has not described iron oxide and Fe(II) behavior adequately in past studies, with Fe(II) adsorption possibly having more to do with structure defects, or aggregations state (*30, 31*). Others have demonstrated various results for aqueous Fe(II) adsorption, such as being due to structural Fe(II)/Fe(III) stoichiometry (*33*), continuing adsorption after apparent site saturation (*305*), a two-stage process (initial rapid adsorption of Fe(II) followed by slower adsorption (*31, 237, 318*)), and an Fe(II) concentration dependence (0.5 mM Fe(II) resulted in the highest exchange of aqueous to structural iron (*254*)). Any of these factors could manifest in a large E_{OC} decrease, followed by a smaller E_{OC} decrease as seen in our data. We plotted E_{OC} vs. Fe(II) dose, iron oxide dose, and mediator dose (where applicable), **Figures 4.3B**, **7C.** The E_{OC} decreases follow somewhat of a pattern, with the curve dropping steeply with minimal Fe(II) additions and then leveling off as more Fe(II) is added, reaching a plateau. This is true in both buffered and unbuffered experiments.

4.4.5. E_{OC} and pH in Unbuffered Suspensions

Due to the unexpected pH behavior during experiments in buffered solutions (section 4.4.1), we chose three representative minerals (GT, MT, ST), differing in structural iron content and monitored E_{OC} and pH simultaneously, **Figure 4.1** without using a buffer. As already discussed, when aqueous Fe(II) was added to the unbuffered iron oxide solution, the pH decreased as expected, with ST decreasing about half the value of MT and GT, possibly confirming that structural Fe(III) plays a role in Fe(II) adsorption (*33*). After this initial decrease, the pH of MT and ST remains level, but GT pH starts increasing immediately. Hydroxide release is primarily due to ligand exchange, or ternary surface complexation (*310*), but further probing would be required to assess if either of these is the cause.

The E_{OC} decreases in the unbuffered system are much smaller than the very large decreases we saw in buffered solutions, there are also differences amongst the three minerals.

For GT, the E_{OC} decreases consist of a series of small steps toward more cathodic potentials, as the pH is adjusted to the starting pH before additions of Fe(II). After the pH adjustment, the E_{OC} has dropped 480 mV, around the same value as the buffered solutions (~ 490 mV), except the buffered solution E_{OC} value was lower (-360 buffered, -260 unbuffered), this is also true for MT and ST **Figure 4.3, C7**. For MT the steps are not as uniform as GT. In MT after the first potential decrease levels, NaOH is added, E_{OC} decreases immediately and rebounds quickly, the second NaOH addition produces the same result.

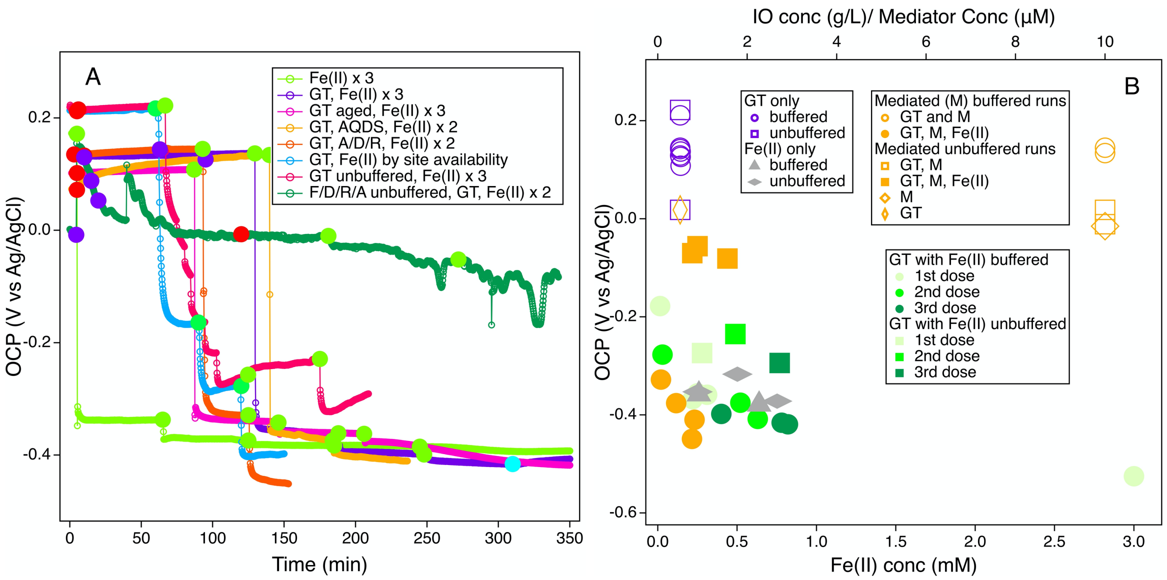

Figure 4.3. Open circuit potential vs. time (A) and vs. Fe(II), iron oxide, mediator concentration (B) of select (A), or all (B) runs for GT (for all iron oxides see Figure S7). Dots in (A) indicate addition of iron oxide (red), Fe(II) (green), mediator (purple) or nitrobenzene (teal). Conditions: 10 mM NaCl, 10 mM HEPES (for buffered runs), 0.5 g/L iron oxide, 0.25 mM doses of Fe(II), usually 3 (see legend), significantly less for the Fe(II) by site availability runs, when used mediator concentrations were 10 µM, 3 mm glassy carbon rotating disk electrode at 2000 rpm, 3.0 M KCl Ag/AgCl reference electrode encased in a fritted bridge tube filled with 10 mM NaCl (and 10 mM HEPES for buffered runs).

For the third NaOH addition, the E_{OC} decreases less and does not rebound, but follows a slight upward trend. Overall, the E_{OC} decrease is larger in the unbuffered solution versus the buffered (435, 380 mV). For ST the E_{OC} is well behaved, for GT, after Fe(II) addition and NaOH adjustments the E_{OC} is lowered. For all three minerals, the second and third additions of Fe(II) do not decrease in potential until NaOH is added.

We also monitored E_{OC} and pH of aqueous Fe(II) without minerals present **Figure 4.1**. The pH decrease for Fe(II) without an iron oxide was similar to that for ST/Fe(II). The pH decrease was small compared to GT/Fe(II) and MT/Fe(II), reinforcing that structural Fe(III) is the driving force of Fe(II) adsorption (*34*). Even though the E_{OC} trends for Fe(II) aqueous are similar to ST/Fe(II), Fe(II) decreases to approximately -350 mV and ST/Fe(II) decreases to -235 mV. Potential evidence for Fe(II) not getting oxidized unless a mineral is present (*265*).

4.4.6. Comparison to Thermodynamic Calculations

To compare and validate the experimental (unbuffered) values we plotted Eh vs. pH of the experimental and theoretical data together **Figure 4.4**, for three representative minerals with Fe(II) added and Fe(II) alone**.** The color gradient (experimental) represents the passage of time, light blue being the first addition of Fe(II) and purple being the end of the run, ~ 30 min after the third addition of Fe(II). For the thermodynamic calculations, we used Geochemist's Workbench (GWB) 12. The GWB React module was used to predict the species expected to form under our experimental conditions. From React we extracted activities with changing pH, which were subsequently used in equilibrium equations obtained from GWB Rxn. The equilibrium reactions and the log K's that were used to construct the diagrams in **Figure 4.4**, which can all be found in Appendix C **Table C3**. We did not include the exhaustive list of all species formed, only the ones that were close in values to our system.

The Eh/pH diagram for experimental aqueous Fe(II) only in electrolyte (**Figure 4.4A**) matches thermodynamic values precisely for the Fe(II)/$Fe(OH)_3$ couple, indicating that Fe(II) is in equilibrium with a precipitated ferric hydroxide. This is consistent with pH values dropping as aqueous Fe(II) is added (**Figure 4.1**). It is not surprising that under these conditions experimental values match theoretical values exactly, but more complex behavior arises when iron oxides are present.

For the experiments that include aqueous Fe(II) and minerals (**Figure 4.4B-D**), our experimental values either lie above (MT) or between (GT, ST) the thermodynamic values. It is possible that for GT and ST, whose data points fall in between the theoretical data points indicate a mixed potential of two or more of the redox couples listed. Magnetite experimental data points fall above theoretical values, which most likely has to do with magnetite stoichiometry.

Magnetite’s lattice is composed of Fe(II) and Fe(III) species. Stoichiometric magnetite is magnetite whose ratio of Fe(II) to Fe(III) is 0.5. The thermodynamic values assume this ratio and therefore it is expected that magnetite that is slightly more oxidized (has more Fe(III) in the lattice than predicted) would have higher E_{OC} values. Previous work from our lab has shown that the magnetite used for our experiments was non-stoichiometric and gave higher E_{OC} values than stoichiometric magnetite (*279*).

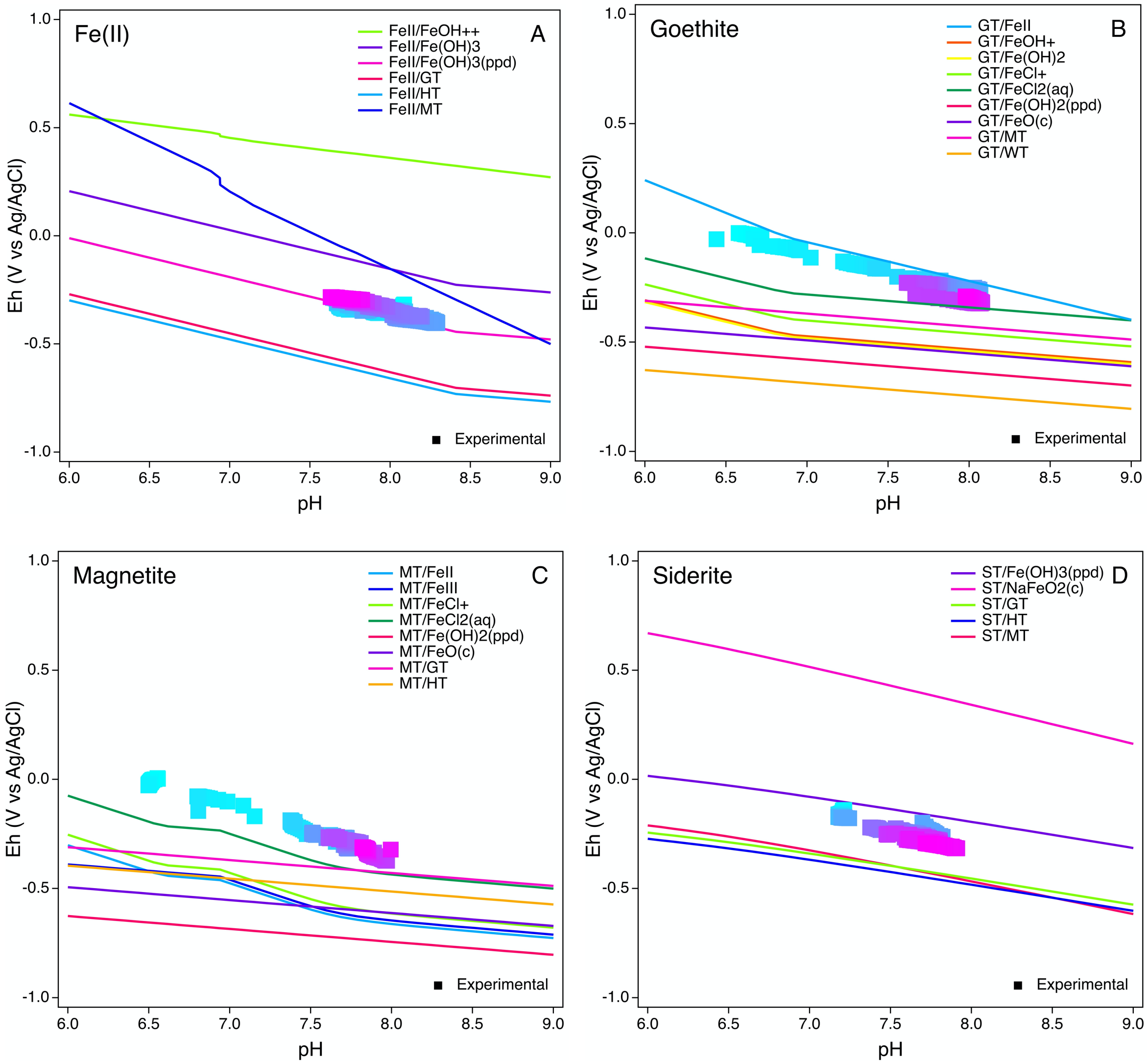

Figure 4.4. Experimental and computed Eh vs. pH values for Fe(II) (A), Goethite (B), Magnetite (C), and Siderite (D). Light blue to purple indicates time passed and Fe(II) additions (3 total). Experimental conditions: 10 mM NaCl, 0.5 g/L iron oxide, 3 additions of 0.25 mM Fe(II), 3 mm glassy carbon rotating disk electrode at 2000 rpm, 3.0 M KCl Ag/AgCl reference electrode encased in a fritted bridge tube filled with 10 mM NaCl. Computed values were obtained using

GWB12 React and Rxn. Equations can be found in Table C3. Redox couples are not written in the standard format but written in terms of main species used in the calculations listed first.

Another reason for the difference between the theoretical and experimental values could have to do with the time scale of our experiments. It is feasible that an initial RMI phase forms quickly and is similar for all iron oxides but then changes with time. Our study was performed over the time scale of hours, but studies performed over days have shown that E_{OC} decreases with time. For example, it was shown that initially, the E_{OC} of goethite and Fe(II) matched the thermodynamic data of amorphous $Fe(OH)_3$, but after 61 days it matched a more stable phase, possibly lepidocrocite, or maghemite (*246*). The GT/Fe(II) predicted equilibrium was not achieved within the 61 days of the experiment (or in our data over the course of hours), consistent with data from others that also plotted above the thermodynamic GT/Fe(II) values (*319*). So while it is possible (and consistent with our data and others) that a common RMI phase forms quickly (*256, 307*) with additional perturbations having smaller effects and eventually an equilibrium is achieved between the mineral and Fe(II), a variety of other effects have been shown, from growth of only the parent mineral when Fe(II) is added (*31, 256*), to a variety of unknown Fe(III) products (if the mineral had structural Fe(II) (*265*)), to formation of secondary minerals (after contaminant reduction (*257*)).

Less dynamic parameters to consider are the slope of the Eh/pH line. The slope in our experimental values did not change regardless of the mineral used. Slope changes have been shown in iron oxide Fe(II) systems and even slope reversals (negative to positive) (*253*). The slope could potentially be used as a predictor of the types of species that could form over time. For example, in our modeled systems, we had 28 different aqueous species and several minerals, which could be narrowed down by matching the thermodynamically predicted slopes to our experimental slopes.

4.5. Conclusions

One advantage of CP is that it can easily be applied to monitor dynamic conditions in real-time. In this work, we showed the changing E_{OC} and pH values as various components (Fe(II), NaOH, etc.) were added to a system that changed with time. The E_{OC} values for the iron oxides behaved as expected and demonstrated the ability of the working electrode to equilibrate with the oxides without the use of a mediator. Once aqueous Fe(II) was added we were able to determine processes based on the concurrent pH and E_{OC} fluctuations. More importantly, in addition to electrochemically verifying that structural Fe(III) plays a part in Fe(II) adsorption, we showed that (within the time scale of hours) the mineral substrate was not important in the E_{OC} value. All iron oxide/Fe(II) E_{OC} values, no matter what mineral was used, converged to a similar limiting E_{OC} value of approximately -450 mV vs. Ag/AgCl. This could imply that the E_{OC} value is not the driving factor in iron oxides reduction capacity, as different iron oxides have shown different reactivities towards various contaminants. Rather, it may have more to do with “storing charge” (incorporation and conduction of electrons) in the mineral structure and electron availability.

4.6 Acknowledgements

This work was supported by the U.S. Department of Defense, Strategic Environmental Research and Development Program (SERDP Grant #ER-2620). Preliminary kinetic measurements were performed by Kei Inoue.

Chapter 5 Summary

The work presented here focuses on the electrochemical characterization of a wide range of electron transfer mediators. Chapter 1 introduces the three groups of ETMs studied, examines their importance in the environment, and some of the difficulties that arise in obtaining their redox potentials. Methods used for ETM characterization are also discussed.

In Chapter 2, we performed SCV and SWV to obtain redox potentials of a wide range of phenols and anilines. DFT was used to calculate the corresponding redox potentials. Correlations were performed between the experimental and theoretical values to kinetic data so that they could be verified for their use as descriptors in QSARs. The experimental and theoretical numbers did not correlate well amongst each other, but statistically significant results were obtained for correlations between the experimental values and the kinetic data, and the theoretical values and the kinetic data. Although the latter required that phenols and anilines be separated into groups, whereas the former did not. Best results were obtained once the theoretical numbers were calibrated to the experimental values, allowing for the phenols and anilines to be grouped.

In Chapter 3, a wide range of NOM fractions was characterized in an aprotic solvent, along with electrochemically well-behaved model compounds using SCV and SWV. Using the model compounds, we converted the redox potentials of NOM to aqueous conditions, and these matched well with reported values. Most of the NOM fractions behaved very similarly in terms of redox potential, but qualitative measurements in SCV showed that NOM most likely has a continuum of redox potentials, with a potential widow about twice that of model quinones.

In Chapter 4, CP was performed to characterize the dynamic temporal transformation of iron oxides when coupled with aqueous Fe(II). The experimental results suggest that (*i*) the initial RMI formation due to the addition of Fe(II) was rapid, with additional perturbations having less of an effect on E_{OC}, (*ii*) that the effect is the same for all the iron oxides, based on their converging E_{OC} values, and (*iii*) Fe(II) adsorption is not governed strictly by surface site availability.

Here we have shown that electrochemical methods can be used to diagnose various processes, from electron transfer, film formation, reversibility of redox reactions, and chemical reactions. Electrochemistry can be used to verify values obtained theoretically, and both experimental and theoretical values can be used in correlations to predict reactivities of important descriptors, from contaminant degradation to factors in disease processes. Electrochemistry measurements are simple to make, and potentiostats are inexpensive to purchase and maintain. The value of electrochemistry is understated and it has yet to reach its full potential. Electrochemistry is one of the only methods that can be used to synthesize a species and characterize it in one electrochemical cell.

References

1. D. R. Lovley *et al.*, Humic substances as a mediator for microbially catalyzed metal reduction. *Acta Hydrochim. Hydrobiol.* **26**, 152-157 (1998).

2. R. D. C. Milton, R.; Abdellaoui, S.; Leech, D.; De Lacey, A. L.; Pita, M.; Minteer, S. D., Bioelectrochemical Haber-Bosch Process: An Ammonia Producing H2/N2 Fuel Cell. *Angew. Chem., Int. Ed.* **56**, 2680-2683 (2017).

3. L. S. Reid, V. T. Taniguchi, H. B. Gray, A. G. Mauk, Oxidation-reduction equilibrium of cytochrome b5. *J. Am. Chem. Soc.* **104**, 7516-7519 (1982).

4. M. Spiro, Polyelectrodes: the behavior and applications of mixed redox systems. *Chem. Soc. Rev.* **15**, 141-165 (1986).

5. M. L. Fultz, R. A. Durst, Mediator compounds for the electrochemical study of biological redox systems: A compilation. *Anal. Chim. Acta* **140**, 1-18 (1982).

6. W. Stumm, J. J. Morgan, *Aquatic Chemistry: Chemical Equilibria and Rates in Natural Waters*. (Wiley, New York, ed. 3rd, 1996), pp. 1022.

7. N. Cotelle, P. Hapiot, J. Pinson, C. Rolando, H. Vézin, Polyphenols Deriving from Chalcones: Investigations of Redox Activities. *The Journal of Physical Chemistry B* **109**, 23720-23729 (2005).

8. C. Tommos, G. T. Babcock, Proton and hydrogen currents in photosynthetic water oxidation. *Biochimica et Biophysica Acta (BBA) - Bioenergetics* **1458**, 199-219 (2000).

9. T. J. Meyer, M. H. V. Huynh, H. H. Thorp, The Possible Role of Proton-Coupled Electron Transfer (PCET) in Water Oxidation by Photosystem II. *Angew. Chem., Int. Ed.* **46**, 5284-5304 (2007).

10. M. Uchimiya, A. T. Stone, Reversible redox chemistry of quinones: Impact on biogeochemical cycles. *Chemosphere* **77**, 451-458 (2009).

11. R. Sutton, G. Sposito, Molecular structure in soil humic substances: The new view. *Environ. Sci. Technol.* **39**, 9009-9015 (2005).

12. M. J. M. Wells, H. A. Stretz, Supramolecular architectures of natural organic matter. *Sci. Total Environ.* **671**, 1125-1133 (2019).

13. N. Walpen, G. J. Getzinger, M. H. Schroth, M. Sander, Electron-donating phenolic and electron-accepting quinone moieties in peat dissolved organic matter: Quantities and redox transformations in the context of peat biogeochemistry. *Environ. Sci. Technol.* **52**, 5236-5245 (2018).

14. J. A. Hakala, R. L. Fimmen, Y. P. Chin, S. G. Agrawal, C. P. Ward, Assessment of the geochemical reactivity of Fe-DOM complexes in wetland sediment pore waters using a nitroaromatic probe compound. *Geochim. Cosmochim. Acta* **73**, 1382-1393 (2009).

15. E. S. Kane *et al.*, Response of anaerobic carbon cycling to water table manipulation in an Alaskan rich fen. *Soil Biol. Biochem.* **58**, 50-60 (2013).

16. T. Borch *et al.*, Biogeochemical redox processes and their impact on contaminant dynamics. *Environ. Sci. Technol.* **44**, 15-23 (2010).

17. A. G. Bravo *et al.*, Molecular composition of organic matter controls methylmercury formation in boreal lakes. *Nature Comm.* **8**, 14255 (2017).

18. F. M. Dunnivant, R. P. Schwarzenbach, D. L. Macalady, Reduction of substituted nitrobenzenes in aqueous solutions containing natural organic matter. *Environ. Sci. Technol.* **26**, 2133-2141 (1992).

19. A. Kappler, S. B. Haderlein, Natural organic matter as reductant for chlorinated aliphatic pollutants. *Environ. Sci. Technol.* **37**, 2714-2719 (2003).

20. J. L. Weishaar *et al.*, Evaluation of specific ultraviolet absorbance as an indicator of the chemical composition and reactivity of dissolved organic carbon. *Environ. Sci. Technol.* **37**, 4702-4708 (2003).

21. R. G. P. T. Jayasooriya *et al.*, Fulvic acid promotes extracellular anti-cancer mediators from RAW 264.7 cells, causing to cancer cell death in vitro. *International Immunopharmacology* **36**, 241-248 (2016).

22. H.-L. Yang *et al.*, Humic acid induces apoptosis in human premyelocytic leukemia HL-60 cells. *Life Sci.* **75**, 1817-1831 (2004).

23. A. D. Redman, L. Macalady Donald, D. Ahmann, Natural organic matter affects aresnic speciation and sorption onto hematite. *Environ. Sci. Technol.* **36**, 2889-2896 (2002).

24. L. A. Warren, E. A. Haack, Biogeochemical controls on metal behaviour in freshwater environments. *Earth-Science Reviews* **54**, 261-320 (2001).

25. Y. Xie *et al.*, The comparison of Se(IV) and Se(VI) sequestration by nanoscale zero-valent iron in aqueous solutions: The roles of solution chemistry. *J. Hazard. Mater.* **338**, 306-312 (2017).

26. N. Hertkorn *et al.*, Natural organic matter and the event horizon of mass spectrometry. *Anal. Chem.* **80**, 8908-8919 (2008).

27. E. B. Kujawinski, P. G. Hatcher, M. A. Freitas, High-resolution Fourier transform ion cyclotron resonance mass spectrometry of humic and fulvic acids: Improvements and comparisons. *Anal. Chem.* **74**, 413-419 (2002).

28. M. M. Tfaily *et al.*, Advanced solvent based methods for molecular characterization of soil organic matter by high-resolution mass spectrometry. *Anal. Chem.* **87**, 5206-5215 (2015).

29. S. M. Stewart, T. B. Hofstetter, P. Joshi, C. A. Gorski, Linking thermodynamics to pollutant reduction kinetics by Fe^{2+} bound to iron oxides. *Environ. Sci. Technol.* **52**, 5600-5609 (2018).

30. D. Faivre, Ed., *Iron Oxides: From Nature to Applications*, (Wiley-VCH, 2016), pp. 598.

31. S. D. Taylor *et al.*, Visualizing the iron atom exchange front in the Fe(II)-catalyzed recrystallization of goethite by atom probe tomography. *Proc. Natl. Acad. Sci. USA* **116**, 2866 (2019).

32. K. B. Gregory, P. Larese-Casanova, G. F. Parkin, M. M. Scherer, Abiotic Transformation of Hexahydro-1,3,5-trinitro-1,3,5-triazine by FeII Bound to Magnetite. *Environ. Sci. Technol.* **38**, 1408-1414 (2004).

33. C. A. Gorski, M. M. Scherer, Influence of magnetite stoichiometry on Fe^{II} uptake and nitrobenzene reduction. *Environ. Sci. Technol.* **43**, 3675-3680 (2009).

34. M. Elsner, R. P. Schwarzenbach, S. B. Haderlein, Reactivity of Fe(II)-bearing minerals toward reductive transformation of organic contaminants. *Environ. Sci. Technol.* **38**, 799-807 (2004).

35. R. M. Cornell, U. Schwertmann, *The Iron Oxides: Structure, Properties, Reactions, Occurrences And Uses*. (John Wiley & Sons, 2003).

36. C. Léger *et al.*, Enzyme Electrokinetics: Using Protein Film Voltammetry To Investigate Redox Enzymes and Their Mechanisms†. *Biochemistry* **42**, 8653-8662 (2003).

37. A. J. Motheo, L. Pinhedo, Electrochemical degradation of humic acid. *Sci. Total Environ.* **256**, 67-76 (2000).

38. A. Malkia, L. Murtomaki, A. Urtti, K. Kontturi, Drug permeation in biomembranes In vitro and in silico prediction and influence of physicochemical properties. *Eur. J. Pharm. Sci.* **23**, 13-47 (2004).

39. M. Pumera, Electrochemistry of graphene: new horizons for sensing and energy storage. *The Chemical Record* **9**, 211-223 (2009).

40. H. Zhu *et al.*, Graphite–carbon nanotube composite electrodes for all vanadium redox flow battery. *J. Power Sources* **184**, 637-640 (2008).

41. S. Canonica, P. G. Tratnyek, Quantitative structure-activity relationships for oxidation reactions of organic chemicals in water. *Environ. Toxicol. Chem.* **22**, 1743-1754 (2003).

42. P. G. Tratnyek, in *Perspectives in Environmental Chemistry,* L. Macalady Donald, Ed. (Oxford University Press, 1998), pp. 167-194.

43. Y. Lee, U. von Gunten, Quantitative structure-Activity relationships (QSARs) for the transformation of organic micropollutants during oxidative water treatment. *Water Res.* **46**, 6177-6195 (2012).

44. J. C. Suatoni, R. E. Snyder, R. O. Clark, Voltammetric studies of phenol and aniline ring substitution. *Anal. Chem.* **33**, 1894-1897 (1961).

45. A. T. Stone, Reductive dissolution of manganese(III/IV) oxides by substituted phenols. *Environ. Sci. Technol.* **21**, 979-988 (1987).

46. S. Laha, R. G. Luthy, Oxidation of aniline and other primary aromatic amines by manganese dioxide. *Environ. Sci. Technol.* **24**, 363-373 (1990).

47. J. Klausen, S. B. Haderlein, R. P. Schwarzenbach, Oxidation of substituted anilines by aqueous MnO_2: Effect of co-solutes on initial and quasi-steady-state kinetics. *Environ. Sci. Technol.* **31**, 2642-2649 (1997).

48. A. J. Salter-Blanc, E. J. Bylaska, M. A. Lyon, S. Ness, P. G. Tratnyek, Structure-activity relationships for rates of aromatic amine oxidation by manganese dioxide. *Environ. Sci. Technol.* **50**, 5094-5102 (2016).

49. P. G. Tratnyek, J. Hoigné, Oxidation of substituted phenols in the environment: A QSAR analysis of rate constants for reaction with singlet oxygen. *Environ. Sci. Technol.* **25**, 1596-1604 (1991).

50. E. Rorije, J. G. M. Peijnenburg, QSARs for oxidation of phenols in the aqueous environment, suitable for risk assessment. *Journal of Chemometrics* **10**, 79-93 (1996).

51. P. G. Tratnyek, in *Perspectives in Environmental Chemistry,* D. L. Macalady, Ed. (Oxford, New York, 1998), pp. 167-194.

52. P. G. Tratnyek, J. Hoigné, Kinetics of reactions of chlorine dioxide (OClO) in water. II. Quantitative structure-activity relationships for phenolic compounds. *Water Res.* **28**, 57-66 (1994).

53. L. Meites, P. Zuman, *CRC Handbook Series in Organic Electrochemistry*. (CRC, Cleveland, OH, 1979).

54. R. A. Larson, R. G. Zepp, Reactivity of the carbonate radical with aniline derivatives. *Environ. Toxicol. Chem.* **7**, 265-274 (1988).

55. S. Padmaja, J. Rajaram, V. Ramakrishnan, Substituent effect on rates of one-electron oxidation of anilines by borate radical - a flash photolysis study. *Indian J. Chem., Sec. A* **29A**, 422-424 (1990).

56. A. V. Marenich, J. Ho, M. L. Coote, C. J. Cramer, D. G. Truhlar, Computational electrochemistry: prediction of liquid-phase reduction potentials. *Phys. Chem. Chem. Phys.* **16**, 15068-15106 (2014).

57. J. Ho, M. L. Coote, C. J. Cramer, D. G. Truhlar, in *Organic Electrochemistry, Fifth Edition,* O. Hammerich, B. Speiser, Eds. (CRC Press, 2015), pp. 229-259.

58. P. Winget, E. J. Weber, C. J. Cramer, D. G. Truhlar, Computational electrochemistry: Aqueous one-electron oxidation potentials for substituted anilines. [Erratum to document cited in CA132:222169]. *Phys. Chem. Chem. Phys.* **2**, 1871 (2000).

59. P. Winget, E. J. Weber, C. J. Cramer, D. G. Truhlar, Computational electrochemistry: Aqueous one-electron oxidation potentials for substituted anilines. *Phys. Chem. Chem. Phys.* **2**, 1231-1239 (2000).

60. P. Winget, C. J. Cramer, D. G. Truhlar, Computation of equilibrium oxidation and reduction potentials for reversible and dissociative electron-transfer reactions in solution. *Theor. Chem. Acc.* **112**, 217-227 (2004).

61. J. Moens, P. Jaque, F. De Proft, P. Geerlings, The study of redox reactions on the basis of conceptual DFT principles: EEM and vertical quantities. *J. Phys. Chem. A* **112**, 6023-6031 (2008).

62. D. H. Evans, One-electron and two-electron transfers in electrochemistry and homogeneous solution reactions. *Chem. Rev.* **108**, 2113-2144 (2008).

63. J. J. Guerard, J. S. Arey, Critical evaluation of implicit solvent models for predicting aqueous oxidation potentials of neutral organic compounds. *J. Chem. Theory Comput.* **9**, 5046-5058 (2013).

64. W. A. Arnold, One electron oxidation potential as a predictor of rate constants of N-containing compounds with carbonate radical and triplet excited state organic matter. *Environ. Sci. Proc. Impacts* **16**, 832-838 (2014).

65. P. R. Erickson *et al.*, Controlling factors in the rates of oxidation of anilines and phenols by triplet methylene blue in aqueous solution. *J. Phys. Chem. A* **119**, 3233-3243 (2015).

66. M. Jonsson, J. Lind, T. E. Eriksen, G. Merenyi, Redox and acidity properties of 4-substituted aniline radical cations in water. *J. Am. Chem. Soc.* **116**, 1423-1427 (1994).

67. W. A. Arnold *et al.*, QSARs for phenols and phenolates: Oxidation potential as a predictor of reaction rate constants with photochemically produced oxidants. *Environ. Sci. Proc. Impacts* **19**, 324-338 (2017).

68. C. G. Zoski, *Handbook of Electrochemistry*. (Elsevier, 2006).

69. L. Meites, *Polarographic Techniques*. (New York, Wiley Interscience, 1965), pp. 752.

70. O. Hammerich, B. Speiser, Eds., *Organic Electrochemistry, Fifth Edition*, (CRC Press, 2015).

71. A. J. Bard, L. R. Faulkner, *Electrochemical Methods. Fundamentals and Applications*. (Wiley, New York, 2001), pp. 833.

72. T. A. Enache, Phenol and para-substituted phenols electrochemical oxidation pathways. *J. Electroanal. Chem.* **655**, 9-16 (2011).

73. D. Bejan, A. Duca, Voltammetry of aniline with different electrodes and electrolytes. *Croat. Chem. Acta* **71**, 745-756 (1998).

74. R. M. W. Amon, H.-P. Fitznar, R. Benner, Linkages among the bioreactivity, chemical composition, and diagenetic state of marine dissolved organic matter. *Limnol. Oceanogr.* **46**, 287-297 (2001).

75. J. Wang, M. Jiang, F. Lu, Electrochemical quartz crystal microbalance investigation of surface fouling due to phenol oxidation. *J. Electroanal. Chem.* **444**, 127 (1998).

76. C. Cyrille, R. Marc, S. Jean-Michel, in *Organic Electrochemistry, Fifth Edition,* O. Hammerich, B. Speiser, Eds. (CRC Press, 2015), pp. 481-509.

77. C. Li, M. Z. Hoffman, One-electron redox potentials of phenols in aqueous solution. *J. Phys. Chem. B* **103**, 6653-6656 (1999).

78. H. Li, L. S. Lee, D. G. Schulze, C. A. Guest, Role of soil manganese in the oxidation of aromatic amines. *Environ. Sci. Technol.* **37**, 2686-2693 (2003).

79. M. Skarpeli-Liati *et al.*, Using nitrogen isotope fractionation to assess the oxidation of substituted anilines by manganese oxide. *Environ. Sci. Technol.* **45**, 5596-5604 (2011).

80. M. Skarpeli-Liati *et al.*, pH-Dependent equilibrium isotope fractionation associated with the compound specific nitrogen and carbon isotope analysis of substituted anilines by SPME-GC/IRMS. *Anal. Chem.* **83**, 1641-1648 (2011).

81. S. Steenken, P. Neta, One-electron redox potentials of phenols. Hydroxy- and aminophenols and related compounds of biological interest. *J. Phys. Chem.* **86**, 3661-3667 (1982).

82. J. Q. Chambers, in *The Chemistry of the Quinonoid Compounds*. (Interscience, New York, 1974), vol. 2, pp. 737-791.

83. T. A. Brown, B. A. Jackson, B. J. Bythell, A. C. Stenson, Benefits of multidimensional fractionation for the study and characterization of natural organic matter. *J. Chromatogr. A* **1470**, 84-96 (2016).

84. J. Chen, B. Gu, E. J. LeBoeuf, H. Pan, S. Dai, Spectroscopic characterization of structural and functional properties of natural organic matter fractions. *Chemosphere* **48**, 59-68 (2002).

85. Y.-P. Chin, G. Aiken, E. O'Loughlin, Molecular weight, polydispersity, and spectroscopic properties of aquatic humic substances. *Environ. Sci. Technol.* **28**, 1853-1858 (1994).

86. Y.-P. Chin, S. J. Traina, C. R. Swank, D. Backhus, Abundance and properties of dissolved organic matter in pore waters of a freshwater wetland. *Limnol. Oceanogr.* **43**, 1287-1296 (1998).

87. J. Guigue *et al.*, Ultrahigh-resolution FT-ICR mass spectrometry for molecular characterisation of pressurised hot water-extractable organic matter in soils. *Biogeochemistry* **128**, 307-326 (2016).

88. B. P. Kelleher, A. J. Simpson, Humic substances in soils: Are they really chemically distinct? *Environ. Sci. Technol.* **40**, 4605-4611 (2006).

89. M. Kleber, M. G. Johnson, in *Advances in Agronomy*. (2010), pp. 77-142.

90. B. P. Koch, K.-U. Ludwichowski, G. Kattner, T. Dittmar, M. Witt, Advanced characterization of marine dissolved organic matter by combining reversed-phase liquid chromatography and FT-ICR-MS. *Mar. Chem.* **111**, 233-241 (2008).

91. D. L. Macalady, K. Walton-Day, in *Aquatic Redox Chemistry,* P. G. Tratnyek, T. J. Grundl, S. B. Haderlein, Eds. (American Chemical Society, Washington, DC, 2011), vol. 1071, chap. 5, pp. 85-111.

92. B. F. Mann *et al.*, Indexing permafrost soil organic matter degradation using high-resolution mass spectrometry. *PloS One* **10**, e0130557 (2015).

93. J. Mao, N. Chen, X. Cao, Characterization of humic substances by advanced solid state NMR spectroscopy: Demonstration of a systematic approach. *Org. Geochem.* **42**, 891-902 (2011).

94. E. C. Minor, M. M. Swenson, B. M. Mattson, A. R. Oyler, Structural characterization of dissolved organic matter: a review of current techniques for isolation and analysis. *Environ. Sci. Proc. Impacts* **16**, 2064-2079 (2014).

95. P. N. Nelson, J. A. Baldock, Estimating the molecular composition of a diverse range of natural organic materials from solid-state ^{13}C NMR and elemental analyses. *Biogeochemistry* **72**, 1-34 (2005).

96. T. Reemtsma, Determination of molecular formulas of natural organic matter molecules by (ultra-) high-resolution mass spectrometry: Status and needs. *J. Chromatogr. A* **1216**, 3687-3701 (2009).

97. T. Riedel, T. Dittmar, A method detection limit for the analysis of natural organic matter via Fourier transform ion cyclotron resonance mass spectrometry. *Anal. Chem.* **86**, 8376-8382 (2014).

98. P. L. Brezonik *et al.*, Chemical differences of aquatic humic substances extracted by XAD-8 and DEAE-cellulose. *J. Environ. Chem. Eng.* **3**, 2982-2990 (2015).

99. J. Burdon, Are the traditional concepts of the structures of humic substances realistic? *Soil Sci.* **166**, 752-769 (2001).

100. J. Raeke, O. J. Lechtenfeld, M. Wagner, P. Herzsprung, T. Reemtsma, Selectivity of solid phase extraction of freshwater dissolved organic matter and its effect on ultrahigh resolution mass spectra. *Environ. Sci. Proc. Impacts* **18**, 918-927 (2016).

101. U. J. Wünsch *et al.*, Quantifying the impact of solid-phase extraction on chromophoric dissolved organic matter composition. *Mar. Chem.* **207**, 33-41 (2018).

102. Y. Li *et al.*, How representative are dissolved organic matter (DOM) extracts? A comprehensive study of sorbent selectivity for DOM isolation. *Water Res.* **116**, 316-323 (2017).

103. N. Hertkorn *et al.*, Comparative analysis of partial structures of a peat humic and fulvic acid using one and two dimensional nuclear magnetic resonance spectroscopy. *J. Environ. Qual.* **31**, 375-387 (2002).

104. K. A. Thorn, L. G. Cox, N-15 NMR spectra of naturally abundant nitrogen in soil and aquatic natural organic matter samples of the International Humic Substances Society. *Org. Geochem.* **40**, 484-499 (2009).

105. I. Kögel-Knabner, The macromolecular organic composition of plant and microbial residues as inputs to soil organic matter: Fourteen years on. *Soil Biol. Biochem.* **105**, A3-A8 (2017).

106. N. Mahieu, E. W. Randall, D. S. Powlson, Statistical analysis of published carbon-13 CPMAS NMR spectra of soil organic matter. *Soil Sci. Soc. Am. J.* **63**, 307-319 (1999).

107. J. Niemeyer, Y. Chen, J. M. Bollog, Characterization of humic acids, composts, and peat by diffuse reflectance Fourier-transform infrared spectroscopy. *Soil Sci. Soc. Am. J.* **56**, 135-140 (1992).

108. A. J. Simpson *et al.*, Unraveling the structural components of soil humin by use of solution-state nuclear magnetic resonance spectroscopy. *Environ. Sci. Technol.* **41**, 876-883 (2007).

109. D. Zhang, D. Duan, Y. Huang, Y. Yang, Y. Ran, Composition and structure of natural organic matter through advanced nuclear magnetic resonance techniques. *Chemical and Biological Technologies in Agriculture* **4**, 8 (2017).

110. J. Zhong, R. L. Sleighter, E. Salmon, G. A. McKee, P. G. Hatcher, Combining advanced NMR techniques with ultrahigh resolution mass spectrometry: A new strategy for molecular scale characterization of macromolecular components of soil and sedimentary organic matter. *Org. Geochem.* **42**, 903-916 (2011).

111. I. V. Perminova *et al.*, The structural arrangement and relative abundance of aliphatic units may effect long-wave absorbance of natural organic matter as revealed by ^{1}H NMR spectroscopy. *Environ. Sci. Technol.* **52**, 12526-12537 (2018).

112. C. Romera-Castillo, M. Chen, Y. Yamashita, R. Jaffé, Fluorescence characteristics of size-fractionated dissolved organic matter: Implications for a molecular assembly based structure? *Water Res.* **55**, 40-51 (2014).

113. R. M. Cory, D. M. McKnight, Fluorescence spectroscopy reveals ubiquitous presence of oxidized and reduced quinones in dissolved organic matter. *Environ. Sci. Technol.* **39**, 8142-8149 (2005).

114. U. J. Wünsch, K. R. Murphy, C. A. Stedmon, The one-sample PARAFAC approach reveals molecular size distributions of fluorescent components in dissolved organic matter. *Environ. Sci. Technol.* **51**, 11900-11908 (2017).

115. P. Kowalczuk, J. Ston-Egiert, W. J. Cooper, R. F. Whitehead, M. J. Durako, Characterization of chromophoric dissolved organic matter (CDOM) in the Baltic Sea by excitation emission matrix fluorescence spectroscopy. *Mar. Chem.* **96**, 273-292 (2005).

116. L. Klapper *et al.*, Fulvic acid oxidation state detection using fluorescence spectroscopy. *Environ. Sci. Technol.* **36**, 3170-3175 (2002).

117. H. Chen *et al.*, Molecular insights into arctic soil organic matter degradation under warming. *Environ Sci Technol* **52**, 4555-4564 (2018).

118. P. Herzsprung *et al.*, High field FT-ICR mass spectrometry data sets enlighten qualitative DOM alteration in lake sediment porewater profiles. *Org. Geochem.* **108**, 51-60 (2017).

119. B. P. Koch, T. Dittmar, From mass to structure: an aromaticity index for high-resolution mass data of natural organic matter. *Rapid Commun. Mass Spectrom.* **30**, 250-250 (2016).

120. A. Zherebker *et al.*, Structural investigation of coal humic substances by selective isotopic exchange and high-resolution mass spectrometry. *Faraday Discussions*, (2019).

121. M. H. B. Hayes, Solvent systems for the isolation of organic components from soils. *Soil Sci. Soc. Am. J.* **70**, 986-994 (2006).

122. M. W. I. Schmidt *et al.*, Persistence of soil organic matter as an ecosystem property. *Nature (London, U. K.)* **478**, 49-56 (2011).

123. T. Heitmann, T. Goldhammer, J. Beer, C. Blodau, Electron transfer of dissolved organic matter and its potential significance for anaerobic respiration in a northern bog. *Global Change Biol.* **13**, 1771-1785 (2007).

124. C. P. Ward, S. G. Nalven, B. C. Crump, G. W. Kling, R. M. Cory, Photochemical alteration of organic carbon draining permafrost soils shifts microbial metabolic pathways and stimulates respiration. *Nature Comm.* **8**, 772 (2017).

125. M. P. Waldrop *et al.*, Molecular investigations into a globally important carbon pool: Permafrost-protected carbon in Alaskan soils. *Global Change Biol.* **16**, 2543-2554 (2010).

126. O. Pisani *et al.*, Long-term doubling of litter inputs accelerates soil organic matter degradation and reduces soil carbon stocks. *Biogeochemistry* **127**, 1-14 (2016).

127. G. Y. K. Moinet *et al.*, The temperature sensitivity of soil organic matter decomposition is constrained by microbial access to substrates. *Soil Biol. Biochem.* **116**, 333-339 (2018).

128. E. Lipczynska-Kochany, Effect of climate change on humic substances and associated impacts on the quality of surface water and groundwater: A review. *Sci. Total Environ.* **640-641**, 1548-1565 (2018).

129. I. F. Creed *et al.*, The river as a chemostat: Fresh perspectives on dissolved organic matter flowing down the river continuum. *Canadian Journal of Fisheries and Aquatic Sciences* **72**, 1272-1285 (2015).

130. R. L. Fimmen, R. M. Cory, Y.-P. Chin, T. D. Trouts, D. M. McKnight, Probing the oxidation-reduction properties of terrestrially and microbially derived dissolved organic matter. *Geochim. Cosmochim. Acta* **71**, 3003-3015 (2007).

131. S. Canonica, H. Laubscher, Inhibitory effect of dissolved organic matter on triplet-induced oxidation of aquatic contaminants. *Photochemical & Photobiological Sciences* **7**, 547-551 (2008).

132. A. M. Graham, G. R. Aiken, C. C. Gilmour, Effect of dissolved organic matter source and character on microbial Hg methylation in Hg-S-DOM solutions. *Environ. Sci. Technol.* **47**, 5746-5754 (2013).

133. M. Haitzer, G. R. Aiken, J. N. Ryan, Binding of mercury(II) to aquatic humic substances: Influence of pH and source of humic substances. *Environ. Sci. Technol.* **37**, 2436-2441 (2003).

134. H.-Y. N. Holman *et al.*, Catalysis of PAH biodegradation by humic acid shown in synchrotron infrared studies. *Environ. Sci. Technol.* **36**, 1276-1280 (2002).

135. A. Höllrigl-Rosta, R. Vinken, M. Lenz, A. Schäffer, Sorption and dialysis experiments to assess the binding of phenolic xenobiotics to dissolved organic matter in soil. *Environ. Toxicol. Chem.* **22**, 743-752 (2003).

136. L. E. Jacobs, R. L. Fimmen, Y.-P. Chin, H. E. Mash, L. K. Weavers, Fulvic acid mediated photolysis of ibuprofen in water. *Water Res.* **45**, 4449-4458 (2011).

137. W. Jiang *et al.*, Cr(VI) adsorption and reduction by humic acid coated on magnetite. *Environ. Sci. Technol.* **48**, 8078-8085 (2014).

138. M. E. Karpuzcu, A. J. McCabe, W. A. Arnold, Phototransformation of pesticides in prairie potholes: Effect of dissolved organic matter in triplet-induced oxidation. *Environ. Sci. Proc. Impacts* **18**, 237-245 (2016).

139. J. W. Moreau *et al.*, The effect of natural organic matter on mercury methylation by Desulfobulbus propionicus 1pr3. *Front Microbiol* **6**, 1389 (2015).

140. B. A. Poulin *et al.*, Effects of sulfide concentration and dissolved organic matter characteristics on the structure of nanocolloidal metacinnabar. *Environ. Sci. Technol.* **51**, 13133-13142 (2017).

141. P. Sharma, M. Rolle, B. Kocar, S. Fendorf, A. Kappler, Influence of natural organic matter on As transport and retention. *Environ. Sci. Technol.* **45**, 546-553 (2011).

142. P. G. Tratnyek, M. M. Scherer, B. Deng, S. Hu, Effects of natural organic matter, anthropogenic surfactants, and model quinones on the reduction of contaminants by zero-valent iron. *Water Res.* **35**, 4435-4443 (2001).

143. J. Wenk, U. von Gunten, S. Canonica, Effect of dissolved organic matter on the transformation of contaminants induced by excited triplet states and the hydroxyl radical. *Environ. Sci. Technol.* **45**, 1334-1340 (2011).

144. P. S. Craig, T. J. Shaw, P. L. Miller, P. J. Pellechia, J. L. Ferry, Use of multiparametric techniques to quantify the effects of naturally occurring ligands on the kinetics of Fe(II) oxidation. *Environ. Sci. Technol.* **43**, 337-342 (2009).

145. C. Peng *et al.*, Oxidation of Fe(II)–organic matter complexes in the presence of the mixotrophic nitrate-reducing Fe(II)-oxidizing bacterium Acidovorax sp. BoFeN1. *Environ. Sci. Technol.* **52**, 5753-5763 (2018).

146. J. Wu, G. W. Luther, III, Complexation of Fe(III) by natural organic ligands in the Northwest Atlantic Ocean by a competitive ligand equilibration method and a kinetic approach. *Mar. Chem.* **50**, 159-177 (1995).

147. E. E. Daugherty, B. Gilbert, P. S. Nico, T. Borch, Complexation and redox buffering of iron(II) by dissolved organic matter. *Environ. Sci. Technol.*, (2017).

148. A. M. Jones, P. J. Griffin, T. D. Waite, Ferrous iron oxidation by molecular oxygen under acidic conditions: The effect of citrate, EDTA and fulvic acid. *Geochim. Cosmochim. Acta* **160**, 117 (2015).

149. M. Aeschbacher, C. Graf, R. P. Schwarzenbach, M. Sander, Antioxidant properties of humic substances. *Environ. Sci. Technol.* **46**, 4916-4925 (2012).

150. M. Aeschbacher, M. Sander, R. P. Schwarzenbach, Novel electrochemical approach to assess the redox properties of humic substances. *Environ. Sci. Technol.* **44**, 87-93 (2010).

151. C. Blodau, M. Bauer, S. Regenspurg, D. Macalady, Electron accepting capacity of dissolved organic matter as determined by reaction with metallic zinc. *Chem. Geol.* **260**, 186-195 (2009).

152. M. Bauer, T. Heitmann, D. L. Macalady, C. Blodau, Electron transfer capacities and reaction kinetics of peat dissolved organic matter. *Environ. Sci. Technol.* **41**, 139-145 (2007).

153. L. Klupfel, A. Piepenbrock, A. Kappler, M. Sander, Humic substances as fully regenerable electron acceptors in recurrently anoxic environments. *Nature Geosci.* **7**, 195-200 (2014).

154. M. P. Lau, M. Sander, J. Gelbrecht, M. Hupfer, Solid phases as important electron acceptors in freshwater organic sediments. *Biogeochemistry* **123**, 49-61 (2015).

155. D. T. Scott, D. M. McKnight, E. L. Blunt-Harris, S. E. Kolesar, D. R. Lovley, Quinone moieties act as electron acceptors in the reduction of humic substances by humics-reducing microorganisms. *Environ. Sci. Technol.* **32**, 2984-2989 (1998).

156. G. C. Wallace, M. Sander, Y.-P. Chin, W. A. Arnold, Quantifying the electron donating capacities of sulfide and dissolved organic matter in sediment pore waters of wetlands. *Environ. Sci. Proc. Impacts*, (2017).

157. Z.-G. Yu, S. Orsetti, S. B. Haderlein, K.-H. Knorr, Electron transfer between sulfide and humic acid: Electrochemical evaluation of the reactivity of Sigma-Aldrich humic acid toward sulfide. *Aquatic Geochemistry* **22**, 117-130 (2015).

158. I. Bauer, A. Kappler, Rates and extent of reduction of Fe(III) and O_2 by humic substances. *Environ. Sci. Technol.* **43**, 4902-4908 (2009).

159. J. Chen, B. Gu, R. A. Royer, W. D. Burgos, The roles of natural organic matter in chemical and microbial reduction of ferric iron. *Sci. Total Environ.* **307**, 167-178 (2003).

160. A. Kappler, M. Benz, B. Schink, A. Brune, Electron shuttling via humic acids in microbial iron(III) reduction in a freshwater sediment. *FEMS Microbiol. Ecol.* **47**, 85-92 (2004).

161. G. Liu *et al.*, Microbial reduction of Fe(III)-bearing clay minerals in the presence of humic acids. *Scientific Reports* **7**, 45354 (2017).

162. S. Rakshit, M. Uchimiya, G. Sposito, Iron(III) bioreduction in soil in the presence of added humic substances. *Soil Sci. Soc. Am. J.* **73**, 65-71 (2009).

163. Y. Yuan, X. Cai, Y. Wang, S. Zhou, Electron transfer at microbe-humic substances interfaces: Electrochemical, microscopic and bacterial community characterizations. *Chem. Geol.* **456**, 1-9 (2017).

164. M. Wolf, A. Kappler, J. Jiang, R. U. Meckenstock, Effects of humic substances and quinones at low concentrations on ferrihydrite reduction by *Geobacter metallireducens*. *Environ. Sci. Technol.* **43**, 5679-5685 (2009).

165. G. Davies *et al.*, Tight metal binding by humic acids and its role in biomineralization. *Journal of the Chemical Society, Dalton Transactions*, 4047-4060 (1997).

166. S. C. B. Myneni, Soft x-ray spectroscopy and spectromicroscopy studies of organic molecules in the environment. *Reviews in Mineralogy and Geochemistry* **49**, 485-579 (2002).

167. J. T. Nurmi, P. G. Tratnyek, in *Aquatic Redox Chemistry,* P. G. Tratnyek, T. J. Grundl, S. B. Haderlein, Eds. (American Chemical Society, Washington, DC, 2011), vol. 1071, pp. 129-151.

168. N. Gupta, H. Linschitz, Hydrogen-bonding and protonation effects in electrochemistry of quinones in aprotic solvents. *J. Am. Chem. Soc.* **119**, 6384-6391 (1997).

169. V. Gutmann, G. Gritzner, K. Danksagmuller, Solvent effects on the redox potential of hexacyanoferrate(III)-hexacyanoferrate(II). *Inorg. Chim. Acta* **17**, 81-86 (1976).

170. R. Lu *et al.*, Probing the redox process of p-benzoquinone in dimethyl sulphoxide by using fluorescence spectroelectrochemistry. *Front. Environ. Sci. Eng.* **11**, 14 (2017).

171. R. Petrucci, G. Marrosu, P. Astolfi, G. Lupidi, L. Greci, Cyclic voltammetry, spectroelectrochemistry and electron spin resonance as combined tools to study thymoquinone in aprotic medium. *Electrochim. Acta* **60**, 230-238 (2012).

172. K. Sasaki, T. Kashimura, M. Ohura, Y. Ohsaki, N. Ohta, Solvent effect in the electrochemical reduction of p-quinones in several aprotic solvents. *J. Electrochem. Soc.* **137**, 2437-2443 (1990).

173. S. L. J. Tan, M. L. Novianti, R. D. Webster, Effects of low to intermediate water concentrations on proton-coupled electron transfer (PCET) reactions of flavins in aprotic solvents and a comparison with the PCET reactions of quinones. *The Journal of Physical Chemistry B* **119**, 14053-14064 (2015).

174. M. E. Tessensohn, H. Hirao, R. D. Webster, Electrochemical properties of phenols and quinones in organic solvents are strongly influenced by hydrogen-bonding with water. *Journal of Physical Chemistry* **117**, 1081-1090 (2012).

175. N. G. Tsierkezos, Cyclic voltammetric studies of ferrocene in nonaqueous solvents in the temperature range from 248.15 to 298.15 K. *J. Solution Chem.* **36**, 289-302 (2007).

176. X. Zhu, C. Wang, Accurate estimation of the one-electron reduction potentials of various substituted quinones in DMSO and CH_3CN. *J. Org. Chem.* **75**, 5037-5047 (2010).

177. J. T. Nurmi, P. G. Tratnyek, in *Proceedings of the 20th Anniversary Conference of the International Humic Substances Conference (IHSS), 21-26 July 2002, Northeastern University, Boston, MA*. (2002), pp. 58-60.

178. J. T. Nurmi, P. G. Tratnyek, Electrochemical properties of natural organic matter (NOM), fractions of NOM, and model biogeochemical electron shuttles. *Environ. Sci. Technol.* **36**, 617-624 (2002).

179. W. Rochus, S. Sipos, Micelle formation by humic substances. *Agrochimica* **22**, 446-454 (1978).

180. R. R. Engebretson, W. R. von, Micro-organization in dissolved humic acids. *Environ. Sci. Technol.* **28**, 1934-1941 (1994).

181. R. Von Wandruszka, The micellar model of humic acid: Evidence from pyrene fluorescence measurements. *Soil Sci.* **163**, 921-930 (1998).

182. T. F. Guetzloff, J. A. Rice, Does humic acid form a micelle? *Sci. Total Environ.* **152**, 31-35 (1994).

183. A. Piccolo, S. Nardi, G. Concheri, Macromolecular changes of humic substances induced by interaction with organic acids. *European Journal of Soil Science* **47**, 319-328 (1996).

184. Z. Yang, A. Kappler, J. Jiang, Reducing capacities and distribution of redox-active functional groups in low molecular weight fractions of humic acids. *Environ. Sci. Technol.* **50**, 12105-12113 (2016).

185. A. J. Simpson *et al.*, The application of ^{1}H HR-MAS NMR spectroscopy for the study of structures and associations of organic components at the solid-aqueous interface of a whole soil. *Envrionmental Sciences and Technology* **35**, 3321-3325 (2001).

186. D. Martin, H. G. Hauthal, *Dimethyl Sulphoxide*. (Halsted Press, 1975).

187. T. Heinze *et al.*, Effective preparation of cellulose derivatives in a new simple cellulose solvent. *Macromolecular Chemistry and Physics* **201**, 627-631 (2000).

188. F. Lu, J. Ralph, Non-degradative dissolution and acetylation of ball-milled plant cell walls: High-resolution solution-state NMR. *The Plant Journal* **35**, 535-544 (2003).

189. M. M. Tfaily *et al.*, Sequential extraction protocol for organic matter from soils and sediments using high resolution mass spectrometry. *Anal. Chim. Acta* **972**, 54-61 (2017).

190. D. S. H. Chan *et al.*, Effect of DMSO on protein structure and interactions assessed by collision-induced dissociation and unfolding. *Anal. Chem.* **89**, 9976-9983 (2017).

191. T. Arakawa, Y. Kita, S. N. Timasheff, Protein precipitation and denaturation by dimethyl sulfoxide. *Biophysical Chemistry* **131**, 62-70 (2007).

192. H. J. Sterling, J. S. Prell, C. A. Cassou, E. R. Williams, Protein conformation and supercharging with DMSO from aqueous solution. *J. Am. Soc. Mass Spectrom.* **22**, 1178 (2011).

193. C. Fan, J. Lu, W. Zhang, I. Suzuki, G. Li, Enhanced electron-transfer reactivity of cytochrome b5 by dimethylsulfoxide and N,N'-dimethylformamide. *Anal. Sci.* **18**, 1031-1033 (2002).

194. C. Fan, G. Wagner, G. Li, Effect of dimethyl sulfoxide on the electron transfer reactivity of hemoglobin. *Bioelectrochemistry* **54**, 49-51 (2001).

195. Q. Li, P. Mabrouk, Spectroscopic and electrochemical studies of horse myoglobin in dimethyl sulfoxide. *JBIC Journal of Biological Inorganic Chemistry* **8**, 83-94 (2003).

196. B. W. Berry, M. C. Martínez-Rivera, C. Tommos, Reversible voltammograms and a Pourbaix diagram for a protein tyrosine radical. *Proc. Natl. Acad. Sci. USA* **109**, 9739-9743 (2012).

197. A. S. Pavitt, E. J. Bylaska, P. G. Tratnyek, Oxidation potentials of phenols and anilines: Correlation analysis of electrochemical and theoretical values. *Environ. Sci. Proc. Impacts* **19**, 339-349 (2017).

198. S. A. Petrova, M. B. Kolodyazhny, O. S. Ksenzhek, Electrochemical properties of some naturally occurring quinones. *J. Electroanal. Chem.* **277**, 189-196 (1990).

199. R. Ojani, J. Raoof, M. Ebrahimi, A cyclic voltammetric study of the aqueous electrochemistry of some anthraquinone derivatives on carbon paste electrode. *Iran. J. Chem. Chem. Eng.* **20**, 75-81 (2001).

200. S. I. Bailey, I. M. Ritchie, A cyclic voltammetric study of the aqueous electrochemistry of some quinones. *Electrochim. Acta* **30**, 3-12 (1985).

201. Y. Kumagai, Y. Shinkai, T. Miura, A. K. Cho, The chemical biology of naphthoquinones and Its environmental implications. *Annual Review of Pharmacology and Toxicology* **52**, 221-247 (2012).

202. R. Salazar, J. Vidal, M. Martínez-Cifuentes, R. Araya-Maturana, O. Ramírez-Rodríguez, Electrochemical characterization of hydroquinone derivatives with different substituents in acetonitrile. *New J. Chem.* **39**, 1237-1246 (2015).

203. M. T. Huynh, C. W. Anson, A. C. Cavell, S. S. Stahl, S. Hammes-Schiffer, Quinone 1 e− and 2 e−/2 H+ reduction potentials: Identification and analysis of deviations from systematic scaling relationships. *J. Am. Chem. Soc.* **138**, 15903-15910 (2016).

204. A. Slowey, M. Marvin-DiPasquale, How to overcome inter-electrode variability and instability to quantify dissolved oxygen, Fe(II), Mn(II), and S(II) in undisturbed soils and sediments using voltammetry. *Geochemical Transactions* **13**, 6 (2012).

205. M. Zelic, Reverse scan as a source of information in square wave voltammetry. *Croat. Chem. Acta* **79**, 49-55 (2006).

206. T. Andres, L. Eckmann, D. K. Smith, Voltammetry of nitrobenzene with cysteine and other acids in DMSO. Implications for the biological reactivity of reduced nitroaromatics with thiols. *Electrochim. Acta* **92**, 257-268 (2013).

207. H. Hotta, H. Sakamoto, S. Nagano, T. Osakai, Y. Tsujino, Unusually large numbers of electrons for the oxidation of polyphenolic antioxidants. *Biochimica et Biophysica Acta (BBA) - General Subjects* **1526**, 159-167 (2001).

208. M. D. Ryan, A. Yueh, W. Y. Chen, The Electrochemical Oxidation of Substituted Catechols. *J. Electrochem. Soc.* **127**, 1489-1495 (1980).

209. Ł. Górski, F. Ciepiela, M. Jakubowska, Automatic baseline correction in voltammetry. *Electrochim. Acta* **136**, 195-203 (2014).

210. M. Aeschbacher, D. Vergari, R. P. Schwarzenbach, M. Sander, Electrochemical analysis of proton and electron transfer equilibria of the reducible moieties in humic acids. *Environ. Sci. Technol.* **45**, 8385-8394 (2011).

211. J. M. Saveant, *Elements of Molecular and Biomolecular Electrochemistry*. (John Wiley & Sons New Jersey, 2006).

212. A. L. Eckermann, D. J. Feld, J. A. Shaw, T. J. Meade, Electrochemistry of redox-active self-assembled monolayers. *Coord. Chem. Rev.* **254**, 1769-1802 (2010).

213. Y. Yuan *et al.*, Onsite quantifying electron donating capacity of dissolved organic matter. *Sci. Total Environ.* **662**, 57-64 (2019).

214. C. A. Gorski, L. Klupfel, A. Voegelin, M. Sander, T. B. Hofstetter, Redox properties of structural Fe in clay minerals. 2. Electrochemical and spectroscopic characterization of electron transfer irreversibility in ferruginous smectite, SWa-1. *Environ. Sci. Technol.* **46**, 9369-9377 (2012).

215. C. A. Gorski, L. E. Klupfel, A. Voegelin, M. Sander, T. B. Hofstetter, Redox properties of structural iron in clay minerals: 3. Relationships between smectite redox and structural properties. *Environ. Sci. Technol.* **47**, 13477-13485 (2013).

216. M. E. G. Lyons, Transport and kinetics in electroactive polymers. *Adv. Chem. Phys.* **94**, 297-624 (1996).

217. S. Kim, R. W. Kramer, P. G. Hatcher, Graphical Method for Analysis of Ultrahigh-Resolution Broadband Mass Spectra of Natural Organic Matter, the Van Krevelen Diagram. *Anal. Chem.* **75**, 5336-5344 (2003).

218. R. L. Sleighter, P. G. Hatcher, Molecular characterization of dissolved organic matter (DOM) along a river to ocean transect of the lower Chesapeake Bay by ultrahigh resolution electrospray ionization Fourier transform ion cyclotron resonance mass spectrometry. *Mar. Chem.* **110**, 140-152 (2008).

219. J. Lehmann *et al.*, Spatial complexity of soil organic matter forms at nanometre scales. *Nature Geosci.* **1**, 238-242 (2008).

220. M. Witt, J. Fuchser, B. P. Koch, Fragmentation studies of fulvic acids using collision induced dissociation Fourier transform ion cyclotron resonance mass spectrometry. *Anal. Chem.* **81**, 2688-2694 (2009).

221. K. R. Murphy *et al.*, Photochemistry illuminates ubiquitous organic matter fluorescence spectra. *Environ. Sci. Technol.* **52**, 11243-11250 (2018).

222. R. L. Sleighter, P. G. Hatcher, The application of electrospray ionization coupled to ultrahigh resolution mass spectrometry for the molecular characterization of natural organic matter. *Journal of Mass Spectrometry* **42**, 559-574 (2007).

223. S. Er, C. Suh, M. P. Marshak, A. Aspuru-Guzik, Computational design of molecules for an all-quinone redox flow battery. *Chem. Sci.* **6**, 885-893 (2014).

224. S. E. Treimer, D. H. Evans, Electrochemical reduction of acids in dimethyl sulfoxide. CE mechanisms and beyond. *J. Electroanal. Chem.* **449**, 39 (1998).

225. G. Gritzner, Solvent effects on half-wave potentials. *The Journal of Physical Chemistry* **90**, 5478-5485 (1986).

226. V. V. Pavlishchuk, A. W. Addison, Conversion constants for redox potentials measured versus different reference electrodes in acetonitrile solutions at 25°C. *Inorg. Chim. Acta* **298**, 97-102 (2000).

227. D. Bao *et al.*, Electrochemical Oxidation of Ferrocene: A Strong Dependence on the Concentration of the Supporting Electrolyte for Nonpolar Solvents. *The Journal of Physical Chemistry A* **113**, 1259-1267 (2009).

228. R. M. Powell, P. D. Powell, in *Encyclopedia of Environmental Analysis and Remediation*. (Wiley, New York, 1998), vol. 8, pp. 4729-4761.

229. D. P. Dissanayake, in *Metal Oxides,* J. L. G. Fierro, Ed. (CRC Press, Boca Raton, FL, 2006), vol. 108, chap. 17, pp. 543-568.

230. R. A. Brown, R. L. Lewis, R. J. Fiacco, Jr., M. C. Leahy, in *International Conference on Remediation of Chlorinated and Recalcitrant Compounds, 5th*. (Monterey, CA, 2006), pp. d 04 ppr/01-d 04 ppr/08.

231. C. Mueller, E. Loebel, P. Rissing, Site remediation with nanoscale iron particles - technology review. *Altlasten Spektrum* **15**, 75-83 (2006).

232. *Identification and Characterization Methods for Reactive Minerals Responsible for Natural Attenuation of Chlorinated Organic Compounds in Ground Water* (EOA 600/R-09/115, 2009).

233. P. G. Tratnyek, R. L. Johnson, V. Lowry Gregory, R. A. Brown, in *Chlorinated Solvent Source Zone Remediation,* B. H. Kueper, H. F. Stroo, C. M. Vogel, C. H. Ward, Eds. (Springer, New York, 2014), vol. 7, chap. 10, pp. 307-351.

234. T. P. Klupinski, Y.-P. Chin, S. J. Traina, Abiotic Degradation of Pentachloronitrobenzene by Fe(II): Reactions on Goethite and Iron Oxide Nanoparticles. *Environ. Sci. Technol.* **38**, 4353-4360 (2004).

235. A. Neumann, T. B. Hofstetter, M. Skarpeli-Liati, R. P. Schwarzenbach, Reduction of Polychlorinated Ethanes and Carbon Tetrachloride by Structural Fe(II) in Smectites. *Environ. Sci. Technol.* **43**, 4082-4089 (2009).

236. M. L. McCormick, P. Adriaens, Carbon tetrachloride transformation on the surface of nanoscale biogenic magnetite particles. *Environ. Sci. Technol.* **38**, 1045-1053 (2004).

237. K. Pecher, S. B. Haderlein, R. P. Schwarzenbach, Reduction of polyhalogenated methanes by surface-bound Fe(II) in aqueous suspensions of iron oxides. *Environ. Sci. Technol.* **36**, 1734-1741 (2002).

238. T. B. Hofstetter, C. G. Heijman, S. B. Haderlein, C. Holliger, R. P. Schwarzenbach, Complete reduction of TNT and other (poly)nitroaromatic compounds under iron-reducing subsurface conditions. *Environ. Sci. Technol.* **33**, 1479-1487 (1999).

239. D. Kim, T. J. Strathmann, Role of organically complexed iron(II) species in the reductive transformation of RDX in anoxic environments. *Environ. Sci. Technol.* **41**, 1257-1264 (2007).

240. J. B. Niedźwiecka *et al.*, Iron and Electron Shuttle Mediated (Bio)degradation of 2,4-Dinitroanisole (DNAN). *Environ. Sci. Technol.* **51**, 10729-10735 (2017).

241. D. Colón, E. J. Weber, J. L. Anderson, QSAR study of the reduction of nitroaromatics by Fe(II) species. *Environ. Sci. Technol.* **40**, 4976-4982 (2006).

242. T. B. Hofstetter *et al.*, Substituent effects on nitrogen isotope fractionation during abiotic reduction of nitroaromatic compounds. *Environ. Sci. Technol.* **42**, 1997-2003 (2008).

243. J. Klausen, S. P. Troeber, S. B. Haderlein, R. P. Schwarzenbach, Reduction of substituted nitrobenzenes by Fe(II) in aqueous mineral suspensions. *Environ. Sci. Technol.* **29**, 2396-2404 (1995).

244. X. Liang *et al.*, Heterogeneous Reduction of 2-Chloronitrobenzene by Co-substituted Magnetite Coupled with Aqueous Fe2+: Performance, Factors, and Mechanism. *ACS Earth and Space Chemistry*, (2019).

245. T. S. Pasakarnis *et al.*, Influence of chloride and Fe(II) content on the reduction of Hg(II) by magnetite. *Environ. Sci. Technol.* **47**, 6987-6994 (2013).

246. A. R. Felmy *et al.*, Heterogeneous Reduction of PuO2 with Fe(II): Importance of the Fe(III) Reaction Product. *Environ. Sci. Technol.* **45**, 3952-3958 (2011).

247. E. Liger, L. Charlet, P. Van Cappellen, Surface catalysis of uranium(VI) reduction by iron(II). *Geochim. Cosmochim. Acta* **63**, 2939-2955 (1999).

248. T. Peretyazhko *et al.*, Reduction of Tc(VII) by Fe(II) sorbed on Al (hydr)oxides. *Environ. Sci. Technol.* **42**, 5499-5506 (2008).

249. J. Culpepper *et al.*, Reduction of PCE and TCE by magnetite revisited. *Environ. Sci. Proc. Impacts* **20**, 1340-1349 (2018).

250. J. E. Amonette, D. J. Workman, D. W. Kennedy, J. S. Fruchter, Y. A. Gorby, Dechlorination of carbon tetrachloride by Fe(II) associated with goethite. *Environ. Sci. Technol.* **34**, 4606-4613 (2000).

251. C. A. Gorski, M. M. Scherer, in *Aquatic Redox Chemistry,* P. G. Tratnyek, T. J. Grundl, S. B. Haderlein, Eds. (American Chemical Society, Washington, DC, 2011), vol. 1071, chap. 15, pp. 315-343.

252. P. Larese-Casanova, M. M. Scherer, Fe(II) sorption on hematite: New insights based on spectroscopic measurements. *Environ. Sci. Technol.* **41**, 471-477 (2007).

253. S. V. Yanina, K. M. Rosso, Linked reactivity at mineral-water interfaces through bulk crystal conduction. *Science* **320**, 218-222 (2008).

254. A. J. Frierdich *et al.*, Iron Atom Exchange between Hematite and Aqueous Fe(II). *Environ. Sci. Technol.* **49**, 8479-8486 (2015).

255. A. G. B. Williams, M. M. Scherer, Spectroscopic evidence for Fe(II)-Fe(III) electron transfer at the iron oxide-water interface. *Environ. Sci. Technol.* **38**, 4782-4790 (2004).

256. R. M. Handler, B. L. Beard, C. M. Johnson, M. M. Scherer, Atom exchange between aqueous Fe(II) and goethite: An Fe isotope tracer study. *Environ. Sci. Technol.* **43**, 1102-1107 (2009).

257. P. Larese-Casanova, A. Kappler, S. B. Haderlein, Heterogeneous oxidation of Fe(II) on iron oxides in aqueous systems: Identification and controls of Fe(III) product formation. *Geochim. Cosmochim. Acta* **91**, 171-186 (2012).

258. K. M. Rosso, D. M. A. Smith, M. Dupuis, An ab initio model of electron transport in hematite (a-Fe2O3) basal planes. *J. Chem. Phys.* **118**, 6455-6466 (2003).

259. J. Wang, J. R. Rustad, A simple model for the effect of hydration on the distribution of ferrous iron at reduced hematite (012) surfaces. *Geochim. Cosmochim. Acta* **70**, 5285-5292 (2006).

260. N. Iordanova, M. Dupuis, K. M. Rosso, Charge transport in metal oxides: A theoretical study of hematite α-Fe2O3. *The Journal of Chemical Physics* **122**, 144305 (2005).

261. S. Kerisit, A. R. Felmy, E. J. Bylaska, E. S. Ilton. (American Chemical Society, 2011), pp. GEOC-10.

262. D. Mishra, J. Farrell, paper presented at the 228th ACS National Meeting, Philadelphia, PA, 2004.

263. A. F. White, M. L. Peterson, The reduction of aqueous metal species on the surfaces of Fe(II)-containing oxides: the role of surface passivation. *ACS Symp. Ser.* **715**, 323-341 (1998).

264. K. C. Namkung, A. E. Burgess, D. H. Bremner, A Fenton-like oxidation process using corrosion of iron metal sheet surfaces in the presence of hydrogen peroxide. A batch process study using model pollutants. *Environ. Technol.* **26**, 341-352 (2005).

265. J. Entwistle, D. E. Latta, M. M. Scherer, A. Neumann, Abiotic degradation of chlorinated solvents by clay minerals and Fe(II): Evidence for reactive mineral intermediates. *Environ. Sci. Technol.*, (2019).

266. H. Qin, X. Guan, J. Z. Bandstra, R. L. Johnson, P. G. Tratnyek, Modeling the kinetics of hydrogen formation by zerovalent iron: Effects of sulfidation on micro- and nano-scale particles. *Environ. Sci. Technol.* **52**, 13887-13896 (2018).

267. A. M. Jones, C. A. Murphy, T. D. Waite, R. N. Collins, Fe(II) Interactions with Smectites: Temporal Changes in Redox Reactivity and the Formation of Green Rust. *Environ. Sci. Technol.* **51**, 12573-12582 (2017).

268. A. S. Pavitt, P. G. Tratnyek, Electrochemical characterization of natural organic matter by direct voltammetry in an aprotic solvent. *Environ. Sci. Proc. Impacts* **21**, 1664-1683 (2019).

269. M. M. Scherer, J. C. Westall, M. Ziomek-Moroz, P. G. Tratnyek, Kinetics of carbon tetrachloride reduction at an oxide-free iron electrode. *Environ. Sci. Technol.* **31**, 2385-2391 (1997).

270. K. Shimizu, A. Lasia, J.-F. Boily, Electrochemical Impedance Study of the Hematite/Water Interface. *Langmuir* **28**, 7914-7920 (2012).

271. A. F. White, M. L. Peterson, M. F. Hochella, Jr., Electrochemistry and dissolution kinetics of magnetite and ilmenite. *Geochim. Cosmochim. Acta* **58**, 1859-1875 (1994).

272. P. A. Castro, E. R. Vago, E. J. Calvo, Surface electrochemical transformations on spinel iron oxide electrodes in aqueous solutions. *J. Chem. Soc., Faraday Trans.* **92**, 3371-3379 (1996).

273. J. T. Nurmi *et al.*, Characterization and properties of metallic iron nanoparticles: Spectroscopy, electrochemistry, and kinetics. *Environ. Sci. Technol.* **39**, 1221-1230 (2005).

274. J. T. Nurmi, P. G. Tratnyek, Electrochemical studies of packed iron powder electrodes: Effects of common constituents of natural waters on corrosion potential. *Corros. Sci.* **50**, 144-154 (2008).

275. V. Sarathy *et al.*, Aging of iron nanoparticles in aqueous solution: effects on structure and reactivity. *The Journal of Physical Chemistry C* **112**, 2286-2293 (2008).

276. C. A. Gorski, J. T. Nurmi, P. G. Tratnyek, T. B. Hofstetter, M. M. Scherer, Redox behavior of magnetite: Implications for contaminant reduction. *Environ. Sci. Technol.* **44**, 55-60 (2010).

277. J. T. Nurmi *et al.*, Recovery of iron/iron oxide nanoparticles from aqueous media: A comparison of methods and their effects. *Journal of Nanoparticle Research* **13**, 1937-1952 (2011).

278. D. Turcio-Ortega, D. Fan, P. G. Tratnyek, E.-J. Kim, Y.-S. Chang, Reactivity of Fe/FeS nanoparticles: Electrolyte composition effects on corrosion electrochemistry. *Environ. Sci. Technol.* **46**, 12484-12492 (2012).

279. M. J. Bradley, P. G. Tratnyek, Electrochemical characterization of magnetite: Assessing extent of passivation with composite electrodes. *ACS Earth & Space Chemistry* **3**, 688-699 (2019).

280. V. Saez, J. Gonzalez-Garcia, M. A. Kulandainathan, F. Marken, Electro-deposition and stripping of catalytically active iron metal nanoparticles at boron-doped diamond electrodes. *Electrochem. Comm.* **9**, 1127-1133 (2007).

281. H. Antony, S. Peulon, L. Legrand, A. Chaussé, Electrochemical synthesis of lepidocrocite thin films on gold substrate—EQCM, IRRAS, SEM and XRD study. *Electrochim. Acta* **50**, 1015-1021 (2004).

282. K. Hashimoto, M. Cohen, Anodic deposition of ferric oxy-hydroxide films on platinum from perchlorate solutions.

283. L.-Z. Huang, H. C. B. Hansen, M. J. Bjerrum, Electrochemical reduction of nitroaromatic compounds by single sheet iron oxide coated electrodes. *J. Hazard. Mater.* **306**, 175-183 (2016).

284. H. Antony, L. Legrand, A. Chaussé, Carbonate and sulphate green rusts—mechanisms of oxidation and reduction. *Electrochim. Acta* **53**, 7146-7156 (2008).

285. S. Peulon, L. Legrand, H. Antony, A. Chausse, Electrochemical deposition of thin films of green rusts 1 and 2 on inert gold substrate. *Electrochem. Comm.* **5**, 208-213 (2003).

286. B. A. Balko *et al.*, The effect of smectite on the corrosion of iron metal. *Clays Clay Mineral.* **60**, 136-152 (2012).

287. F.-B. Li, L. Tao, C.-H. Feng, X.-Z. Li, K.-W. Sun, Electrochemical evidences for promoted interfacial reactions: The role of Fe(II) adsorbed onto γ-Al_2O_3 and TiO_2 in reductive transformation of 2-nitrophenol. *Environ. Sci. Technol.* **43**, 3656-3661 (2009).

288. L. Lorenzo *et al.*, Electrochemical study of manganese and iron compounds at carbon paste electrodes with electrolytic binder. Application to the characterization of manganese ferrite. *J. Solid State Electrochem.* **1**, 232-240 (1997).

289. M. Aeppli, A. Voegelin, C. A. Gorski, T. B. Hofstetter, M. Sander, Mediated Electrochemical Reduction of Iron (Oxyhydr-)Oxides under Defined Thermodynamic Boundary Conditions. *Environ. Sci. Technol.* **52**, 560-570 (2018).

290. D. Fan, M. Bradley, A. W. Hinkle, R. L. Johnson, P. G. Tratnyek, Chemical reactivity probes for assessing abiotic natural attenuation by reducing iron minerals. *Environ. Sci. Technol.* **50**, 1868-1876 (2016).

291. C. M. D. Kocur, D. Fan, P. G. Tratnyek, R. L. Johnson, Predicting abiotic reduction rates using cryogenically collected soil cores and mediated reduction potential measurements. *Environ. Sci. Technol. Lett.* **7**, 20-26 (2019).

292. C. A. Gorski *et al.*, Redox properties of structural Fe in clay minerals. 1. Electrochemical quantification of electron-donating and -accepting capacities of smectites. *Environ. Sci. Technol.* **46**, 9360-9368 (2012).

293. S. Orsetti, C. Laskov, S. B. Haderlein, Electron transfer between iron minerals and quinones: Estimating the reduction potential of the Fe(II)-goethite surface from AQDS speciation. *Environ. Sci. Technol.* **47**, 14161-14168 (2013).

294. A. L. Hoving, M. Sander, C. Bruggeman, T. Behrends, Redox properties of clay-rich sediments as assessed by mediated electrochemical analysis: Separating pyrite, siderite and structural Fe in clay minerals. *Chem. Geol.* **457**, 149-161 (2017).

295. E. van Bochove, S. Beauchemin, G. Thériault, Continuous Multiple Measurement of Soil Redox Potential Using Platinum Microelectrodes. *Soil Science Society of America Journal - SSSAJ* **66**, (2002).

296. S. P. Faulkner, W. H. Patrick Jr, R. P. Gambrell, Field Techniques for Measuring Wetland Soil Parameters. *Soil Sci. Soc. Am. J.* **53**, 883-890 (1989).

297. Z. Shi, J. T. Nurmi, P. G. Tratnyek, Effects of nano zero-valent iron (nZVI) on oxidation-reduction potential (ORP). *Environ. Sci. Technol.* **45**, 1586-1592 (2011).

298. Z. Shi *et al.*, Methods for characterizing the fate and effects of nano zerovalent iron during groundwater remediation. *J. Contam. Hydrol.* **181**, 17-35 (2015).

299. S. F. Oman, On the seventieth anniversary of the "Suspension Effect": A review of its investigations and interpretations. *Acta Chim. Slov.* **47**, 519-534 (2000).

300. S. F. Oman, M. F. Camoes, K. J. Powell, R. Rajagopalan, P. Spitzer, Guidelines for potentiometric measurements in suspensions. Part A. The suspension effect: (IUPAC technical report). *Pure Appl. Chem.* **79**, 67-79 (2007).

301. D. R. Crow, *Principles and applications of electrochemistry, fourth edition*. (2017), pp. 1-282.

302. K. M. Danielsen, J. L. Gland, K. F. Hayes, Influence of amine buffers on carbon tetrachloride reductive dechlorination by the iron oxide magnetite. *Environ. Sci. Technol.* **39**, 756-763 (2005).

303. A. Buchholz, C. Laskov, S. B. Haderlein, Effects of Zwitterionic Buffers on Sorption of Ferrous Iron at Goethite and Its Oxidation by CCl4. *Environ. Sci. Technol.* **45**, 3355-3360 (2011).

304. A. M. Stemig, T. A. Do, V. M. Yuwono, W. A. Arnold, R. L. Penn, Goethite nanoparticle aggregation: effects of buffers, metal ions, and 4-chloronitrobenzene reduction. *Environmental Science: Nano*, (2014).

305. M. Elsner *et al.*, Mechanisms and products of surface-mediated reductive dehalogenation of carbon tetrachloride by Fe(II) on goethite. *Environ. Sci. Technol.* **38**, 2058-2066 (2004).

306. W. Stumm, G. F. Lee, Oxygenation of ferrous iron. *Indust. Eng. Chem.* **53**, 143-146 (1961).

307. H. D. Pedersen, D. Postma, R. Jakobsen, O. Larsen, Fast transformation of iron oxyhydroxides by the catalytic action of aqueous Fe(II). *Geochim. Cosmochim. Acta* **69**, 3967-3977 (2005).

308. S. Geological, *Chemistry of iron in natural water*. (Washington : U.S. Govt. Print. Off., 1962., 1962).

309. J. D. Hem, *Study and Interpretation of the Chemical Characteristics of Natural Water*. Water-Supply Paper No. 2254 (U.S. Geological Survey, Washington, DC, ed. 3rd, 1985), vol. 2254, pp. 263.

310. R. M. Cornell, U. Schwertmann, *The Iron Oxides: Structure, Properties, Reactions, Occurrence and Uses*. (VCH, Weinheim, Federal Republic of Germany, 1996), pp. 573.

311. M. Spiro, Polyelectrodes: The behaviour and applications of mixed redox systems. *Chem. Soc. Rev.* **15**, 141-165 (1986).

312. H. Bülter *et al.*, Electrochemical analysis of nanostructured iron oxides using cyclic voltammetry and scanning electrochemical microscopy. *Electrochim. Acta* **222**, 1326-1334 (2016).

313. C. A. Gorski, R. Edwards, M. Sander, T. B. Hofstetter, S. M. Stewart, Thermodynamic characterization of iron oxide–aqueous Fe^{2+} redox couples. *Environ. Sci. Technol.* **50**, 8538-8547 (2016).

314. A. Al-Busaidi, P. Cookson, T. Yamamoto, Methods of pH determination in calcareous soils: use of electrolytes and suspension effect. *Soil Research* **43**, 541-545 (2005).

315. S. Thiele-Bruhn, S. Wessel-Bothe, M.-O. Aust, Time-resolved in-situ pH measurement in differently treated, saturated and unsaturated soils. *Journal of Plant Nutrition and Soil Science* **178**, 425-432 (2015).

316. G. Sposito, *The Surface Chemistry of Soils*. (Oxford, New York, 1984), pp. 234.

317. R. O. James, G. A. Parks, in *Surf. Colloid Sci.,* E. Matijević, Ed. (Springer US, Boston, MA, 1982), pp. 119-216.

318. B. H. Jeon, B. A. Dempsey, W. D. Burgos, Kinetics and mechanisms for reactions of Fe(II) with iron(III) oxides. *Environ. Sci. Technol.* **37**, 3309-3315 (2003).

319. E. Silvester *et al.*, Redox potential measurements and Mössbauer spectrometry of Fe^{II} adsorbed onto Fe^{III} (oxyhydr)oxides. *Geochim. Cosmochim. Acta* **69**, 4801-4815 (2005).

Appendix A: Supporting Information to Chapter 2[4]

A.1. Properties of Phenols and Anilines

Table A.1. Rate constants for oxidation of phenols and anilines by MnO_2

No.	IUPAC Name	$\log k_{rel}$ Stone and Morgan[a]	$\log k_{rel}$ Laha and Luthy[b]	$\log k_{rel}$ Klausen et al.[c]	$\log k_{rel}$ Salter-Blanc et al.[d]
1	phenol	−0.244, −0.301			
2	3-methylphenol	0.061			
3	4-methylphenol	0.724, 0.487			
4	4-ethylphenol	0.704			
5	4-nitrophenol	−2.560			
6	2-chlorophenol	−0.195			
7	3-chlorophenol	−1.006			
8	4-chlorophenol	0, 0			
9	4-hydroxyacetophenone	−2.438, −2.495			
10	2-hydroxybenzoic acid	−1.529, −1.921			
11	4-hydroxybenzoic acid	−1.304, −1.228			
12	aniline		−0.626	0.48	-0.100
13	2-methylaniline			0.79	
14	3-methylaniline			0.79	
15	4-methylaniline		0.737	1.6	
16	2-methoxyaniline			1.6	
17	3-methoxyaniline			0.68	
18	4-methoxyaniline		2.862	2.5	
19	3-nitroaniline				−1.34
20	4-nitroaniline		−3.643		~ −4.11[e]
21	3-chloroaniline			−0.96	
22	4-chloroaniline		0.0	0.0	0.0
23	2-methyl-5-nitroaniline				−1.40
24	4-methyl-3-nitroaniline				−1.20
25	2-methoxy-5-nitroaniline				−0.279
26	4-aminobenzoic acid		−1.107		

---

[4] Reprint of the Supporting Information to A. S. Pavitt, E. J. Bylaska, P. G. Tratnyek, Oxidation potentials of phenols and anilines: correlation analysis of electrochemical and theoretical values, Environ. Sci.: Proc. Impacts, 19, 339-349 (2017). Copyright 2017 The Royal Society of Chemistry.

a) Sets A and B from Stone (1987) (*1*) are distinguished with red and blue diamonds, respectively, in Figures 1A, 5, and 6.

b) Calculated from k_{exp} data reported in Laha and Luthy (1990) (*2*)

c) Calculated from concentration vs. time data in Figure 8 of Klausen et al.(1997) (*3*)

d) From Salter Blanc et al. (2016). (*4*)

e) Approximate value because reaction was slow.

Table A.2. Substituted phenols used in electrochemical measurements.

No.	Name	CAS-RN	Source (Purity %)	pK_a [a]
1	phenol	108-95-2	Sigma (99)	10.02
2	2-methylphenol (o-cresol)	95-48-7	Sigma	10.37
3	3-methylphenol (m-cresol)	108-39-4	TCI (98)	10.13
4	4-methylphenol (p-cresol)	106-44-5	Matheson, Coleman & Bell	10.36
5	4-ethylphenol	123-07-9	Avocado (97)	10.32
6	2-methoxyphenol (o-guaiacol)	90-05-1	Alfa Aesar (98)	9.98
7	3-methoxyphenol (m-guaiacol)	150-19-6	Acros (97)	9.49
8	4-methoxyphenol (p-guaiacol)	150-76-5	Acros (99)	9.94
9	2-nitrophenol	88-75-5	Acros (99)	6.63
10	3-nitrophenol	554-84-7	Acros (99)	7.89
11	4-nitrophenol	100-02-7	Sigma-Aldrich (99)	7.07
12	2,4-dinitrophenol	51-28-5	Acros (98)	4.35
13	2-methyl-4,6-dinitrophenol (DNOC)	534-52-1	Sigma-Aldrich (99.9)	4.45
14	4-methyl-2,6-dinitrophenol (DNPC)	609-93-8	Combi-Blocks (95)	4.57
15	2-phenylphenol	90-43-7	Aldrich (99)	9.69
16	2-chlorophenol	95-57-8	Acros (98)	7.97
17	3-chlorophenol	108-43-0	Acros (99)	8.79
18	4-chlorophenol	106-48-9	Sigma-Aldrich (99)	8.96
19	2-hydroxyphenol (catechol)	120-80-9	Aldrich (99.5)	9.34, 12.39
20	3-hydroxyphenol (resorcinol)	108-46-3	Aldrich (99)	9.26, 10.73
21	4-hydroxyphenol (hydroquinone)	123-31-9	Aldrich (99)	9.68, 11.55
22	4-cyanophenol	767-00-0	Acros (99)	7.81
23	3-hydroxyacetophenone	121-71-1	TCI (98)	8.92
24	4-hydroxyacetophenone	99-93-4	MP Biomedicals (99.8)	7.79
25	2-hydroxybenzoic acid (o-salicylic acid)	69-72-7	Sigma-Aldrich (99)	13.23
26	3-hydroxybenzoic acid (m-salicylic acid)	99-06-9	Sigma-Aldrich (99)	9.55
27	4-hydroxybenzoic acid (p-salicylic acid)	99-96-7	Aldrich (99)	9.67
28	triclosan	3380-34-5	Sigma-Aldrich (97)	7.68
29	dopamine	51-61-6	Ark Pharm (97)	10.01,12.93
30	bisphenol A	80-05-7	Acros (97)	9.78, 10.39
31	3-aminophenol	591-27-5	Aldrich (98)	9.82
32	4-aminophenol	123-30-8	Sigma-Aldrich (98)	10.4
33	2,5-dimethylphenol	95-87-4	Aldrich (99)	10.47
34	2,6-dimethoxyphenol	91-10-1	Fluka (98)	9.37

35	4-ethyl-2-methoxyphenol	2785-89-9	Alfa Aesar (98)	10.3
36	2-methoxy-4-formylphenol (vanillin)	121-33-5	Aldrich (99)	7.81
37	2,4,6-trimethylphenol	527-60-6	Aldrich (99)	11.07
38	2,4,6-trichlorophenol	88-06-2	Sigma (98)	5.99

a) Estimated using ChemAxon's Instant JChem as described in Salter-Blanc et al. (2016).(*4*)

Table A.3. Substituted anilines used in electrochemical measurements.

No.	**Name**	**CAS-RN**	**Source (Purity %)**	**pK_a [a]**
1	aniline	62-53-3	Aldrich (99.5)	4.64
2	2-methylaniline (o-toluidine)	95-53-4	Alfa Aesar (99)	4.48
3	3-methylaniline (m-toluidine)	108-44-1	Acros (99)	4.86
4	4-methylaniline (p-toluidine)	106-49-0	Alfa Aesar (99)	4.99
5	2-methoxyaniline (o-anisidine)	90-04-0	Acros (99)	4.42
6	3-methoxyaniline (m-anisidine)	536-90-3	Acros (99)	4.01
7	4-methoxyaniline (p-anisidine)	104-94-9	Acros (99)	5.11
8	3-aminobenzoic acid	99-05-8	Sigma	3.27
9	4-aminobenzoic acid	150-13-0	Sigma (99)	2.69
10	2-nitroaniline	88-74-4	Alfa Aesar (98)	0.25
11	3-nitroaniline	99-09-2	Acros (98)	1.72
12	4-nitroaniline	100-01-6	Acros (99)	1.43
13	2-chloroaniline	95-51-2	Alfa Aesar (98)	2.79
14	3-chloroaniline	108-42-9	Acros (99)	3.47
15	4-chloroaniline	106-47-8	Acros (98)	3.49
16	2-methyl-5-nitroaniline	99-55-8	Acros (96)	1.73
17	4-methyl-3-nitroaniline	119-32-4	Acros (97)	2.43
18	2-methoxy-5-nitroaniline	99-59-2	TCI (98)	1.83

a) Estimated using ChemAxon's Instant JChem as described in Salter-Blanc et al. (2016).(*4*)

A.2. Electrochemical Method Development

The experimental methods used by Suatoni et al.(*5*) were matched as closely as possible and are described in the main text, with deviations elaborated and justified below. The concentration of the IPA was varied from 0% to 75% (v/v in water) to characterize the effects that IPA had on the voltammetry. As illustrated in **Figure A.1** for aniline, IPA caused modest changes in peak size and position, but the overall shape of the CVs was equivalent. The effect of IPA on peak resolution varied with compound, and a few phenols/anilines gave notably better resolved peaks with 25% IPA than 50% IPA (Suatoni's conditions). Therefore, we performed most experiments using both 25% and 50% IPA and chose the results with the most pronounced peaks to extract oxidation potentials.

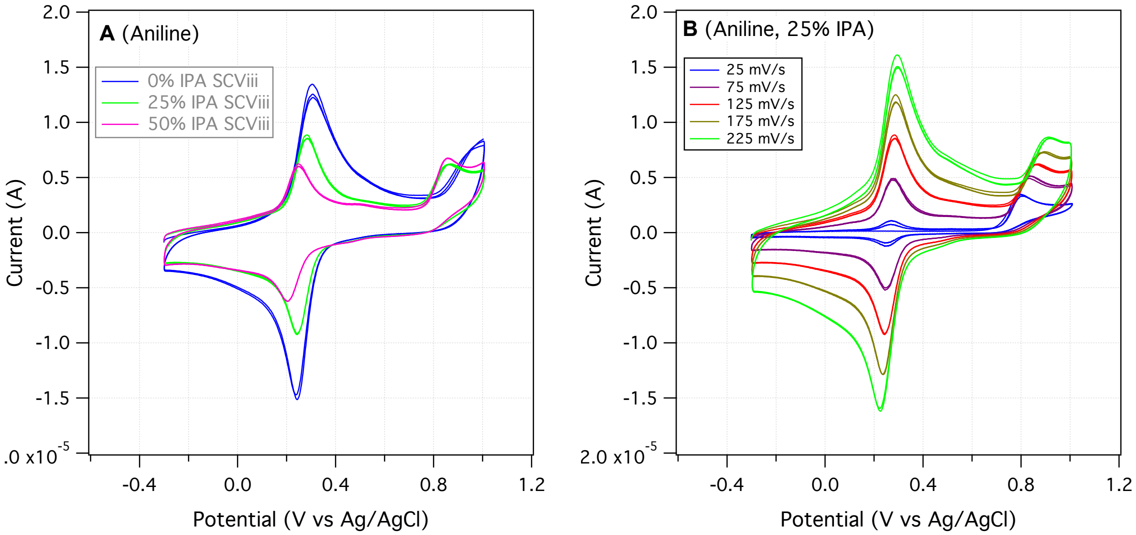

Figure A.1. (**A**) SCV of aniline, at three different IPA concentrations, at a scan rate of 125 mV/s. (**B**) SCV of aniline at 25% IPA and varying scan rates. Both voltammograms were done with a glassy carbon working electrode and a step size of 2 mV.

In all cases, peak potential changed slightly with the change in IPA concentration, as can be expected from the slight change in pH, pH at 50% IPA was approximately 5.6, at 25% 5.1 and at 0% 4.7. Theoretically the reduction potentials should increase with decreasing pH, conversely at low pH reduction becomes easier and at high pH oxidation is more facile.(*6*) Our experimental data however did not reflect this and out of the seventeen phenols and five anilines tested the reverse was true for eleven phenols and four anilines. It was not apparent as to why the phenols and anilines did not follow this expected trend, but possibly due to solvent effects. In comparing the phenol groups 2-nitrophenol oxidation potential decreased as expected (4 mV), but the 4-nitrophenol increased by 12 mV as pH increased. 4-Nitroaniline oxidation potential increased by 6 mV, while the 3-nitroaniline decreased by 12 mV. Both 4-chlorophenol and aniline inreased by 31 and 38 mV, respectively, and 4-chloroaniline increased by 4 mV.

The scan rate was varied for SCVs and an example of the results for aniline can be seen in **Figure A.1-B**. The main reason for varying scan rate is to characterize the reversibility of the electrode reactions.(*7*) For fast reversible reactions, peak potentials do not change with scan rate, as is the case with the large peak at ~ 300 mV in **Figure A.1-B**. However, the peak at ~ 900 mV in that figure shifts as a function of scan rate. In general depending on the type of reaction (if there is a chemical step coupled to electron transfer) if the scan rate is slow compared to the chemical reaction then only the chemical reaction will be characterized in the voltammogram, but if the scan rate is fast and the chemical reaction is slow then only the electron transfer step will be present.(*8*)

For SWV both scan rate and amplitude were varied. SWVi-iv corresponds to varying amplitude from 50 mV (SWVi), 75 mV (SWVii), 100 mV (SWViii), and 125 mV (SWViv) at a constant scan rate of 60 mV/s. SWVv-ix corresponds to a constant 50 mV amplitude and a scan rate of 30 mV/s (SWVv), 60 mV/s (SWVvi), 120 mV/s (SWVvii), 180 mV/s (SWVviii), and 240 mV/s (SWVix). All SWVs had a step size of 2 mV. Varying the amplitude and the scan rate in SWV are used to measure electrode kinetics. Varying the amplitude can be used for species in the solution phase and adsorbed at the electrode, whereas varying the scan rate and the resulting peak to peak separations apply mostly to solution phase species.(*9*)

In SWV a plot of the forward and reverse currents vs. the potential, as shown in **Figure A.2** can be used to show reversibility of the redox couple. In the first scan (SWVi), much like the first pass in the cyclic voltammogram (**Figure A.3**), a primary irreversible peak is observed at ~ 800 mV. This irreversibility is evidenced by the absence of a reverse current peak in SWVi and the absence of a cathodic peak in SCV. In SWVii a reverse current peak is still absent at ~800 mV, but a reverse current peak appears at ~350 mV. This reverse current peak is analogous to the reverse cathodic peak in the cyclic voltammogram.

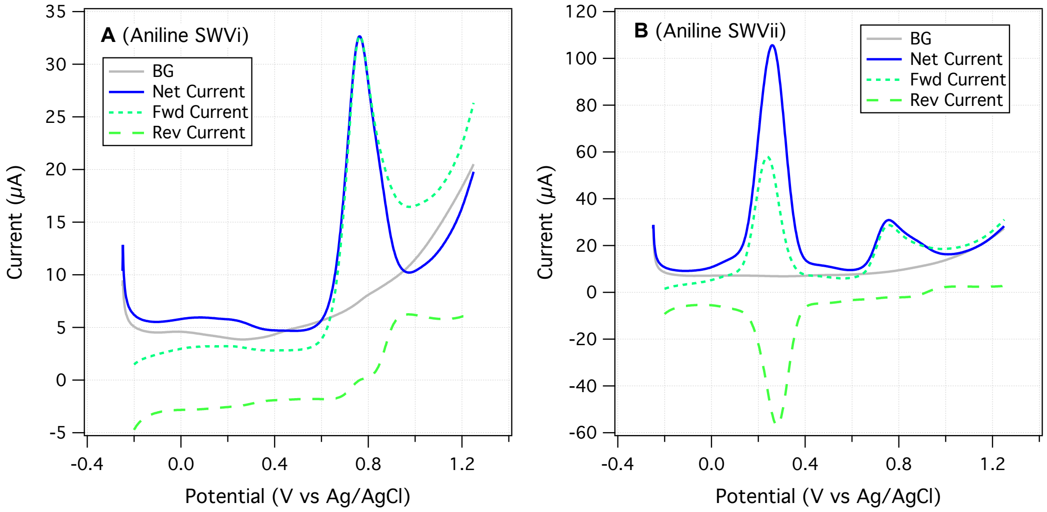

Figure A.2. Forward, reverse and net current square wave voltammogram of aniline in 25% IPA/ buffer solution at a scan rate of 60 mV/s and a step size of 2 mV. (**A**) 50 mV amplitude (**B**) 75 mV amplitude.

A.3. Classification of Voltammograms

As described in the main text, we classified our voltammograms into four types. For phenols, most compounds were type I or type II, except four phenols that were type III (4-nitrophenol, 4-cyanophenol, DNOC, and 4-hydroxyacetphenone); and two phenols that were type IV (4-aminophenol and dopamine). Almost all of the compounds gave the same type by SCV and SWV, except for 2,4-dinitrophenol (whose current went up and down and therefore could be considered a type II or III), 4-cyanophenol (which fell into a type III for SCV, but whose current went up and down in SWV (type II or III)), and 4-hydroxyacetophenone (which was a type III in SCV, but a type II in SWV). The majority of the anilines were type I except for p-toluidine (type II) and 4-methyl-3-nitroaniline and 2-methoxy-5-nitroaniline (both were type I for SWV, but for SCV fell into type III and type II respectively).

Comparing the voltammograms of SCV and SWV both were in agreement of the four types listed. Type I SCVs main features as described in the main text were a primary anodic peak that decresed with subsequent scans, while after the first pass a secondary reversible peak appeared. This can be seen in **Figure A3-A** and is confirmed by the SWV voltammogram in **Figure A4-A.** For type II SCVs, as can be seen in **Figure A3-B**, there is one prominent anodic peak that decreases, usually drastically with each pass and subsequent scan rates. The same behavior is seen with the SWV voltammogram in **Figure A4-B**, where there is a primary prominent peak that decreased significantly between the first and second scan. At first glance, this is not evident from the voltammogram shown, but the current does decrease with subsequent scans and was verified by obtaining the currents in the peak search function in the Aftermath software. For type III voltammograms where the current response increases with scan rate, the same behavior is seen with SCV, **Figure A3-C** and SWV, **Figure A4-C**. Type IV voltammograms exhibited a reversible or quasi-reversible set of peaks. This can be seen in **Figure A3-D** for dopamine which had an approximate 200 mV separation between the anodic and cathodic peaks. For 4-aminophenol (not shown), the peak seperation was 60 mV denoting a one electron transfer reaction. This reversible peak is verified in SWV **Figure A4-D**. The forward and reverse current peaks have the same potential and the ratio of the peaks for the forward and reverse currents are approximately 0.70, which indicates quasi-reversibility.(*10*) For 4-aminophenol (not shown) the ratio of currents is closer to 1.0 denoting reversibility.

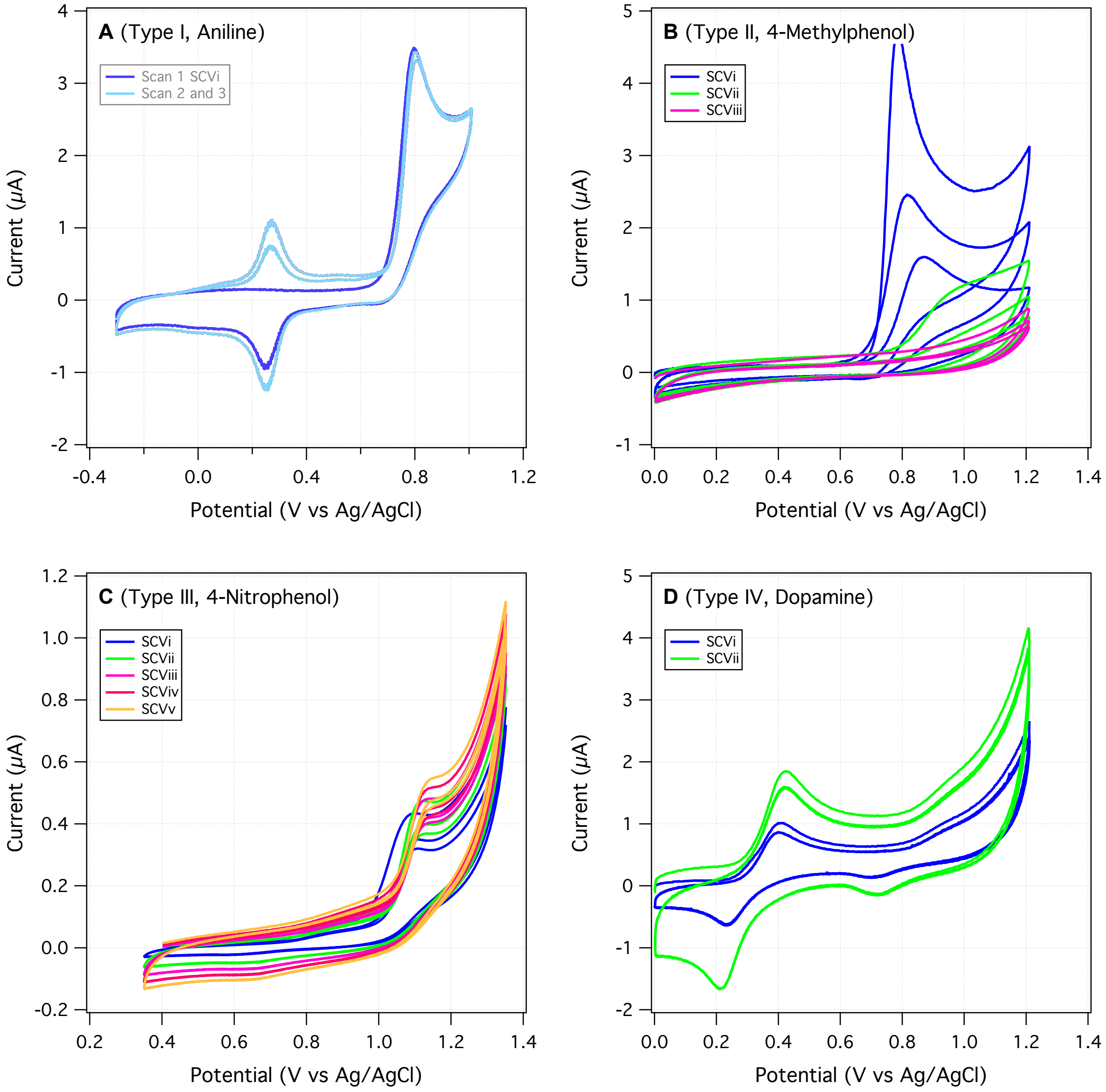

Figure A.3. Four types of staircase cyclic voltammograms at varying scan rates. (**A**) Aniline at 25 mV/s, first pass denoted by dark blue. (**B**) 4-methylphenol (**C**) 4-nitrophenol (**D**) Dopamine. (Conditions: All voltammograms were done using a glassy carbon working electrode. Step size 2 mV, scan rates: 25 mV/s (SCVi), 75 mV/s (SCVii), 125 mV/s (SCViii), 175 mV/s (SCViv), and 225 mV/s (SCVv). A, B and D were done in 25% IPA/ Buffer (pH 5.1) C in 50% IPA/Buffer (pH 5.6).

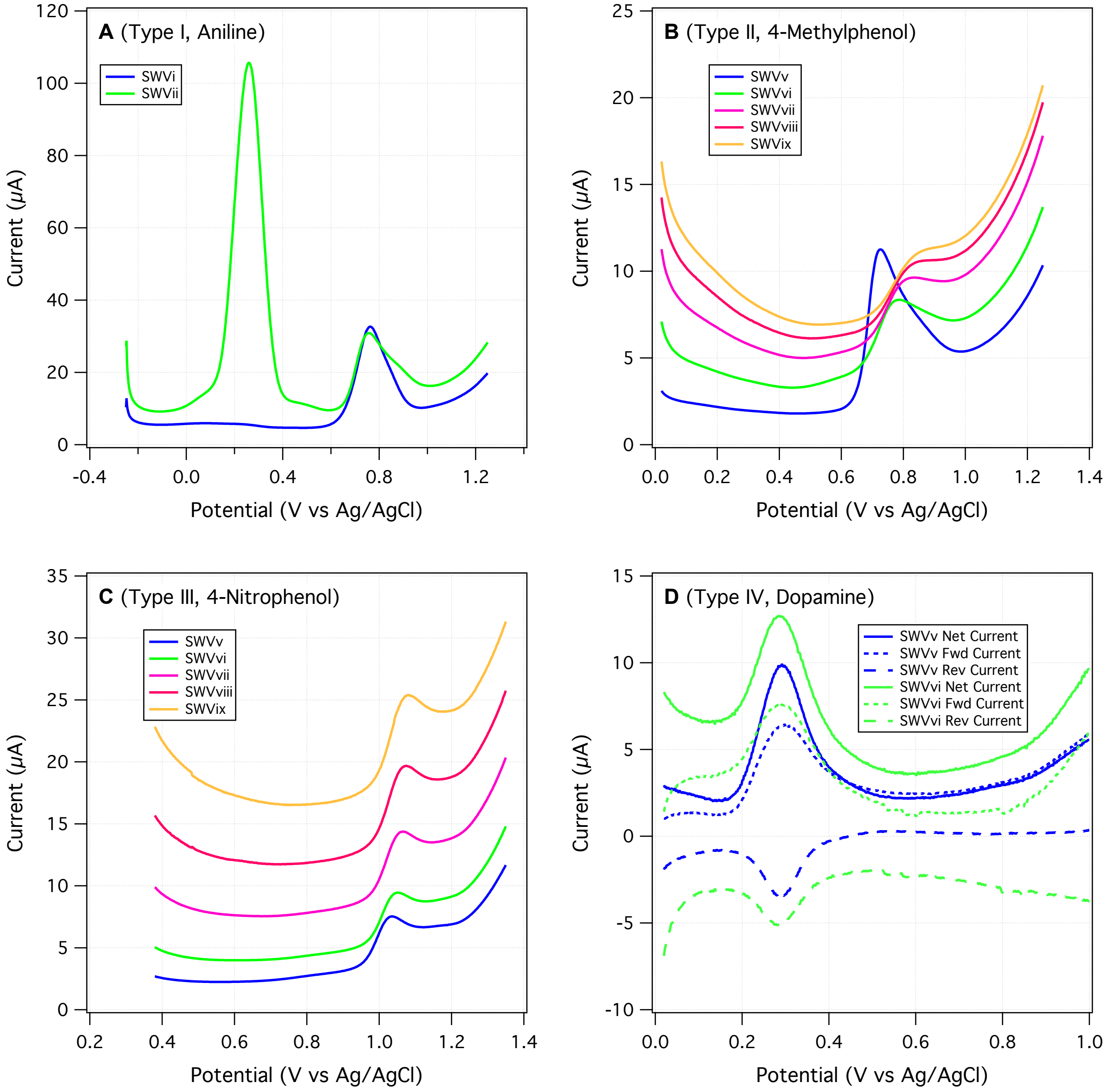

Figure A.4. Four types of square wave voltammograms with a step size of 2 mV, amplitude of 50 mV and varying scan rates: 30 mV/s (SWVv), 60 mV/s (SWVvi), 120 mV/s (SWVvii), 180 mV/s (SWVviii), and 240 mV/s (SWVix). (**A**) Aniline step size 2 mV, scan rate 60 mV/s amplitude 50 mV (SWVi) and 75 mV (SWVii), (**B**) 4-methylpheol (**C**), 4-nitrophenol, (**D**) Forward, reverse and net current for Dopamine at 30 mV/s and 60 mV/s.

A.4. Electrochemical Data Analysis

To help visualize the overall significance of the variablity in electrochemical oxidation potentials over the range of relevant experimental conditions, **Figure A5** provides a summary all of the primary peak potential data (colored markers) and representative values (black markers).

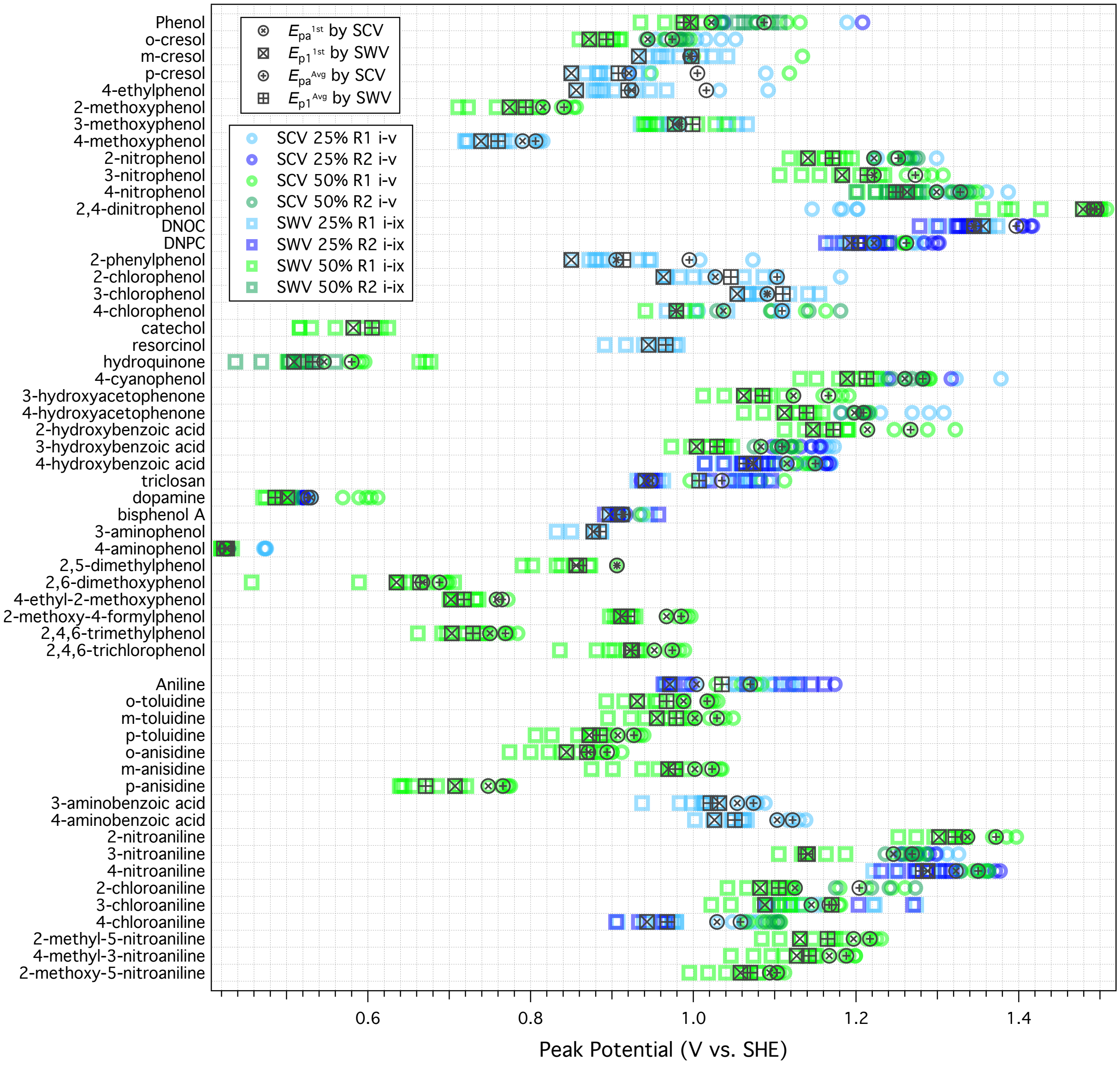

Figure A.5. Summary of newly measured peak potentials for phenols and anilines vs. waveform (circles = SCV (E_{pa}), squares = SWV (E_{p1})); scan rate 25 to 330 mV/s; blue denote 25% IPA, green 50% IPA; and replicates (lighter shades are R1 and darker shades R2). Black symbols are 1st scans and average values (calculated over scan rate and replicates), these values are tabulated in **Tables A4, A5**.

Table A.4. Recommended values of new electrochemically measured oxidation potentials for substituted phenols. All values in V vs SHE.

		Suatoni	E_{pa1} by SCV		E_{pa} by SWV	
No.	**Name**	$E_{1/2}$ [a]	1st Scan	Avg	1st Scan	Avg
1	phenol	0.874	1.022	1.087	0.997	0.988
2	2-methylphenol	0.797	0.944	0.974	0.872	0.893

3	3-methylphenol	0.848	0.996	0.996	0.933	0.998
4	4-methylphenol	0.784	0.921	1.005	0.850	0.908
5	4-ethylphenol	0.808	0.924	1.016	0.856	0.920
6	2-methoxyphenol	0.697	0.815	0.841	0.774	0.794
7	3-methoxyphenol	0.860	0.983	0.983	0.977	0.999
8	4-methoxyphenol	0.647	0.790	0.806	0.739	0.760
9	2-nitrophenol	1.087	1.222	1.252	1.141	1.171
10	3-nitrophenol	1.096	1.222	1.273	1.183	1.214
11	4-nitrophenol	1.165	1.299	1.328	1.263	1.249
12	2,4-dinitrophenol		1.492	1.496	1.479	1.493
13	2-methyl-4,6-dinitrophenol		1.345	1.397	1.356	1.345
14	4-methyl-2,6-dinitrophenol		1.222	1.262	1.193	1.203
15	2-phenylphenol	0.804	0.905	0.995	0.850	0.914
16	2-chlorophenol	0.866	1.027	1.103	0.963	1.046
17	3-chlorophenol	0.975	1.091	1.091	1.054	1.110
18	4-chlorophenol	0.894	1.037	1.109	0.979	0.979
19	2-hydroxyphenol				0.582	0.605
20	3-hydroxyphenol				0.945	0.966
21	4-hydroxyphenol		0.546	0.580	0.509	0.532
22	4-cyanophenol		1.260	1.282	1.189	1.213
23	3-hydroxyacetophenone	0.995	1.123	1.166	1.062	1.085
24	4-hydroxyacetophenone	1.032	1.198	1.209	1.112	1.139
25	2-hydroxybenzoic acid	1.086	1.214	1.267	1.147	1.172
26	3-hydroxybenzoic acid		1.083	1.109	1.004	1.029
27	4-hydroxybenzoic acid	0.957	1.115	1.150	1.074	1.065
28	triclosan		0.948	1.035	0.941	1.007
29	dopamine		0.530	0.526	0.501	0.486
30	bisphenol A		0.914	0.914	0.897	0.912
31	3-aminophenol				0.877	0.884
32	4-aminophenol		0.426	0.425	0.427	0.423
33	2,5-dimethylphenol		0.906	0.906	0.856	0.860
34	2,6-dimethoxyphenol	0.620	0.667	0.688	0.635	0.664
35	4-ethyl-2-methoxyphenol		0.758	0.765	0.702	0.718
36	2-methoxy-4-formylphenol		0.967	0.985	0.911	0.919
37	2,4,6-trimethylphenol		0.750	0.769	0.703	0.729
38	2,4,6-trichlorophenol		0.952	0.974	0.923	0.925

a) Adjusted to SHE from the originally reported values (vs. SCE) by adding 241 mV.

Table A.5. Recommended values of new electrochemically measured oxidation potentials for substituted anilines. All values in V vs SHE.

		Suatoni	**E_{pa} by SCV**		**E_{p1} by SWV**	
No.	**Name**	**$E_{1/2}$ [a]**	**1st Scan**	**Avg**	**1st Scan**	**Avg**
1	aniline	0.866	1.004	1.070	0.971	1.035
2	2-methylaniline	0.836	0.988	1.017	0.931	0.967
3	3-methylaniline	0.847	1.002	1.029	0.955	0.979
4	4-methylaniline	0.778	0.907	0.927	0.872	0.885
5	2-methoxyaniline	0.739	0.871	0.894	0.844	0.869
6	3-methoxyaniline	0.856	1.002	1.023	0.969	0.978
7	4-methoxyaniline	0.634	0.748	0.766	0.707	0.671
8	3-aminobenzoic acid	0.909	1.054	1.074	1.032	1.021
9	4-aminobenzoic acid	0.955	1.103	1.122	1.026	1.051
10	2-nitroaniline	1.230	1.337	1.372	1.302	1.322
11	3-nitroaniline	1.095	1.246	1.269	1.141	1.138
12	4-nitroaniline	1.176	1.323	1.350	1.288	1.282
13	2-chloroaniline	0.983	1.125	1.204	1.082	1.105
14	3-chloroaniline	1.015	1.145	1.167	1.088	1.170
15	4-chloroaniline	0.916	1.029	1.058	0.943	0.968
16	2-methyl-5-nitroaniline	1.062	1.197	1.217	1.131	1.165
17	4-methyl-3-nitroaniline		1.167	1.188	1.127	1.142
18	2-methoxy-5-nitroaniline		1.094	1.103	1.058	1.070

a) Adjusted to SHE from the originally reported values (vs. SCE) by adding 241 mV.

A.5. Electrochemical Data Comparison

To help visualize the overall agreement between the recommended electrochemical oxidation potentials from this work and previously reported values measured under similar conditions, we have summarized all of our data (from **Table A.3, A.4**) and selected literature data (not tabulated) in **Figure A.3**. The data from Li et al.(*6*) were anodic peak potentials obtained at pH 12 and Simić et al.(*11*) listed anodic peak potentials at pH 7. From experimental data for phenol in Li et., we estimated an average decrease of 55.3 mV per pH unit, and that slope was used to calculate potentials adjusted to pH 5.35 (the average of 5.6 and 5.1, the range of pH measured in this work). The same slope was assumed for adjusting the potentials in Simic et al. to pH 5.35. For the anilines, all of which have pK_a's above this pH, no change in potential was assumed. The data from Erickson et al.(*12*) were for anilines and since all anilines had a pK_a < pH, conditions where potential is not dependent on pH, no adjustment was made.

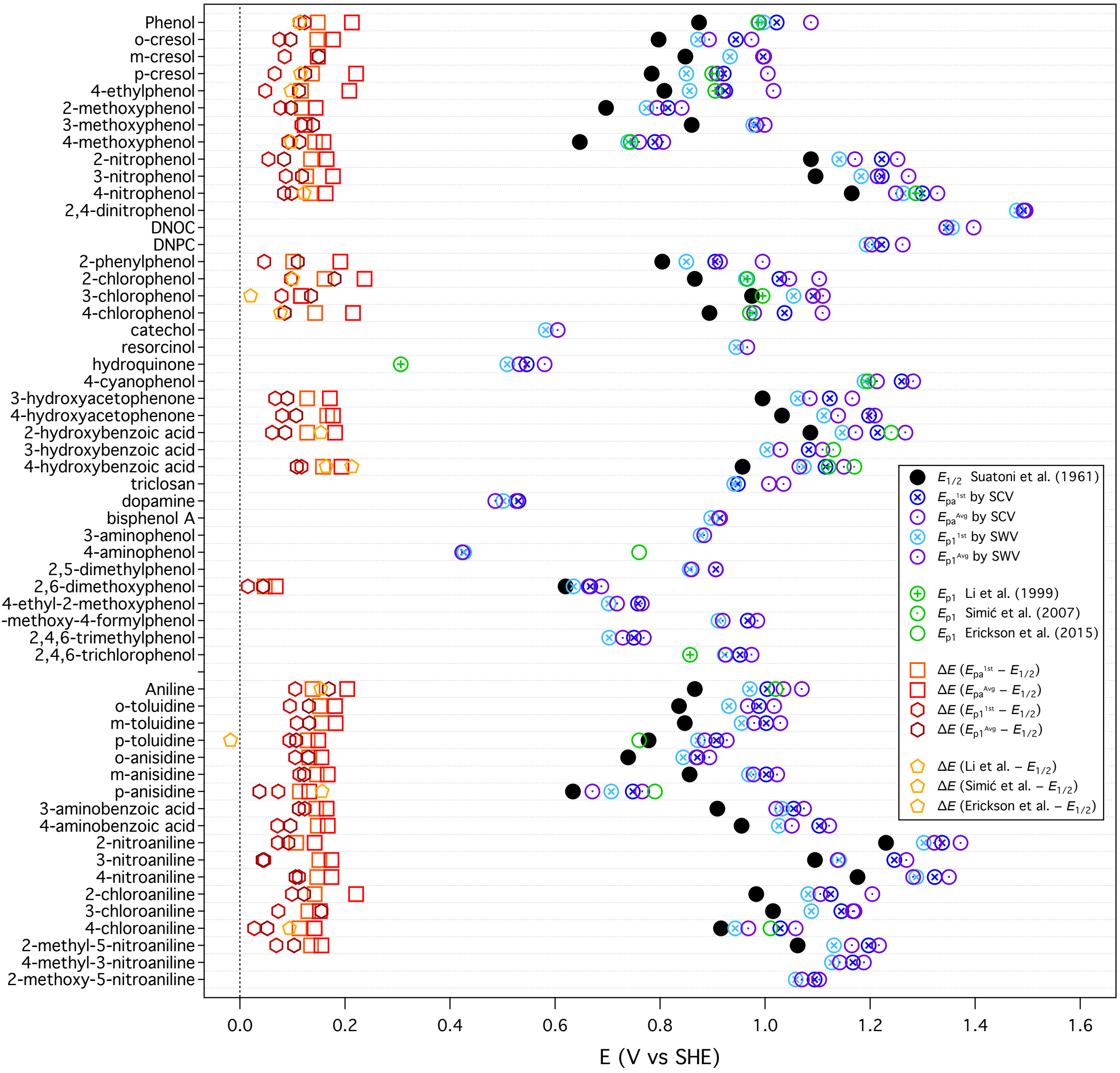

Figure A.6. Summary of peak potentials (E_{pa}^{1st} and E_{pa}^{Avg} from SCV; E_{p1}^{1st} and E_{p1}^{Avg} from SWV) for phenols and anilines vs. literature data from Suatoni et al.(*5*) and others.(*6, 11, 12*) ΔE is the difference between experimental and literature values. The data from Li et al and Simić et al. were adjusted to pH 5.35, as described above.

A.6. Computational Methods

For calculation of oxidation potentials (ΔG^0_{ox} and E_{ox}) for the phenols and anilines, we used methods similar to those in our previous work on oxidation of aromatic amines,(*4*) while adopting some modifications based on (*i*) recent work on similar problems,(*13*) (*ii*) other work on the general problem of computational electrochemistry,(*14-16*) and (*iii*) recent advances in the NWChem code (Including bug fixes for the M06-2x functional and porting of COSMO-SMD method. Available in development tree (http://www.nwchem-sw.org/index.php/Developer) and available in release 6.7, February 2017). For both phenols and anilines, only the initial oxidation step was modeled, assuming it involves only the loss of a single electron from the neutral form of the parent compound to give the corresponding radical cation (i.e., equations A1-A2).

$$\mathrm{HOAr}_{(aq)} \rightarrow \mathrm{HOAr}^{\bullet+}_{(aq)} + e^-_{(g)} \tag{A1}$$

$$\mathrm{NH_2Ar}_{(aq)} \rightarrow \mathrm{NH_2Ar}^{\bullet+}_{(aq)} + e^-_{(g)} \tag{A2}$$

For these half-reactions, ΔG^0_{ox} and E_{ox} were calculated from gas phase reaction energy, entropy, and solvation energy differences computed with the NWChem program suite.(*17*) The electronic structure calculations were carried out using density functional theory (DFT) calculations(*18*) using the 6-311++G(2d,2p) basis set(*19, 20*) and the B3LYP,(*21, 22*) and M06-2X(*23*) exchange correlation functionals. These functionals were found to produce good correlations for oxidation in our previous work,(*4*) In these calculations, the geometries of the neutral and radical cation species were optimized first and then the vibrational frequencies were determined by using a finite difference approach. The free energies in the gas phase were determined using the gas-phase optimized structures and frequencies as input for free energy formulae derived from statistical mechanics.(*24, 25*)

Solvation energies for solutes were approximated as a sum of non-covalent electrostatic, cavitation, and dispersion energies (using the same methods we used in recent work on nitro reduction of energetic compounds(*26*)). The electrostatic contributions to the solvation energies were estimated by using the self-consistent reaction field theory of Klamt and Schüürmann (COSMO),(*27*) with the cavity defined by a set of overlapping atomic spheres with radii suggested by Stefanovich and Truong(*28*) (H– 1.172 Å, C– 2.096 Å, C= 1.635 Å, O– 1.576 Å, and Cl– 1.750 Å). In addition, the solvation energy were estimated using the COSMO-SMD method implemented into NWChem by the Cramer group. The dielectric constant of water used for all of the solvation calculations was 78.4.(*27*) The cavitation and dispersion contributions to the solvation energy are less straight-forward to handle because the interactions take place at short distances, so several methods have been proposed to do this.(*29-36*) One of the simplest approaches for estimating these terms is to use empirically derived expressions that depend only on the solvent accessible surface area. In this study, the widely used formula of Sitkoff *et al.*(*33*) was used to augment the COSMO calculations,

$$\Delta G_{cav+disp} = \gamma A + b \tag{A3}$$

where ɣ and *b* are constants set to 5 cal/mol-Å^2 and 0.86 kcal mol^{-1} respectively. Sitkoff *et al.* parameterized the constants ɣ and *b* to the experimentally determined free energies of solvation of alkanes(*37*) by using a least-squares fit. The Shrake-Rupley algorithm was used to determine the solvent accessible surface areas.(*38*) The COSMO-SMD code automatically takes into account atomic sphere radii and the cavitation and dispersion contributions to the solvation energy.

The calculated free energies of reaction was converted to one-electron oxidation potentials (E_{ox}) vs. the standard hydrogen electrode (SHE) using equation A4

$$E_{ox} = -\left(\frac{-\Delta G_{ox}^{0}}{nF} + E_{H}^{0} \right) \tag{A4}$$

where *n* is the number of electrons transferred (in this case, *n* = 1), *F* is the Faraday constant (*F* = 23.061 kcal mol^{-1}), and E^0_{h} (the absolute potential of the SHE) = 98.6 kcal mol^{-1} = 4.28 V.

The EMSL Arrows scientific service was used to carry out and keep track of the large number of calculations (>500 E_{ox} calculations) used in this study. EMSL Arrows is a new scientific service (started in August 2016) that combines NWChem, SQL and NOSQL databases, email, and web APIs that simplifies molecular and materials modeling and can be used carry out and manage large numbers of complex calculations with diverse levels of theories. More information on EMSL Arrows can be found at the www.arrows.emsl.pnl.gov/api and http://www.nwchem-sw.org/index.php/EMSL_Arrows# websites.

Table A.6. Calculated potentials (E_1) for the one-electron oxidation of phenols. All data in Volts vs. SHE. The corresponding values corrected by calibration (E_{1c}) are given in **Tables A.9**.

		B3LYP		**M026X**	
No.	**Name**	**COSMO**	**SMD**	**COSMO**	**SMD**
1	phenol	1.5664	1.7382	1.7623	1.9004
2	2-methylphenol	1.469	1.6026	1.6768	1.9621
3	3-methylphenol	1.5367	1.8477	1.7058	1.9029
4	4-methylphenol	1.334	1.6386	1.5477	1.6695
5	2,4-dimethylphenol	1.2309	1.359	1.4122	1.5606
6	2,5-dimethylphenol	1.3419	1.4638	1.5271	1.6459
7	2,4,6-trimethylphenol	1.1395	1.1305	1.428	1.6335
8	2-ethylphenol	1.4533	1.4654	1.6668	1.7985
9	3-ethylphenol	1.4696	1.4907	1.7088	2.0151
10	4-ethylphenol	1.3706	1.4725	1.5898	1.7145
11	2-t-butylphenol	1.4332	1.5678	1.7157	1.7645
12	3-t-butylphenol	1.4285	1.4434	1.6637	1.969
13	4-t-butylphenol	1.3438	1.5009	1.6327	1.8703
14	2-methoxyphenol	1.257	1.2141	1.4984	1.6445
15	3-methoxyphenol	1.3152	1.2365	1.6173	1.7664
16	4-methoxyphenol	1.0197	1.176	1.2455	1.3756
17	2,6-dimethoxyphenol	1.251	1.6515	1.5693	1.7056
18	2-methoxy-4-ethylphenol	1.0576	1.1983	1.2653	1.6607
19	2-methoxy-4-formylphenol	1.3775	1.5171	1.6381	1.4337
20	2-ethoxyphenol	1.2621	1.4159	1.4971	1.8255
21	3-ethoxyphenol	1.2865	1.4346	1.5086	1.9633
22	4-ethoxyphenol	1.0132	1.1668	1.2438	1.3621
23	2-nitrophenol	2.0103	2.6041	2.2212	2.4025
24	3-nitrophenol	1.9082	2.5475	2.1526	2.3624
25	4-nitrophenol	2.1704	2.3792	2.3239	2.5027
26	2,4-dinitrophenol	2.5103	2.1743	2.7433	3.5361
27	2-methyl-4,6-dinitrophenol	2.2734	2.3786	2.5381	2.6395
28	4-methyl-2,6-dinitrophenol	2.2468	2.3852	2.337	2.481
29	2-phenylphenol	1.4069	1.7238	1.7343	2.0495
30	3-phenylphenol	1.4964	1.433	1.8019	2.1329
31	4-phenylphenol	1.2003	1.3526	1.6044	1.6618
32	2-chlorophenol	1.6829	1.8981	1.8768	1.9621
33	3-chlorophenol	1.6487	2.0187	1.9067	2.2325
34	4-chlorophenol	1.5256	1.5859	1.7491	1.7759
35	2,4-dichlorophenol	1.6297	1.8565	1.8649	2.084
36	2,4,6-trichlorophenol	1.7459	1.9267	1.9616	2.1419

37	pentachlorophenol (PCP)	1.8762	2.1674	2.1516	2.4407
38	2-hydroxyphenol	1.2572	1.4419	1.4219	1.6006
39	3-hydroxyphenol	1.3877	1.5898	1.6386	1.8304
40	4-hydroxyphenol	1.065	1.2548	1.2278	1.4097
41	2-cyanophenol	1.8109	2.0866	2.0221	2.282
42	3-cyanophenol	1.7759	2.05	2.0075	2.2788
43	4-cyanophenol	1.8133	2.0726	2.0987	2.3015
44	2-hydroxyacetophenone	1.783	1.9483	1.9862	2.4141
45	3-hydroxyacetophenone	1.7199	2.2134	1.9077	2.3993
46	4-hydroxyacetophenone	1.813	1.6931	2.0712	2.2344
47	2-hydroxybenzoic acid	1.9288	2.1219	2.09	2.7013
48	3-hydroxybenzoic acid	1.7943	1.5741	1.9654	2.2047
49	4-hydroxybenzoic acid	1.9212	2.0784	2.0872	2.7039
50	4-sulfonatophenol [a]	1.3246	2.1543	1.6096	2.4189
51	4-alanylphenol [a]	1.6921	2.0828	1.9513	2.5268
52	triclosan	1.4401	1.6444	1.6857	2.0753
53	dopamine	1.1791	1.5809	1.4789	1.7901
54	p-coumaric acid	1.4431	2.0574	1.6794	2.2915
55	bisphenol A	1.3205	1.7158	1.7178	2.2197

a) IUPAC or common name: 52, 4-hydroxybenzenesulfonate; 53, 2-amino-4’hydroxypropiophenone.

Table A.7. Calculated potentials (E_1) for the one-electron oxidation of anilines. All data in Volts vs. SHE. The corresponding values corrected by calibration (E_{1c}) are given in **Tables A.10**.

		B3LYP		M062X	
No.	**Name**	**COSMO**	**SMD**	**COSMO**	**SMD**
1	aniline	0.9805	1.0183	1.1785	1.2119
2	2-methylaniline	0.8313	0.9369	1.1173	1.1429
3	3-methylaniline	0.9317	1.0226	1.1221	1.1588
4	4-methylaniline	0.8039	0.8351	0.9915	1.0171
5	2,4-dimethylaniline	0.7374	0.7553	0.9442	0.9369
6	2,5-dimethylaniline	0.8453	0.8693	1.0487	1.1078
7	2,4,6-trimethylaniline	0.6955	0.6753	0.9006	0.8046
8	2-ethylaniline	0.917	0.9957	1.1251	1.1466
9	3-ethylaniline	0.9127	0.8801	1.1699	1.1896
10	4-ethylaniline	0.8368	0.9179	1.0404	1.0468
11	2-t-butylaniline	0.8763	0.8301	1.0055	1.1167
12	3-t-butylaniline	0.8933	0.9265	1.1725	1.2876
13	4-t-butylaniline	0.8681	0.8327	1.0465	1.0131
14	2-methoxyaniline	0.6992	0.7342	0.9036	0.936
15	3-methoxyaniline	0.8778	0.9408	1.1245	1.1797
16	4-methoxyaniline	0.5727	0.6365	0.791	0.8341
17	2,6-dimethoxyaniline	0.618	0.4657	0.834	0.8915
18	4-ethyl-2-methoxyaniline	0.5692	0.6144	0.8259	0.9248
19	2-methoxy-4-formylaniline [a]	1.1	1.14	1.1995	1.3145
20	2-ethoxyaniline	0.7372	0.6548	0.9595	1.1361
21	3-ethoxyaniline	0.8531	0.9374	1.1621	1.2069
22	4-ethoxyaniline	0.5570	0.473	0.7745	0.815
23	2-nitroaniline	1.5473	1.6337	1.6911	2.06
24	3-nitroaniline	1.3237	1.3951	1.5071	1.5805
25	4-nitroaniline	1.5719	1.6412	1.6844	1.7172
26	2,4-dinitroaniline	2.1061	2.1971	2.3424	1.9168
27	4,6-dinitro-2-methylaniline	1.5557	1.6286	1.7708	1.8659
28	2,6-dinitro-4-methylaniline	1.8677	1.9147	2.0529	2.1039
29	2-phenylaniline	0.9411	0.882	1.1762	1.2141
30	3-phenylaniline	0.9749	1.0319	1.2111	1.2448
31	4-phenylaniline	0.7967	0.951	1.1303	1.1752
32	2-chloroaniline	1.1252	1.1379	1.3386	1.3826
33	3-chloroaniline	1.1251	1.1768	1.3333	1.3793
34	4-chloroaniline	0.9966	1.0502	1.2474	1.2615
35	2,4-dichloroaniline	1.129	1.2353	1.3199	1.4207
36	2,4,6-trichloroaniline	1.2614	1.4721	1.4858	1.6926

37	pentachloroaniline	1.4367	1.6959	1.6451	1.8982
38	2-hydroxyaniline [a]	0.9115	0.7316	1.1203	1.1487
39	3-hydroxyaniline [a]	0.9359	0.8228	1.1784	1.2444
40	4-hydroxyaniline [a]	0.6033	0.4921	0.795	0.8627
41	2-cyanoaniline	1.2937	1.41	1.493	1.6046
42	3-cyanoaniline	1.175	1.2807	1.3498	1.4472
43	4-cyanoaniline	1.2328	1.3515	1.4277	1.5235
44	2-acetylaniline	1.2314	1.2774	1.4345	1.6863
45	3-acetylaniline	1.127	0.9587	1.34	1.368
46	4-acetylaniline	1.2386	1.2975	1.4659	1.4827
47	2-aminobenzoic acid	1.3466	1.3814	1.5662	1.5996
48	3-aminobenzoic acid	1.1802	0.8996	1.4011	1.4911
49	4-aminobenzoic acid	1.2981	1.3658	1.4835	1.5299
50	4-sulfonatoaniline [a]	1.0971	1.7675	1.292	1.9484
51	4-alanylaniline [a]	1.4162	1.7355	1.4955	1.3438

a) IUPAC or common name: 20, 4-amino-3-methoxybenzaldehyde; 40-42, aminophenol (2,3, and 4); 52, 4-aminobenzenesulfonate; 53, 2-amino-1-(4-aminophenyl)-1-propanone.

A.7. Computational Data Analysis

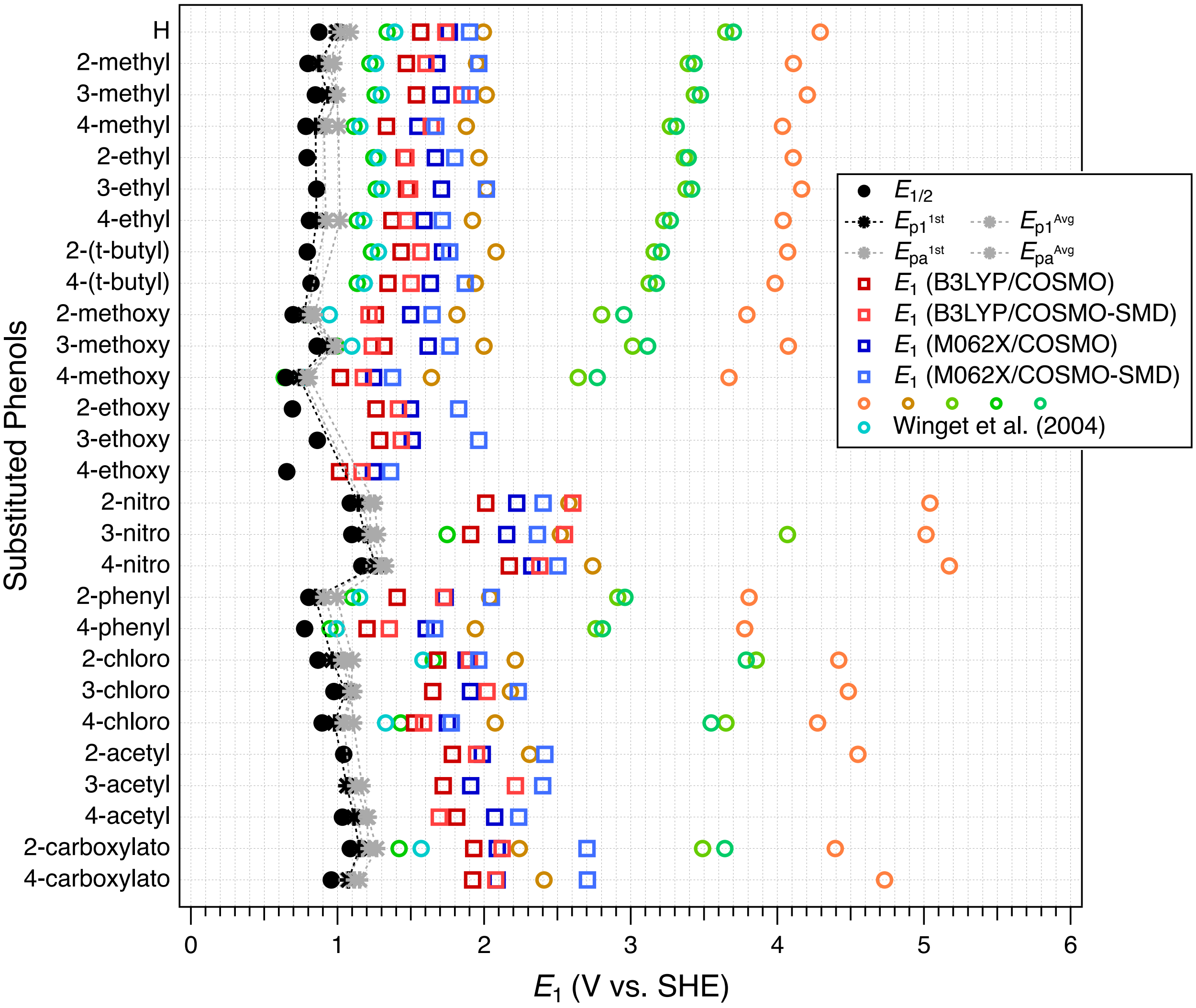

Figure A.7. Summary of calculated one-electron oxidation potentials (E_1) for phenols, including values reported in previous work and here (**Table A.6**). Color markers represent various computational conditions (squares = this study; circles = Winget et al.). Black symbols are $E_{1/2}$ from Suatoni et al. and $E_{p1}{}^{1st}$ from **Table A.4**.

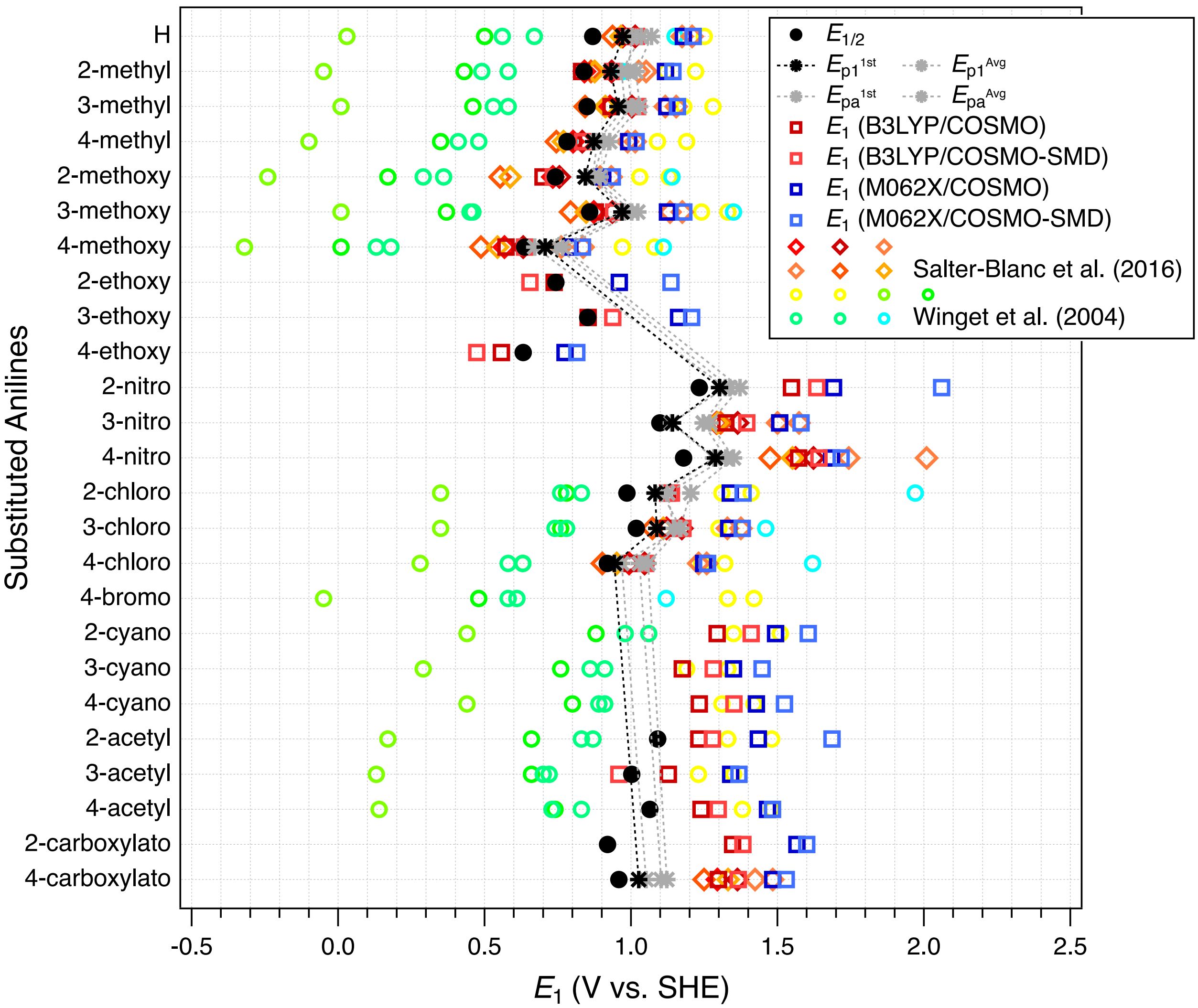

Figure A.8. Summary of calculated one-electron oxidation potentials (E_1) for anilines, including values reported in previous work and here (**Table A.7**). Color markers represent various computational conditions (squares = this study; circles = Salter et al. and Winget et al.). Black symbols are $E_{1/2}$ from Suatoni et al. and E_{p1}^{1st} from **Table A.5**.

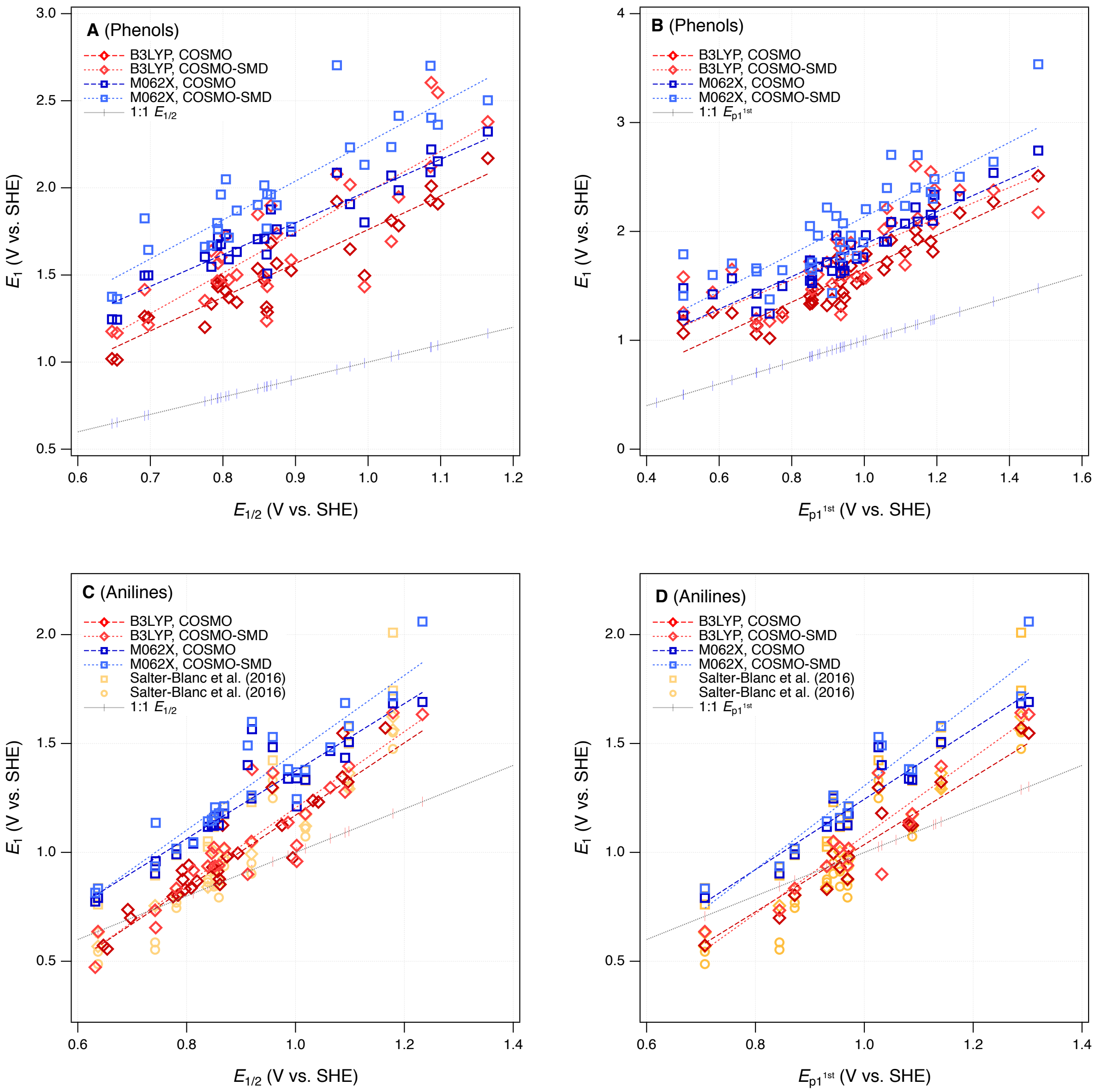

Figure A.9. Calibrations of calculated one-electron oxidation potentials (E_1) to experimental potentials from Suatoni et al. ($E_{1/2}$) and this work (E_{p1}^{1st}). Data are from **Tables A.6-A.7** and **A.4-A.5**, respectively. For the anilines, selected E_1's from our prior work are included. Markers and colors represent various conditions used in calculating E_1. The 1:1 line is based on the measured potential on the X axis.

Table A.8. Regression equations from calibrations in **Figure A.9**.

Fig	Calibration Variables	Intercept (a)	Slope (b)	r^2	s_{xy}	*n*
		Phenols				
S9a	E_1 (B3LYP/COSMO) vs. $E_{1/2}$	−0.18 ± 0.14	1.94 ± 0.16	0.855	0.113	28
S9a	E_1 (B3LYP/COSMO-SMD) vs. $E_{1/2}$	−0.35 ± 0.27	2.33 ± 0.31	0.689	0.222	28
S9a	E_1 (M062X/COSMO) vs. $E_{1/2}$	0.16 ± 0.11	1.82 ± 0.13	0.883	0.094	28
S9a	E_1 (M062X/COSMO-SMD) vs. $E_{1/2}$	0.03 ± 0.20	2.23 ± 0.23	0.783	0.167	28
S9b	E_1 (B3LYP/COSMO) vs. $E_{\mathrm{p1}}^{\mathrm{1st}}$	0.12 ± 0.11	1.54 ± 0.11	0.849	0.147	36
S9b	E_1 (B3LYP/COSMO-SMD) vs. $E_{\mathrm{p1}}^{\mathrm{1st}}$	0.42 ± 0.19	1.42 ± 0.19	0.611	0.256	36
S9b	E_1 (M062X/COSMO) vs. $E_{\mathrm{p1}}^{\mathrm{1st}}$	0.39 ± 0.10	1.49 ± 0.10	0.866	0.133	36
S9b	E_1 (M062X/COSMO-SMD) vs. $E_{\mathrm{p1}}^{\mathrm{1st}}$	0.42 ± 0.18	1.71 ± 0.18	0.716	0.244	36
		Anilines				
S9c	E_1 (B3LYP/COSMO) vs. $E_{1/2}$	−0.56 ± 0.11	1.77 ± 0.12	0.895	0.086	28
S9c	E_1 (B3LYP/COSMO-SMD) vs. $E_{1/2}$	−0.54 ± 0.15	1.75 ± 0.16	0.835	0.121	25
S9c	E_1 (M062X/COSMO) vs. $E_{1/2}$	−0.18 ± 0.12	1.55 ± 0.13	0.863	0.096	25
S9c	E_1 (M062X/COSMO-SMD) vs. $E_{1/2}$	−0.32 ± 0.14	1.78 ± 0.32	0.806	0.109	10
S9d	E_1 (B3LYP/COSMO) vs. $E_{\mathrm{p1}}^{\mathrm{1st}}$	−0.74 ± 0.15	1.78 ± 0.14	0.922	0.085	15
S9d	E_1 (B3LYP/COSMO-SMD) vs. $E_{\mathrm{p1}}^{\mathrm{1st}}$	−0.71 ± 0.19	1.79 ± 0.19	0.877	0.109	15
S9d	E_1 (M062X/COSMO) vs. $E_{\mathrm{p1}}^{\mathrm{1st}}$	−0.37 ± 0.14	1.62 ± 0.14	0.914	0.081	15
S9d	E_1 (M062X/COSMO-SMD) vs. $E_{\mathrm{p1}}^{\mathrm{1st}}$	−0.61 ± 0.181	1.92 ± 0.18	0.900	0.104	15

Intercept and slope are reported ± 1 standard deviation.
No ad hoc outliers were excluded from the regressions.

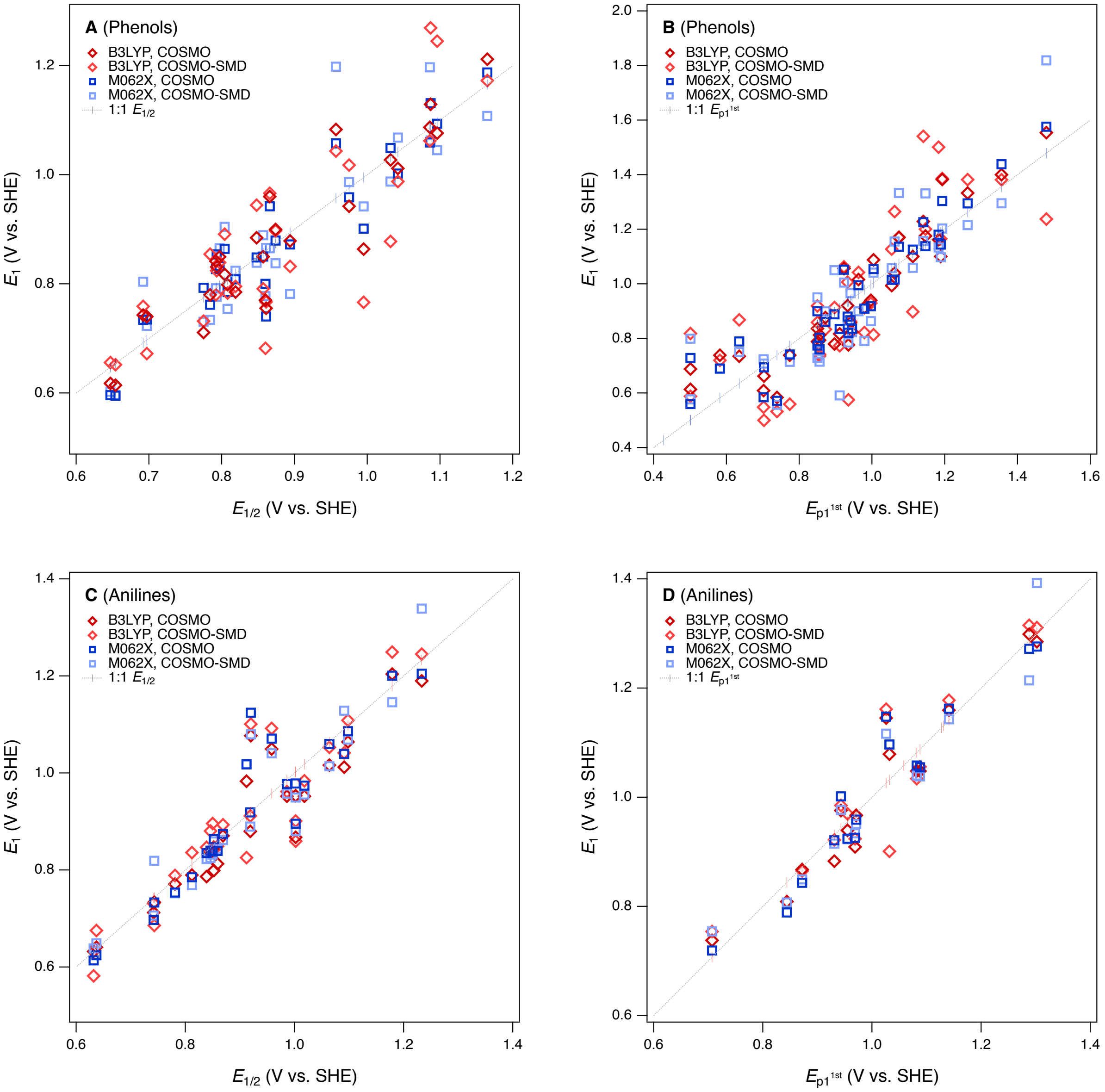

Figure A.10. Summary of calibrated calculated one-electron oxidation potentials (E_{1c}) for phenols (**Tables A.9, A.11**) and anilines (**Tables A.10, A.12**) vs. measured potentials used in the corresponding calibration. Markers and colors represent various computational conditions. The 1:1 line is based on the measured potential on the X axis.

Table A.9. Calculated potentials with correction by calibration (E_{1c}) to $E_{1/2}$ for the one-electron oxidation of phenols. Based on values of E_1 in **Table A.6**. All data in Volts vs. SHE.

		B3LYP		**M026X**	
No.	**Name**	**COSMO**	**SMD**	**COSMO**	**SMD**
1	phenol	0.900	0.897	0.879	0.838
2	2-methylphenol	0.849	0.839	0.833	0.865
3	3-methylphenol	0.884	0.944	0.848	0.839
4	4-methylphenol	0.780	0.854	0.762	0.734
5	2,4-dimethylphenol	0.727	0.734	0.688	0.685
6	2,5-dimethylphenol	0.784	0.779	0.751	0.724
7	2,4,6-trimethylphenol	0.679	0.636	0.696	0.718
8	2-ethylphenol	0.841	0.780	0.827	0.792
9	3-ethylphenol	0.850	0.791	0.850	0.889
10	4-ethylphenol	0.799	0.783	0.785	0.754
11	2-t-butylphenol	0.831	0.824	0.854	0.777
12	3-t-butylphenol	0.829	0.771	0.825	0.868
13	4-t-butylphenol	0.785	0.795	0.808	0.824
14	2-methoxyphenol	0.740	0.672	0.735	0.723
15	3-methoxyphenol	0.770	0.682	0.800	0.778
16	4-methoxyphenol	0.618	0.656	0.596	0.602
17	2,6-dimethoxyphenol	0.737	0.860	0.774	0.750
18	2-methoxy-4-ethylphenol	0.637	0.665	0.607	0.730
19	2-methoxy-4-formylphenol	0.802	0.802	0.811	0.628
20	2-ethoxyphenol	0.743	0.759	0.734	0.804
21	3-ethoxyphenol	0.755	0.767	0.740	0.866
22	4-ethoxyphenol	0.614	0.652	0.595	0.596
23	2-nitrophenol	1.129	1.269	1.131	1.063
24	3-nitrophenol	1.076	1.245	1.093	1.045
25	4-nitrophenol	1.212	1.172	1.187	1.108
26	2,4-dinitrophenol	1.387	1.084	1.417	1.571
27	2-methyl-4,6-dinitrophenol	1.265	1.172	1.305	1.169
28	4-methyl-2,6-dinitrophenol	1.251	1.175	1.194	1.098
29	2-phenylphenol	0.817	0.891	0.864	0.905
30	3-phenylphenol	0.864	0.766	0.901	0.942
31	4-phenylphenol	0.711	0.732	0.793	0.731
32	2-chlorophenol	0.960	0.966	0.942	0.865
33	3-chlorophenol	0.942	1.018	0.959	0.987
34	4-chlorophenol	0.879	0.832	0.872	0.782
35	2,4-dichlorophenol	0.932	0.948	0.936	0.920
36	2,4,6-trichlorophenol	0.992	0.978	0.989	0.946

37	pentachlorophenol (PCP)	1.060	1.081	1.093	1.080
38	2-hydroxyphenol	0.740	0.770	0.693	0.703
39	3-hydroxyphenol	0.808	0.834	0.812	0.806
40	4-hydroxyphenol	0.641	0.690	0.586	0.618
41	2-cyanophenol	1.026	1.047	1.022	1.009
42	3-cyanophenol	1.008	1.031	1.014	1.007
43	4-cyanophenol	1.027	1.041	1.064	1.018
44	2-hydroxyacetophenone	1.012	0.987	1.002	1.068
45	3-hydroxyacetophenone	0.979	1.101	0.959	1.061
46	4-hydroxyacetophenone	1.027	0.878	1.049	0.987
47	2-hydroxybenzoic acid	1.087	1.062	1.059	1.197
48	3-hydroxybenzoic acid	1.017	0.827	0.991	0.974
49	4-hydroxybenzoic acid	1.083	1.043	1.058	1.198
50	4-sulfonatophenol [a]	0.775	1.076	0.796	1.070
51	4-alanylphenol [a]	0.965	1.045	0.983	1.119
52	triclosan	0.835	0.857	0.837	0.916
53	dopamine	0.700	0.830	0.724	0.788
54	p-coumaric acid	0.836	1.034	0.834	1.013
55	bisphenol A	0.773	0.888	0.855	0.981

a) IUPAC or common name: 52, 4-hydroxybenzenesulfonate; 53, 2-amino-4’hydroxypropiophenone.

Table A.10. Calculated potentials with correction by calibration (E_{1c}) to $E_{1/2}$ for the one-electron oxidation of anilines. Based on values of E_1 in **Table A.7**. All data in Volts vs. SHE.

		B3LYP		M062X	
No.	**Name**	**COSMO**	**SMD**	**COSMO**	**SMD**
1	aniline	0.871	0.893	0.874	0.862
2	2-methylaniline	0.787	0.847	0.835	0.823
3	3-methylaniline	0.843	0.896	0.838	0.832
4	4-methylaniline	0.771	0.789	0.754	0.752
5	2,4-dimethylaniline	0.734	0.743	0.723	0.707
6	2,5-dimethylaniline	0.794	0.808	0.791	0.803
7	2,4,6-trimethylaniline	0.710	0.697	0.695	0.632
8	2-ethylaniline	0.835	0.880	0.840	0.825
9	3-ethylaniline	0.832	0.814	0.869	0.849
10	4-ethylaniline	0.790	0.836	0.785	0.769
11	2-t-butylaniline	0.812	0.786	0.763	0.808
12	3-t-butylaniline	0.822	0.841	0.870	0.904
13	4-t-butylaniline	0.807	0.787	0.789	0.750
14	2-methoxyaniline	0.712	0.731	0.697	0.706
15	3-methoxyaniline	0.813	0.849	0.839	0.843
16	4-methoxyaniline	0.641	0.675	0.624	0.649
17	2,6-dimethoxyaniline	0.666	0.578	0.652	0.681
18	4-ethyl-2-methoxyaniline	0.639	0.663	0.647	0.700
19	2-methoxy-4-formylaniline [a]	0.938	0.963	0.888	0.919
20	2-ethoxyaniline	0.734	0.686	0.733	0.819
21	3-ethoxyaniline	0.799	0.847	0.864	0.859
22	4-ethoxyaniline	0.632	0.582	0.614	0.638
23	2-nitroaniline	1.190	1.245	1.205	1.339
24	3-nitroaniline	1.064	1.109	1.086	1.069
25	4-nitroaniline	1.204	1.249	1.200	1.146
26	2,4-dinitroaniline	1.505	1.567	1.625	1.258
27	4,6-dinitro-2-methylaniline	1.195	1.242	1.256	1.230
28	2,6-dinitro-4-methylaniline	1.370	1.406	1.438	1.363
29	2-phenylaniline	0.848	0.815	0.873	0.863
30	3-phenylaniline	0.867	0.901	0.895	0.880
31	4-phenylaniline	0.767	0.855	0.843	0.841
32	2-chloroaniline	0.952	0.962	0.977	0.958
33	3-chloroaniline	0.952	0.984	0.974	0.956
34	4-chloroaniline	0.880	0.912	0.919	0.890
35	2,4-dichloroaniline	0.954	1.017	0.965	0.979
36	2,4,6-trichloroaniline	1.029	1.153	1.072	1.132

37	pentachloroaniline	1.128	1.280	1.175	1.248
38	2-hydroxyaniline [a]	0.832	0.730	0.837	0.826
39	3-hydroxyaniline [a]	0.846	0.782	0.874	0.880
40	4-hydroxyaniline [a]	0.658	0.593	0.627	0.665
41	2-cyanoaniline	1.047	1.117	1.077	1.083
42	3-cyanoaniline	0.980	1.043	0.985	0.994
43	4-cyanoaniline	1.013	1.084	1.035	1.037
44	2-acetylaniline	1.012	1.041	1.039	1.129
45	3-acetylaniline	0.953	0.859	0.978	0.949
46	4-acetylaniline	1.016	1.053	1.060	1.014
47	2-aminobenzoic acid	1.077	1.101	1.124	1.080
48	3-aminobenzoic acid	0.983	0.826	1.018	1.019
49	4-aminobenzoic acid	1.050	1.092	1.071	1.041
50	4-sulfonatoaniline [a]	0.936	1.321	0.947	1.276
51	4-alanylaniline [a]	1.116	1.303	1.079	0.936

a) IUPAC or common name: 20, 4-amino-3-methoxybenzaldehyde; 40-42, aminophenol (2,3,and 4); 52, 4-aminobenzenesulfonate; 53, 2-amino-1-(4-aminophenyl)-1-propanone.

Table A.11. Calculated potentials with correction by calibration (E_{1c}) to E_{p1} for the one-electron oxidation of phenols. Based on values of E_1 in **Table A.6**. All data in Volts vs. SHE.

		B3LYP		**M026X**	
No.	**Name**	**COSMO**	**SMD**	**COSMO**	**SMD**
1	phenol	0.940	0.929	0.918	0.864
2	2-methylphenol	0.876	0.834	0.861	0.900
3	3-methylphenol	0.920	1.007	0.880	0.865
4	4-methylphenol	0.789	0.859	0.774	0.729
5	2,4-dimethylphenol	0.721	0.662	0.683	0.665
6	2,5-dimethylphenol	0.794	0.736	0.760	0.715
7	2,4,6-trimethylphenol	0.662	0.500	0.694	0.708
8	2-ethylphenol	0.866	0.737	0.854	0.804
9	3-ethylphenol	0.877	0.755	0.882	0.931
10	4-ethylphenol	0.812	0.742	0.802	0.755
11	2-t-butylphenol	0.853	0.809	0.887	0.784
12	3-t-butylphenol	0.850	0.721	0.852	0.904
13	4-t-butylphenol	0.795	0.762	0.831	0.846
14	2-methoxyphenol	0.738	0.559	0.741	0.714
15	3-methoxyphenol	0.776	0.575	0.821	0.785
16	4-methoxyphenol	0.584	0.532	0.572	0.557
17	2,6-dimethoxyphenol	0.735	0.868	0.789	0.750
18	2-methoxy-4-ethylphenol	0.609	0.548	0.585	0.724
19	2-methoxy-4-formylphenol	0.817	0.773	0.835	0.591
20	2-ethoxyphenol	0.742	0.702	0.740	0.820
21	3-ethoxyphenol	0.758	0.715	0.748	0.900
22	4-ethoxyphenol	0.580	0.526	0.570	0.549
23	2-nitrophenol	1.229	1.541	1.226	1.157
24	3-nitrophenol	1.162	1.501	1.180	1.133
25	4-nitrophenol	1.333	1.382	1.295	1.215
26	2,4-dinitrophenol	1.554	1.237	1.576	1.819
27	2-methyl-4,6-dinitrophenol	1.400	1.382	1.438	1.295
28	4-methyl-2,6-dinitrophenol	1.383	1.386	1.304	1.203
29	2-phenylphenol	0.836	0.919	0.899	0.951
30	3-phenylphenol	0.894	0.714	0.945	0.999
31	4-phenylphenol	0.702	0.657	0.812	0.724
32	2-chlorophenol	1.016	1.042	0.995	0.900
33	3-chlorophenol	0.993	1.127	1.015	1.058
34	4-chlorophenol	0.913	0.822	0.909	0.791
35	2,4-dichlorophenol	0.981	1.013	0.987	0.971
36	2,4,6-trichlorophenol	1.057	1.062	1.052	1.005

37	pentachlorophenol (PCP)	1.141	1.232	1.179	1.179
38	2-hydroxyphenol	0.739	0.720	0.690	0.688
39	3-hydroxyphenol	0.823	0.825	0.835	0.823
40	4-hydroxyphenol	0.613	0.588	0.560	0.577
41	2-cyanophenol	1.099	1.175	1.092	1.086
42	3-cyanophenol	1.076	1.150	1.083	1.085
43	4-cyanophenol	1.100	1.165	1.144	1.098
44	2-hydroxyacetophenone	1.081	1.078	1.068	1.164
45	3-hydroxyacetophenone	1.040	1.265	1.016	1.155
46	4-hydroxyacetophenone	1.100	0.897	1.125	1.059
47	2-hydroxybenzoic acid	1.176	1.200	1.138	1.331
48	3-hydroxybenzoic acid	1.088	0.813	1.054	1.041
49	4-hydroxybenzoic acid	1.171	1.170	1.136	1.333
50	4-sulfonatophenol [a]	0.782	1.223	0.816	1.166
51	4-alanylphenol [a]	1.022	1.173	1.045	1.229
52	triclosan	0.858	0.863	0.867	0.966
53	dopamine	0.688	0.818	0.728	0.799
54	p-coumaric acid	0.860	1.155	0.863	1.092
55	bisphenol A	0.780	0.913	0.888	1.050

a) IUPAC or common name: 52, 4-hydroxybenzenesulfonate; 53, 2-amino-4’hydroxypropiophenone.

Table A.12. Calculated potentials with correction by calibration ($E_{1\mathrm{c}}$) to E_{p1} for the one-electron oxidation of anilines. Based on values of E_1 in **Table A.7**. All data in Volts vs. SHE.

		B3LYP		M062X	
No.	**Name**	**COSMO**	**SMD**	**COSMO**	**SMD**
1	aniline	0.967	0.967	0.959	0.951
2	2-methylaniline	0.883	0.922	0.921	0.915
3	3-methylaniline	0.939	0.970	0.924	0.923
4	4-methylaniline	0.868	0.865	0.843	0.849
5	2,4-dimethylaniline	0.830	0.820	0.814	0.808
6	2,5-dimethylaniline	0.891	0.884	0.879	0.897
7	2,4,6-trimethylaniline	0.807	0.776	0.787	0.739
8	2-ethylaniline	0.931	0.955	0.926	0.917
9	3-ethylaniline	0.929	0.890	0.954	0.939
10	4-ethylaniline	0.886	0.911	0.874	0.865
11	2-t-butylaniline	0.908	0.862	0.852	0.901
12	3-t-butylaniline	0.918	0.916	0.955	0.990
13	4-t-butylaniline	0.904	0.864	0.877	0.847
14	2-methoxyaniline	0.809	0.809	0.789	0.807
15	3-methoxyaniline	0.909	0.924	0.926	0.934
16	4-methoxyaniline	0.738	0.754	0.719	0.754
17	2,6-dimethoxyaniline	0.763	0.659	0.746	0.784
18	4-ethyl-2-methoxyaniline	0.736	0.742	0.741	0.801
19	2-methoxy-4-formylaniline [a]	1.034	1.035	0.972	1.004
20	2-ethoxyaniline	0.830	0.764	0.824	0.911
21	3-ethoxyaniline	0.895	0.922	0.949	0.948
22	4-ethoxyaniline	0.729	0.663	0.709	0.744
23	2-nitroaniline	1.285	1.311	1.276	1.393
24	3-nitroaniline	1.159	1.178	1.162	1.143
25	4-nitroaniline	1.299	1.315	1.272	1.214
26	2,4-dinitroaniline	1.599	1.626	1.679	1.318
27	4,6-dinitro-2-methylaniline	1.290	1.308	1.325	1.292
28	2,6-dinitro-4-methylaniline	1.465	1.468	1.500	1.415
29	2-phenylaniline	0.945	0.891	0.958	0.952
30	3-phenylaniline	0.964	0.975	0.979	0.968
31	4-phenylaniline	0.864	0.930	0.929	0.932
32	2-chloroaniline	1.048	1.034	1.058	1.040
33	3-chloroaniline	1.048	1.056	1.055	1.038
34	4-chloroaniline	0.976	0.985	1.002	0.977
35	2,4-dichloroaniline	1.050	1.088	1.047	1.060
36	2,4,6-trichloroaniline	1.124	1.221	1.149	1.201

37	pentachloroaniline	1.223	1.346	1.248	1.308
38	2-hydroxyaniline [a]	0.928	0.807	0.923	0.918
39	3-hydroxyaniline [a]	0.942	0.858	0.959	0.968
40	4-hydroxyaniline [a]	0.755	0.673	0.722	0.769
41	2-cyanoaniline	1.143	1.186	1.154	1.155
42	3-cyanoaniline	1.076	1.114	1.065	1.073
43	4-cyanoaniline	1.108	1.153	1.113	1.113
44	2-acetylaniline	1.108	1.112	1.117	1.198
45	3-acetylaniline	1.049	0.934	1.059	1.032
46	4-acetylaniline	1.112	1.123	1.137	1.092
47	2-aminobenzoic acid	1.172	1.170	1.199	1.153
48	3-aminobenzoic acid	1.079	0.901	1.097	1.096
49	4-aminobenzoic acid	1.145	1.161	1.148	1.117
50	4-sulfonatoaniline [a]	1.032	1.386	1.029	1.334
51	4-alanylaniline [a]	1.211	1.368	1.155	1.020

a) IUPAC or common name: 20, 4-amino-3-methoxybenzaldehyde; 40-42, aminophenol (2,3, and 4); 52, 4-aminobenzenesulfonate; 53, 2-amino-1-(4-aminophenyl)-1-propanone

Table A.13. Fitting coefficients and statistics for the linear regression of log k_{rel} (literature and newly collected data from Table A1) versus selected sets of oxidation potentials.

Fig	**Descriptor Variable**	**Intercept (a)**	**Slope (b)**	**r^2**	**s_{xy}**	***n***
1A	$E_{1/2}$ (from Suatoni et al.)	9.45 ± 0.56	−10.76 ± 0.60	0.903	0.468	36
5A	E_{p1st} (by SWV)	10.19 ± 0.55	−10.60 ± 0.55	0.916	0.436	36
5B	E_1 (M062X/COSMO) Anilines only	7.92 ± 0.53	−6.59 ± 0.43	0.932	0.474	19
5B	E_1 (M062X/COSMO) Phenols only	7.77 ± 0.90	−4.55 ± 0.47	0.869	0.409	16
6A	E_{1c} (M062X/COSMO vs. $E_{1/2}$)	9.08 ± 0.55	−10.29 ± 0.61	0.908	0.470	31
6B	E_{1c} (M062X/COSMO vs. E_{p1st})	10.25 ± 0.59	−10.59 ± 0.59	0.918	0.445	31

Intercept and slope are reported ± 1 standard deviation.

No ad hoc outliers were excluded from the regressions.

A.8. References (Appendix A Only)

1. A. T. Stone, Reductive dissolution of manganese(III/IV) oxides by substituted phenols. *Environ. Sci. Technol.* **21**, 979-988 (1987).

2. S. Laha, R. G. Luthy, Oxidation of aniline and other primary aromatic amines by manganese dioxide. *Environ. Sci. Technol.* **24**, 363-373 (1990).

3. J. Klausen, S. B. Haderlein, R. P. Schwarzenbach, Oxidation of substituted anilines by aqueous MnO_2: Effect of co-solutes on initial and quasi-steady-state kinetics. *Environ. Sci. Technol.* **31**, 2642-2649 (1997).

4. A. J. Salter-Blanc, E. J. Bylaska, M. A. Lyon, S. Ness, P. G. Tratnyek, Structure-activity relationships for rates of aromatic amine oxidation by manganese dioxide. *Environ. Sci. Technol.* **50**, 5094-5102 (2016).

5. J. C. Suatoni, R. E. Snyder, R. O. Clark, Voltammetric studies of phenol and aniline ring substitution. *Anal. Chem.* **33**, 1894-1897 (1961).

6. C. Li, M. Z. Hoffman, One-electron redox potentials of phenols in aqueous solution. *J. Phys. Chem. B* **103**, 6653-6656 (1999).

7. B. W. Berry, M. C. Martínez-Rivera, C. Tommos, Reversible voltammograms and a Pourbaix diagram for a protein tyrosine radical. *Proc. Natl. Acad. Sci. USA* **109**, 9739-9743 (2012).

8. R. S. Nicholson, I. Shain, Theory of stationary electrode polarography. *Anal. Chem.* **36**, 706-723 (1964).

9. R. Gulaboski, M. Lovrić, V. Mirceski, I. Bogeski, M. Hoth, A new rapid and simple method to determine the kinetics of electrode reactions of biologically relevant compounds from the half-peak width of the square-wave voltammograms. *Biophysical Chemistry* **138**, 130-137 (2008).

10. J. Osteryoung, Square wave voltammetry. *Anal. Chem.* **57**, 101A-110A (1985).

11. A. Simic, D. Manojlović, D. Šegan, M. Todorović, Electrochemical behavior and antioxidant and prooxidant activity of natural phenolics. *Molecules* **12**, 2327-2340 (2007).

12. P. R. Erickson *et al.*, Controlling factors in the rates of oxidation of anilines and phenols by triplet methylene blue in aqueous solution. *J. Phys. Chem. A* **119**, 3233-3243 (2015).

13. W. A. Arnold *et al.*, QSARs for phenols and phenolates: Oxidation potential as a predictor of reaction rate constants with photochemically produced oxidants. *Environ. Sci. Proc. Impacts* **19**, 324-338 (2017).

14. A. V. Marenich, J. Ho, M. L. Coote, C. J. Cramer, D. G. Truhlar, Computational electrochemistry: prediction of liquid-phase reduction potentials. *Phys. Chem. Chem. Phys.* **16**, 15068-15106 (2014).

15. J. Moens, P. Jaque, F. De Proft, P. Geerlings, The study of redox reactions on the basis of conceptual DFT principles: EEM and vertical quantities. *J. Phys. Chem. A* **112**, 6023-6031 (2008).

16. J. J. Guerard, J. S. Arey, Critical evaluation of implicit solvent models for predicting aqueous oxidation potentials of neutral organic compounds. *J. Chem. Theory Comput.* **9**, 5046-5058 (2013).

17. M. Valiev *et al.*, NWChem: A comprehensive and scalable open-source solution for large scale molecular simulations. *Comput. Phys. Commun.* **181**, 1477-1489 (2010).

18. W. Kohn, L. J. Sham, Self-consistent equations including exchange and correlation effects. *Phys. Rev. B* **A140**, 1133-1138 (1965).

19. T. Clark, J. Chandrasekhar, G. W. Spitznagel, P. v. R. Schleyer, Efficient diffuse function-augmented basis sets for anion calculations. III. The 3-21+G basis set for first-row elements, Li to F. *J. Comput. Chem.* **4**, 294-301 (1983).

20. R. Krishnan, J. S. Binkley, R. Seeger, J. A. Pople, Self-consistent molecular orbital methods. XX. A basis set for correlated wave functions. *J. Chem. Phys.* **72**, 650-654 (1980).

21. A. D. Becke, Density-functional thermochemistry. III. The role of exact exchange. *J. Chem. Phys.* **98**, 5648-5652 (1993).

22. C. Lee, W. Yang, R. G. Parr, Development of the Colle-Salvetti correlation-energy formula into a functional of electron density. *Phys. Rev. B* **37**, 785-789 (1988).

23. Y. Zhao, D. G. Truhlar, The M06 suite of density functionals for main group thermochemistry, thermochemical kinetics, noncovalent interactions, excited states, and transition elements: two new functionals and systematic testing of four M06-class functionals and 12 other functionals. *Theor. Chem. Acc.* **120**, 215-241 (2008).

24. G. Herzberg, *Molecular Spectra and Molecular Structure III. Electronic Spectra and Electronic Structure of Polyatomic Molecules*. (Van Nostrand, Princeton, NJ, 1966).

25. D. A. McQuarrie, Statistical Mechanics. (1973).

26. A. J. Salter-Blanc, E. J. Bylaska, H. Johnston, P. G. Tratnyek, Predicting reduction rates of energetic nitroaromatic compounds using calculated one-electron reduction potentials. *Environ. Sci. Technol.* **49**, 3778–3786 (2015).

27. A. Klamt, G. Schüürmann, COSMO: A new approach to dielectric screening in solvents with explicit expressions for the screening energy and its gradient. *J. Chem. Soc., Perkin Trans. 2*, 799-803 (1993).

28. E. V. Stefanovich, T. N. Truong, Optimized atomic radii for quantum dielectric continuum solvation models. *Chem. Phys. Lett.* **244**, 65-74 (1995).

29. R. A. Pierotti, Aqueous solutions of nonpolar gases. *J. Phys. Chem.* **69**, 281-288 (1965).

30. F. M. Floris, J. Tomasi, J. L. Pascual Ahuir, Dispersion and repulsion contributions to the solvation energy: Refinements to a simple computational model in the continuum approximation. *J. Comput. Chem.* **12**, 784-791 (1991).

31. B. Honig, K. A. Sharp, A. Yang, Macroscopic models of aqueous solutions: Biological and chemical applications. *J. Phys. Chem.* **97**, 1101-1109 (1993).

32. J. Tomasi, M. Persico, Molecular interactions in solution: An overview of methods based on continuous distributions of the solvent. *Chem. Rev.* **94**, 2027-2094 (1994).

33. D. Sitkoff, K. A. Sharp, B. Honig, Accurate calculation of hydration free energies using macroscopic solvent models. *J. Phys. Chem.* **98**, 1978-1988 (1994).

34. C. J. Cramer, D. G. Truhlar, Implicit solvation models: Equilibrium, structure, spectra, and dynamics. *Chem. Rev.* **99**, 2161-2200 (1999).

35. F. Eckert, A. Klamt, Fast solvent screening via quantum chemistry: COSMO-RS approach. *AIChE J.* **48**, 369-385 (2002).

36. M. J. Huron, P. Claverie, Calculation of the interaction energy of one molecule with its whole surrounding. II. Method of calculating electrostatic energy. *J. Phys. Chem.* **78**, 1853-1861 (1974).

37. A. Ben-Naim, Y. Marcus, Solvation thermodynamics of nonionic solutes. *J. Chem. Phys.* **81**, 2016-2027 (1984).

38. A. Shrake, J. A. Rupley, Environment and exposure to solvent of protein atoms. Lysozyme and insulin. *J. Mol. Biol.* **79**, 351-364 (1973).

Appendix B: Supporting Information to Chapter 3[5]

B.1. Properties of NOM and Model Compounds

Table B.1. Samples of natural organic matter (NOM) characterized in this study.[1]

No.	Name	Fraction [2]	Source [3]	Class [4]	Ref [5]
1	Bamboo	NOM	D. Macalady	T	
2	Bemidji	FA	G. Aiken	A	(*1, 2*)
3	Black River	NOM	D. Macalady	A	(*3*)
4	Cabbage Tree	NOM	D. Macalady	T	
5	Coal Creek	FA	G. Aiken	A	(*1, 4-7*)
6	Coal Creek	HA	G. Aiken	A	(*1, 7*)
7	Elliott Soil	FA Std II	IHSS	T	(*8-10*)
8	Elliott Soil	HA Std I	IHSS	T	(*8-13*)
9	Elliott Soil	HA Std IV	IHSS	T	(*9-13*)
10	Everglades 2BS	HPOA	USGS	A	(*6, 14, 15*)
11	Everglades F1	HPOA	USGS	A	(*6, 14-16*)
12	Everglades F1	TPIA	USGS	A	(*15*)
13	Everglades LOX8	HPOA	USGS	A	(*17*)
14	Georgetown	NOM	B. Gu	A	(*18, 19*)
15	Georgetown Carbohydrate	NOM	B. Gu	A	(*18-20*)
16	Georgetown Polyphenolic	NOM	B. Gu	A	(*18-20*)
17	Great Dismal Swamp	FA	Y. P. Chin	A	(*21, 22*)
18	Inangahua River	NOM	D. Macalady	A	(*3, 23*)
19	Kauri	NOM	D. Macalady	T	
20	Kitty Hawk	NOM	D. Macalady	A	(*24*)
21	Lake Fryxell	FA	G. Aiken	A	(*1, 4-6, 18*)
22	Leonardite[6]	HA Std I	IHSS	T	(*8, 10-12*)

---

[5] Reprint of the Supporting Information to A. S. Pavitt and P. G. Tratnyek, Electrochemical Characterization of Natural Organic Matter by Direct Voltammetry in an Aprotic Solvent, *Environ. Sci.: Proc. Impacts,* **21**, 1664-1683 (2019). Copyright 2019 The Royal Society of Chemistry.

No.	Name	Fraction [2]	Source [3]	Class [4]	Ref [5]
23	Leonardite[6]	HA Std I	IHSS	T	(*8-13*)
24	MW-6	NOM	D. Macalady	A	(*3, 22*) (*23*)
25	Nordic Reservoir	NOM	IHSS	A	(*10*)
26	North Sea	DOM	B. Koch	A	(*25*)
27	Ogeechee River	FA	G. Aiken	A	(*4, 6, 7, 15*)
28	Pacific Ocean	FA	USGS	A	(*6, 7, 14, 15*)
29	Pahokee Peat	FA Std II	IHSS	T	(*8-10, 12, 18*)
30	Pahokee Peat[6]	HA Std I	IHSS	T	(*8-13, 18*)
31	Pahokee Peat[6]	HA Std I	IHSS	T	(*8-13, 18*)
32	Pine Barrens	NOM	Y. P. Chin	T	(*18*)
33	Pony Lake	FA	Y. P. Chin	A	(*7-9, 13, 21*)
34	Prairie Pothole P8	DOM	Y. P. Chin	A	(*26*)
35	Red Tussock	NOM	D. Macalady	T	
36	Rio Negro	NOM	D. Macalady	A	(*3, 23*)
37	Schönbuch Soil Anoxic	FA	A. Kappler	T	unpublished
38	Schönbuch Soil Anoxic	HA	A. Kappler	T	unpublished
39	Schönbuch Soil H_2O Anoxic	FA	A. Kappler	T	unpublished
40	Schönbuch Soil H_2O Anoxic	HA	A. Kappler	T	unpublished
41	Schönbuch Soil H_2O Oxic	HS	A. Kappler	T	unpublished
42	Schönbuch Soil Oxic	HA	A. Kappler	T	unpublished
43	Shelter Is. San Diego	HA	J. Coates	A	(*18*)
44	Soil	HA Ref	IHSS	T	(*18-20*)
45	Sutton Stream	NOM	D. Macalady	A	
46	Suwannee River	FA Std II	IHSS	A	(*1, 4-9, 12-14, 18*)
47	Suwannee River	HA Std III	IHSS	A	(*1, 6, 8-13, 15, 27*)
48	Suwannee River[7]	NOM	J. Needoba	A	(*8, 10, 13, 23*)
49	Suwannee River[7]	NOM	IHSS	A	(*8, 10, 13, 23*)
50	Suwannee River[7]	NOM	D. Macalady	A	(*8, 10, 13, 23*)
51	Toolik Lake	FA	Y. P. Chin	A	(*21*)
52	Walnut	NOM	D. Macalady	T	(*3, 22*)
53	Waskish Peat	HA Ref	IHSS	T	(*8-10*)
54	Williams Lake	HPOA	USGS	A	(*6, 14-16*)

[1]Order is alphabetical by common name. [2]Type of fraction NOM, DOM, HA, FA, HPOA, and TPIA. [3]Source is primary supplier. [4]Class equals aquatic (A) or terrestrial (T). [5]References: primary, authoritative, or most relevant to redox. [6]Samples 22, 23 and 30, 31 were samples from the same source and the same supplier, but samples 22 and 30 were obtained at a much earlier date (ca. 2002) than 23 and 31. [7]Samples 48-50 are from the same source, but were obtained from different suppliers.

Table B.2. Model compounds.

No.	Name	CAS-RN	Source (Purity %)
1	Anthraquinone-2,6-disulfonic acid disodium salt (AQDS)	853-68-9	Combi Blocks (98)
2	5-hydroxy-1,4-naphthoquinone (juglone)	481-39-0	Acros (97)
3	2-hydroxy-1,4-naphthoquinone (lawsone)	83-72-7	Aldrich (97)
4	2-methyl-1,4-naphthoquinone (menadione)	58-27-5	Acros (98)
5	Menaquinone-4	863-61-6	Sigma-Aldrich
6	1,2-naphthoquinone-4-sulfonic acid sodium salt (o-NQS)	521-24-4	Sigma (99)
7	(E)-3-(4-hydroxyphenyl)pent-2-enedioic acid (SA)	57100-28-4	Exclusive Chemistry

Model compounds were chosen for their fast and reversible redox reactions and well documented redox potentials. Note: The following model compounds were not fully soluble: 7 in DMSO and 1, 2, 3, 4, 5 in H_2O.

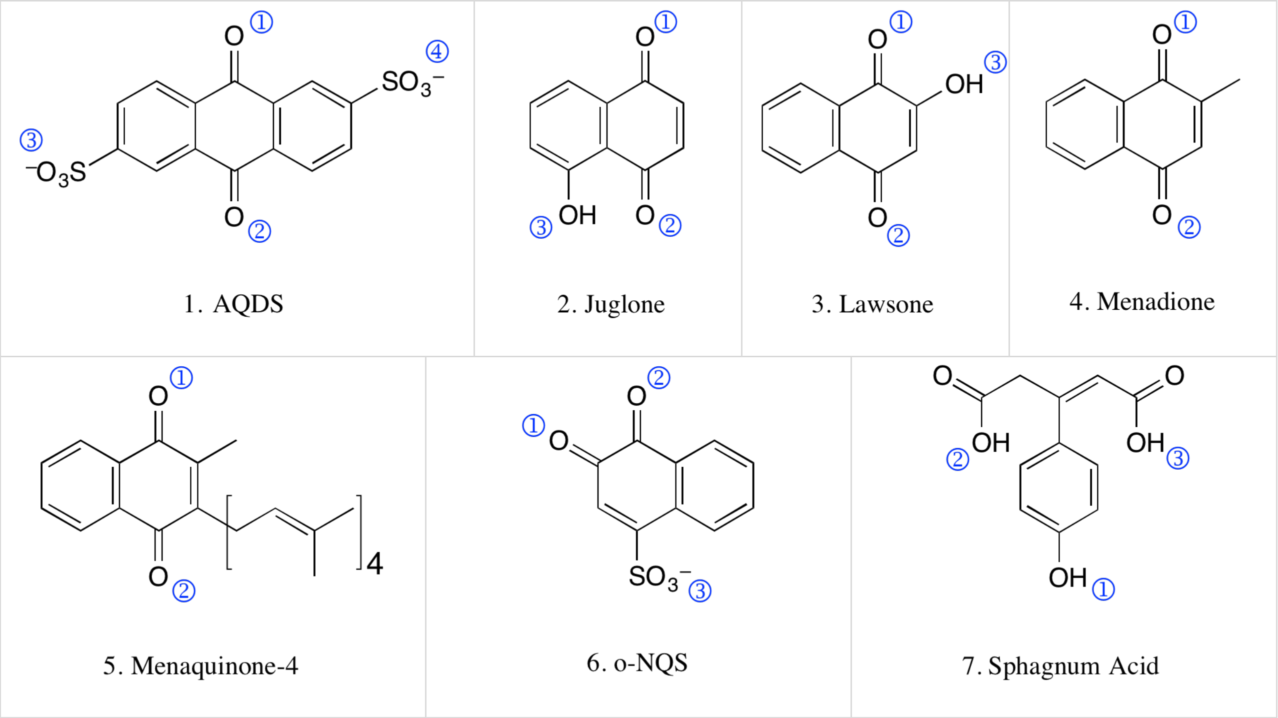

1. AQDS
2. Juglone
3. Lawsone
4. Menadione
5. Menaquinone-4
6. o-NQS
7. Sphagnum Acid

Figure B.1. Chemical structures of model compounds. Numbers refer to pKa's in **Table B.3**

Table B.3. Calculated pK_a's of model compounds in DMSO and H_2O. [1]

No.	Name	pK_a1 O/R	pK_a2 O/R	pK_a3 O/R	pK_a4 O/R
			in H_2O		
1	AQDS	/7.17	/7.17	0.59/0.73	0.59/0.73
2	Juglone	/9.78	/9.63	9.42/9.51	
3	Lawsone	/9.32	/8.66	4.58/8.66	
4	Menadione	/10.29	/9.67		
5	Menaquinone-4	/17.01	/16.82		
6	o-NQS	/8.05	/8.38	0.55/0.93	
7	Sphagnum Acid	8.46/9.77	4.35/16.07	4.33/15.65	
			in DMSO		
1	AQDS	/10.51	/10.51	4.53/4.68	4.53/4.68
2	Juglone	/17.19	/17.12	17.48/16.96	
3	Lawsone	/16.72	/18.34	8.33/16.49	
4	Menadione	/18.17	/17.32		
5	Menaquinone-4	/28.55	/28.36		
6	o-NQS	/14.62	/12.17	4.4/5.23	
7	Sphagnum Acid	14.79/16.83	10.21/26.88	8.14/26.28	

[1] Numbers on pK_a's refer to positions labelled on the structures in **Figure B.1**. O/R signifies oxidized or reduced form respectively. In cases where only the reduced form had a pK_a, a forward slash (/) precedes the value.

B.2. Peak Potentials of NOM and Model Compounds

Table B.4. Peak potentials of NOM.

No.	Name	E_{pa1}[1]	E_{pa2}[1]	E_{pc1}[2]	E_{pc2}[2]	E_{p1}[3]	E_{p2}[3]
1	Bamboo NOM	−0.887				−1.004	
2	Bemidji FA	−1.754	−0.915	−1.260		−0.810	
3	Black River NOM					−1.513	
4	Cabbage Tree NOM	−0.986				−0.803	
5	Coal Creek FA	−1.028		−1.278		−1.160	
6	Coal Creek HA			−1.353		−1.201	
7	Elliott Soil FA Std II	−0.853		−1.254		−0.824	
8	Elliott Soil HA Std I	−0.818		−1.359		−0.869	
9	Elliott Soil HA Std IV	−0.859		−1.457		−0.872	
10	Everglades 2BS HPOA	−0.851		−1.441		−0.822	
11	Everglades F1 HPOA	−0.844		−1.332		−0.820	
12	Everglades F1 TPIA	−0.820		−1.369		−0.820	

No.	**Name**	E_{pa1}^{1}	E_{pa2}^{1}	E_{pc1}^{2}	E_{pc2}^{2}	E_{p1}^{3}	E_{p2}^{3}
13	Everglades LOX8 HPOA	–0.832		–1.391		–0.819	
14	Georgetown NOM	–0.846		–1.353		–0.843	
15	Georgetown NOM CH	–0.794		–1.391		–0.780	
16	Georgetown NOM PP	–0.836		–1.345	–0.899	–0.767	
17	Great Dismal Swamp FA	–0.808		–1.357		–0.754	
18	Inangahua River NOM	–0.805				–0.797	
19	Kauri NOM	–1.002				–0.905	
20	Kitty Hawk NOM	–1.804	-0.846	–1.355		–0.834	
21	Lake Fryxell FA	–1.050		–1.258		–1.142	
22	Leonardite HA Std I	–0.863		–1.330		–0.867	
23	Leonardite HA Std I	–0.855		–1.387		–0.848	
24	MW-6 NOM	–0.838				–0.858	
25	Nordic Reservoir NOM	–0.863				–0.810	
26	North Sea DOM	–0.744		–1.443		–0.738	
27	Ogeechee River FA	–0.869		–1.266		–1.164	
28	Pacific Ocean FA	–0.846		–1.409		–0.832	
29	Pahokee Peat FA Std II	–0.857		–1.365		–0.854	
30	Pahokee Peat HA Std I	–0.863		–1.292		–0.854	
31	Pahokee Peat HA Std I	–0.863		–1.314		–0.862	
32	Pine Barrens NOM	–0.806		–1.334		–0.776	
33	Pony Lake FA	–0.955		–1.427		–0.891	
34	Prairie Pot Hole P8 DOM	–0.814		–1.381		–0.819	
35	Red Tussock NOM	–1.790	-0.844			–0.848	
36	Rio Negro NOM	–1.661	–0.857	–1.272		–0.880	
37	Schönbuch Anoxic FA	–0.867		–1.371	–0.972	–0.791	
38	Schönbuch Anoxic HA	–0.810		–1.316		–0.790	
39	Schönbuch H_2O Anoxic FA	–1.062				–0.948	
40	Schönbuch H_2O Anoxic HA	–0.830				–0.831	
41	Schönbuch H_2O Oxic HS	flat					
42	Schönbuch Oxic HA	–0.988		–1.090		-1.071	
43	Shelter Is. San Diego HA			–1.484		–0.959	
44	Soil HA Ref	–0.873		–1.286		–0.811	
45	Sutton Stream NOM	–0.832				–0.763	
46	Suwannee River FA Std II	–0.824		–1.385	–0.905	–0.817	
47	Suwannee River HA Std III			–1.395		–0.800	

No.	Name	E_{pa1}^1	E_{pa2}^1	E_{pc1}^2	E_{pc2}^2	E_{p1}^3	E_{p2}^3
48	Suwannee River NOM	−0.808		−1.349		−0.802	
49	Suwannee River NOM	−0.846		−1.363		−0.819	
50	Suwannee River NOM	−1.780	−0.859	−1.381		−0.836	
51	Toolik Lake FA	−0.824		−1.363		−0.778	
52	Walnut NOM	−0.969				−0.800	
53	Waskish Peat HA Ref	−0.798		−1.399		−0.817	
54	Williams Lake HPOA	−0.846		−1.431		−0.818	

Potentials reported in V vs Ag/Ag$^+$. Experiments performed in 0.1 M TBAFP in DMSO, with a Pt working electrode. NOM concentrations were 1.0 mg/mL except where NOM did not fully dissolve in DMSO. Scan rate was 25 mV s^{-1}, step size 2 mV, and amplitude 25 mV. $^1E_{pa}$ and $^2E_{pc}$ denote SCV anodic and cathodic peak respectively. ^3E_p denotes SWV peaks.

Table B.5. Peak potentials of model compounds.

No.	Name	E_{pa1}^1	E_{pa2}^1	E_{pc1}^2	E_{pc2}^2	E_{p1}^3	E_{p2}^3
in H_2O							
1	AQDS	−0.331		−0.459		−0.421	
2	Juglone	−0.177		−0.213		−0.215	
3	Lawsone	−0.274		−0.441		−0.308	
4	Menadione	−0.128		−0.302		−0.326	−0.131
5	Menaquinone-4	−0.282		−0.823	−0.431	−0.836	−0.315
6	o-NQS	0.169		−0.095		−0.093	0.145
7	Sphagnum acid	0.678				0.625	
in DMSO							
1	AQDS	−1.673	−1.010	−1.786	−1.078	−1.720	−1.045
2	Juglone	−1.238	−0.633	−1.462	−0.711	−1.307	−0.672
3	Lawsone	−1.585		−1.786	−0.828	−1.681	−0.847
4	Menadione	−1.601	−0.887	−1.849	−0.961	−1.674	−0.921
5	Menaquinone-4	−1.681	−0.953	−1.923	−1.026	−1.799	−0.988
6	o-NQS	−1.300	−0.649	−1.397	−0.732	−1.339	−0.690
7	Sphagnum acid	−1.752	−0.766	−1.486		−0.825	

Potentials reported in V vs Ag/AgCl for H2O and Ag/Ag+ for DMSO. Potentials reported in H2O are averages of all runs using NOVA 2.1 software, in DMSO values are the best run using Igor Multipeak fit. Aqueous runs were performed in a 0.1 M KCl/ 0.1 M Phosphate buffer (pH 7), using a Pt and GC working electrode. Aprotic runs were performed in 0.1 M TBAFP using a Pt working electrode. 1Epa and 2Epc denotes anodic and cathodic potentials respectively of staircase cyclic voltammograms and 3Ep denotes peak potentials of square-wave voltammograms. Scan rate was 25 mV s-1, step size 2 mV, and amplitude 25 mV.

B.3. Control Experiments (Solvent and Mediators)

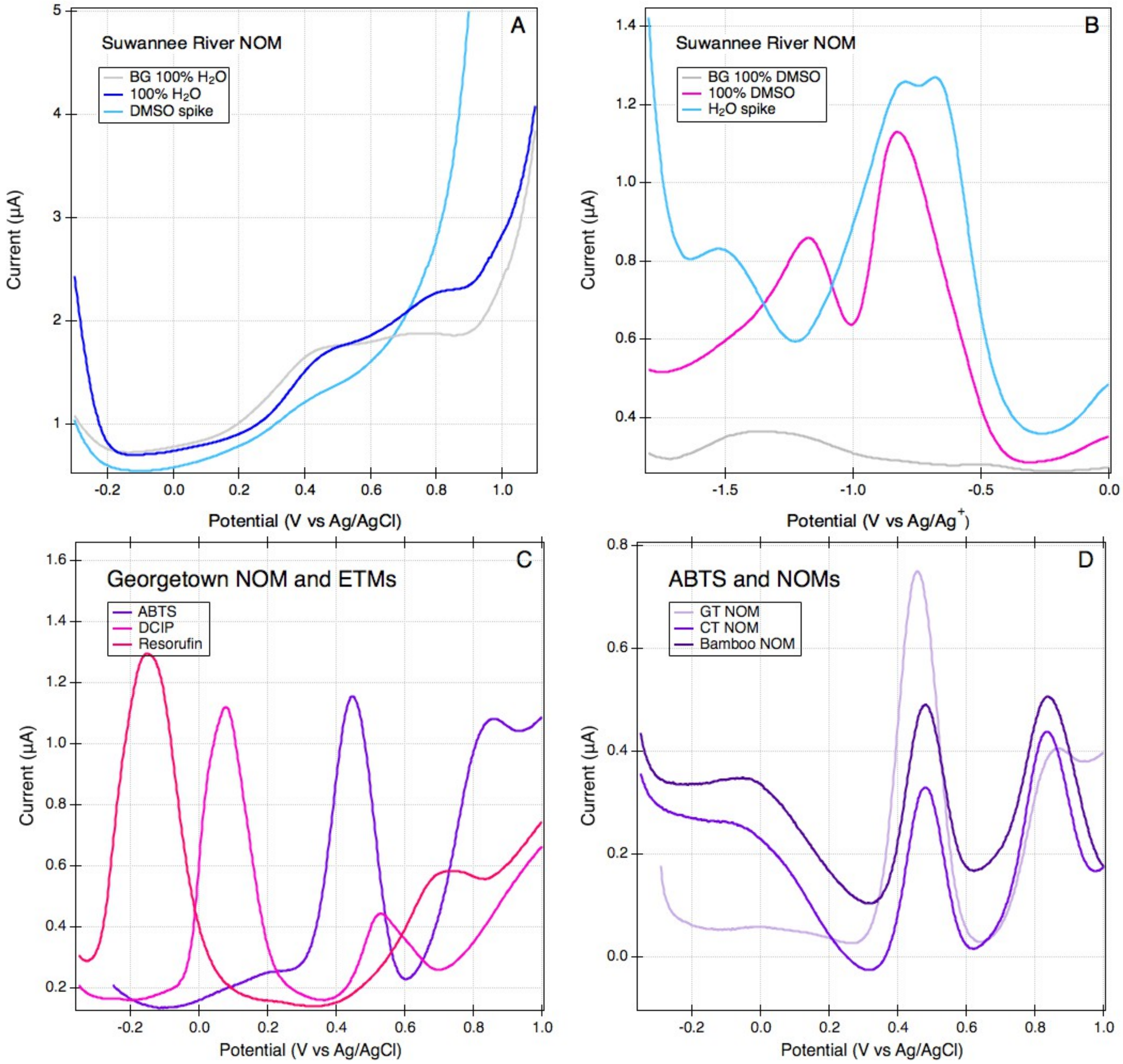

Figure B.2. SWVs of control experiments. All SWVs at a scan rate of 25 mV/s, 2 mV step size, 25 mV amplitude, in 0.1 M KCl and phosphate buffer (pH 7.0) using a GC WE. (A) Suwannee River NOM in 100% H2O (dark blue), 85% H2O/15% DMSO (light blue), background (BG) (grey). (B) Suwannee River NOM in 100% DMSO (pink), 85% DMSO/15% H2O (light blue), BG (grey). (C) SWV of Georgetown NOM using three mediators: ABTS (purple), DCIP (pink), and resorufin (red). (D) SWV of one mediator (ABTS) and three NOMs: Georgetown (light purple), Cabbage Tree (medium purple), and Bamboo (dark purple).

B.4. SCVs and SWVs of Model Compounds

Caption for figures on pages 154-156

Figure B.3. Primary SCV (left) and SWV (right) data for model compounds. Each row represents a model compound sample as listed in Table S2. Varying scan rate identified by i, ii, and iii.

Conditions: 1.5 mM of model compound in 0.1 M TBAFP in DMSO, 1.6 mm Pt working electrode, Pt coil counter electrode and a Ag/Ag+ reference electrode filled with 0.1 M TBAFP and 0.005 M AgNO3 in DMSO. Scan rate: SWVi and SCVi 25 mV s-1, SWVii 125 mV s-1, SWViii 225 mV s-1. Step size 2 mV, amplitude 25 mV.

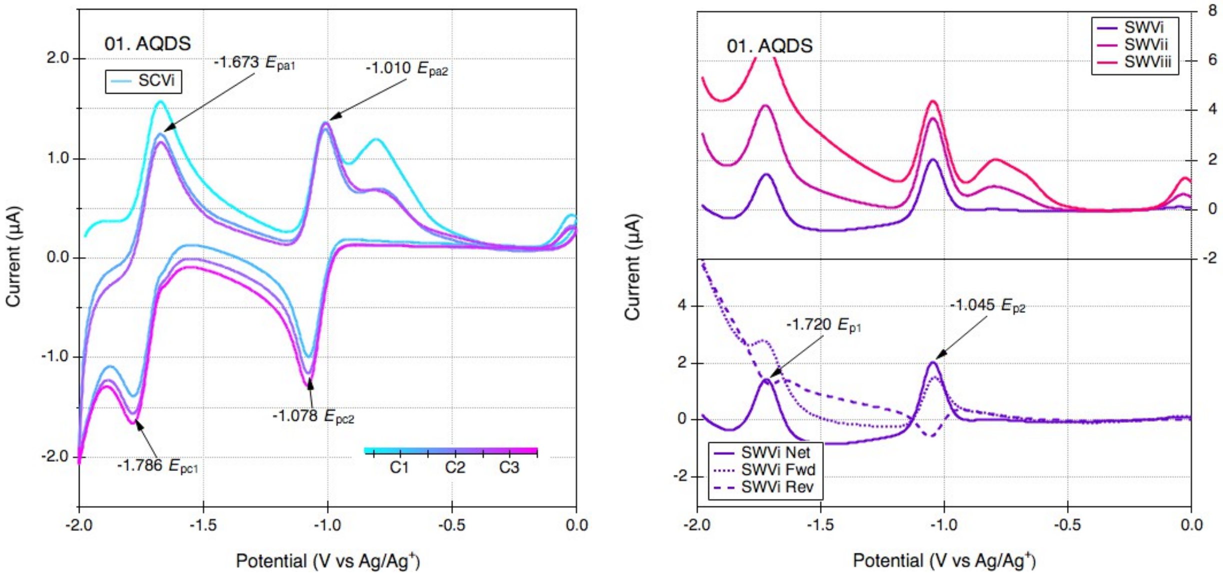

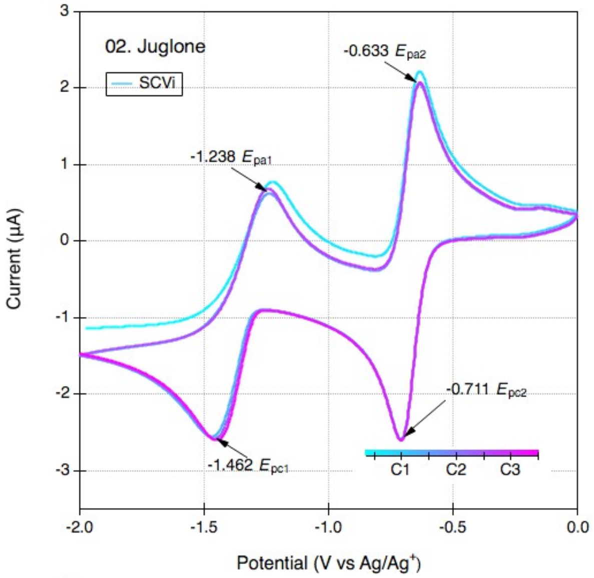
02. Juglone
SCVi
-0.633 E_{pa2}
-1.238 E_{pa1}
-0.711 E_{pc2}
-1.462 E_{pc1}
C1
C2
C3
Current (μA)
Potential (V vs Ag/Ag$^+$)

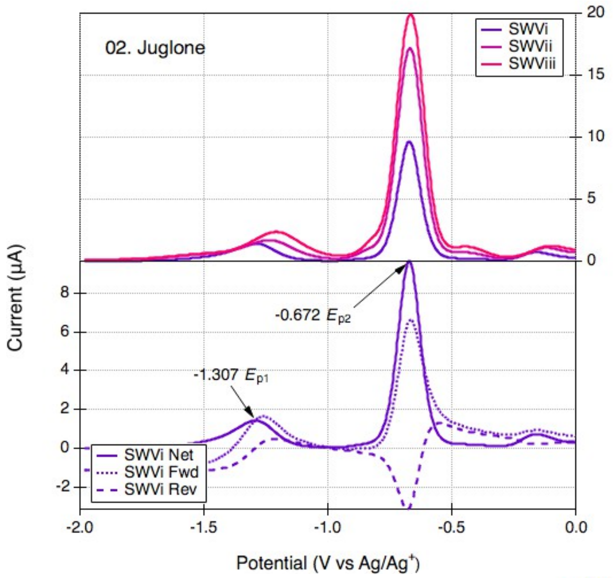
02. Juglone
SWVi
SWVii
SWViii
-0.672 E_{p2}
-1.307 E_{p1}
SWVi Net
SWVi Fwd
SWVi Rev
Current (μA)
Potential (V vs Ag/Ag$^+$)

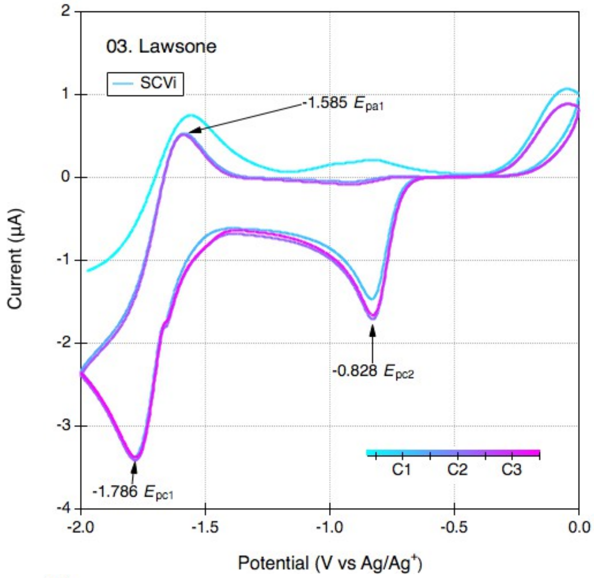
03. Lawsone
SCVi
-1.585 E_{pa1}
-0.828 E_{pc2}
-1.786 E_{pc1}
C1
C2
C3
Current (μA)
Potential (V vs Ag/Ag$^+$)

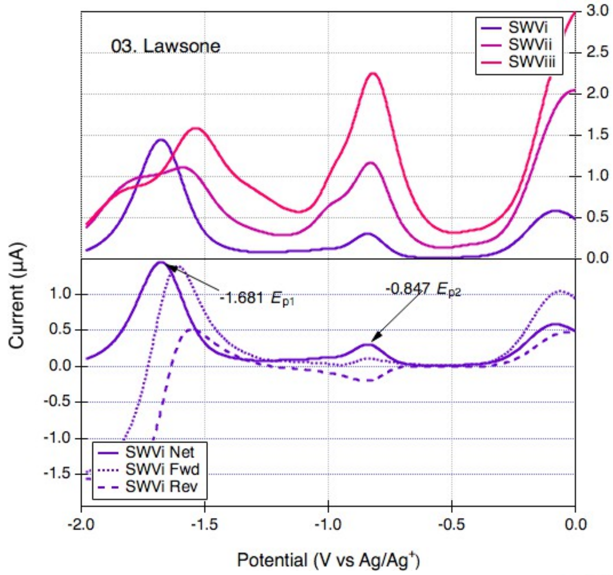
03. Lawsone
SWVi
SWVii
SWViii
-1.681 E_{p1}
-0.847 E_{p2}
SWVi Net
SWVi Fwd
SWVi Rev
Current (μA)
Potential (V vs Ag/Ag$^+$)

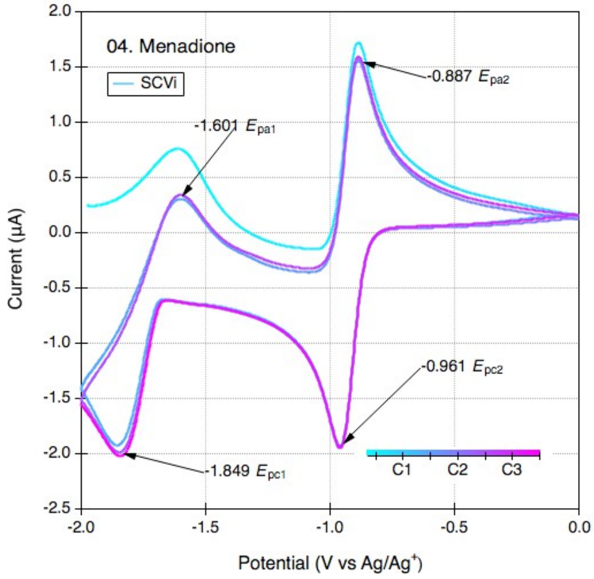
04. Menadione
SCVi
-0.887 E_{pa2}
-1.601 E_{pa1}
-0.961 E_{pc2}
-1.849 E_{pc1}
C1
C2
C3
Current (μA)
Potential (V vs Ag/Ag$^+$)

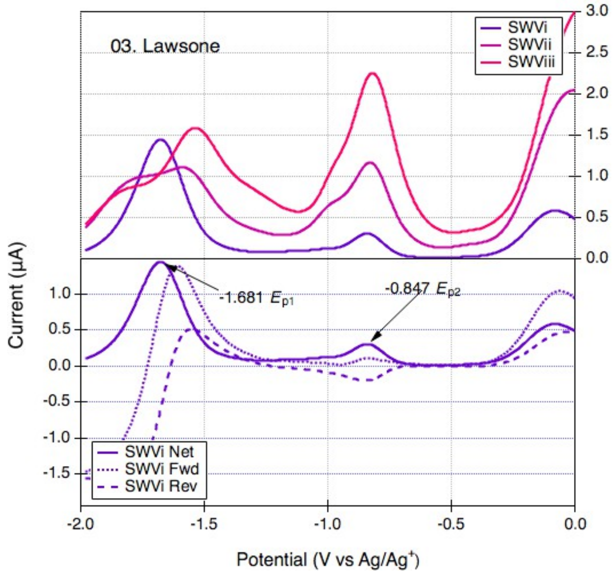
03. Lawsone
SWVi
SWVii
SWViii
-1.681 E_{p1}
-0.847 E_{p2}
SWVi Net
SWVi Fwd
SWVi Rev
Current (μA)
Potential (V vs Ag/Ag$^+$)

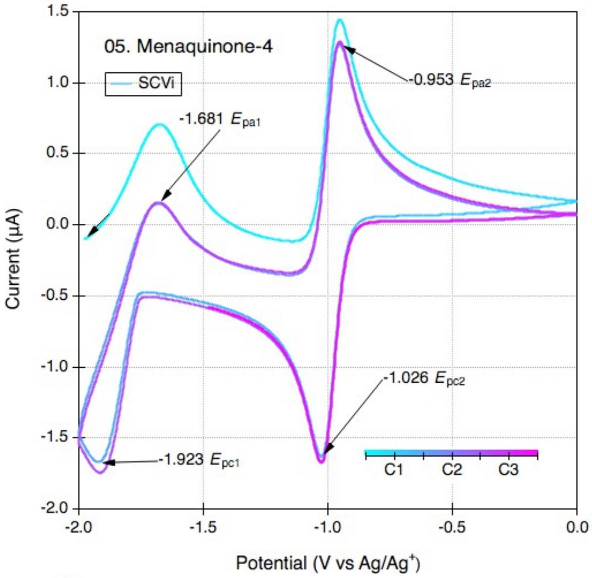
05. Menaquinone-4
SCVi
-1.681 E_{pa1}
-0.953 E_{pa2}
-1.026 E_{pc2}
-1.923 E_{pc1}
C1
C2
C3
Current (µA)
Potential (V vs Ag/Ag$^+$)
1.5
1.0
0.5
0.0
-0.5
-1.0
-1.5
-2.0
-2.0
-1.5
-1.0
-0.5
0.0

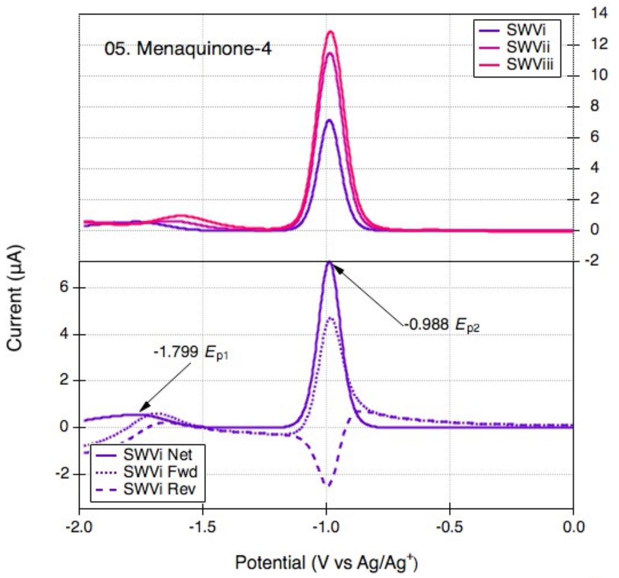
05. Menaquinone-4
SWVi
SWVii
SWViii
-0.988 E_{p2}
-1.799 E_{p1}
SWVi Net
SWVi Fwd
SWVi Rev
Current (µA)
Potential (V vs Ag/Ag$^+$)
14
12
10
8
6
4
2
0
-2
6
4
2
0
-2
-2.0
-1.5
-1.0
-0.5
0.0

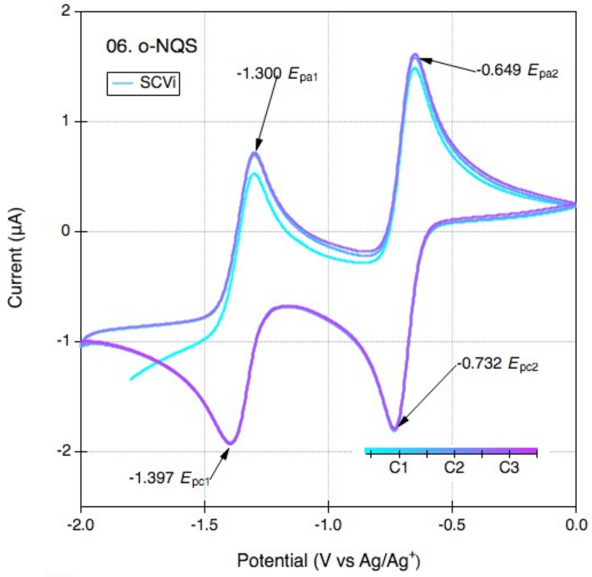
06. o-NQS
SCVi
-1.300 E_{pa1}
-0.649 E_{pa2}
-0.732 E_{pc2}
-1.397 E_{pc1}
C1
C2
C3
Current (µA)
Potential (V vs Ag/Ag$^+$)
2
1
0
-1
-2
-2.0
-1.5
-1.0
-0.5
0.0

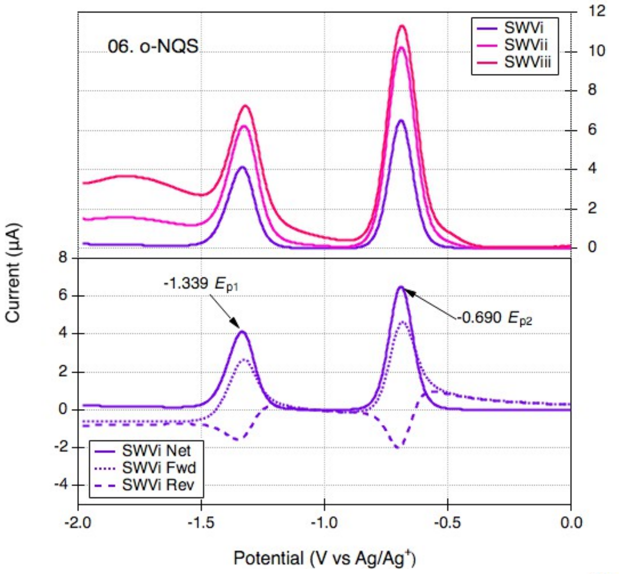
06. o-NQS
SWVi
SWVii
SWViii
-1.339 E_{p1}
-0.690 E_{p2}
SWVi Net
SWVi Fwd
SWVi Rev
Current (µA)
Potential (V vs Ag/Ag$^+$)
12
10
8
6
4
2
0
8
6
4
2
0
-2
-4
-2.0
-1.5
-1.0
-0.5
0.0

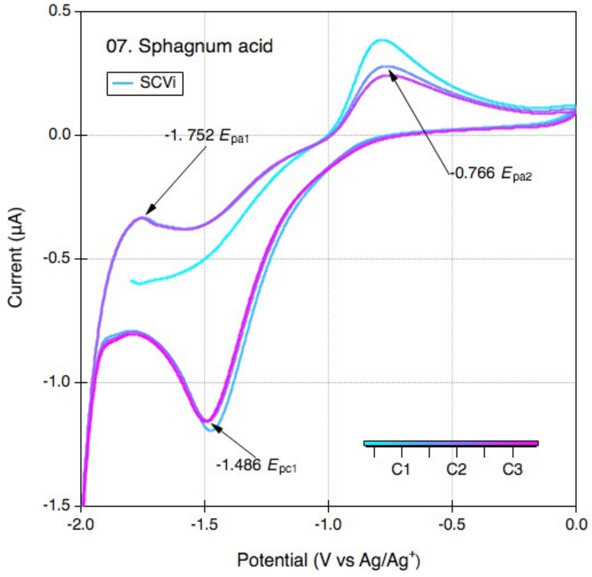
07. Sphagnum acid
SCVi
-1. 752 E_{pa1}
-0.766 E_{pa2}
-1.486 E_{pc1}
C1
C2
C3
Current (µA)
Potential (V vs Ag/Ag$^+$)
0.5
0.0
-0.5
-1.0
-1.5
-2.0
-1.5
-1.0
-0.5
0.0

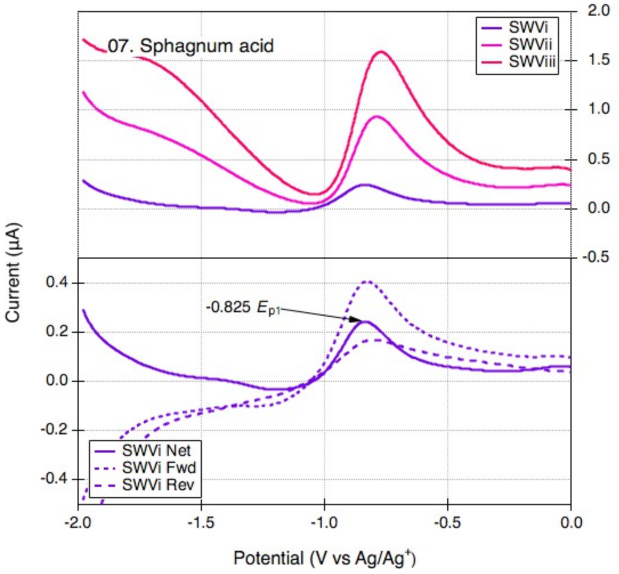
07. Sphagnum acid
SWVi
SWVii
SWViii
-0.825 E_{p1}
SWVi Net
SWVi Fwd
SWVi Rev
Current (µA)
Potential (V vs Ag/Ag$^+$)
2.0
1.5
1.0
0.5
0.0
-0.5
0.4
0.2
0.0
-0.2
-0.4
-2.0
-1.5
-1.0
-0.5
0.0

B.5. SCVs and SWVs of NOM

Caption for figures on pages 157-175

Figure B.4. Primary SCV (left) and SWV (right) data for NOMs. Each row represents a NOM sample as listed in Table S1. Varying scan rate identified by i, ii, and iii.

Conditions: 1.0 mg/mL (except for HS that did not fully dissociate in DMSO) of HS in 0.1 M TBAFP in DMSO, 1.6 mm Pt working electrode, Pt coil counter electrode and a Ag/Ag+ reference electrode filled with 0.1 M TBAFP and 0.005 M AgNO3 in DMSO. Scan rate: SWVi and SCVi 25 mV s-1, SWVii 125 mV s-1, SWViii 225 mV s-1. Step size 2 mV, amplitude 25 mV.

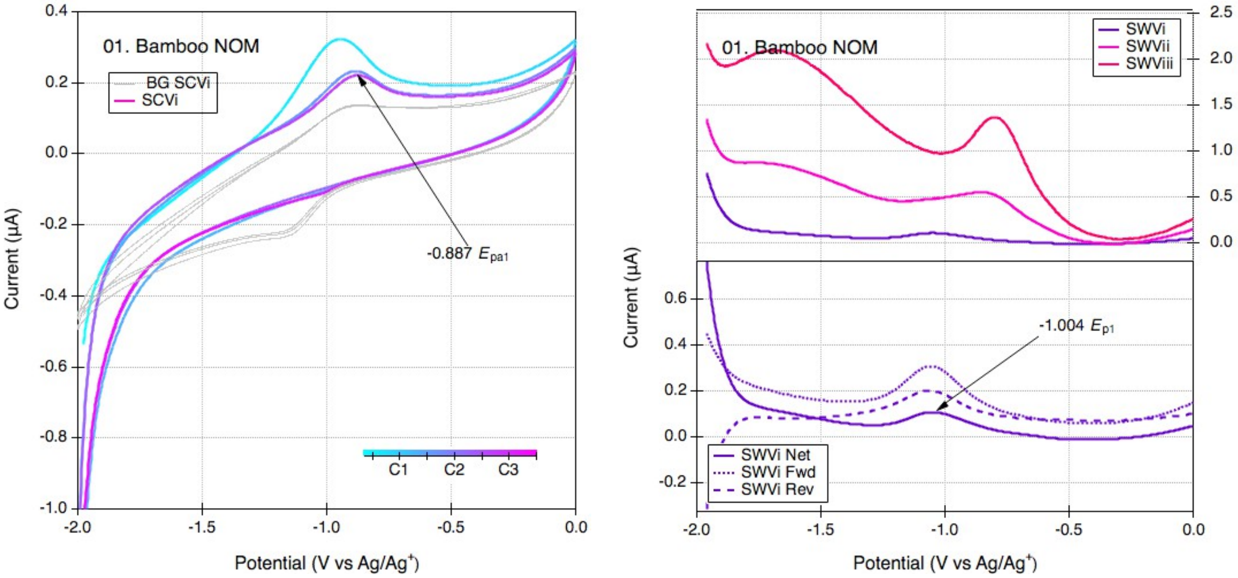

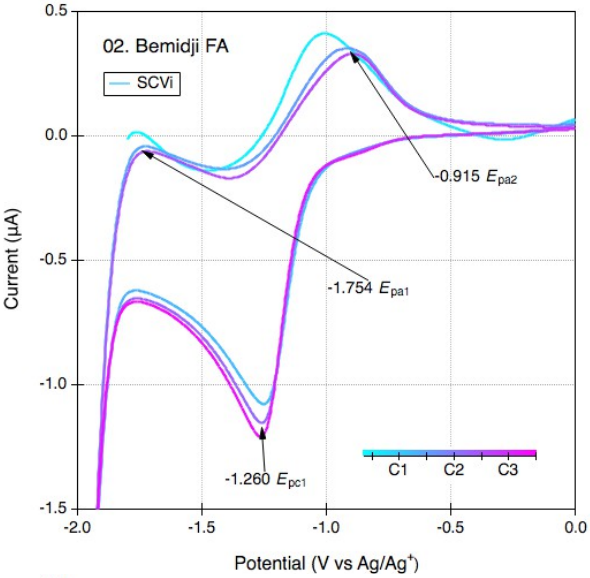
02. Bemidji FA
SCVi
-0.915 E_{pa2}
-1.754 E_{pa1}
-1.260 E_{pc1}
C1
C2
C3
Current (µA)
Potential (V vs Ag/Ag$^+$)
0.5
0.0
-0.5
-1.0
-1.5
-2.0
-1.5
-1.0
-0.5
0.0

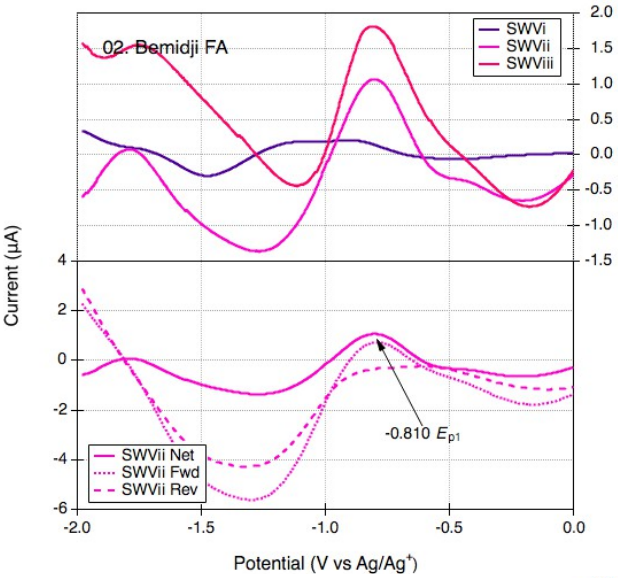
02. Bemidji FA
SWVi
SWVii
SWViii
SWVii Net
SWVii Fwd
SWVii Rev
-0.810 E_{p1}
Current (µA)
Potential (V vs Ag/Ag$^+$)
2.0
1.5
1.0
0.5
0.0
-0.5
-1.0
-1.5
4
2
0
-2
-4
-6
-2.0
-1.5
-1.0
-0.5
0.0

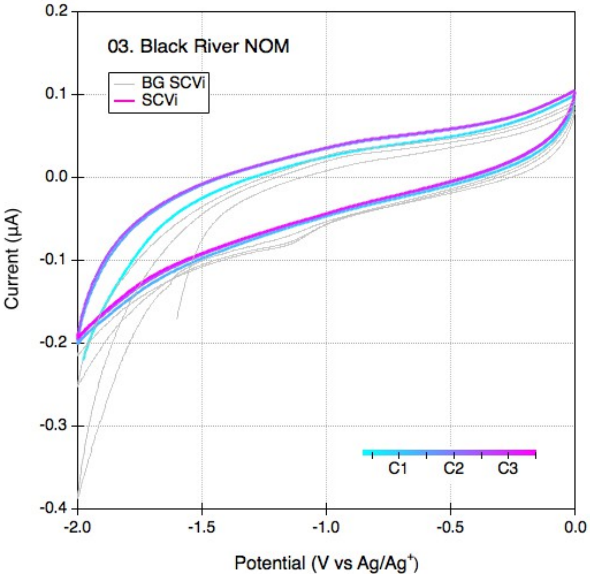
03. Black River NOM
BG SCVi
SCVi
C1
C2
C3
Current (µA)
Potential (V vs Ag/Ag$^+$)
0.2
0.1
0.0
-0.1
-0.2
-0.3
-0.4
-2.0
-1.5
-1.0
-0.5
0.0

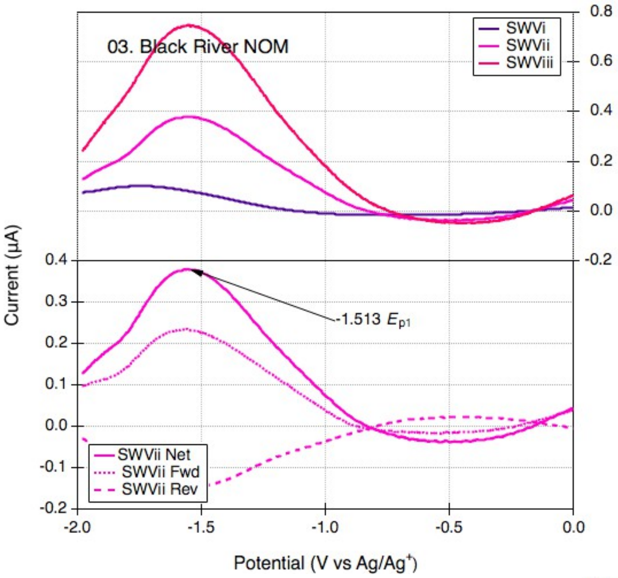
03. Black River NOM
SWVi
SWVii
SWViii
SWVii Net
SWVii Fwd
SWVii Rev
-1.513 E_{p1}
Current (µA)
Potential (V vs Ag/Ag$^+$)
0.8
0.6
0.4
0.2
0.0
-0.2
0.4
0.3
0.2
0.1
0.0
-0.1
-0.2
-2.0
-1.5
-1.0
-0.5
0.0

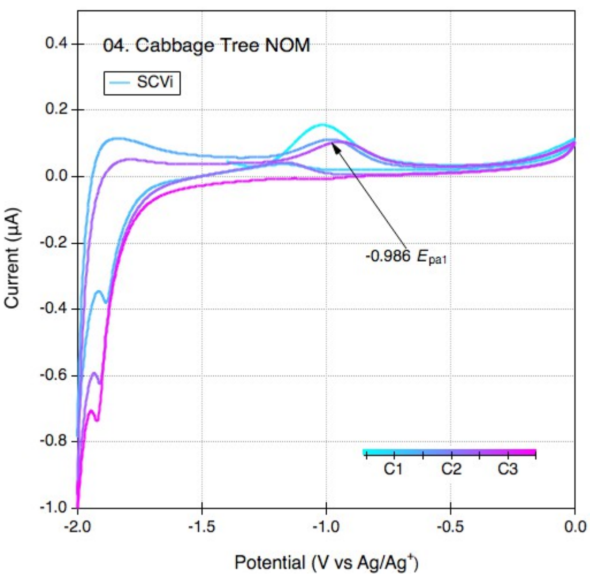
04. Cabbage Tree NOM
SCVi
-0.986 E_{pa1}
C1
C2
C3
Current (µA)
Potential (V vs Ag/Ag$^+$)
0.4
0.2
0.0
-0.2
-0.4
-0.6
-0.8
-1.0
-2.0
-1.5
-1.0
-0.5
0.0

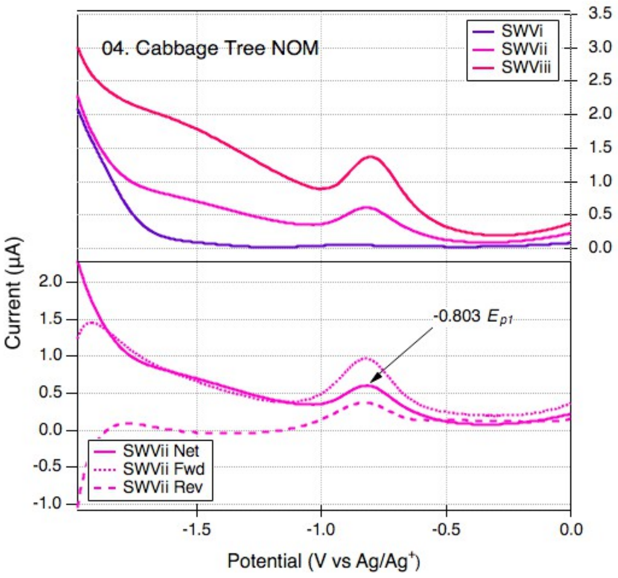
04. Cabbage Tree NOM
SWVi
SWVii
SWViii
SWVii Net
SWVii Fwd
SWVii Rev
-0.803 E_{p1}
Current (µA)
Potential (V vs Ag/Ag$^+$)
3.5
3.0
2.5
2.0
1.5
1.0
0.5
0.0
2.0
1.5
1.0
0.5
0.0
-0.5
-1.0
-1.5
-1.0
-0.5
0.0

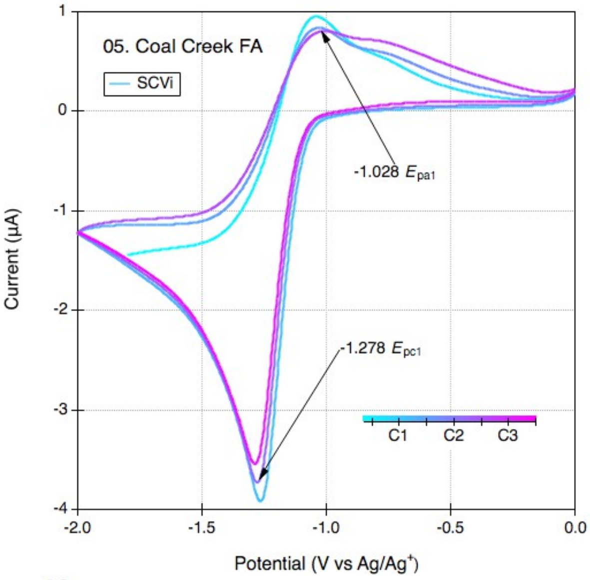
05. Coal Creek FA
SCVi
-1.028 E_{pa1}
-1.278 E_{pc1}
C1
C2
C3
Current (μA)
1
0
-1
-2
-3
-4
-2.0
-1.5
-1.0
-0.5
0.0
Potential (V vs Ag/Ag⁺)

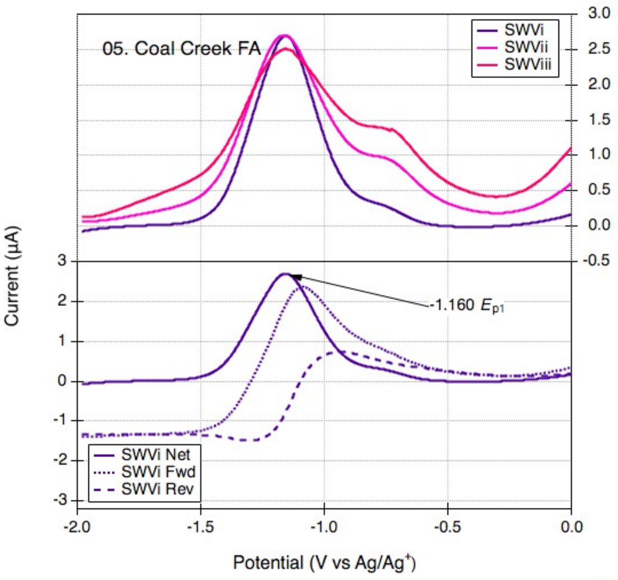
05. Coal Creek FA
SWVi
SWVii
SWViii
3.0
2.5
2.0
1.5
1.0
0.5
0.0
-0.5
-1.160 E_{p1}
SWVi Net
SWVi Fwd
SWVi Rev
Current (μA)
3
2
1
0
-1
-2
-3
-2.0
-1.5
-1.0
-0.5
0.0
Potential (V vs Ag/Ag⁺)

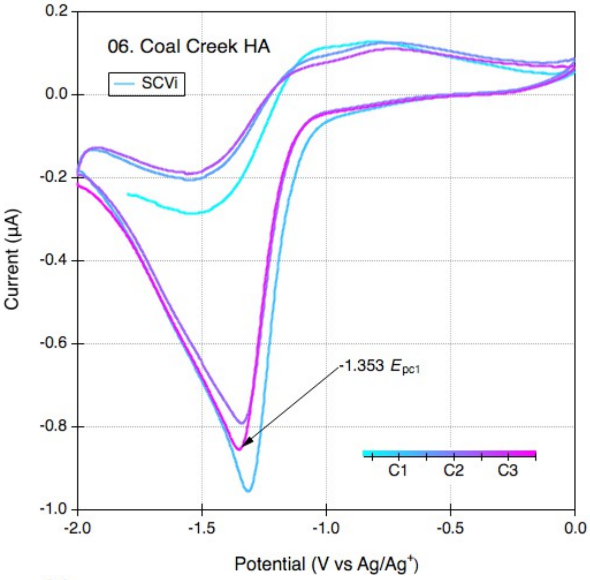
06. Coal Creek HA
SCVi
-1.353 E_{pc1}
C1
C2
C3
Current (μA)
0.2
0.0
-0.2
-0.4
-0.6
-0.8
-1.0
-2.0
-1.5
-1.0
-0.5
0.0
Potential (V vs Ag/Ag⁺)

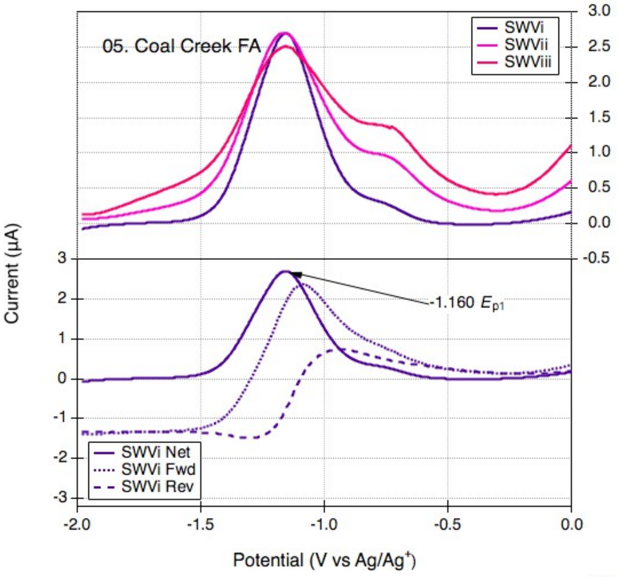
05. Coal Creek FA
SWVi
SWVii
SWViii
3.0
2.5
2.0
1.5
1.0
0.5
0.0
-0.5
-1.160 E_{p1}
SWVi Net
SWVi Fwd
SWVi Rev
Current (μA)
3
2
1
0
-1
-2
-3
-2.0
-1.5
-1.0
-0.5
0.0
Potential (V vs Ag/Ag⁺)

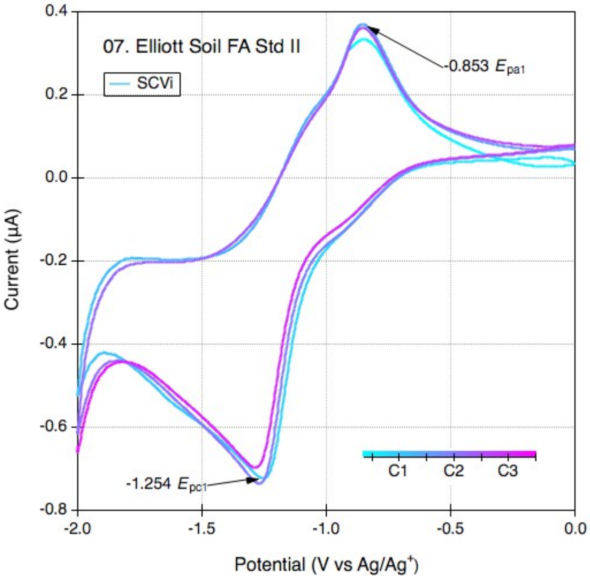
07. Elliott Soil FA Std II
SCVi
-0.853 E_{pa1}
-1.254 E_{pc1}
C1
C2
C3
Current (μA)
0.4
0.2
0.0
-0.2
-0.4
-0.6
-0.8
-2.0
-1.5
-1.0
-0.5
0.0
Potential (V vs Ag/Ag⁺)

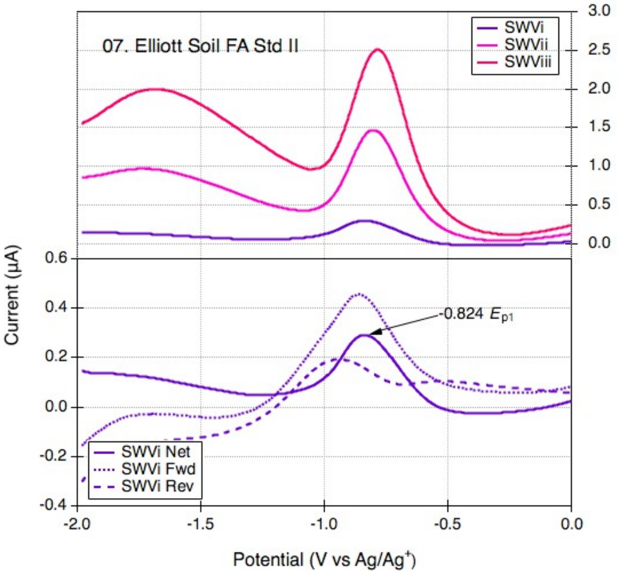
07. Elliott Soil FA Std II
SWVi
SWVii
SWViii
3.0
2.5
2.0
1.5
1.0
0.5
0.0
-0.824 E_{p1}
SWVi Net
SWVi Fwd
SWVi Rev
Current (μA)
0.6
0.4
0.2
0.0
-0.2
-0.4
-2.0
-1.5
-1.0
-0.5
0.0
Potential (V vs Ag/Ag⁺)

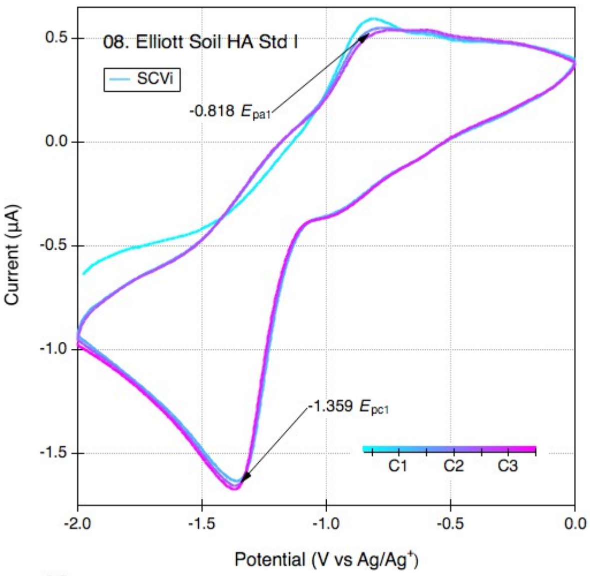
08. Elliott Soil HA Std I
SCVi
-0.818 E_{pa1}
-1.359 E_{pc1}
C1
C2
C3
Current (μA)
Potential (V vs Ag/Ag$^+$)
0.5
0.0
-0.5
-1.0
-1.5
-2.0
-1.5
-1.0
-0.5
0.0

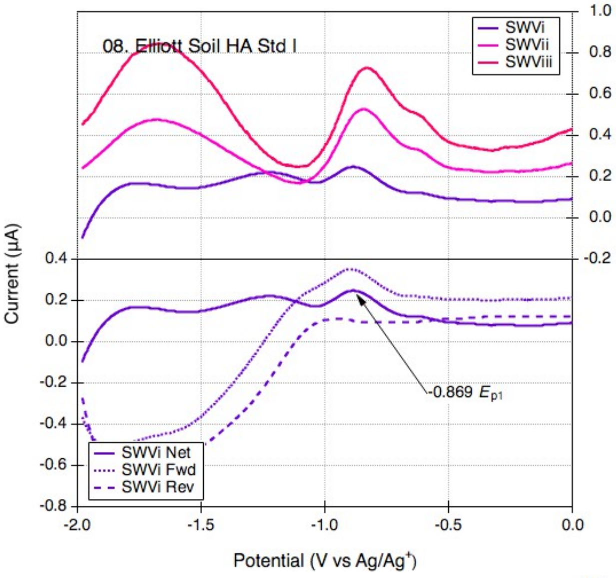
08. Elliott Soil HA Std I
SWVi
SWVii
SWViii
-0.869 E_{p1}
SWVi Net
SWVi Fwd
SWVi Rev
Current (μA)
Potential (V vs Ag/Ag$^+$)
1.0
0.8
0.6
0.4
0.2
0.0
-0.2
0.4
0.2
0.0
-0.2
-0.4
-0.6
-0.8
-2.0
-1.5
-1.0
-0.5
0.0

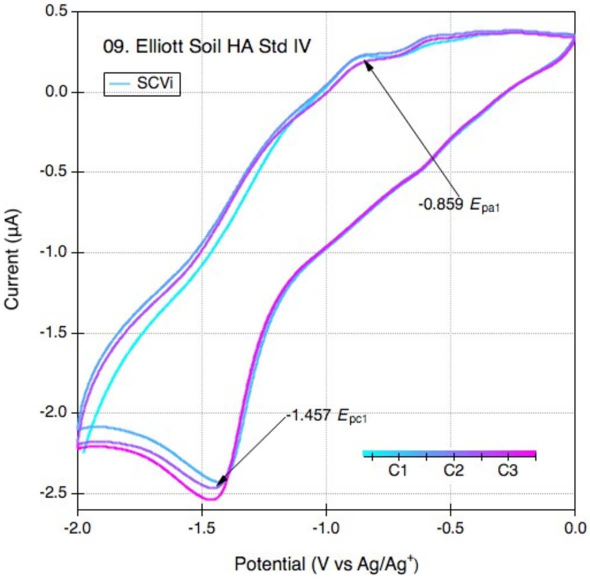
09. Elliott Soil HA Std IV
SCVi
-0.859 E_{pa1}
-1.457 E_{pc1}
C1
C2
C3
Current (μA)
Potential (V vs Ag/Ag$^+$)
0.5
0.0
-0.5
-1.0
-1.5
-2.0
-2.5
-2.0
-1.5
-1.0
-0.5
0.0

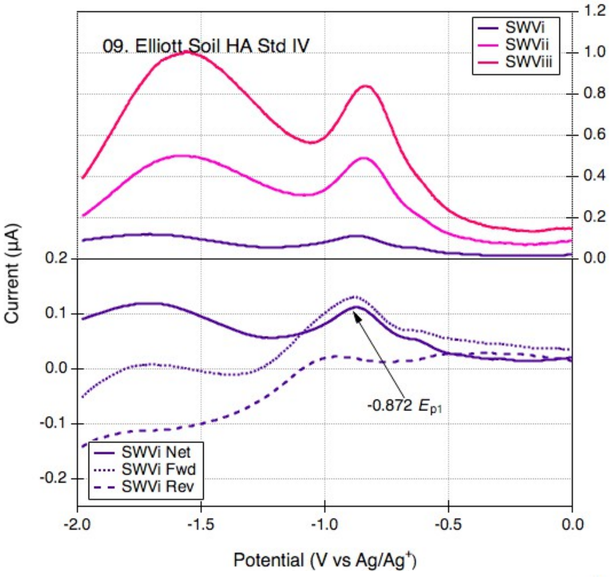
09. Elliott Soil HA Std IV
SWVi
SWVii
SWViii
-0.872 E_{p1}
SWVi Net
SWVi Fwd
SWVi Rev
Current (μA)
Potential (V vs Ag/Ag$^+$)
1.2
1.0
0.8
0.6
0.4
0.2
0.0
0.2
0.1
0.0
-0.1
-0.2
-2.0
-1.5
-1.0
-0.5
0.0

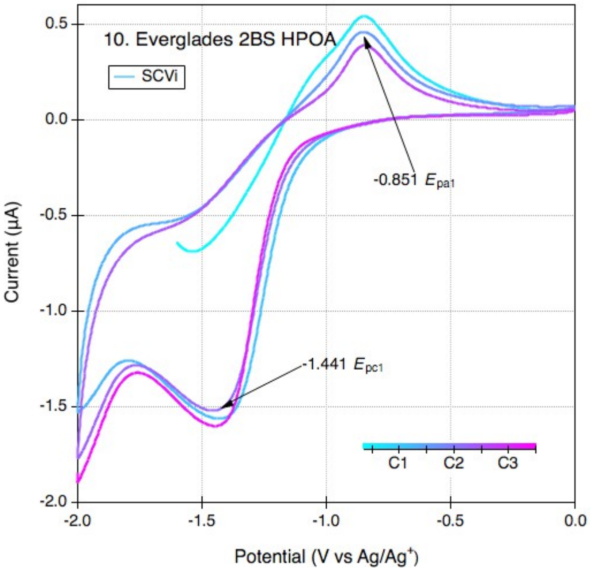
10. Everglades 2BS HPOA
SCVi
-0.851 E_{pa1}
-1.441 E_{pc1}
C1
C2
C3
Current (μA)
Potential (V vs Ag/Ag$^+$)
0.5
0.0
-0.5
-1.0
-1.5
-2.0
-2.0
-1.5
-1.0
-0.5
0.0

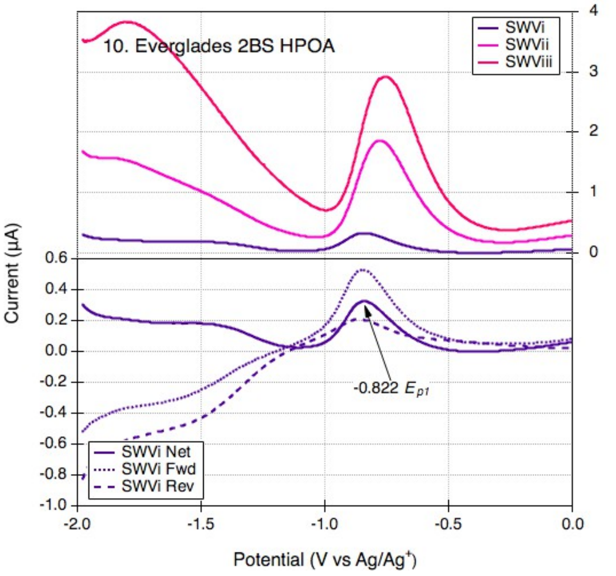
10. Everglades 2BS HPOA
SWVi
SWVii
SWViii
-0.822 E_{p1}
SWVi Net
SWVi Fwd
SWVi Rev
Current (μA)
Potential (V vs Ag/Ag$^+$)
4
3
2
1
0
0.6
0.4
0.2
0.0
-0.2
-0.4
-0.6
-0.8
-1.0
-2.0
-1.5
-1.0
-0.5
0.0

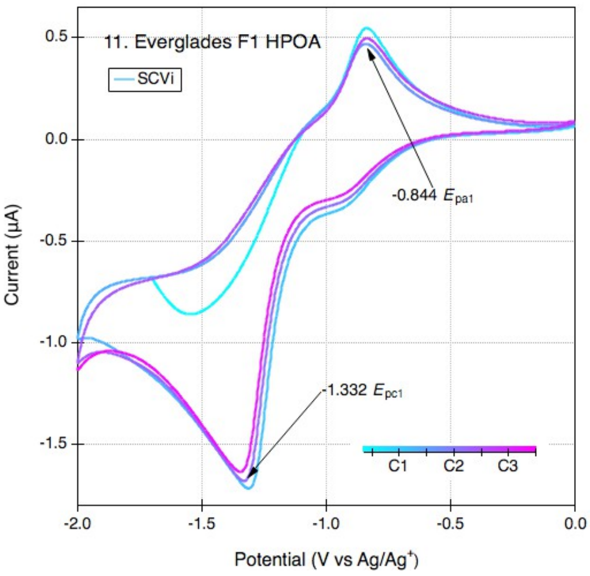
11. Everglades F1 HPOA
SCVi
-0.844 E_{pa1}
-1.332 E_{pc1}
C1
C2
C3
Current (µA)
0.5
0.0
-0.5
-1.0
-1.5
-2.0
-1.5
-1.0
-0.5
0.0
Potential (V vs Ag/Ag$^+$)

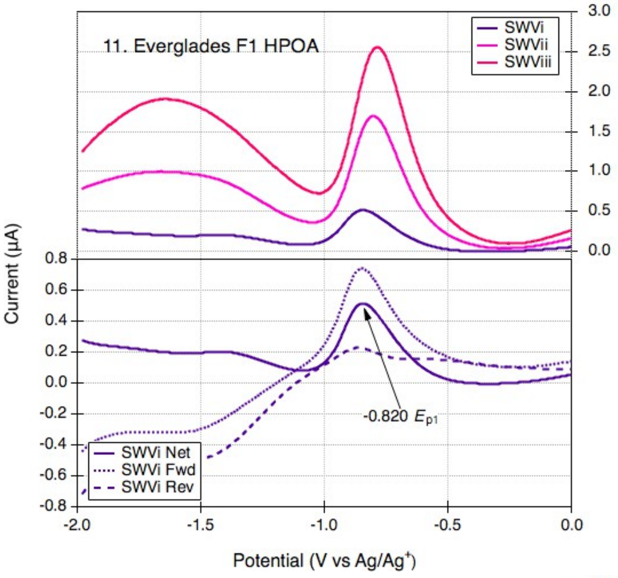
11. Everglades F1 HPOA
SWVi
SWVii
SWViii
3.0
2.5
2.0
1.5
1.0
0.5
0.0
Current (µA)
0.8
0.6
0.4
0.2
0.0
-0.2
-0.4
-0.6
-0.8
-0.820 E_{p1}
SWVi Net
SWVi Fwd
SWVi Rev
-2.0
-1.5
-1.0
-0.5
0.0
Potential (V vs Ag/Ag$^+$)

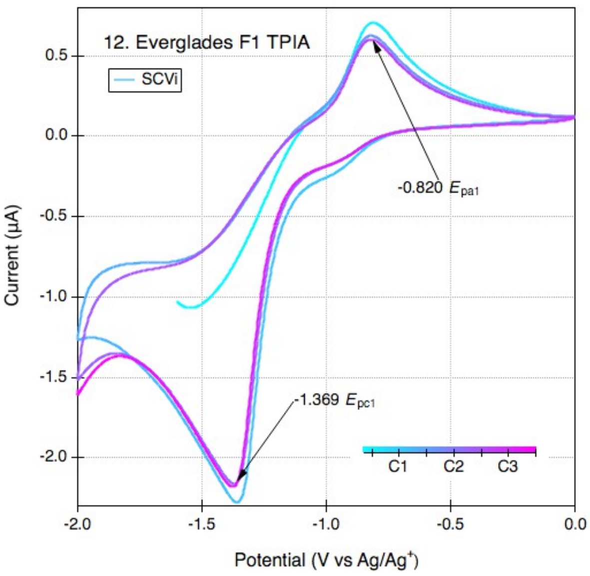
12. Everglades F1 TPIA
SCVi
-0.820 E_{pa1}
-1.369 E_{pc1}
C1
C2
C3
Current (µA)
0.5
0.0
-0.5
-1.0
-1.5
-2.0
-2.0
-1.5
-1.0
-0.5
0.0
Potential (V vs Ag/Ag$^+$)

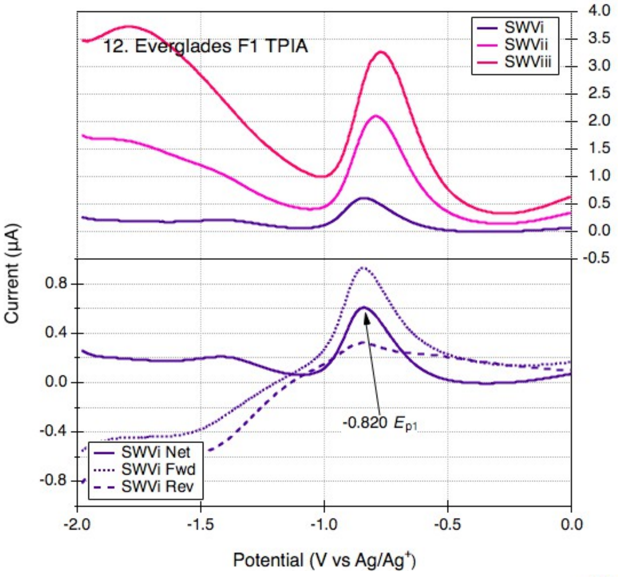
12. Everglades F1 TPIA
SWVi
SWVii
SWViii
4.0
3.5
3.0
2.5
2.0
1.5
1.0
0.5
0.0
-0.5
Current (µA)
0.8
0.4
0.0
-0.4
-0.8
-0.820 E_{p1}
SWVi Net
SWVi Fwd
SWVi Rev
-2.0
-1.5
-1.0
-0.5
0.0
Potential (V vs Ag/Ag$^+$)

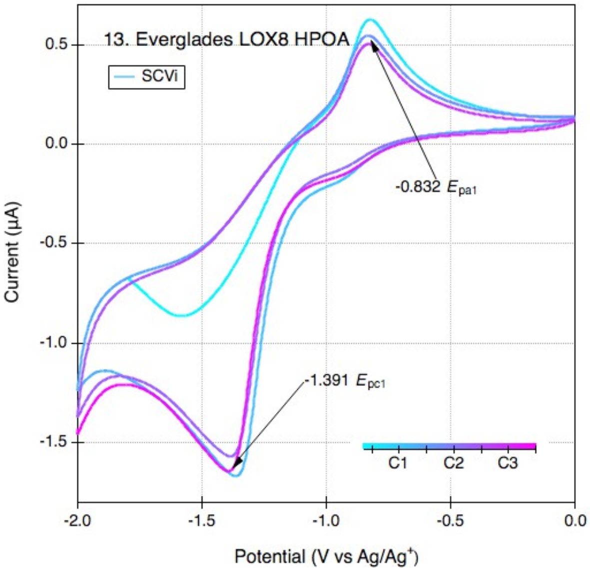
13. Everglades LOX8 HPOA
SCVi
-0.832 E_{pa1}
-1.391 E_{pc1}
C1
C2
C3
Current (µA)
0.5
0.0
-0.5
-1.0
-1.5
-2.0
-1.5
-1.0
-0.5
0.0
Potential (V vs Ag/Ag$^+$)

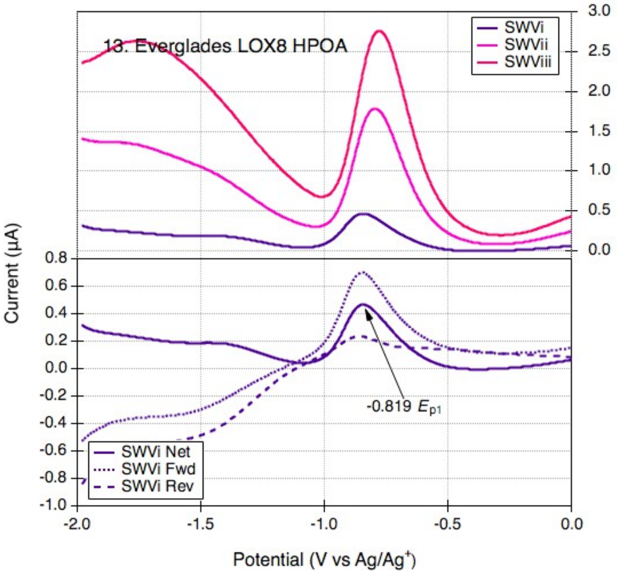
13. Everglades LOX8 HPOA
SWVi
SWVii
SWViii
3.0
2.5
2.0
1.5
1.0
0.5
0.0
Current (µA)
0.8
0.6
0.4
0.2
0.0
-0.2
-0.4
-0.6
-0.8
-1.0
-0.819 E_{p1}
SWVi Net
SWVi Fwd
SWVi Rev
-2.0
-1.5
-1.0
-0.5
0.0
Potential (V vs Ag/Ag$^+$)

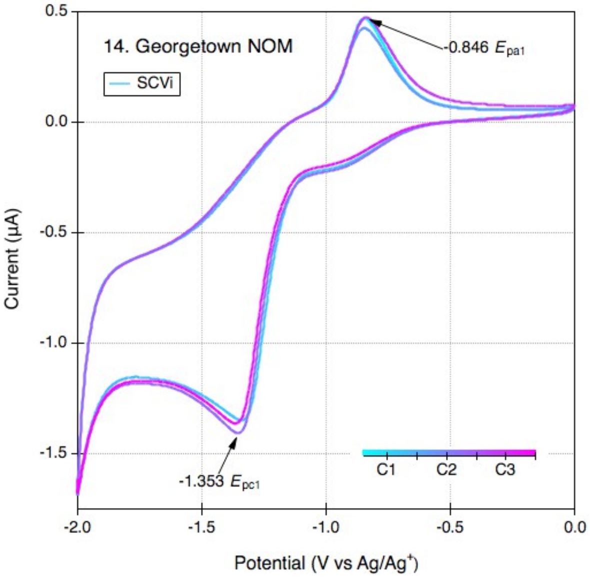
14. Georgetown NOM
SCVi
-0.846 E_{pa1}
-1.353 E_{pc1}
C1
C2
C3
Current (µA)
Potential (V vs Ag/Ag$^+$)
0.5
0.0
-0.5
-1.0
-1.5
-2.0
-1.5
-1.0
-0.5
0.0

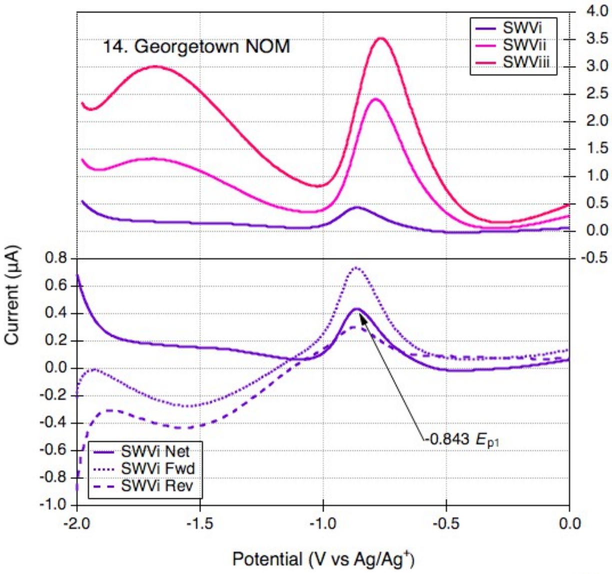
14. Georgetown NOM
SWVi
SWVii
SWViii
SWVi Net
SWVi Fwd
SWVi Rev
-0.843 E_{p1}
Current (µA)
Potential (V vs Ag/Ag$^+$)
4.0
3.5
3.0
2.5
2.0
1.5
1.0
0.5
0.0
-0.5
0.8
0.6
0.4
0.2
0.0
-0.2
-0.4
-0.6
-0.8
-1.0
-2.0
-1.5
-1.0
-0.5
0.0

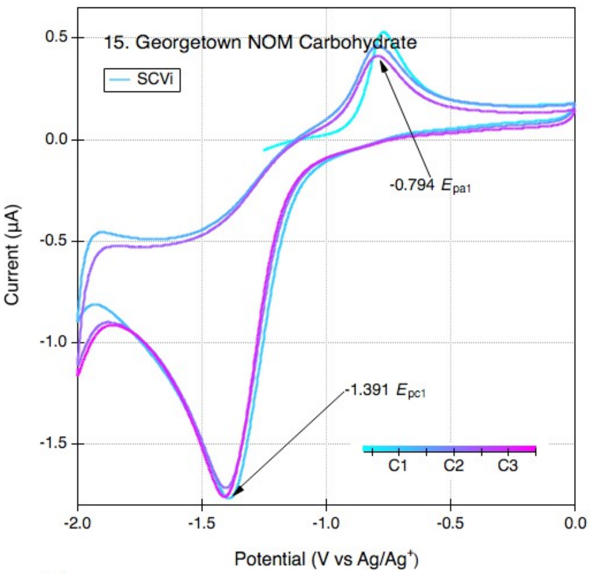
15. Georgetown NOM Carbohydrate
SCVi
-0.794 E_{pa1}
-1.391 E_{pc1}
C1
C2
C3
Current (µA)
Potential (V vs Ag/Ag$^+$)
0.5
0.0
-0.5
-1.0
-1.5
-2.0
-1.5
-1.0
-0.5
0.0

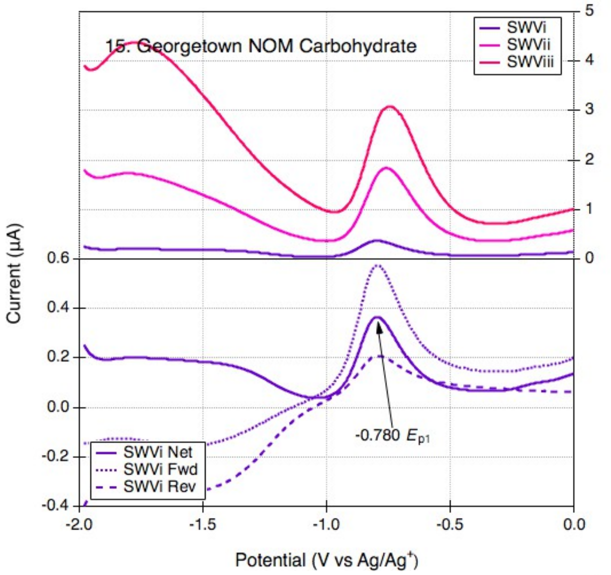
15. Georgetown NOM Carbohydrate
SWVi
SWVii
SWViii
SWVi Net
SWVi Fwd
SWVi Rev
-0.780 E_{p1}
Current (µA)
Potential (V vs Ag/Ag$^+$)
5
4
3
2
1
0
0.6
0.4
0.2
0.0
-0.2
-0.4
-2.0
-1.5
-1.0
-0.5
0.0

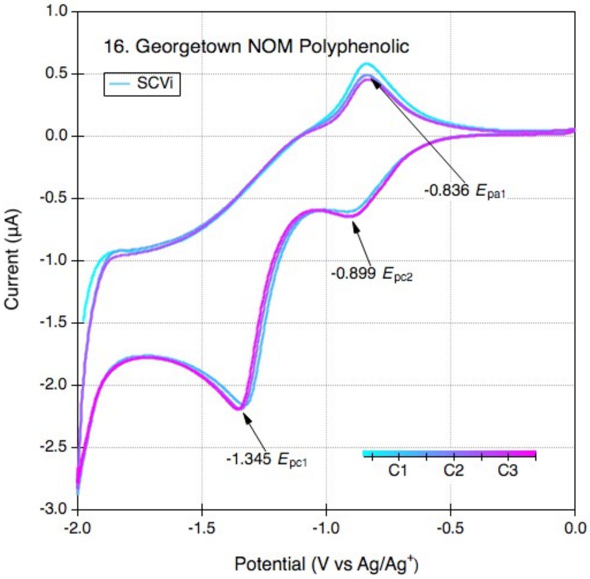
16. Georgetown NOM Polyphenolic
SCVi
-0.836 E_{pa1}
-0.899 E_{pc2}
-1.345 E_{pc1}
C1
C2
C3
Current (µA)
Potential (V vs Ag/Ag$^+$)
1.0
0.5
0.0
-0.5
-1.0
-1.5
-2.0
-2.5
-3.0
-2.0
-1.5
-1.0
-0.5
0.0

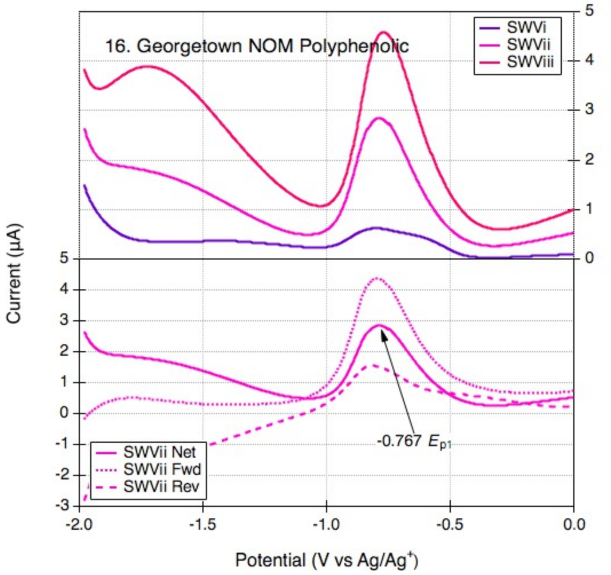
16. Georgetown NOM Polyphenolic
SWVi
SWVii
SWViii
SWVii Net
SWVii Fwd
SWVii Rev
-0.767 E_{p1}
Current (µA)
Potential (V vs Ag/Ag$^+$)
5
4
3
2
1
0
5
4
3
2
1
0
-1
-2
-3
-2.0
-1.5
-1.0
-0.5
0.0

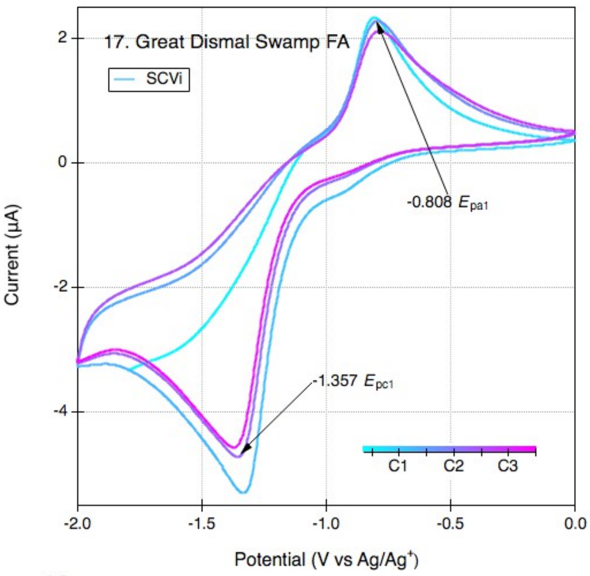
17. Great Dismal Swamp FA
SCVi
-0.808 E_{pa1}
-1.357 E_{pc1}
C1
C2
C3
Current (µA)
2
0
-2
-4
-2.0
-1.5
-1.0
-0.5
0.0
Potential (V vs Ag/Ag$^+$)

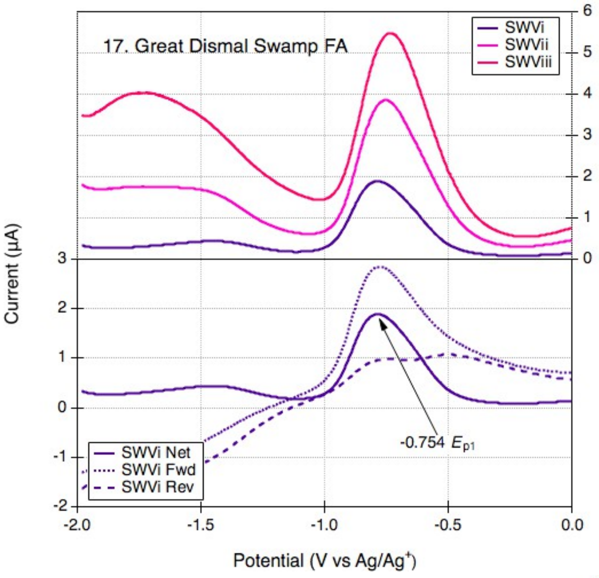
17. Great Dismal Swamp FA
SWVi
SWVii
SWViii
-0.754 E_{p1}
SWVi Net
SWVi Fwd
SWVi Rev
Current (µA)
6
5
4
3
2
1
0
3
2
1
0
-1
-2
-2.0
-1.5
-1.0
-0.5
0.0
Potential (V vs Ag/Ag$^+$)

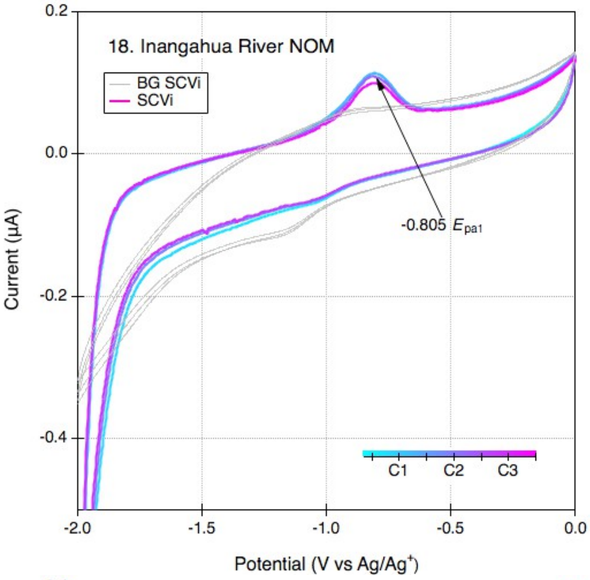
18. Inangahua River NOM
BG SCVi
SCVi
-0.805 E_{pa1}
C1
C2
C3
Current (µA)
0.2
0.0
-0.2
-0.4
-2.0
-1.5
-1.0
-0.5
0.0
Potential (V vs Ag/Ag$^+$)

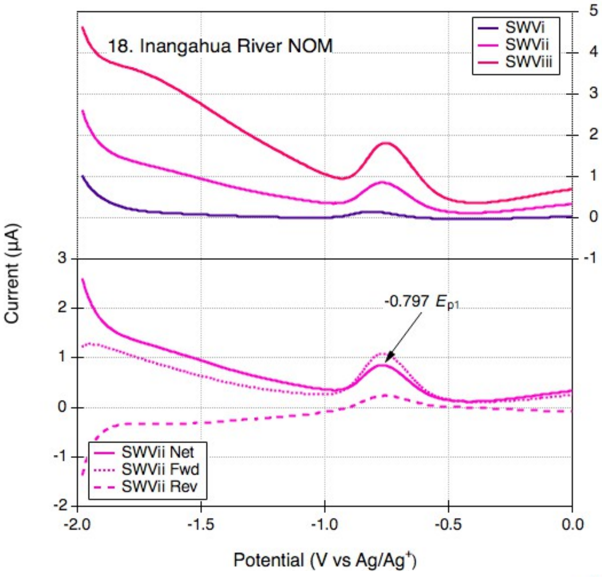
18. Inangahua River NOM
SWVi
SWVii
SWViii
-0.797 E_{p1}
SWVii Net
SWVii Fwd
SWVii Rev
Current (µA)
5
4
3
2
1
0
-1
3
2
1
0
-1
-2
-2.0
-1.5
-1.0
-0.5
0.0
Potential (V vs Ag/Ag$^+$)

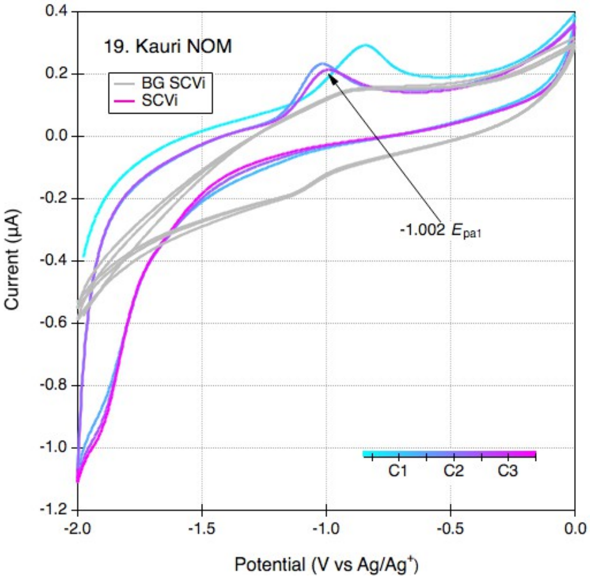
19. Kauri NOM
BG SCVi
SCVi
-1.002 E_{pa1}
C1
C2
C3
Current (µA)
0.4
0.2
0.0
-0.2
-0.4
-0.6
-0.8
-1.0
-1.2
-2.0
-1.5
-1.0
-0.5
0.0
Potential (V vs Ag/Ag$^+$)

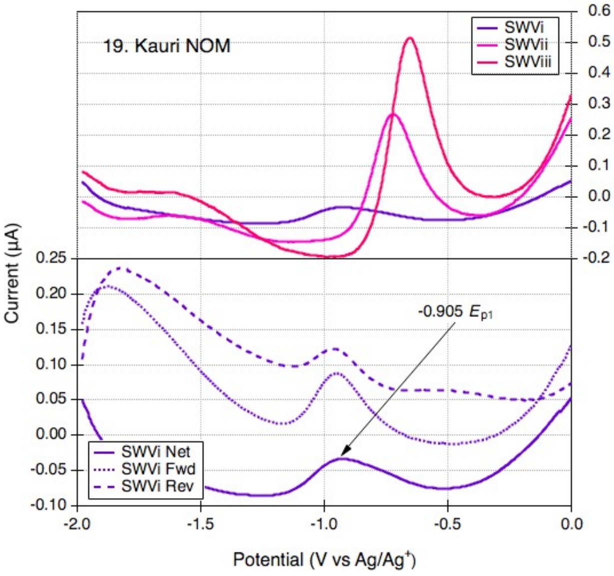
19. Kauri NOM
SWVi
SWVii
SWViii
-0.905 E_{p1}
SWVi Net
SWVi Fwd
SWVi Rev
Current (µA)
0.6
0.5
0.4
0.3
0.2
0.1
0.0
-0.1
-0.2
0.25
0.20
0.15
0.10
0.05
0.00
-0.05
-0.10
-2.0
-1.5
-1.0
-0.5
0.0
Potential (V vs Ag/Ag$^+$)

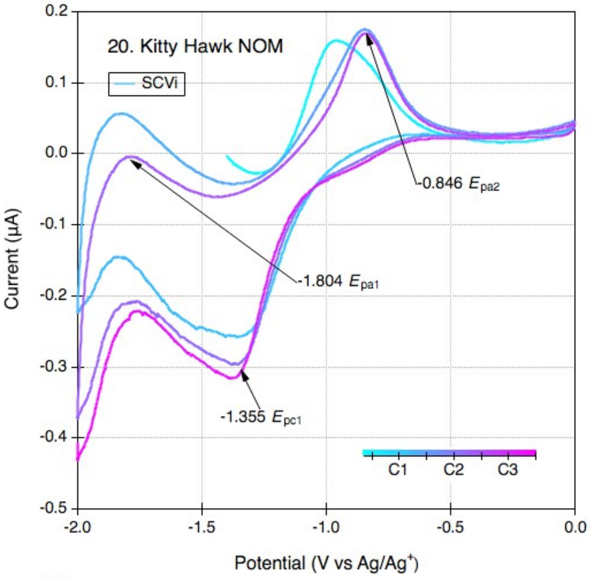
20. Kitty Hawk NOM
SCVi
-0.846 E_{pa2}
-1.804 E_{pa1}
-1.355 E_{pc1}
C1
C2
C3
Current (μA)
0.2
0.1
0.0
-0.1
-0.2
-0.3
-0.4
-0.5
-2.0
-1.5
-1.0
-0.5
0.0
Potential (V vs Ag/Ag$^+$)

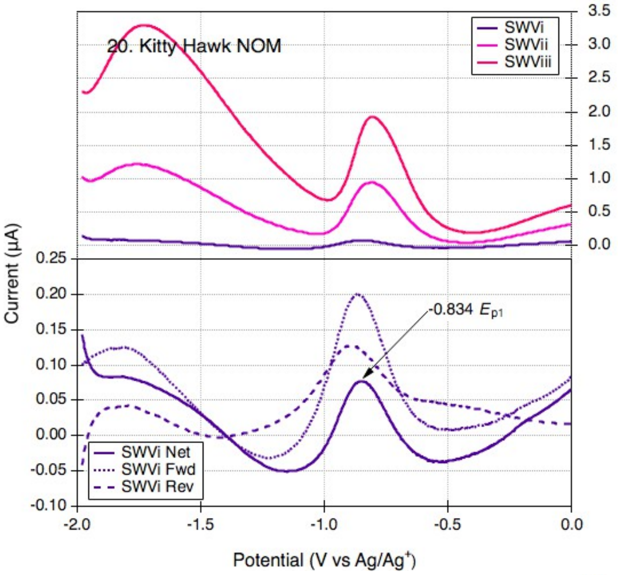
20. Kitty Hawk NOM
SWVi
SWVii
SWViii
3.5
3.0
2.5
2.0
1.5
1.0
0.5
0.0
-0.834 E_{p1}
SWVi Net
SWVi Fwd
SWVi Rev
Current (μA)
0.25
0.20
0.15
0.10
0.05
0.00
-0.05
-0.10
-2.0
-1.5
-1.0
-0.5
0.0
Potential (V vs Ag/Ag$^+$)

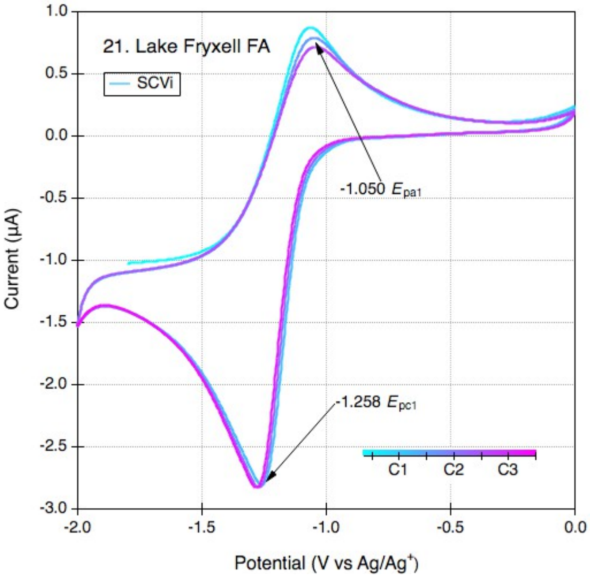
21. Lake Fryxell FA
SCVi
-1.050 E_{pa1}
-1.258 E_{pc1}
C1
C2
C3
Current (μA)
1.0
0.5
0.0
-0.5
-1.0
-1.5
-2.0
-2.5
-3.0
-2.0
-1.5
-1.0
-0.5
0.0
Potential (V vs Ag/Ag$^+$)

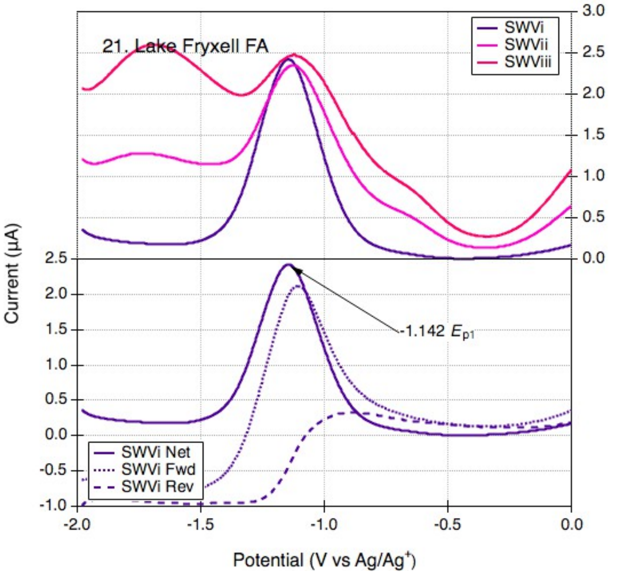
21. Lake Fryxell FA
SWVi
SWVii
SWViii
3.0
2.5
2.0
1.5
1.0
0.5
0.0
-1.142 E_{p1}
SWVi Net
SWVi Fwd
SWVi Rev
Current (μA)
2.5
2.0
1.5
1.0
0.5
0.0
-0.5
-1.0
-2.0
-1.5
-1.0
-0.5
0.0
Potential (V vs Ag/Ag$^+$)

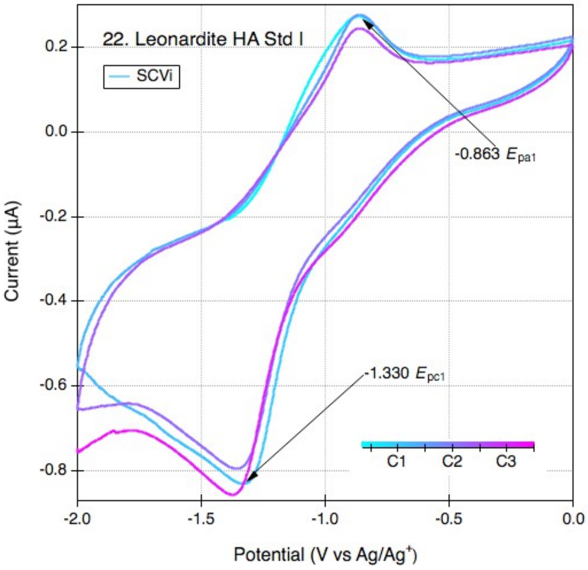
22. Leonardite HA Std I
SCVi
-0.863 E_{pa1}
-1.330 E_{pc1}
C1
C2
C3
Current (μA)
0.2
0.0
-0.2
-0.4
-0.6
-0.8
-2.0
-1.5
-1.0
-0.5
0.0
Potential (V vs Ag/Ag$^+$)

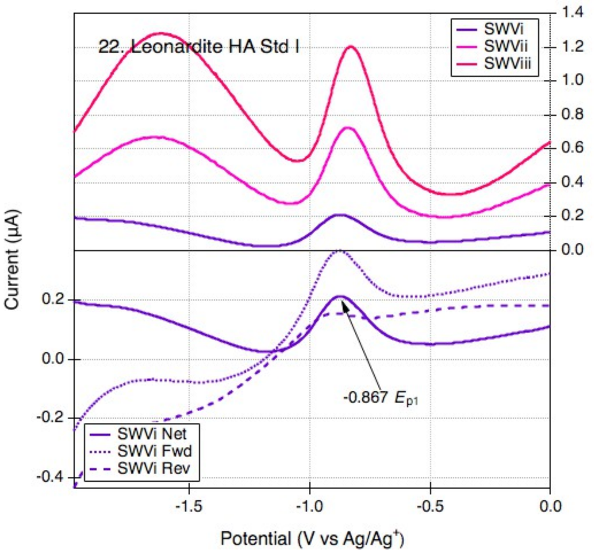
22. Leonardite HA Std I
SWVi
SWVii
SWViii
1.4
1.2
1.0
0.8
0.6
0.4
0.2
0.0
-0.867 E_{p1}
SWVi Net
SWVi Fwd
SWVi Rev
Current (μA)
0.2
0.0
-0.2
-0.4
-1.5
-1.0
-0.5
0.0
Potential (V vs Ag/Ag$^+$)

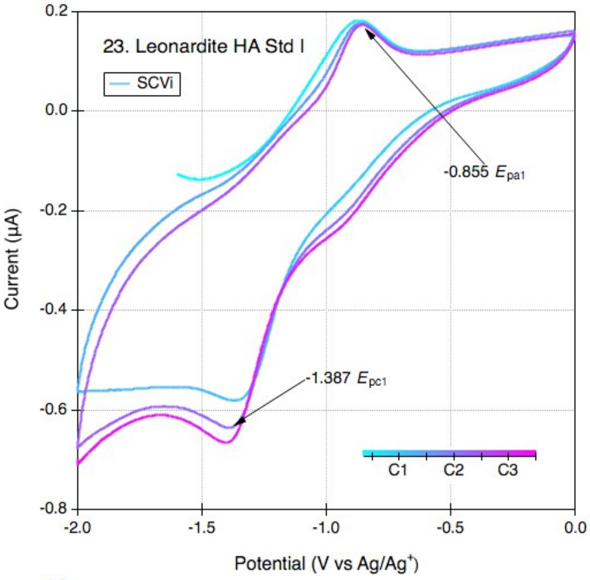
23. Leonardite HA Std I
SCVi
-0.855 E_{pa1}
-1.387 E_{pc1}
C1
C2
C3
Current (μA)
Potential (V vs Ag/Ag$^+$)
0.2
0.0
-0.2
-0.4
-0.6
-0.8
-2.0
-1.5
-1.0
-0.5
0.0

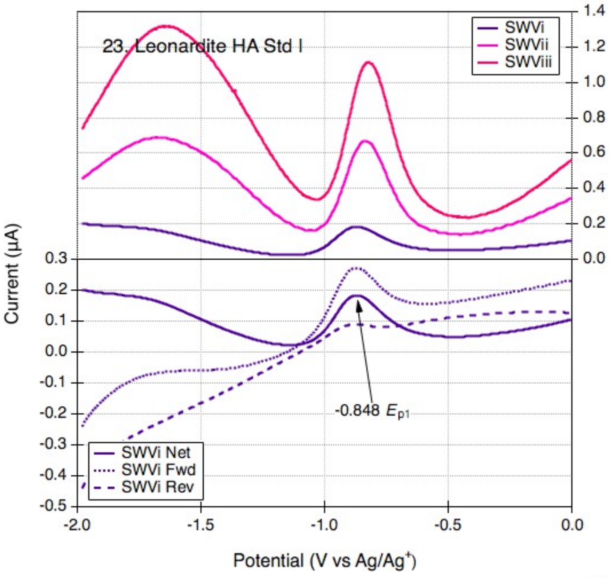
23. Leonardite HA Std I
SWVi
SWVii
SWViii
SWVi Net
SWVi Fwd
SWVi Rev
-0.848 E_{p1}
Current (μA)
Potential (V vs Ag/Ag$^+$)
1.4
1.2
1.0
0.8
0.6
0.4
0.2
0.0
0.3
0.2
0.1
0.0
-0.1
-0.2
-0.3
-0.4
-0.5
-2.0
-1.5
-1.0
-0.5
0.0

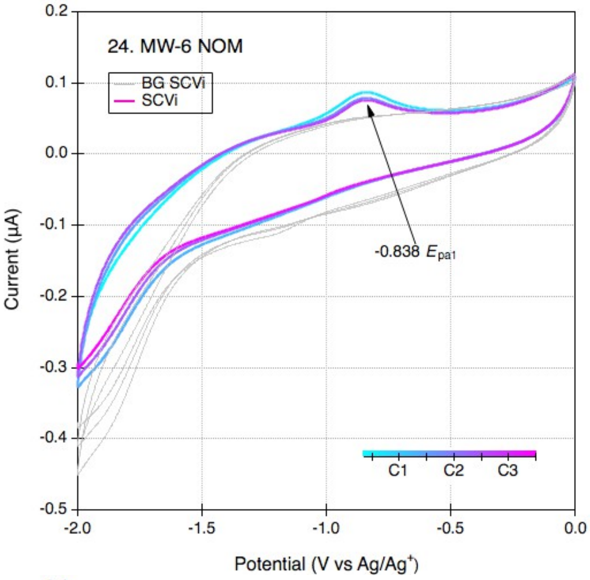
24. MW-6 NOM
BG SCVi
SCVi
-0.838 E_{pa1}
C1
C2
C3
Current (μA)
Potential (V vs Ag/Ag$^+$)
0.2
0.1
0.0
-0.1
-0.2
-0.3
-0.4
-0.5
-2.0
-1.5
-1.0
-0.5
0.0

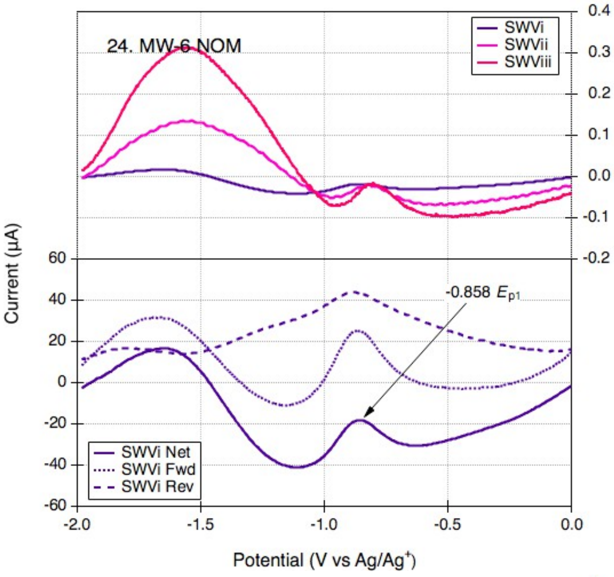
24. MW-6 NOM
SWVi
SWVii
SWViii
SWVi Net
SWVi Fwd
SWVi Rev
-0.858 E_{p1}
Current (μA)
Potential (V vs Ag/Ag$^+$)
0.4
0.3
0.2
0.1
0.0
-0.1
-0.2
60
40
20
0
-20
-40
-60
-2.0
-1.5
-1.0
-0.5
0.0

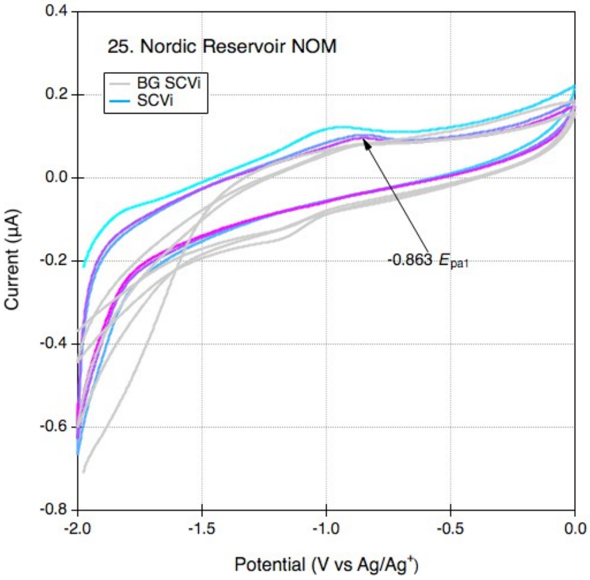
25. Nordic Reservoir NOM
BG SCVi
SCVi
-0.863 E_{pa1}
Current (μA)
Potential (V vs Ag/Ag$^+$)
0.4
0.2
0.0
-0.2
-0.4
-0.6
-0.8
-2.0
-1.5
-1.0
-0.5
0.0

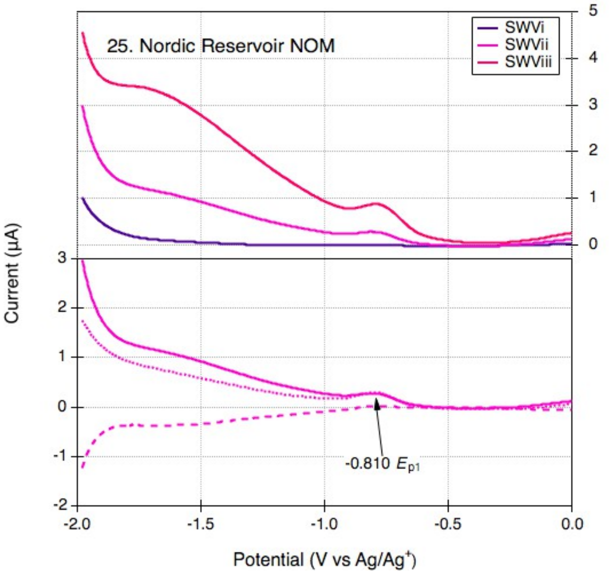
25. Nordic Reservoir NOM
SWVi
SWVii
SWViii
-0.810 E_{p1}
Current (μA)
Potential (V vs Ag/Ag$^+$)
5
4
3
2
1
0
3
2
1
0
-1
-2
-2.0
-1.5
-1.0
-0.5
0.0

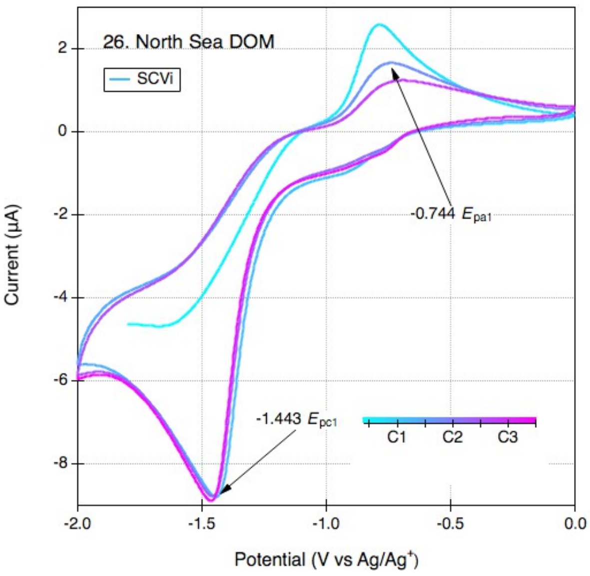
26. North Sea DOM
SCVi
-0.744 E_{pa1}
-1.443 E_{pc1}
C1
C2
C3
Current (μA)
2
0
-2
-4
-6
-8
-2.0
-1.5
-1.0
-0.5
0.0
Potential (V vs Ag/Ag$^+$)

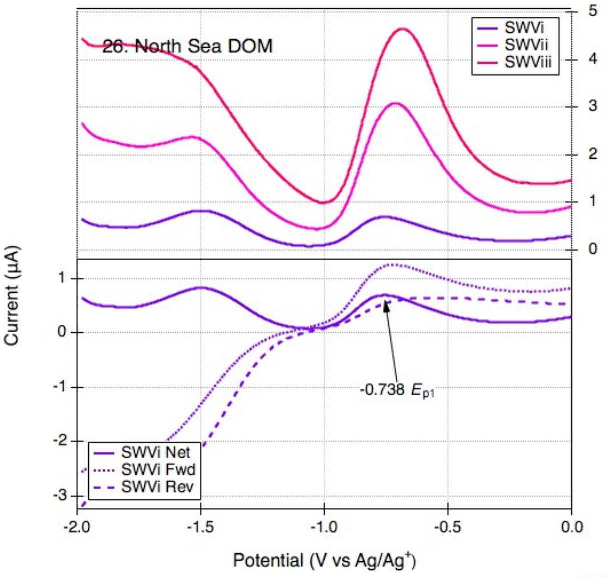
26. North Sea DOM
SWVi
SWVii
SWViii
5
4
3
2
1
0
-0.738 E_{p1}
SWVi Net
SWVi Fwd
SWVi Rev
Current (μA)
1
0
-1
-2
-3
-2.0
-1.5
-1.0
-0.5
0.0
Potential (V vs Ag/Ag$^+$)

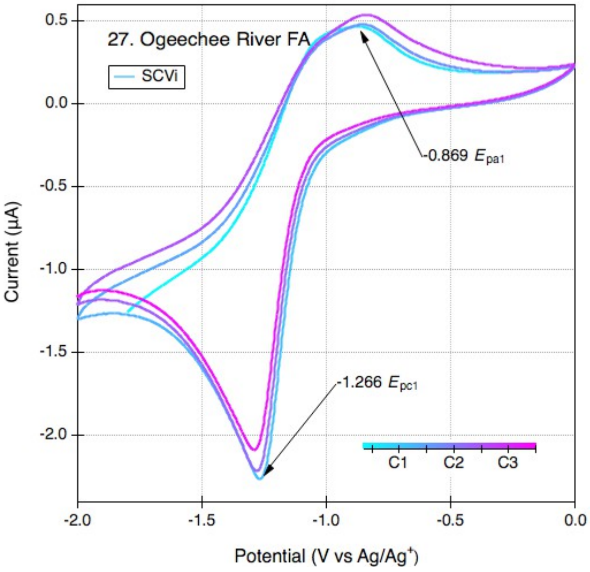
27. Ogeechee River FA
SCVi
-0.869 E_{pa1}
-1.266 E_{pc1}
C1
C2
C3
Current (μA)
0.5
0.0
-0.5
-1.0
-1.5
-2.0
-2.0
-1.5
-1.0
-0.5
0.0
Potential (V vs Ag/Ag$^+$)

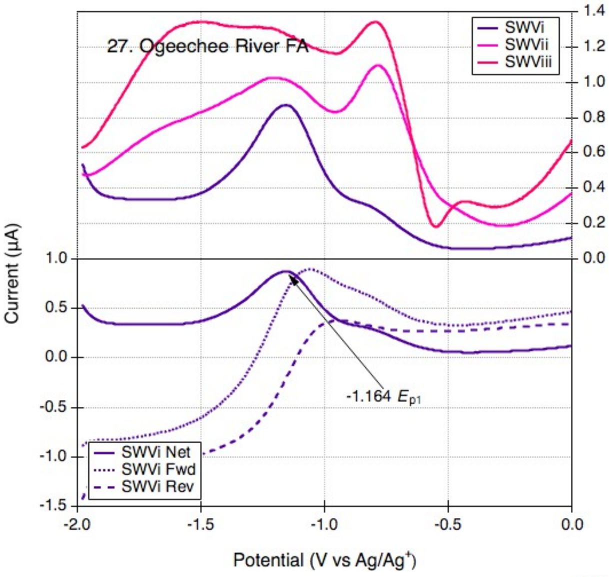
27. Ogeechee River FA
SWVi
SWVii
SWViii
1.4
1.2
1.0
0.8
0.6
0.4
0.2
0.0
-1.164 E_{p1}
SWVi Net
SWVi Fwd
SWVi Rev
Current (μA)
1.0
0.5
0.0
-0.5
-1.0
-1.5
-2.0
-1.5
-1.0
-0.5
0.0
Potential (V vs Ag/Ag$^+$)

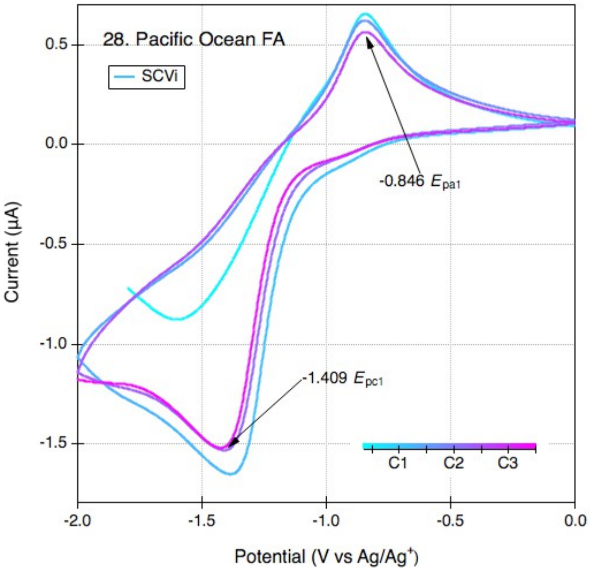
28. Pacific Ocean FA
SCVi
-0.846 E_{pa1}
-1.409 E_{pc1}
C1
C2
C3
Current (μA)
0.5
0.0
-0.5
-1.0
-1.5
-2.0
-1.5
-1.0
-0.5
0.0
Potential (V vs Ag/Ag$^+$)

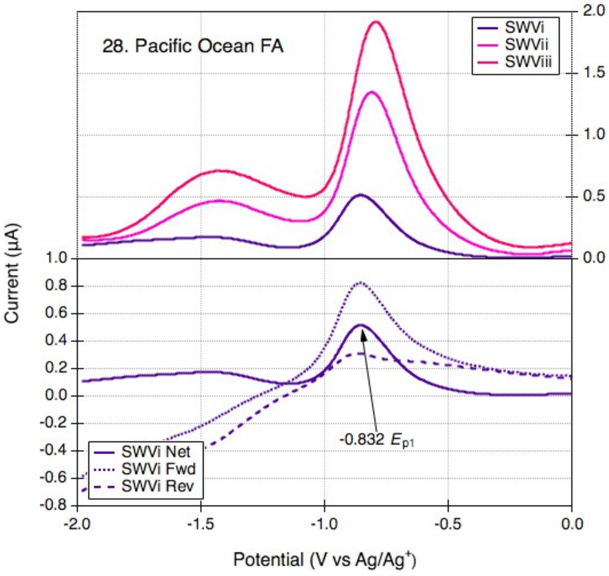
28. Pacific Ocean FA
SWVi
SWVii
SWViii
2.0
1.5
1.0
0.5
0.0
-0.832 E_{p1}
SWVi Net
SWVi Fwd
SWVi Rev
Current (μA)
1.0
0.8
0.6
0.4
0.2
0.0
-0.2
-0.4
-0.6
-0.8
-2.0
-1.5
-1.0
-0.5
0.0
Potential (V vs Ag/Ag$^+$)

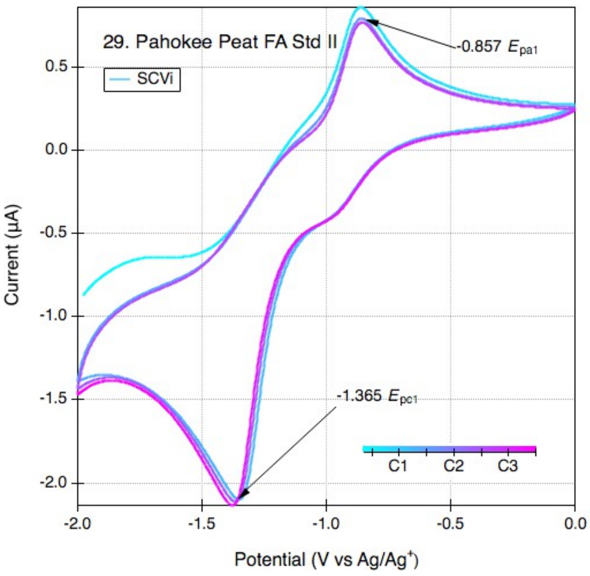
29. Pahokee Peat FA Std II
SCVi
-0.857 E_{pa1}
-1.365 E_{pc1}
C1 C2 C3
Current (µA)
0.5
0.0
-0.5
-1.0
-1.5
-2.0
-2.0
-1.5
-1.0
-0.5
0.0
Potential (V vs Ag/Ag$^+$)

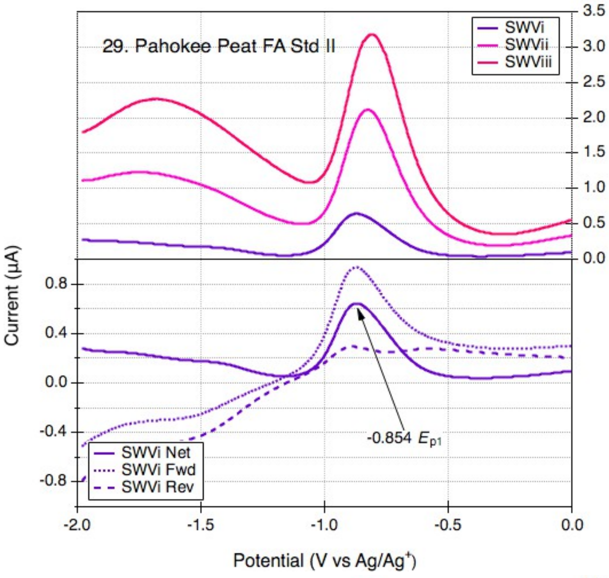
29. Pahokee Peat FA Std II
SWVi
SWVii
SWViii
3.5
3.0
2.5
2.0
1.5
1.0
0.5
0.0
Current (µA)
0.8
0.4
0.0
-0.4
-0.8
-0.854 E_{p1}
SWVi Net
SWVi Fwd
SWVi Rev
-2.0
-1.5
-1.0
-0.5
0.0
Potential (V vs Ag/Ag$^+$)

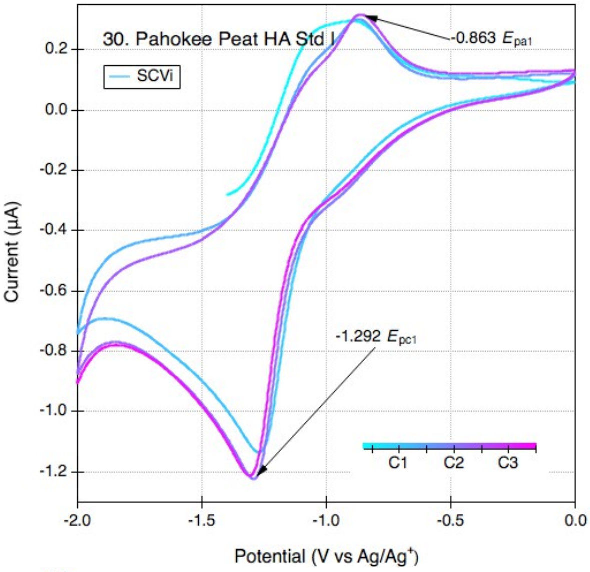
30. Pahokee Peat HA Std I
SCVi
-0.863 E_{pa1}
-1.292 E_{pc1}
C1 C2 C3
Current (µA)
0.2
0.0
-0.2
-0.4
-0.6
-0.8
-1.0
-1.2
-2.0
-1.5
-1.0
-0.5
0.0
Potential (V vs Ag/Ag$^+$)

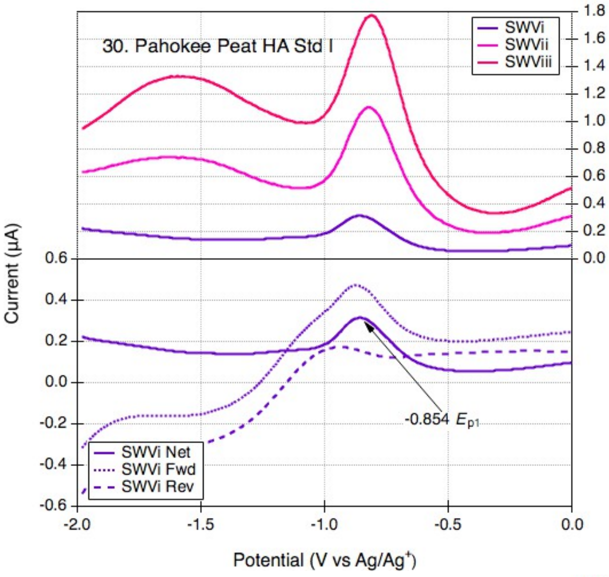
30. Pahokee Peat HA Std I
SWVi
SWVii
SWViii
1.8
1.6
1.4
1.2
1.0
0.8
0.6
0.4
0.2
0.0
Current (µA)
0.6
0.4
0.2
0.0
-0.2
-0.4
-0.6
-0.854 E_{p1}
SWVi Net
SWVi Fwd
SWVi Rev
-2.0
-1.5
-1.0
-0.5
0.0
Potential (V vs Ag/Ag$^+$)

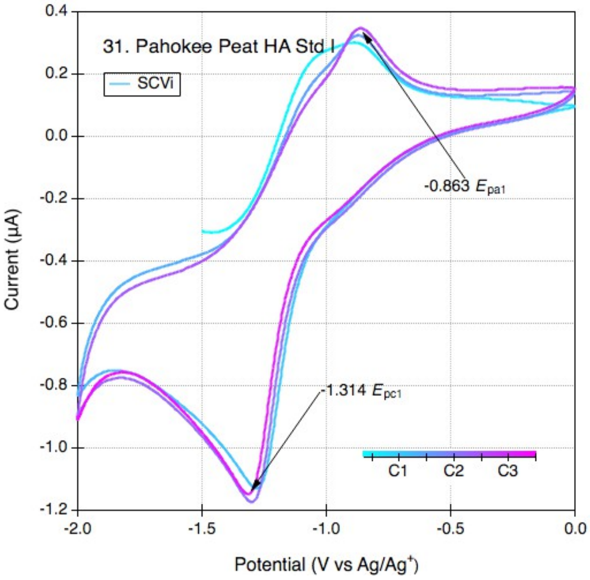
31. Pahokee Peat HA Std I
SCVi
-0.863 E_{pa1}
-1.314 E_{pc1}
C1 C2 C3
Current (µA)
0.4
0.2
0.0
-0.2
-0.4
-0.6
-0.8
-1.0
-1.2
-2.0
-1.5
-1.0
-0.5
0.0
Potential (V vs Ag/Ag$^+$)

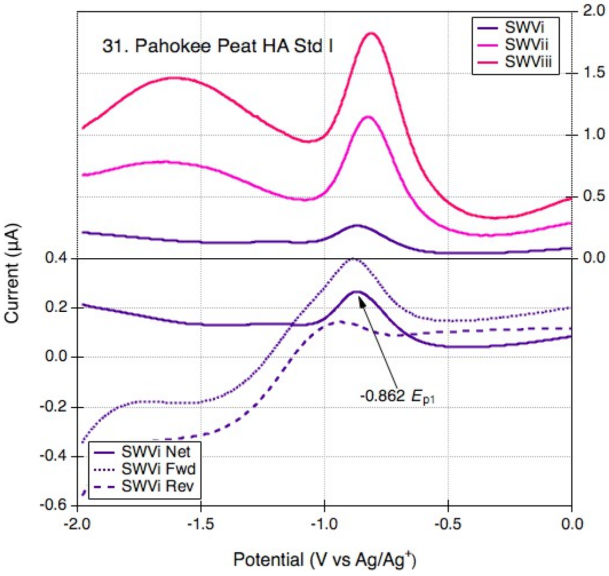
31. Pahokee Peat HA Std I
SWVi
SWVii
SWViii
2.0
1.5
1.0
0.5
0.0
Current (µA)
0.4
0.2
0.0
-0.2
-0.4
-0.6
-0.862 E_{p1}
SWVi Net
SWVi Fwd
SWVi Rev
-2.0
-1.5
-1.0
-0.5
0.0
Potential (V vs Ag/Ag$^+$)

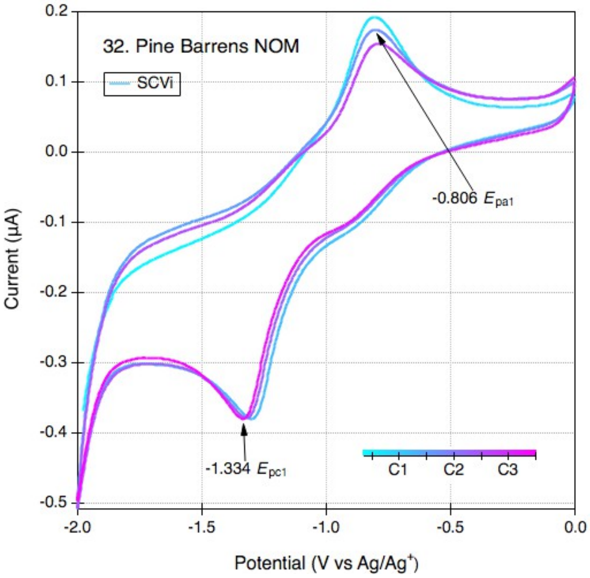
32. Pine Barrens NOM
SCVi
-0.806 E_{pa1}
-1.334 E_{pc1}
C1
C2
C3
Current (μA)
0.2
0.1
0.0
-0.1
-0.2
-0.3
-0.4
-0.5
-2.0
-1.5
-1.0
-0.5
0.0
Potential (V vs Ag/Ag$^+$)

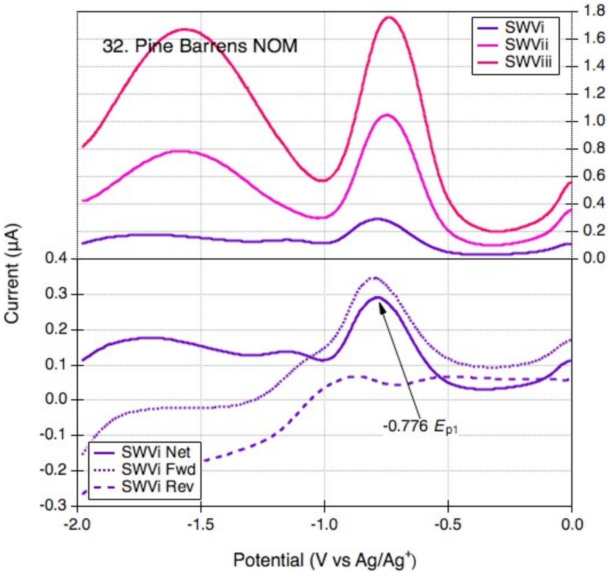
32. Pine Barrens NOM
SWVi
SWVii
SWViii
1.8
1.6
1.4
1.2
1.0
0.8
0.6
0.4
0.2
0.0
Current (μA)
0.4
0.3
0.2
0.1
0.0
-0.1
-0.2
-0.3
-0.776 E_{p1}
SWVi Net
SWVi Fwd
SWVi Rev
-2.0
-1.5
-1.0
-0.5
0.0
Potential (V vs Ag/Ag$^+$)

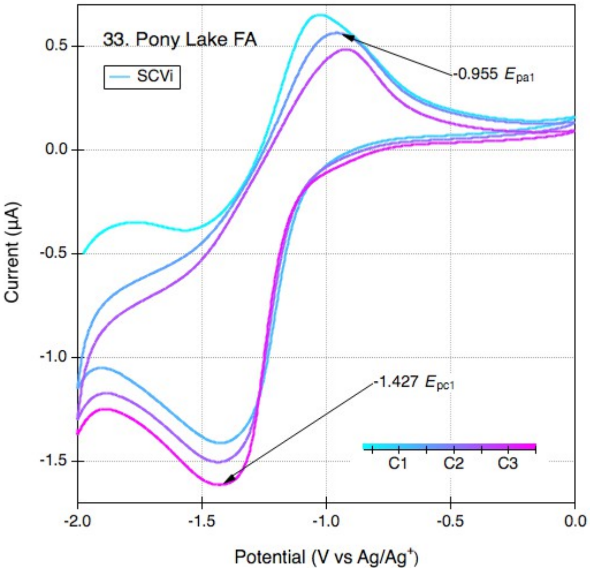
33. Pony Lake FA
SCVi
-0.955 E_{pa1}
-1.427 E_{pc1}
C1
C2
C3
Current (μA)
0.5
0.0
-0.5
-1.0
-1.5
-2.0
-1.5
-1.0
-0.5
0.0
Potential (V vs Ag/Ag$^+$)

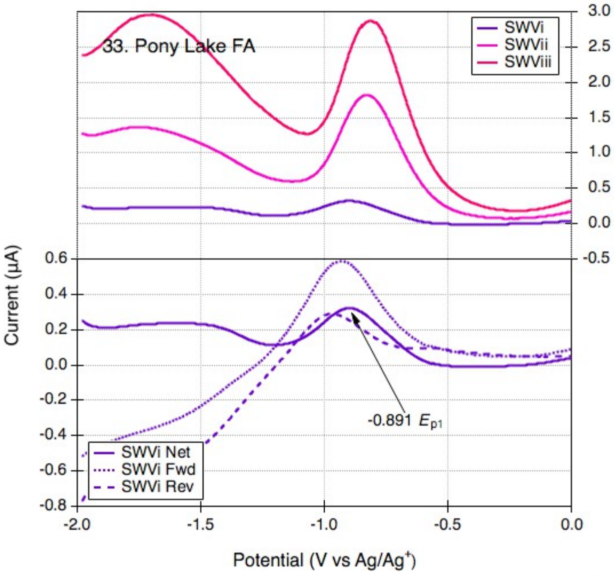
33. Pony Lake FA
SWVi
SWVii
SWViii
3.0
2.5
2.0
1.5
1.0
0.5
0.0
-0.5
Current (μA)
0.6
0.4
0.2
0.0
-0.2
-0.4
-0.6
-0.8
-0.891 E_{p1}
SWVi Net
SWVi Fwd
SWVi Rev
-2.0
-1.5
-1.0
-0.5
0.0
Potential (V vs Ag/Ag$^+$)

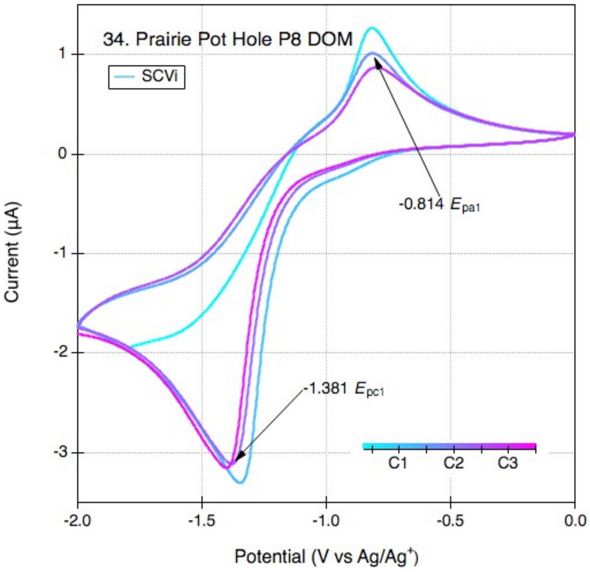
34. Prairie Pot Hole P8 DOM
SCVi
-0.814 E_{pa1}
-1.381 E_{pc1}
C1
C2
C3
Current (μA)
1
0
-1
-2
-3
-2.0
-1.5
-1.0
-0.5
0.0
Potential (V vs Ag/Ag$^+$)

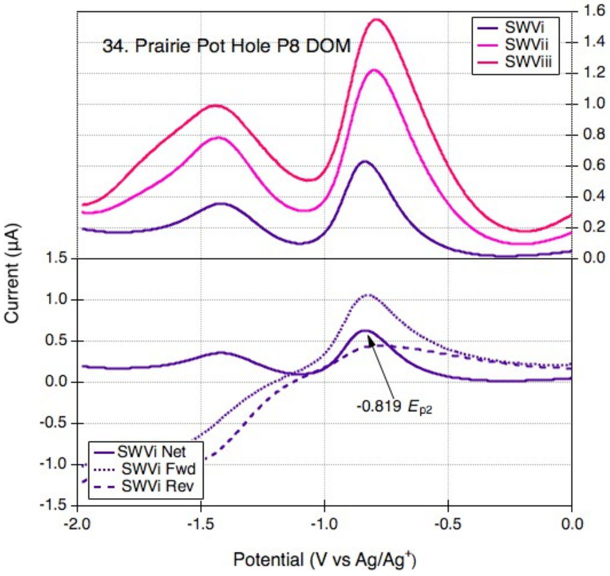
34. Prairie Pot Hole P8 DOM
SWVi
SWVii
SWViii
1.6
1.4
1.2
1.0
0.8
0.6
0.4
0.2
0.0
Current (μA)
1.5
1.0
0.5
0.0
-0.5
-1.0
-1.5
-0.819 E_{p2}
SWVi Net
SWVi Fwd
SWVi Rev
-2.0
-1.5
-1.0
-0.5
0.0
Potential (V vs Ag/Ag$^+$)

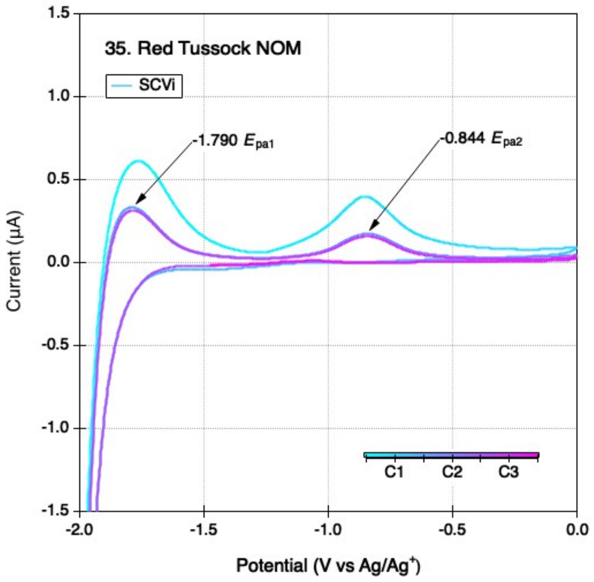
35. Red Tussock NOM
SCVi
-1.790 E_{pa1}
-0.844 E_{pa2}
C1
C2
C3
Current (µA)
1.5
1.0
0.5
0.0
-0.5
-1.0
-1.5
-2.0
-1.5
-1.0
-0.5
0.0
Potential (V vs Ag/Ag$^+$)

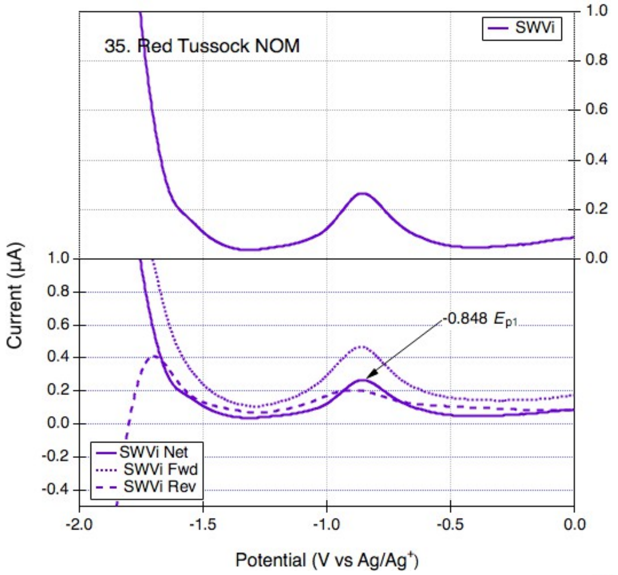
35. Red Tussock NOM
SWVi
1.0
0.8
0.6
0.4
0.2
0.0
-0.848 E_{p1}
SWVi Net
SWVi Fwd
SWVi Rev
Current (µA)
1.0
0.8
0.6
0.4
0.2
0.0
-0.2
-0.4
-2.0
-1.5
-1.0
-0.5
0.0
Potential (V vs Ag/Ag$^+$)

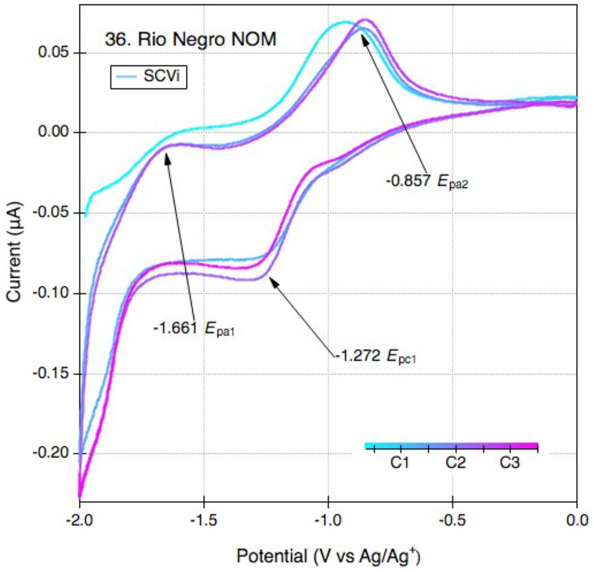
36. Rio Negro NOM
SCVi
-0.857 E_{pa2}
-1.661 E_{pa1}
-1.272 E_{pc1}
C1
C2
C3
Current (µA)
0.05
0.00
-0.05
-0.10
-0.15
-0.20
-2.0
-1.5
-1.0
-0.5
0.0
Potential (V vs Ag/Ag$^+$)

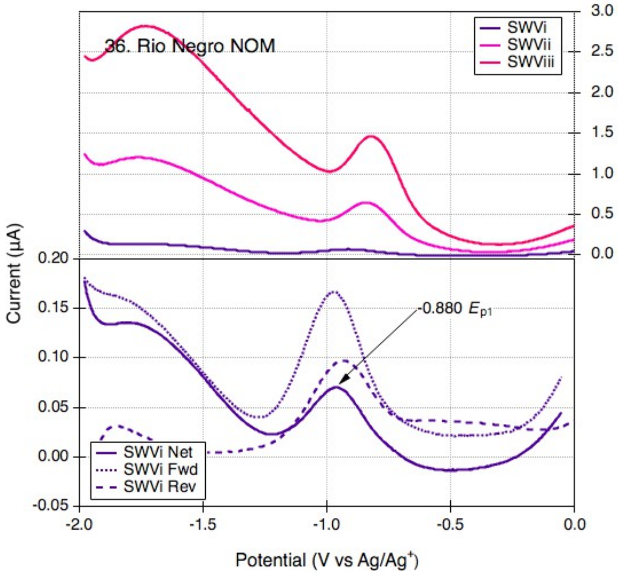
36. Rio Negro NOM
SWVi
SWVii
SWViii
3.0
2.5
2.0
1.5
1.0
0.5
0.0
-0.880 E_{p1}
SWVi Net
SWVi Fwd
SWVi Rev
Current (µA)
0.20
0.15
0.10
0.05
0.00
-0.05
-2.0
-1.5
-1.0
-0.5
0.0
Potential (V vs Ag/Ag$^+$)

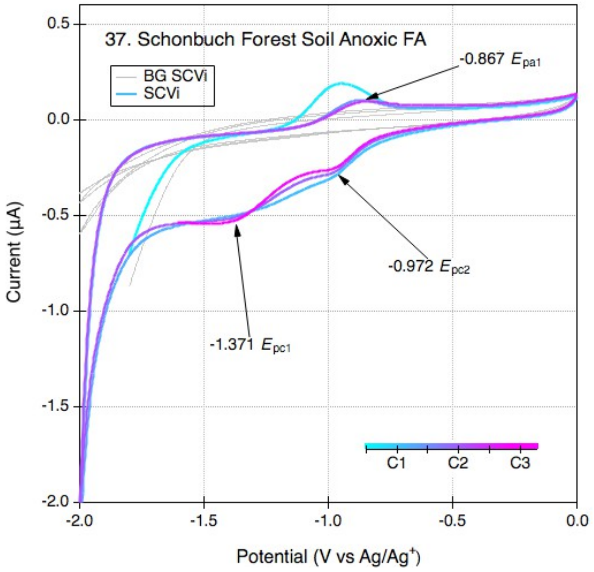
37. Schonbuch Forest Soil Anoxic FA
BG SCVi
SCVi
-0.867 E_{pa1}
-0.972 E_{pc2}
-1.371 E_{pc1}
C1
C2
C3
Current (µA)
0.5
0.0
-0.5
-1.0
-1.5
-2.0
-2.0
-1.5
-1.0
-0.5
0.0
Potential (V vs Ag/Ag$^+$)

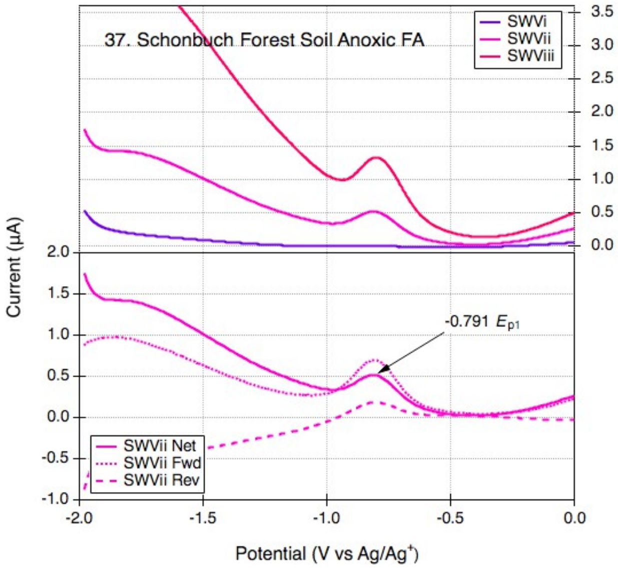
37. Schonbuch Forest Soil Anoxic FA
SWVi
SWVii
SWViii
3.5
3.0
2.5
2.0
1.5
1.0
0.5
0.0
-0.791 E_{p1}
SWVii Net
SWVii Fwd
SWVii Rev
Current (µA)
2.0
1.5
1.0
0.5
0.0
-0.5
-1.0
-2.0
-1.5
-1.0
-0.5
0.0
Potential (V vs Ag/Ag$^+$)

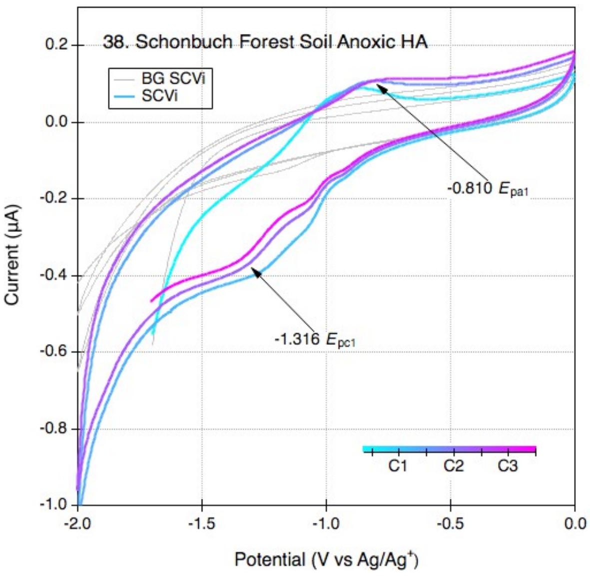
38. Schonbuch Forest Soil Anoxic HA
BG SCVi
SCVi
-0.810 E_{pa1}
-1.316 E_{pc1}
C1
C2
C3
Current (µA)
0.2
0.0
-0.2
-0.4
-0.6
-0.8
-1.0
-2.0
-1.5
-1.0
-0.5
0.0
Potential (V vs Ag/Ag$^+$)

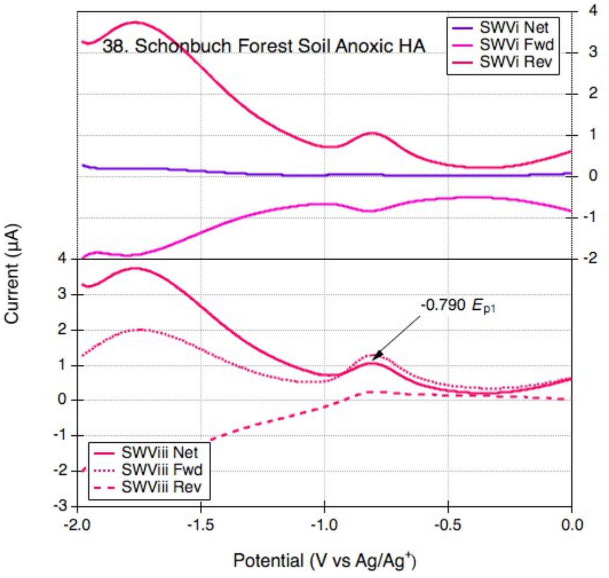
38. Schonbuch Forest Soil Anoxic HA
SWVi Net
SWVi Fwd
SWVi Rev
-0.790 E_{p1}
SWViii Net
SWViii Fwd
SWViii Rev
Current (µA)
4
3
2
1
0
-1
-2
-3
-2.0
-1.5
-1.0
-0.5
0.0
Potential (V vs Ag/Ag$^+$)

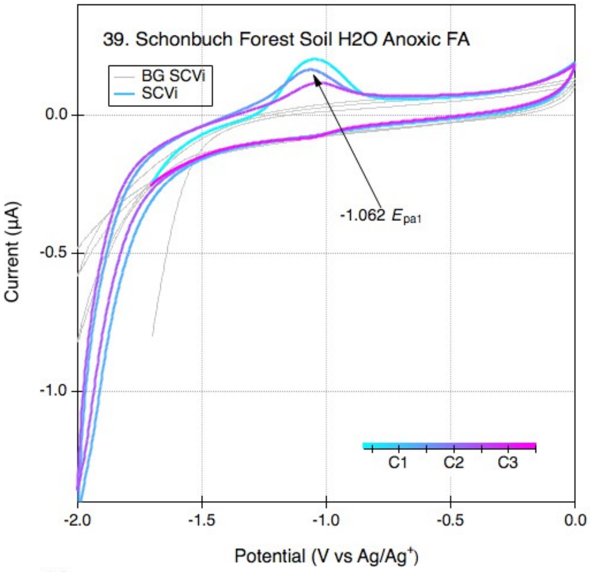
39. Schonbuch Forest Soil H2O Anoxic FA
BG SCVi
SCVi
-1.062 E_{pa1}
C1
C2
C3
Current (µA)
0.0
-0.5
-1.0
-2.0
-1.5
-1.0
-0.5
0.0
Potential (V vs Ag/Ag$^+$)

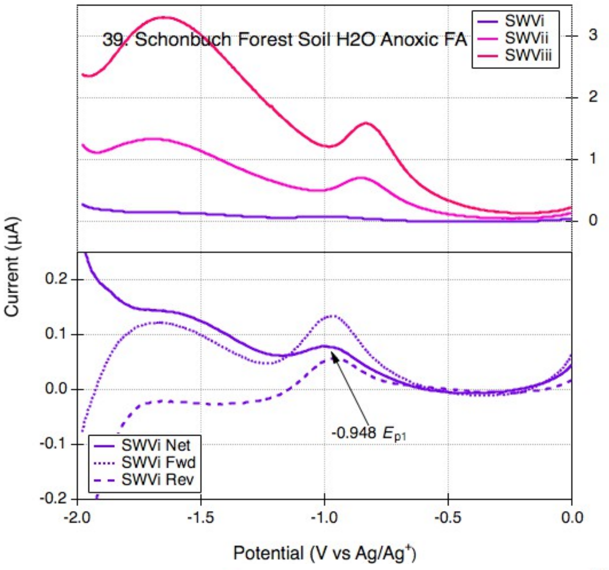
39. Schonbuch Forest Soil H2O Anoxic FA
SWVi
SWVii
SWViii
3
2
1
0
-0.948 E_{p1}
SWVi Net
SWVi Fwd
SWVi Rev
Current (µA)
0.2
0.1
0.0
-0.1
-0.2
-2.0
-1.5
-1.0
-0.5
0.0
Potential (V vs Ag/Ag$^+$)

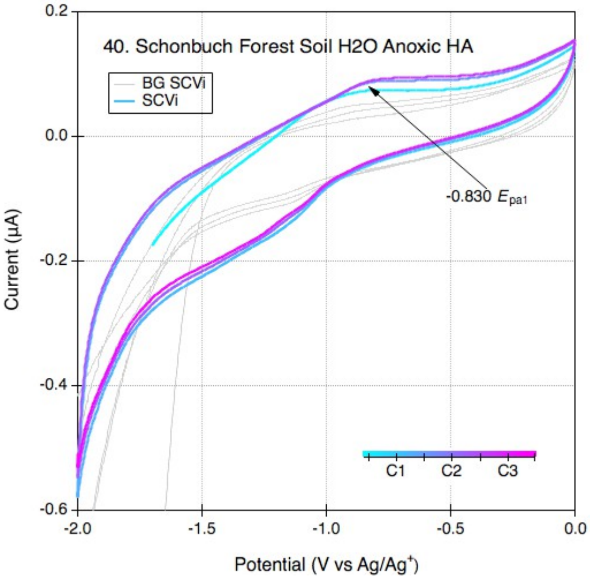
40. Schonbuch Forest Soil H2O Anoxic HA
BG SCVi
SCVi
-0.830 E_{pa1}
C1
C2
C3
Current (µA)
0.2
0.0
-0.2
-0.4
-0.6
-2.0
-1.5
-1.0
-0.5
0.0
Potential (V vs Ag/Ag$^+$)

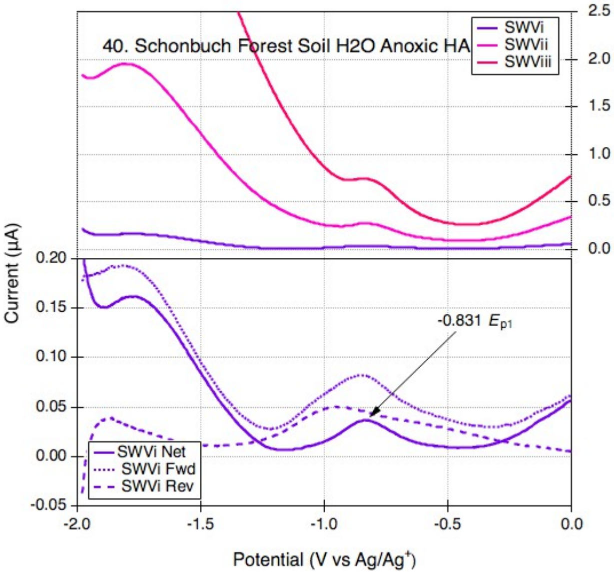
40. Schonbuch Forest Soil H2O Anoxic HA
SWVi
SWVii
SWViii
2.5
2.0
1.5
1.0
0.5
0.0
-0.831 E_{p1}
SWVi Net
SWVi Fwd
SWVi Rev
Current (µA)
0.20
0.15
0.10
0.05
0.00
-0.05
-2.0
-1.5
-1.0
-0.5
0.0
Potential (V vs Ag/Ag$^+$)

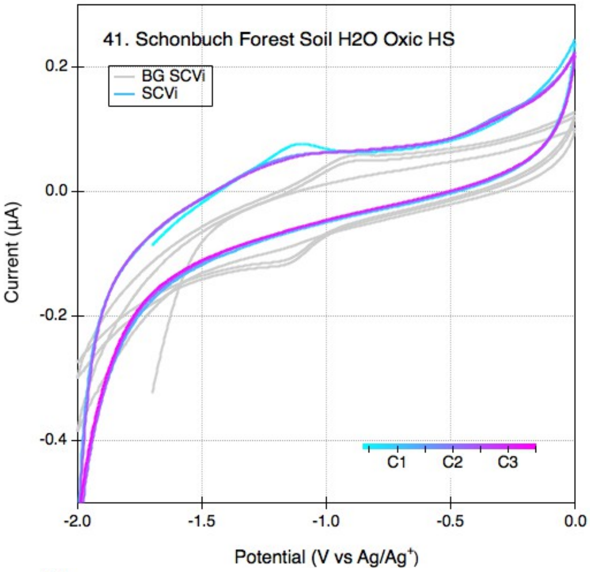
41. Schonbuch Forest Soil H2O Oxic HS
BG SCVi
SCVi
C1
C2
C3
Current (µA)
Potential (V vs Ag/Ag$^+$)
0.2
0.0
-0.2
-0.4
-2.0
-1.5
-1.0
-0.5
0.0

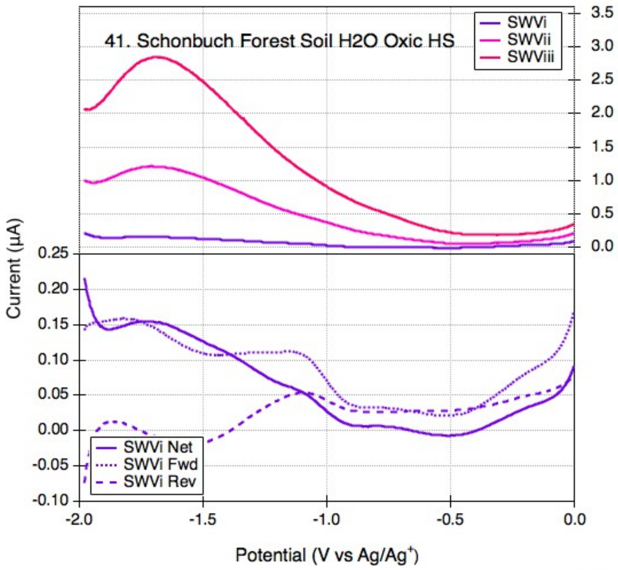
41. Schonbuch Forest Soil H2O Oxic HS
SWVi
SWVii
SWViii
SWVi Net
SWVi Fwd
SWVi Rev
Current (µA)
Potential (V vs Ag/Ag$^+$)
3.5
3.0
2.5
2.0
1.5
1.0
0.5
0.0
0.25
0.20
0.15
0.10
0.05
0.00
-0.05
-0.10
-2.0
-1.5
-1.0
-0.5
0.0

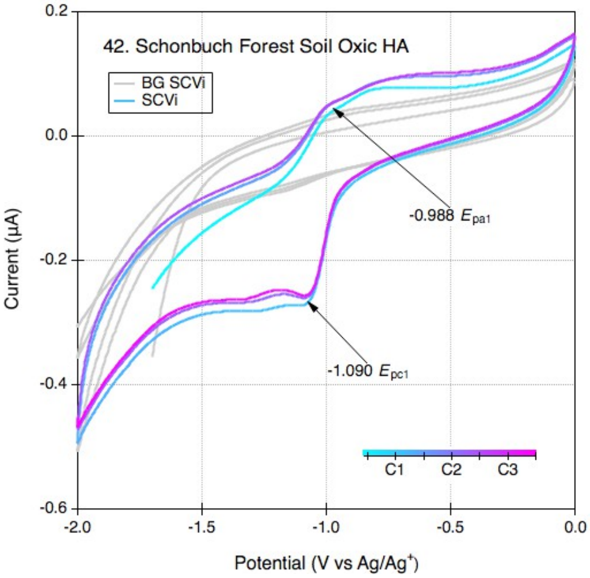
42. Schonbuch Forest Soil Oxic HA
BG SCVi
SCVi
-0.988 E_{pa1}
-1.090 E_{pc1}
C1
C2
C3
Current (µA)
Potential (V vs Ag/Ag$^+$)
0.2
0.0
-0.2
-0.4
-0.6
-2.0
-1.5
-1.0
-0.5
0.0

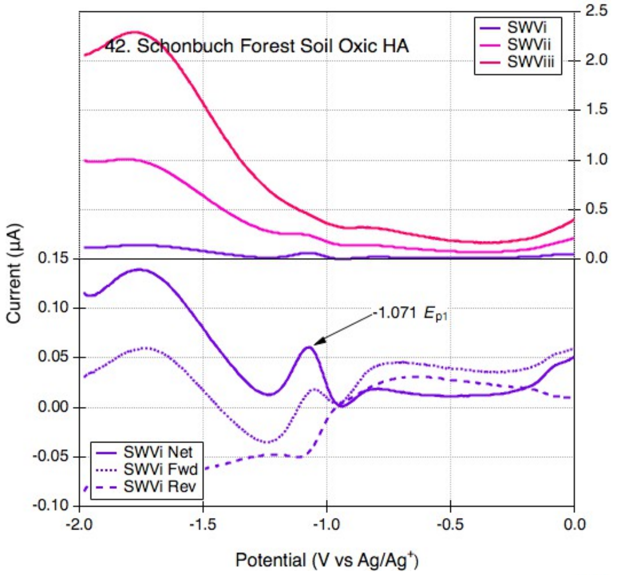
42. Schonbuch Forest Soil Oxic HA
SWVi
SWVii
SWViii
-1.071 E_{p1}
SWVi Net
SWVi Fwd
SWVi Rev
Current (µA)
Potential (V vs Ag/Ag$^+$)
2.5
2.0
1.5
1.0
0.5
0.0
0.15
0.10
0.05
0.00
-0.05
-0.10
-2.0
-1.5
-1.0
-0.5
0.0

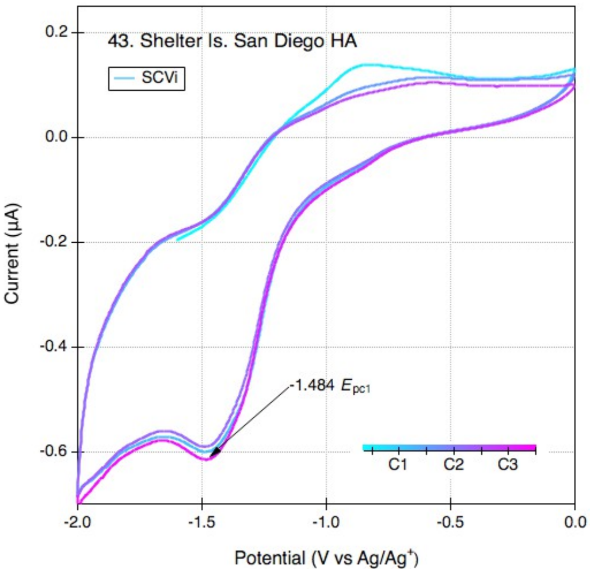
43. Shelter Is. San Diego HA
SCVi
-1.484 E_{pc1}
C1
C2
C3
Current (µA)
Potential (V vs Ag/Ag$^+$)
0.2
0.0
-0.2
-0.4
-0.6
-2.0
-1.5
-1.0
-0.5
0.0

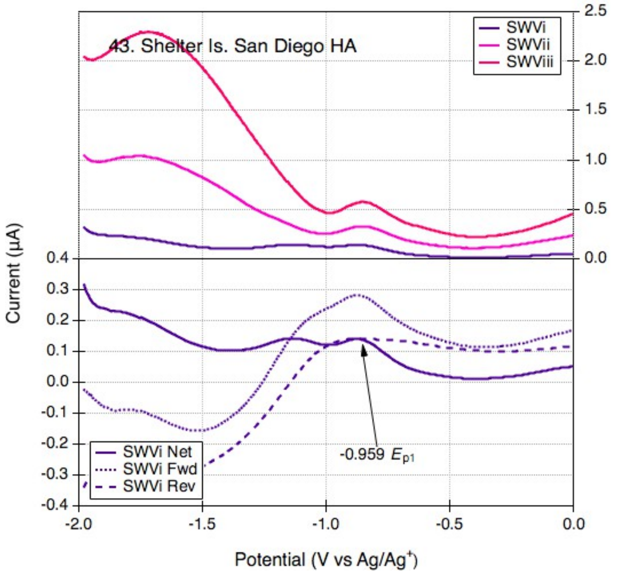
43. Shelter Is. San Diego HA
SWVi
SWVii
SWViii
SWVi Net
SWVi Fwd
SWVi Rev
-0.959 E_{p1}
Current (µA)
Potential (V vs Ag/Ag$^+$)
2.5
2.0
1.5
1.0
0.5
0.0
0.4
0.3
0.2
0.1
0.0
-0.1
-0.2
-0.3
-0.4
-2.0
-1.5
-1.0
-0.5
0.0

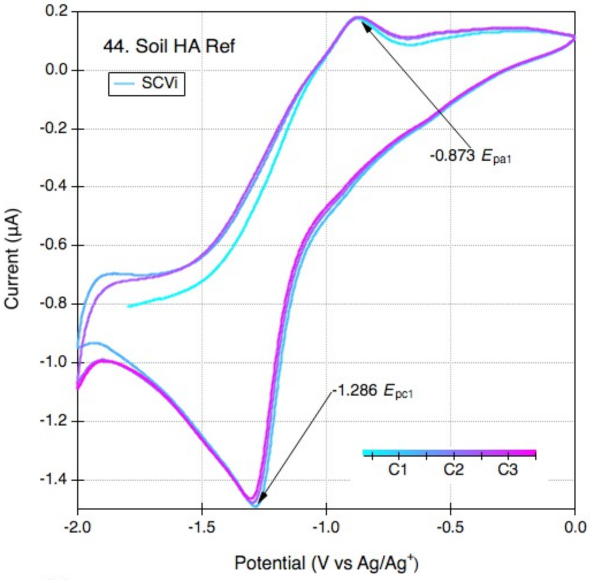
44. Soil HA Ref
SCVi
-0.873 E_{pa1}
-1.286 E_{pc1}
C1
C2
C3
Current (µA)
Potential (V vs Ag/Ag$^+$)
0.2
0.0
-0.2
-0.4
-0.6
-0.8
-1.0
-1.2
-1.4
-2.0
-1.5
-1.0
-0.5
0.0

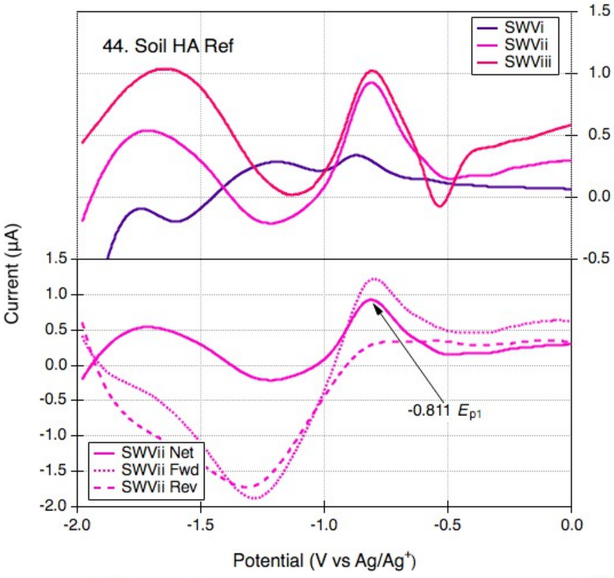
44. Soil HA Ref
SWVi
SWVii
SWViii
SWVii Net
SWVii Fwd
SWVii Rev
-0.811 E_{p1}
Current (µA)
Potential (V vs Ag/Ag$^+$)
1.5
1.0
0.5
0.0
-0.5
1.5
1.0
0.5
0.0
-0.5
-1.0
-1.5
-2.0
-2.0
-1.5
-1.0
-0.5
0.0

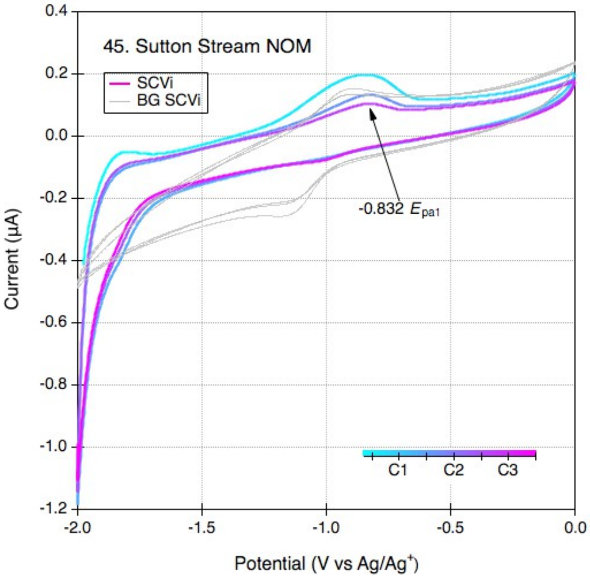
45. Sutton Stream NOM
SCVi
BG SCVi
-0.832 E_{pa1}
C1
C2
C3
Current (µA)
Potential (V vs Ag/Ag$^+$)
0.4
0.2
0.0
-0.2
-0.4
-0.6
-0.8
-1.0
-1.2
-2.0
-1.5
-1.0
-0.5
0.0

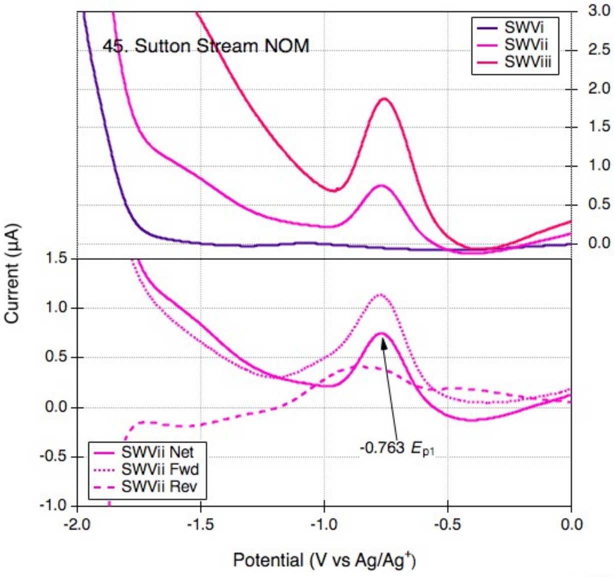
45. Sutton Stream NOM
SWVi
SWVii
SWViii
SWVii Net
SWVii Fwd
SWVii Rev
-0.763 E_{p1}
Current (µA)
Potential (V vs Ag/Ag$^+$)
3.0
2.5
2.0
1.5
1.0
0.5
0.0
1.5
1.0
0.5
0.0
-0.5
-1.0
-2.0
-1.5
-1.0
-0.5
0.0

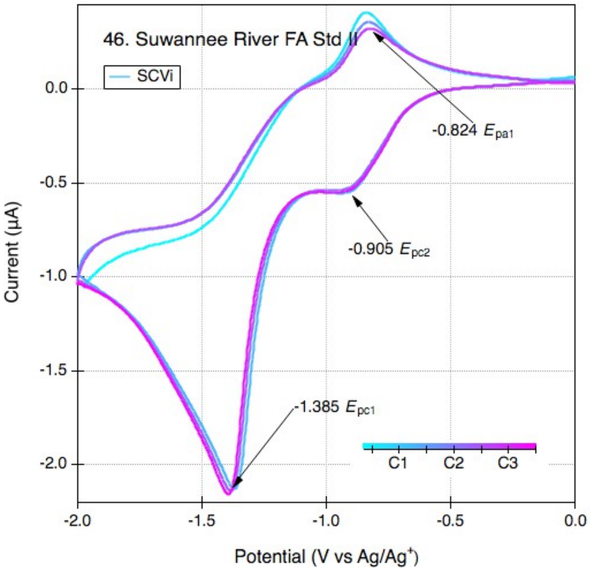
46. Suwannee River FA Std II
SCVi
-0.824 E_{pa1}
-0.905 E_{pc2}
-1.385 E_{pc1}
C1
C2
C3
Current (µA)
Potential (V vs Ag/Ag$^+$)
0.0
-0.5
-1.0
-1.5
-2.0
-2.0
-1.5
-1.0
-0.5
0.0

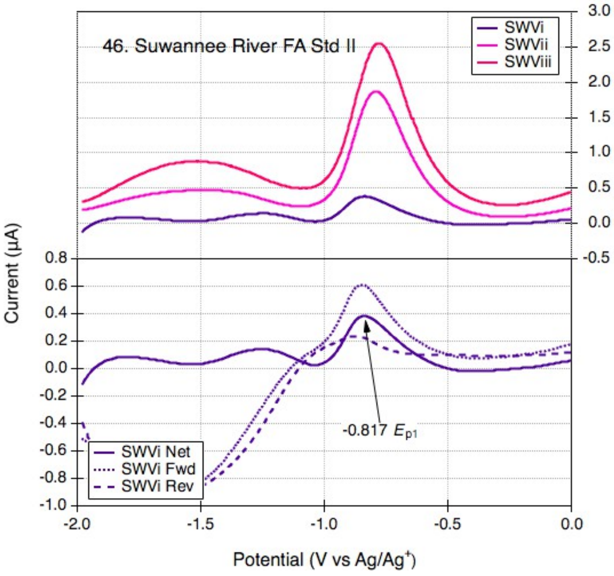
46. Suwannee River FA Std II
SWVi
SWVii
SWViii
SWVi Net
SWVi Fwd
SWVi Rev
-0.817 E_{p1}
Current (µA)
Potential (V vs Ag/Ag$^+$)
3.0
2.5
2.0
1.5
1.0
0.5
0.0
-0.5
0.8
0.6
0.4
0.2
0.0
-0.2
-0.4
-0.6
-0.8
-1.0
-2.0
-1.5
-1.0
-0.5
0.0

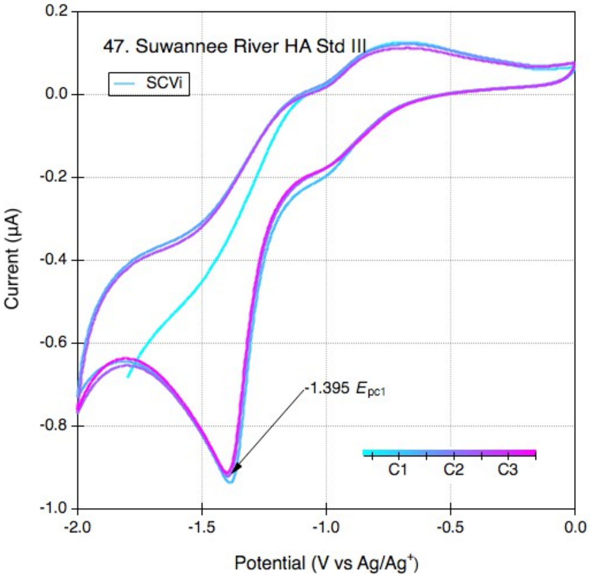
47. Suwannee River HA Std III
SCVi
-1.395 E_{pc1}
C1
C2
C3
Current (μA)
Potential (V vs Ag/Ag$^+$)
0.2
0.0
-0.2
-0.4
-0.6
-0.8
-1.0
-2.0
-1.5
-1.0
-0.5
0.0

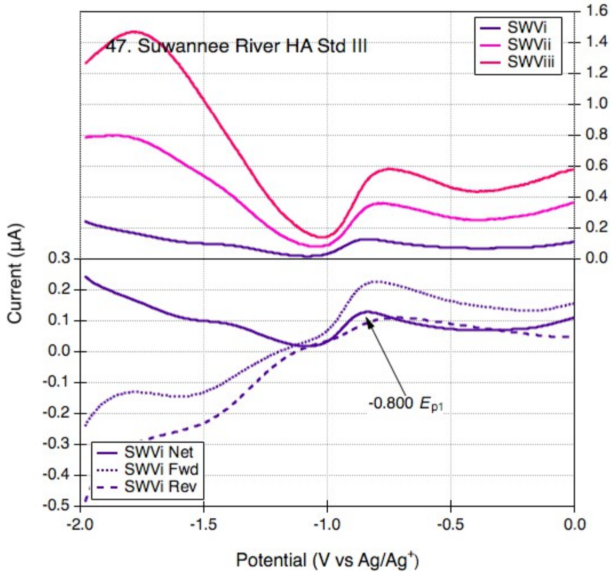
47. Suwannee River HA Std III
SWVi
SWVii
SWViii
-0.800 E_{p1}
SWVi Net
SWVi Fwd
SWVi Rev
Current (μA)
Potential (V vs Ag/Ag$^+$)
1.6
1.4
1.2
1.0
0.8
0.6
0.4
0.2
0.0
0.3
0.2
0.1
0.0
-0.1
-0.2
-0.3
-0.4
-0.5
-2.0
-1.5
-1.0
-0.5
0.0

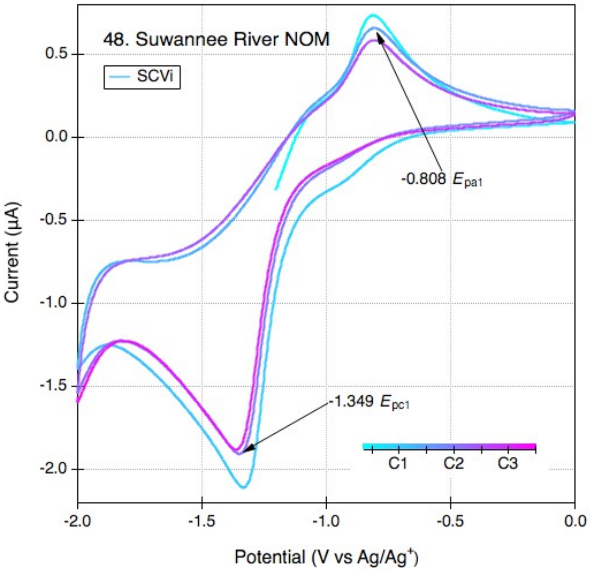
48. Suwannee River NOM
SCVi
-0.808 E_{pa1}
-1.349 E_{pc1}
C1
C2
C3
Current (μA)
Potential (V vs Ag/Ag$^+$)
0.5
0.0
-0.5
-1.0
-1.5
-2.0
-2.0
-1.5
-1.0
-0.5
0.0

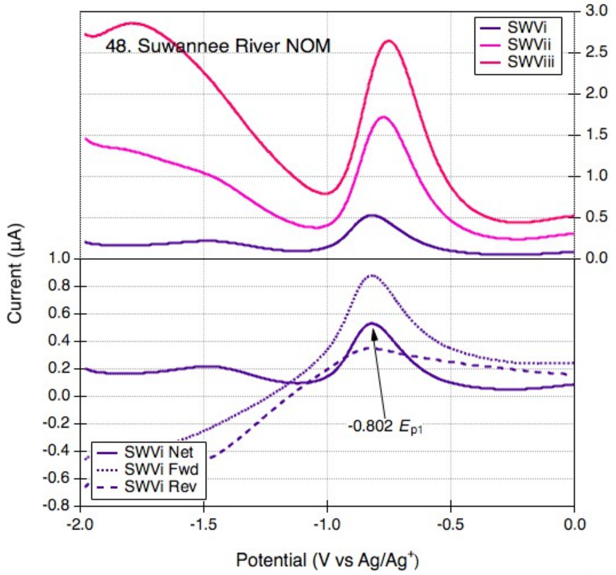
48. Suwannee River NOM
SWVi
SWVii
SWViii
-0.802 E_{p1}
SWVi Net
SWVi Fwd
SWVi Rev
Current (μA)
Potential (V vs Ag/Ag$^+$)
3.0
2.5
2.0
1.5
1.0
0.5
0.0
1.0
0.8
0.6
0.4
0.2
0.0
-0.2
-0.4
-0.6
-0.8
-2.0
-1.5
-1.0
-0.5
0.0

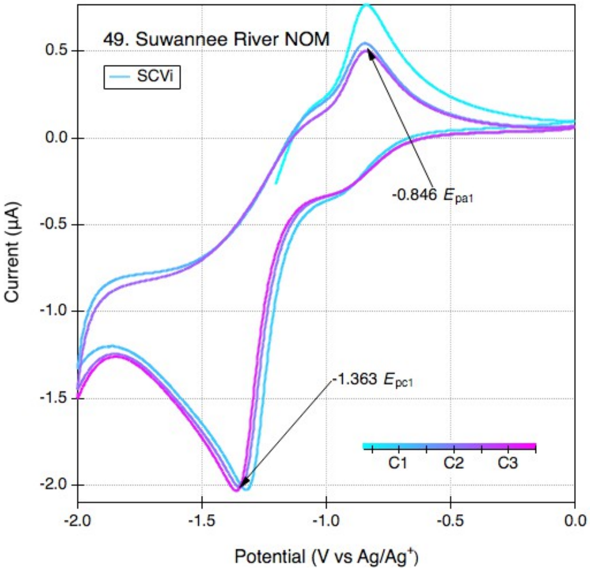
49. Suwannee River NOM
SCVi
-0.846 E_{pa1}
-1.363 E_{pc1}
C1
C2
C3
Current (μA)
Potential (V vs Ag/Ag$^+$)
0.5
0.0
-0.5
-1.0
-1.5
-2.0
-2.0
-1.5
-1.0
-0.5
0.0

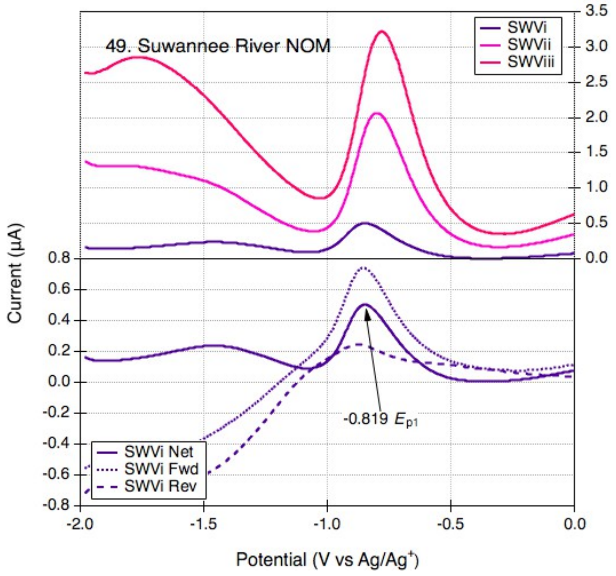
49. Suwannee River NOM
SWVi
SWVii
SWViii
-0.819 E_{p1}
SWVi Net
SWVi Fwd
SWVi Rev
Current (μA)
Potential (V vs Ag/Ag$^+$)
3.5
3.0
2.5
2.0
1.5
1.0
0.5
0.0
0.8
0.6
0.4
0.2
0.0
-0.2
-0.4
-0.6
-0.8
-2.0
-1.5
-1.0
-0.5
0.0

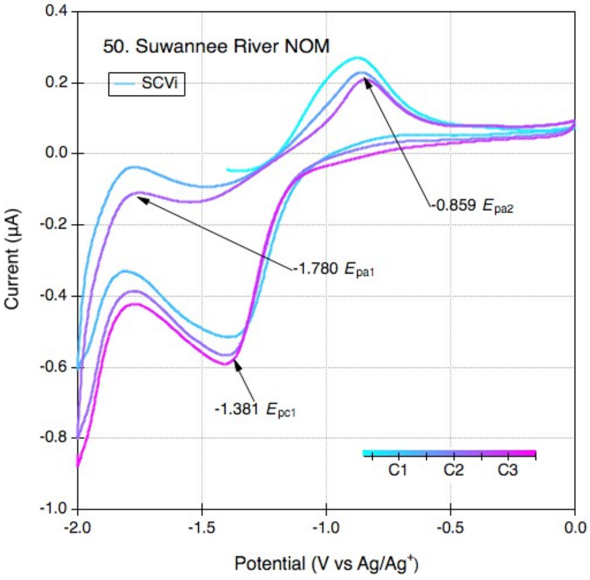
50. Suwannee River NOM
SCVi
-0.859 E_{pa2}
-1.780 E_{pa1}
-1.381 E_{pc1}
C1
C2
C3
Current (μA)
0.4
0.2
0.0
-0.2
-0.4
-0.6
-0.8
-1.0
-2.0
-1.5
-1.0
-0.5
0.0
Potential (V vs Ag/Ag$^+$)

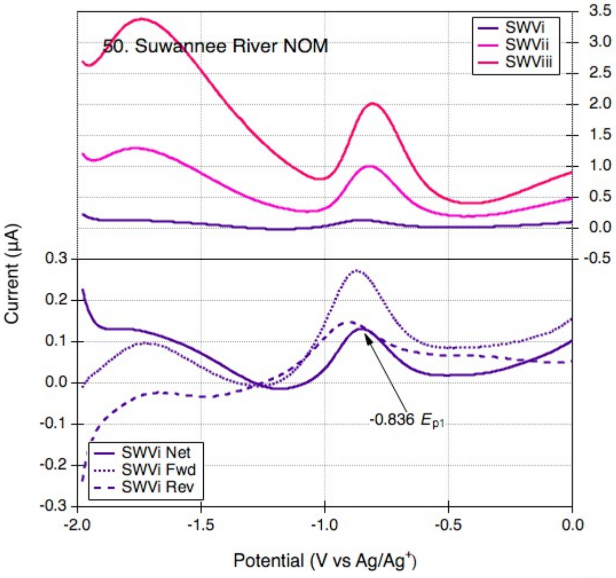
50. Suwannee River NOM
SWVi
SWVii
SWViii
3.5
3.0
2.5
2.0
1.5
1.0
0.5
0.0
-0.5
Current (μA)
0.3
0.2
0.1
0.0
-0.1
-0.2
-0.3
-0.836 E_{p1}
SWVi Net
SWVi Fwd
SWVi Rev
-2.0
-1.5
-1.0
-0.5
0.0
Potential (V vs Ag/Ag$^+$)

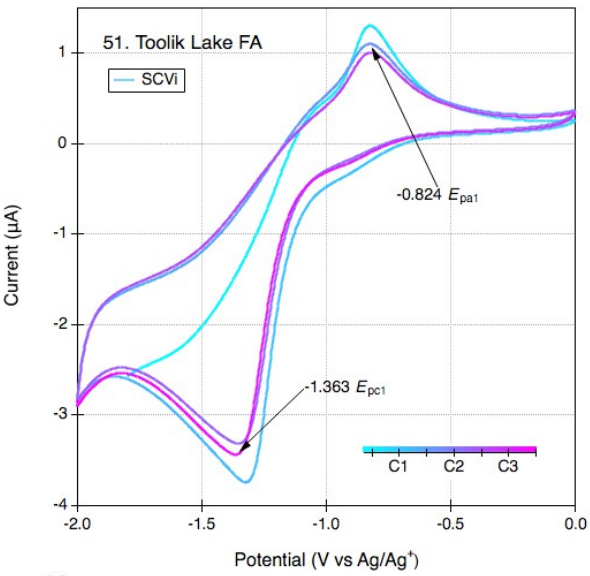
51. Toolik Lake FA
SCVi
-0.824 E_{pa1}
-1.363 E_{pc1}
C1
C2
C3
Current (μA)
1
0
-1
-2
-3
-4
-2.0
-1.5
-1.0
-0.5
0.0
Potential (V vs Ag/Ag$^+$)

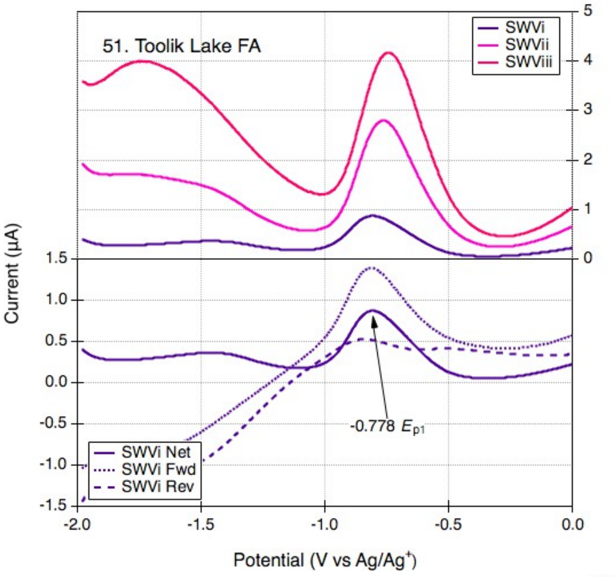
51. Toolik Lake FA
SWVi
SWVii
SWViii
5
4
3
2
1
0
Current (μA)
1.5
1.0
0.5
0.0
-0.5
-1.0
-1.5
-0.778 E_{p1}
SWVi Net
SWVi Fwd
SWVi Rev
-2.0
-1.5
-1.0
-0.5
0.0
Potential (V vs Ag/Ag$^+$)

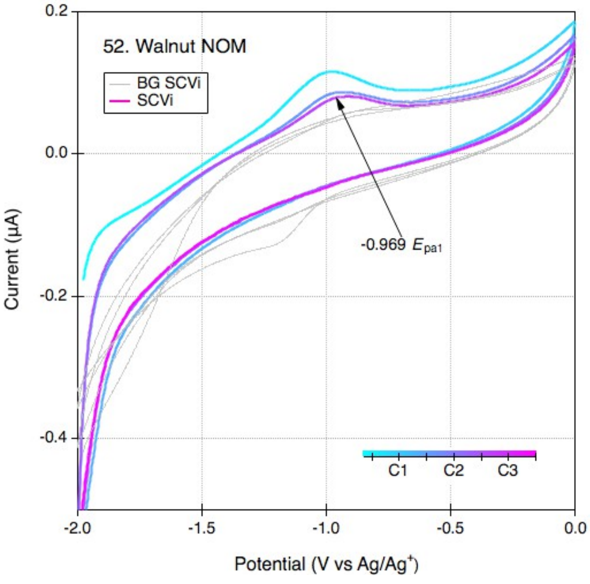
52. Walnut NOM
BG SCVi
SCVi
-0.969 E_{pa1}
C1
C2
C3
Current (μA)
0.2
0.0
-0.2
-0.4
-2.0
-1.5
-1.0
-0.5
0.0
Potential (V vs Ag/Ag$^+$)

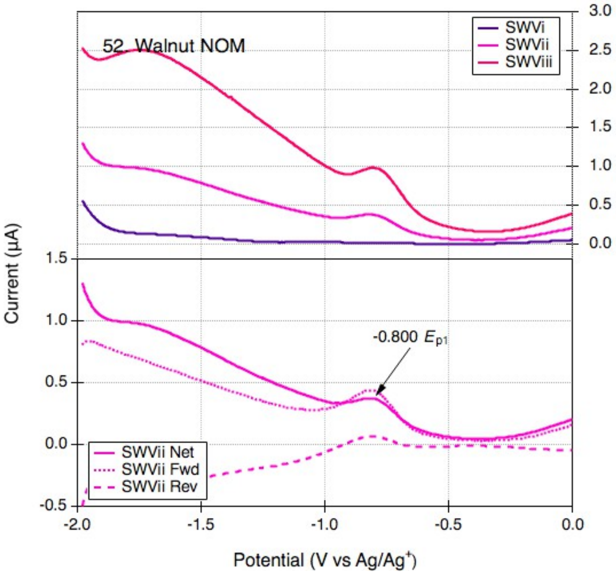
52. Walnut NOM
SWVi
SWVii
SWViii
3.0
2.5
2.0
1.5
1.0
0.5
0.0
Current (μA)
1.5
1.0
0.5
0.0
-0.5
-0.800 E_{p1}
SWVii Net
SWVii Fwd
SWVii Rev
-2.0
-1.5
-1.0
-0.5
0.0
Potential (V vs Ag/Ag$^+$)

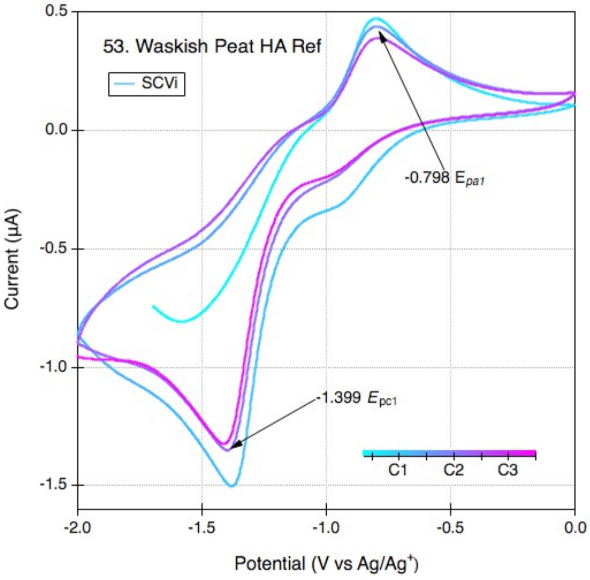
53. Waskish Peat HA Ref
SCVi
-0.798 E_{pa1}
-1.399 E_{pc1}
C1
C2
C3
Current (µA)
Potential (V vs Ag/Ag$^+$)
0.5
0.0
-0.5
-1.0
-1.5
-2.0
-1.5
-1.0
-0.5
0.0

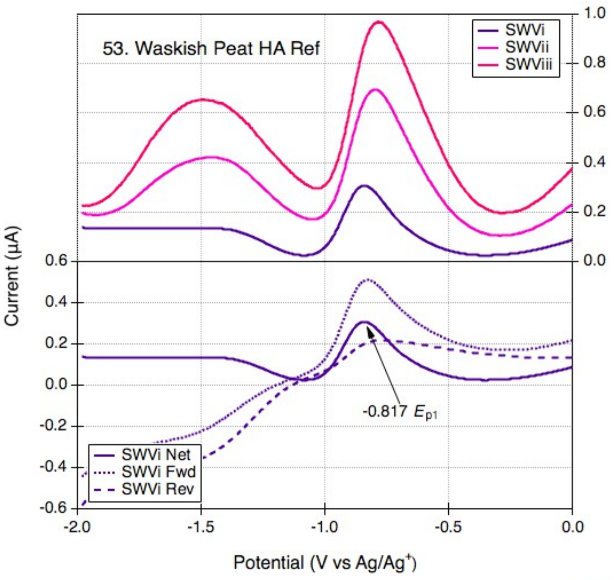
53. Waskish Peat HA Ref
SWVi
SWVii
SWViii
SWVi Net
SWVi Fwd
SWVi Rev
-0.817 E_{p1}
Current (µA)
Potential (V vs Ag/Ag$^+$)
1.0
0.8
0.6
0.4
0.2
0.0
0.6
0.4
0.2
0.0
-0.2
-0.4
-0.6
-2.0
-1.5
-1.0
-0.5
0.0

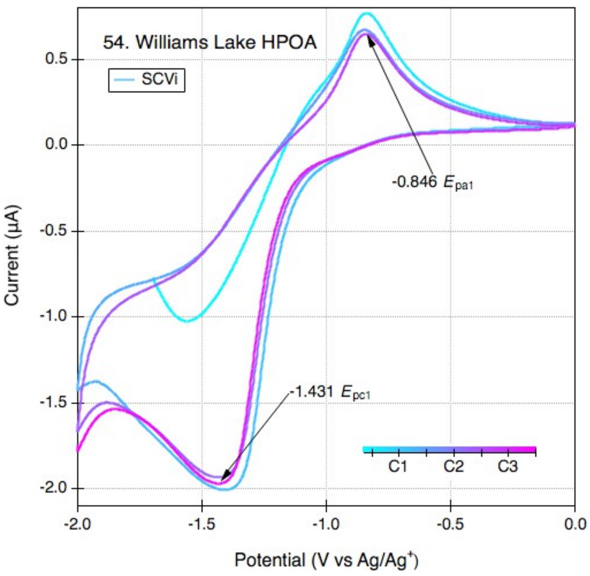
54. Williams Lake HPOA
SCVi
-0.846 E_{pa1}
-1.431 E_{pc1}
C1
C2
C3
Current (µA)
Potential (V vs Ag/Ag$^+$)
0.5
0.0
-0.5
-1.0
-1.5
-2.0
-2.0
-1.5
-1.0
-0.5
0.0

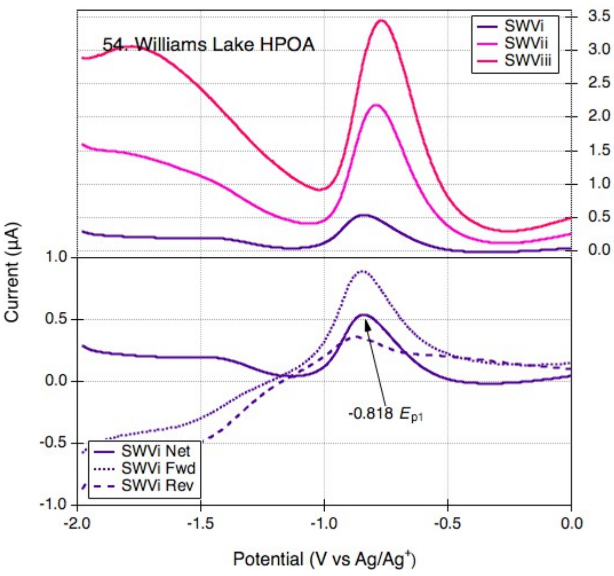
54. Williams Lake HPOA
SWVi
SWVii
SWViii
SWVi Net
SWVi Fwd
SWVi Rev
-0.818 E_{p1}
Current (µA)
Potential (V vs Ag/Ag$^+$)
3.5
3.0
2.5
2.0
1.5
1.0
0.5
0.0
1.0
0.5
0.0
-0.5
-1.0
-2.0
-1.5
-1.0
-0.5
0.0

B.6. Types of SCVs, Characteristics, and Current Breadth

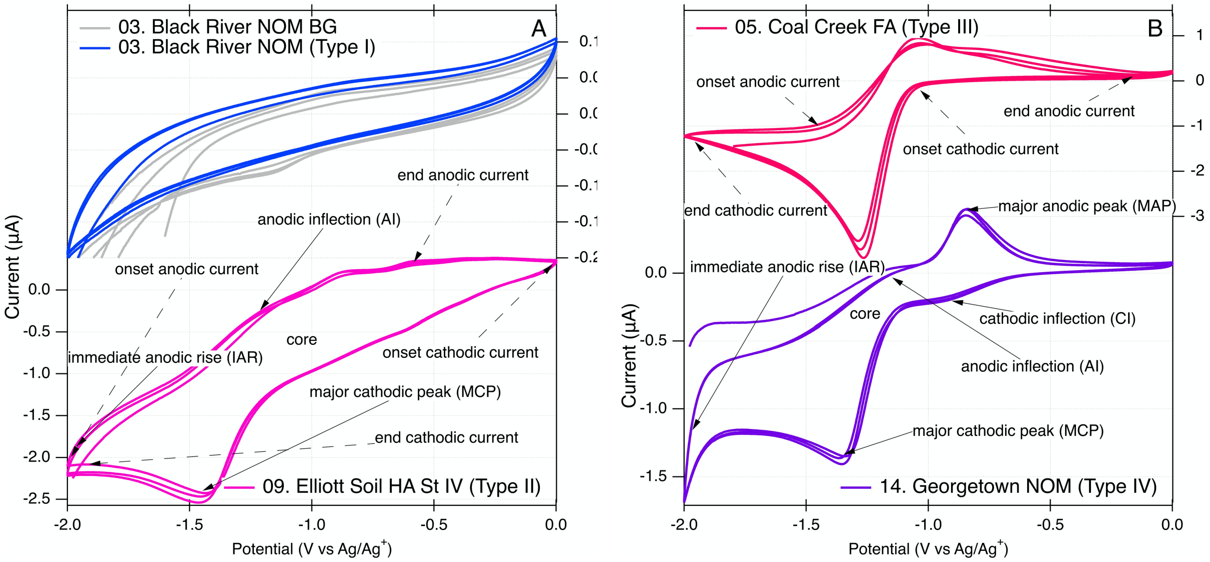

Figure B.5. Four types of SCV responses and definition of current breadth. (A) type I, mostly flat; type II, mostly core; (B) type III, model compound like; type IV, typical NOM response. Teal annotations signify onset and end of current responses (current breadth) as shown in Figure 6. Green annotations signify the six types of characteristics of all the NOMs as tabulated in Table S6. Conditions: 1.0 mg/mL (except for HS, which did not fully dissociate in DMSO) of HS in 0.1 M TBAFP in DMSO, 1.6 mm Pt working electrode, Pt coil counter electrode, and a Ag/Ag+ reference electrode filled with 0.1 M TBAFP and 0.005 M AgNO3 in DMSO. Scan rate: SCVi 25 mV s−1.

Table B.6. Ranking of Characteristics for NOM SCVs.

No.	Name	*Cat*	*Type*	*Core*	IAR	*AI*	MAP	*CI*	*MCP*	*Sum*
1	Bamboo NOM	2	1	2	2	0	1	0	0	6
2	Bemidji FA	3	4	2	3	3	3	1	3	19
3	Black River NOM	1	1	2	1	0	0	0	0	4
4	Cabbage Tree NOM	2	1	1	2	2	1	0	0	7
5	Coal Creek FA	3	3	1	0	0	3	0	3	10
6	Coal Creek HA	5	3	1	0	0	1	1	3	9
7	Elliott Soil FA Std II	4	4	3	2	1	3	1	3	17
8	Elliott Soil HA Std I	6	2	3	3	1	2	1	3	15
9	Elliott Soil HA Std IV	6	2	3	3	1	1	1	2	13
10	Everglades 2BS HPOA	7	4	1	3	1	3	0	2	14
11	Everglades F1 HPOA	7	4	2	2	1	3	2	3	17
12	Everglades F1 TPIA	7	4	1	2	1	3	2	3	16
13	Everglades LOX8 HPOA	7	4	1	2	1	3	2	3	16
14	Georgetown NOM	1	4	1	2	1	3	2	3	16
15	Georgetown NOM CH	1	4	1	2	1	3	0	3	14
16	Georgetown NOM PP	1	4	2	2	1	3	3	3	18
17	Great Dismal Swamp FA	3	4	1	2	1	3	1	3	15
18	Inangahua River NOM	1	1	2	2	0	2	0	0	7
19	Kauri NOM	2	1	2	2	0	2	0	0	7
20	Kitty Hawk NOM	1	4	1	2	0	3	1	2	13
21	Lake Fryxell FA	3	3	1	1	0	3	0	3	11
22	Leonardite HA Std I	6	2	3	3	0	2	1	2	13
23	Leonardite HA Std I	6	2	3	3	0	2	1	2	13
24	MW-6 NOM	1	1	2	2	0	1	0	0	6
25	Nordic Reservoir NOM	1	1	1	2	0	1	0	0	5
26	North Sea DOM	1	4	1	2	2	2	1	3	15
27	Ogeechee River FA	3	3	2	2	0	2	0	3	12
28	Pacific Ocean FA	3	4	1	3	1	3	1	3	16
29	Pahokee Peat FA Std II	4	4	2	2	1	3	2	3	17
30	Pahokee Peat HA Std I	6	4	3	2	1	3	1	3	17
31	Pahokee Peat HA Std I	6	4	3	2	1	3	1	3	17
32	Pine Barrens NOM	2	4	3	2	1	3	2	3	18
33	Pony Lake FA	3	4	2	2	0	3	0	3	14
34	Prairie Pot Hole P8 DOM	1	4	1	2	1	3	0	3	14

No.	**Name**	***Cat***	***Type***	***Core***	**IAR**	***AI***	**MAP**	***CI***	***MCP***	***Sum***
35	Red Tussock NOM	2		1	3	0	2	0	0	6
36	Rio Negro NOM	1	4	2	3	0	3	1	2	15
37	Schönbuch Anoxic FA	4	1	2	2	0	1	2	1	9
38	Schönbuch Anoxic HA	6	1	2	2	0	1	1	1	8
39	Schönbuch H_2O Anoxic FA	4	1	1	2	0	2	0	0	6
40	Schönbuch H_2O Anoxic HA	6	1	2	2	0	1	0	1	7
41	Schönbuch H_2O Oxic HS	2	1	2	2	0	1	0	0	6
42	Schönbuch Oxic HA	6	1	2	2	0	1	0	2	8
43	Shelter Is. San Diego HA	5	2	2	3	1	1	1	2	12
44	Soil HA Ref	6	4	2	2	0	2	0	3	13
45	Sutton Stream NOM	1	1	1	2	0	1	0	0	5
46	Suwannee River FA Std II	3	4	2	1	2	3	3	3	18
47	Suwannee River HA Std III	5	4	2	2	2	2	2	3	17
48	Suwannee River NOM	1	4	1	2	1	3	1	3	15
49	Suwannee River NOM	1	4	2	2	1	3	2	3	17
50	Suwannee River NOM	1	4	1	2	0	3	0	3	13
51	Toolik Lake FA	3	4	1	2	1	3	1	3	15
52	Walnut NOM	2	1	2	2	0	1	0	0	6
53	Waskish Peat HA Ref	6	4	1	3	2	3	2	3	18
54	Williams Lake HPOA	7	4	1	3	1	3	0	3	15

NOM category, type, characteristics, and sum of type and characteristics. Categories: NOM/A (1), NOM/T (2), FA/A (3) FA/T (4), HA/A (5), HA/T (6), HPOA/TPIA (7), where A and T are aqueous and terrestrial respectively. Types: no response (1), mostly core (2), model like (3), typical NOM behavior (4). Characteristics within type; Core, immediate anodic rise (IAR), anodic inflection (AI), major anodic peak (MAP), cathodic inflection (CI), major cathodic peak (MCP), where 0, 1, 2, 3 are lack of, small, medium and large response respectively. Sum is the sum of all columns excluding category.

Table B.7. Estimated Potential Breadths for NOM SCVs and SWVs.

No.	Name	*SCVas*[1]	*SCVae*[1]	*SCVcs*[2]	*SCVce*[2]	*SWVs*[3]	*SWVe*[3]
1	Bamboo NOM	−2.000	−0.689			−1.258	−0.554
2	Bemidji FA	−2.000	−1.373	−1.746	−0.681	−1.230	−0.502
3	Black River NOM					−1.978	−0.685
4	Cabbage Tree NOM	−1.979	−0.726			−1.000	−0.467
5	Coal Creek FA	−1.526	−0.096	−1.960	−1.000	−1.508	−0.546
6	Coal Creek HA	−1.516	−0.193	−1.998	−0.978	−1.512	−1.012
7	Elliott Soil FA Std II	−1.918	−0.143	−1.829	−0.635	−1.155	−0.481
8	Elliott Soil HA Std I	−1.978	−0.012	−1.978	−0.012	−1.036	−0.679
9	Elliott Soil HA Std IV	−1.996	−0.526	−1.978	−0.014	−1.234	−0.689
10	Everglades 2BS HPOA	−1.996	−0.324	−1.756	−0.996	−1.064	−0.471
11	Everglades F1 HPOA	−1.992	−0.227	−1.871	−0.534	−1.082	−0.439
12	Everglades F1 TPIA	−1.994	−0.119	−1.820	−0.701	−1.054	−0.449
13	Everglades LOX8 HPOA	−1.996	−0.227	−1.816	−0.760	−1.064	−0.504
14	Georgetown NOM	−1.994	−0.481	−1.681	−0.653	−1.060	−0.508
15	Georgetown NOM CH	−1.960	−0.356	−1.843	−0.719	−1.008	−0.479
16	Georgetown NOM PP	−1.990	−0.415	−1.736	−1.052	−1.012	−0.393
17	Great Dismal Swamp FA	−1.994	−0.046	−1.863	−0.673	−1.032	−0.369
18	Inangahua River NOM	−1.946	−0.573			−0.943	−0.481
19	Kauri NOM	−1.956	−0.689			−1.179	−0.477
20	Kitty Hawk NOM	−1.998	−1.462	−1.750	−0.691	−1.137	−0.538
21	Lake Fryxell FA	−1.990	−0.286	−1.861	−0.968	−1.536	−0.647
22	Leonardite HA Std I	−1.996	−0.619	−1.742	−0.008	−1.143	−0.574
23	Leonardite HA Std I	−1.998	−0.633	−1.673	−0.028	−1.105	−0.526
24	MW−6 NOM	−1.972	−0.582			−1.115	−0.643
25	Nordic Reservoir NOM	−1.046	−0.707			−0.911	−0.609
26	North Sea DOM	−1.994	−0.046	−1.871	−0.617	−1.014	−0.366
27	Ogeechee River FA	−1.964	−0.300	−1.806	−0.978	−1.512	−0.522
28	Pacific Ocean FA	−1.988	−0.078	−1.847	−0.719	−1.171	−0.425
29	Pahokee Peat FA Std II	−1.994	−0.096	−1.829	−0.637	−1.157	−0.481
30	Pahokee Peat HA Std I	−1.986	−0.546	−1.812	−0.479	−1.036	−0.512
31	Pahokee Peat HA Std I	−1.990	−0.536	−1.808	−0.510	−1.036	−0.508

No.	Name	*SCVas*[1]	*SCVae*[1]	*SCVcs*[2]	*SCVce*[2]	*SWVs*[3]	*SWVe*[3]
32	Pine Barrens NOM	−1.978	−0.346	−1.687	−0.052	−1.004	−0.429
33	Pony Lake FA	−1.994	−0.453	−1.843	−0.903	−1.175	−0.522
34	Prairie Pot Hole P8 DOM	−1.988	−0.096	−1.960	−1.080	−1.054	−0.429
35	Red Tussock NOM	−1.968	−1.508			−1.092	−0.498
36	Rio Negro NOM	−1.994	−1.429	−1.673	−0.195	−1.230	−0.504
37	Schönbuch Anoxic FA	−1.974	−0.726	−1.708	−1.121	−0.984	−0.449
38	Schönbuch Anoxic HA	−1.976	−0.560	−1.982	−0.060	−0.994	−0.401
39	Schönbuch H_2O Anoxic FA	−1.950	−0.776			−1.185	−0.494
40	Schönbuch H_2O Anoxic HA	−1.982	−0.504			−1.161	−0.508
41	Schönbuch H_2O Oxic HS						
42	Schönbuch Oxic HA	−1.990	−0.046	−1.960	−0.018	−1.258	−0.945
43	Shelter Is. San Diego HA	−1.998	−0.494	−1.673	−0.044	−1.449	−0.471
44	Soil HA Ref	−1.986	−0.637	−1.867	−0.024	−1.165	−0.508
45	Sutton Stream NOM	−1.996	−0.088			−0.967	−0.435
46	Suwannee River FA Std II	−1.996	−0.235	−1.978	−1.076	−1.032	−0.463
47	Suwannee River HA Std III	−1.996	−0.165	−1.802	−0.570	−1.064	−0.485
48	Suwannee River NOM	−1.986	−0.068	−1.816	−0.719	−1.074	−0.425
49	Suwannee River NOM	−1.990	−0.139	−1.857	−0.643	−1.070	−0.449
50	Suwannee River NOM	−1.986	−1.508	−1.774	−0.566	−1.137	−0.536
51	Toolik Lake FA	−1.998	−0.248	−1.816	−0.617	−1.068	−0.443
52	Walnut NOM	−1.990	−0.102			−0.971	−0.633
53	Waskish Peat HA Ref	−1.998	−0.123	−1.778	−0.482	−1.068	−0.443
54	Williams Lake HPOA	−1.986	−0.185	−1.829	−0.732	−1.088	−0.485

Estimated start and end of current response for SCV and SWV for all NOM samples. [1]Anodic start (*as*) and end (*ae*), [2]cathodic start (*cs*) and end (*ce*) of current response for SCV. [3]Start (*s*) and end (*e*) of current response for SWV. In the event there were more than one area of onset and end of current (2 peaks in a few of the NOMs) we only used the first peaks for comparison (E_{pa1}, E_{pc1}). It should be noted that the onset of potentials was not always easy to ascertain. For example, it was not immediately clear whether to choose the immediate start of current, or the current rise after the initial plateau. We chose the former, as the responses differed between NOMs from large plateaus (N07, N12, N15, N16) to no plateaus (N08, N09, N23). The difference in behavior between NOM samples suggests response is in excess of non-faradaic processes and therefore was important to include.

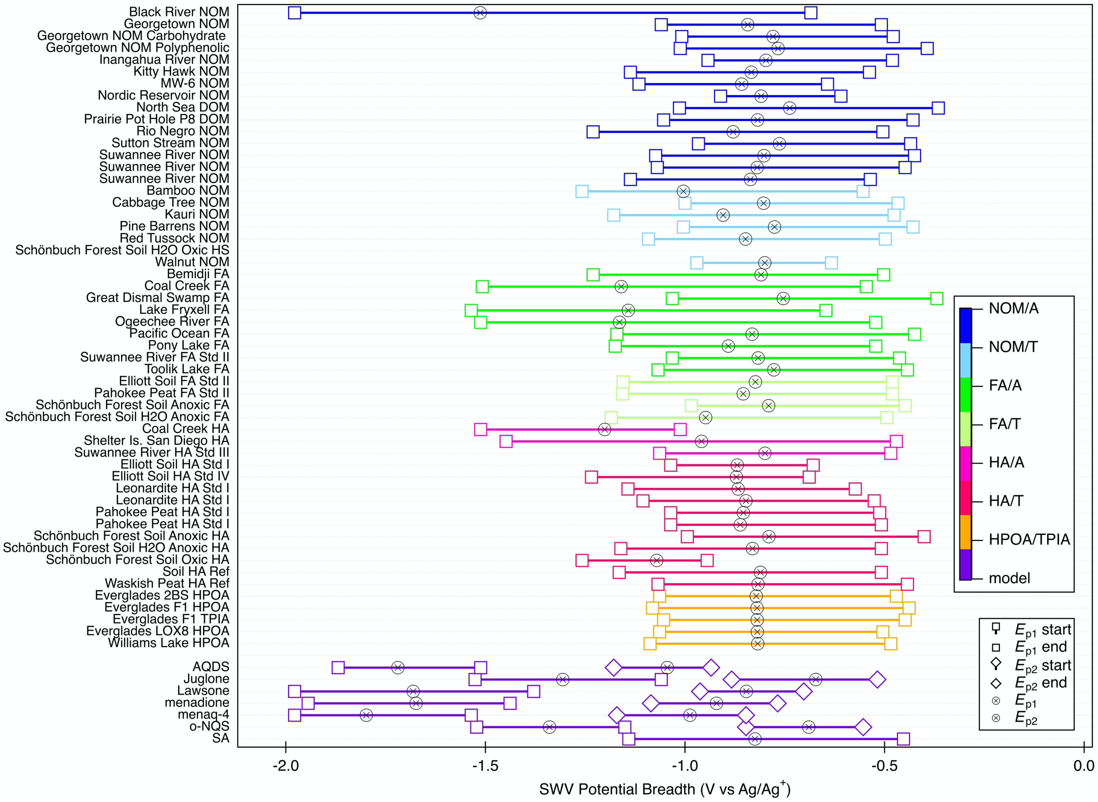

Figure B.6. Summary of the breadth of potential response and the peak potentials for SWV for all NOMs and model compounds. Conditions: 1.0 mg/mL (except for HS, which did not fully dissociate in DMSO) of HS in 0.1 M TBAFP in DMSO, 1.6 mm Pt working electrode, Pt coil counter electrode and a Ag/Ag$^+$ reference electrode filled with 0.1 M TBAFP and 0.005 M $AgNO_3$ in DMSO. Scan rate: 25 mV s^{-1}.

B.7. Grouping NOMs

Discussion for Figures B.7-B.16.

Some groups of NOM samples may be of particular interest for various reasons. To facilitate comparisons within these groups, selected SCV and SWV data (from **Figures B3** and **B4**, respectively) were rearranged into the summary plots below. The groups include: sample category (NOM, FA, and HA in **Figure B.7-B.9**), source region (Antarctic in **Figure B.10**; Everglades in **Figure B.11**), component fraction (**Figure B.12**), differences for Suwanee River NOM categories (**Figure B.13**) and source (**Figure B.14**), aging effects on Georgetown NOM (**Figure B.15**), and our own extractions of plant material (**Figure B.16)**.

In all three category groups (**Figure B.7-B.9**), the more positive SWV peak potential values are similar (~ −0.800 V vs Ag/Ag^+), while currents vary significantly. Comparing the current scale (y-axis) among the three groups shows that their response follows the trend FA > NOM > HA. In a few cases, the SWV data show a second peak at a more negative potential (~ −1.350 V), which may correspond to a prominent cathodic SCV peak around the same potential. This is especially evident for Prairie Pot Hole and Suwannee River NOMs (**Figure B.7**).

The Antarctic FAs (**Figure B.10**) show some unusual discrepancies between the SWVs and the SCV results. Lake Fryxell FA had the largest current response in the SWV, but the largest SCV response was from Toolik Lake FA (anodic and cathodic). The E_{p1} for Lake Fryxell FA and E_{pa1} for Toolik Lake differed notably from the corresponding peak potentials of the other two FAs; wheres all three FAs gave similar E_{pc1}. All of the Everglades HPOA and TPIA samples gave similar potentials for SCV and SWV (**Figure B.11**), so their potential was not significatly affected by the differences in their sulfur content. However, the current varied in the SWV data, with the high S oxidized and the intermediate S having the highest and lowest current responses respectively. The high S oxidized sample also had the highest E_{pc1}, consistent with the more oxidized sample having more reduction capacity.

Georgetown NOM samples (**Figure B.12**), include fractions that were enriched for carbohydrate and polyphenolic components. As expected, and supported by our previous work with these samples,(*18*) this fractionation affected both the SCV and SWV data. The polyphenolic fraction had the largest SWV current response, the largest SCV cathodic response, and the largest SCV initial anodic rise. Carbohydrate enriched GT NOM, had a medium response and the GT NOM (not enriched) was the least responsive.

Of all the sources, Suwannee River was represented by the most samples, including multiple categories and components. **Figure B.13** shows Suwannee River sourced samples by category, and **Figure B.14** compares multiple instances of the same material obtained from different providers. **Figure B.13** shows that Suwannee River NOM gave similar peak potentials, but larger peak currents compared with the HA and somewhat larger compared with FA samples, this is in slight contrast to the samples in **Figures B.7-B.9**, where FA had the largest current response followed by NOM and HA. The comparison of Suwannee River NOM from three providers (**Figure B.14**) shows very consistent peak potentials in all three NOMs, but the current response was much larger for N48 and N49 than N50. This might be consistent with the samples being nominally identical material, but the sample from Macalady was roughly a decade older. The aging of the dry material over a very long time span (years) is hard to compare to **Figure B.15,** which shows Georgetown NOM in DMSO over the time span of 6 days. However, the aging in DMSO was similar in response in that only the current was affected (only for SWV), but the potential remained the same.

Figure B.16 shows SWVs of our own extracted plant material (desribed in MT). Both the black walnut hull and pau d'arco bark potentials were similar in value as with our NOM samples. The black walnut hull had a pronounced response for the non-extracted (dry), and the water extracted sample, but when DMSO was used for extraction the peaks were not as pronounced and had a greater variety in potentials. For the pau d'arco bark the 24 h DMSO extraction sample had the most resolved peak, while the water extracted samples had more shouldering, indicating possible redox activity in that area that was not obtained with the DMSO only and the DMSO/ H_2O extracted samples.

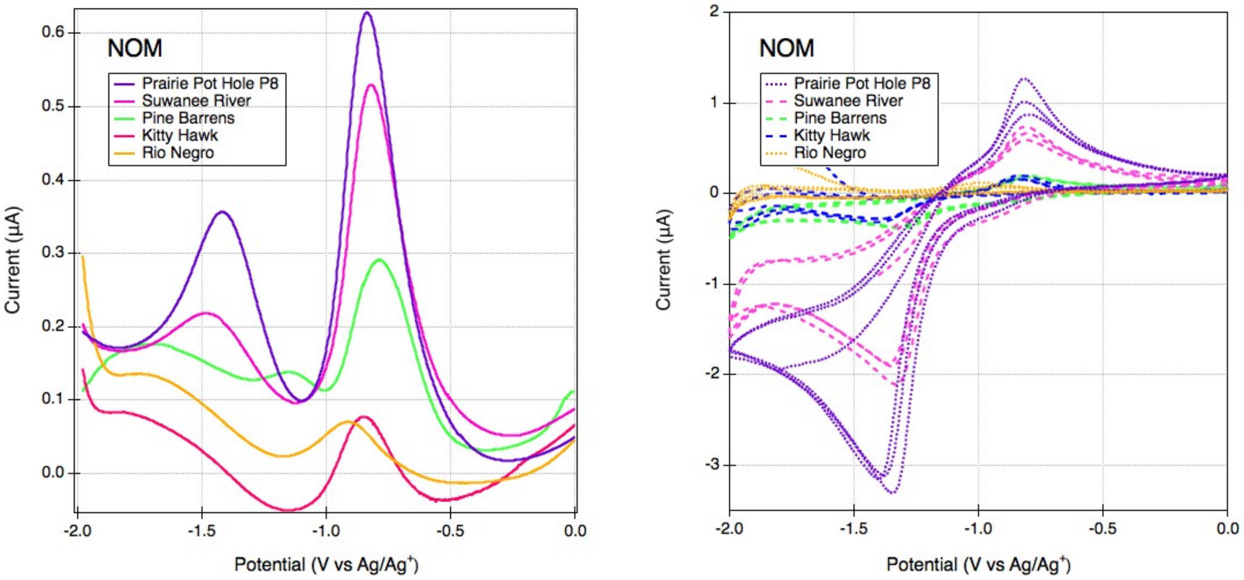

Figure B.7. Comparison of SWV*i* (**A**) and SCV*i* (**B**) of NOMs from different sources. Primary data **Figures B.4.34, 4.48, 4.32, 4.20, 4.36.**

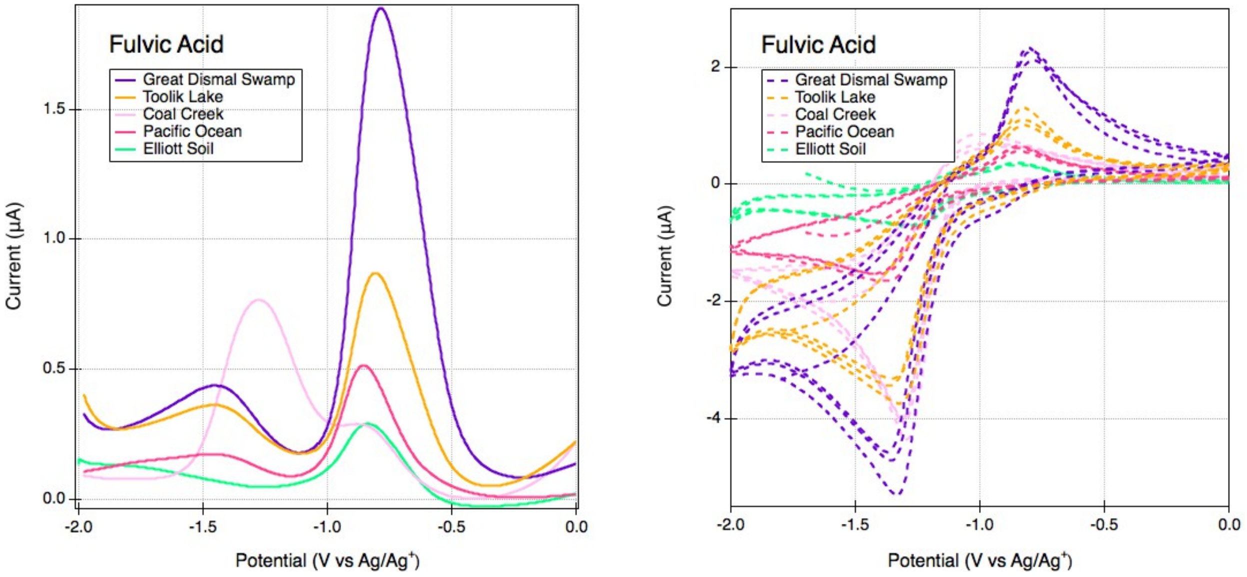

Figure B.8. Comparison of SWV*i* (**A**) and SCV*i* (**B**) of FAs from different sources. Primary data **Figures B.4.17, 4.51, 4.05, 4.28, 4.07.**

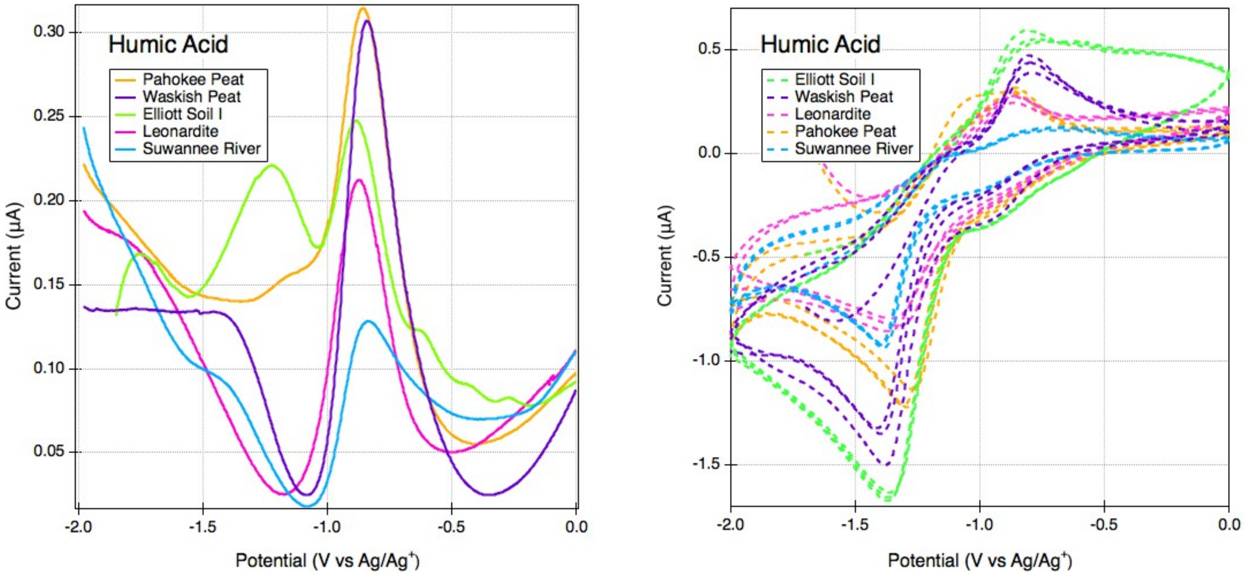

Figure B.9. Comparison of SWV*i* (**A**) and SCV*i* (**B**) of HAs from different sources. Primary data **Figures B.4.30, 4.53, 4.08, 4.22, 4.47.**

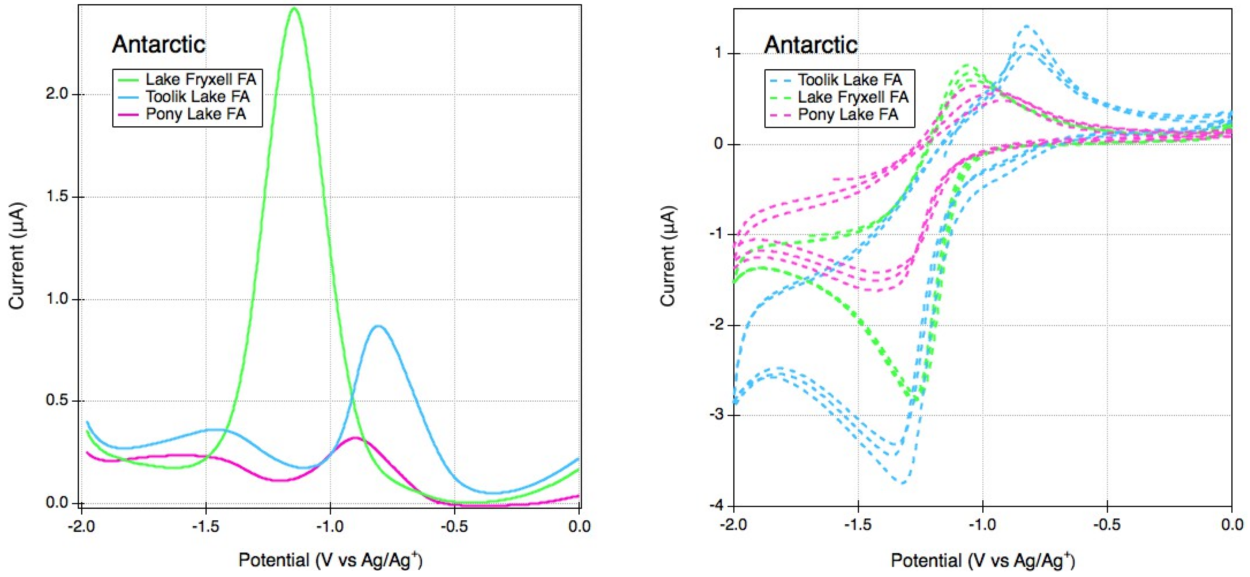

Figure B.10. Comparison of SWV*i* (**A**) and SCV*i* (**B**) of microbially derived FAs. Primary data **Figures B.4.21, 4.51, 4.33.**

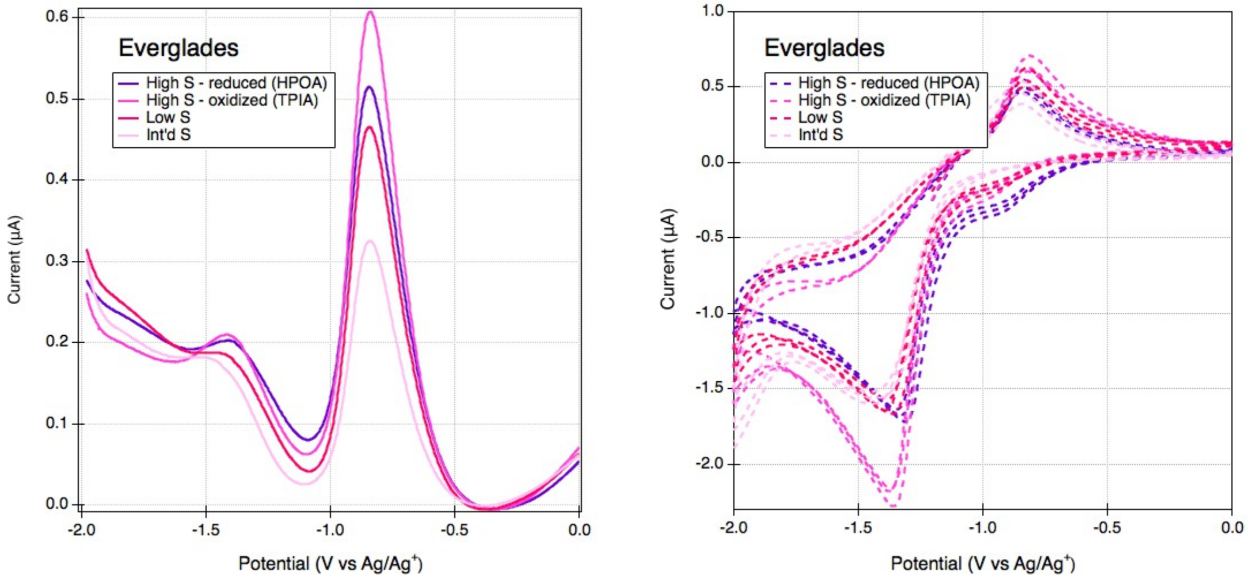

Figure B.11. Comparison of SWVi (A) and SCVi (B) of USGS samples from the Everglades with varying amounts of sulfur. Primary data **Figures B.4.11, 4.12, 4.13, 4.10**.

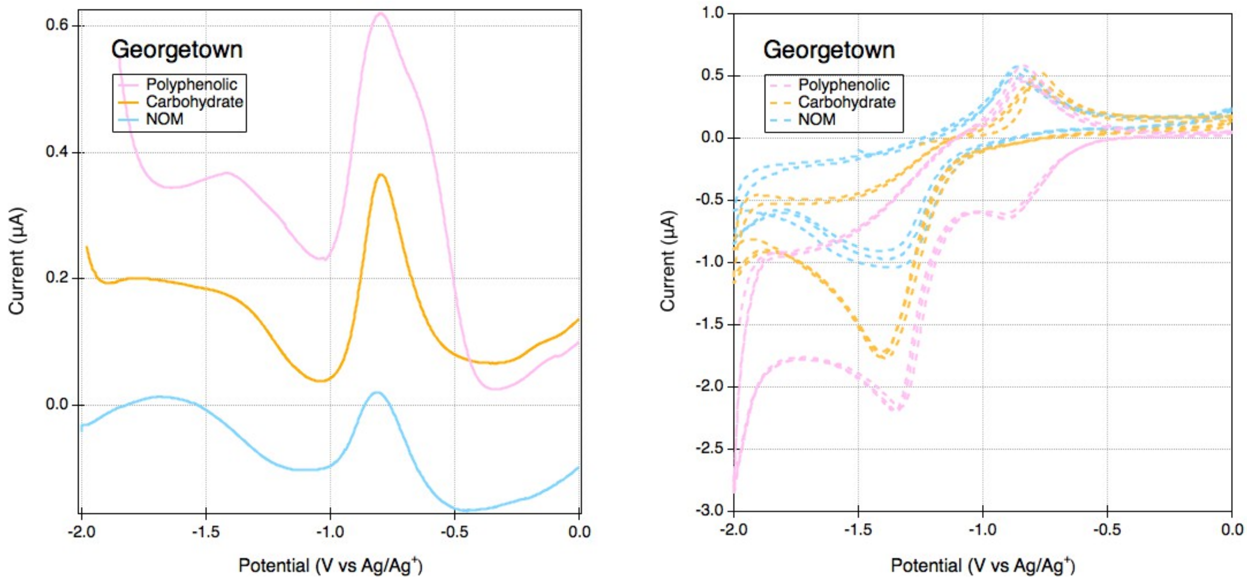

Figure B.12. Comparison of SWVi (A) and SCVi (B) of Georgetown NOM (blue) and fractions enriched in carbohydrate (yellow) and polyphenols (pink). Primary data **Figures B.4.16, 4.15, 4.14.**

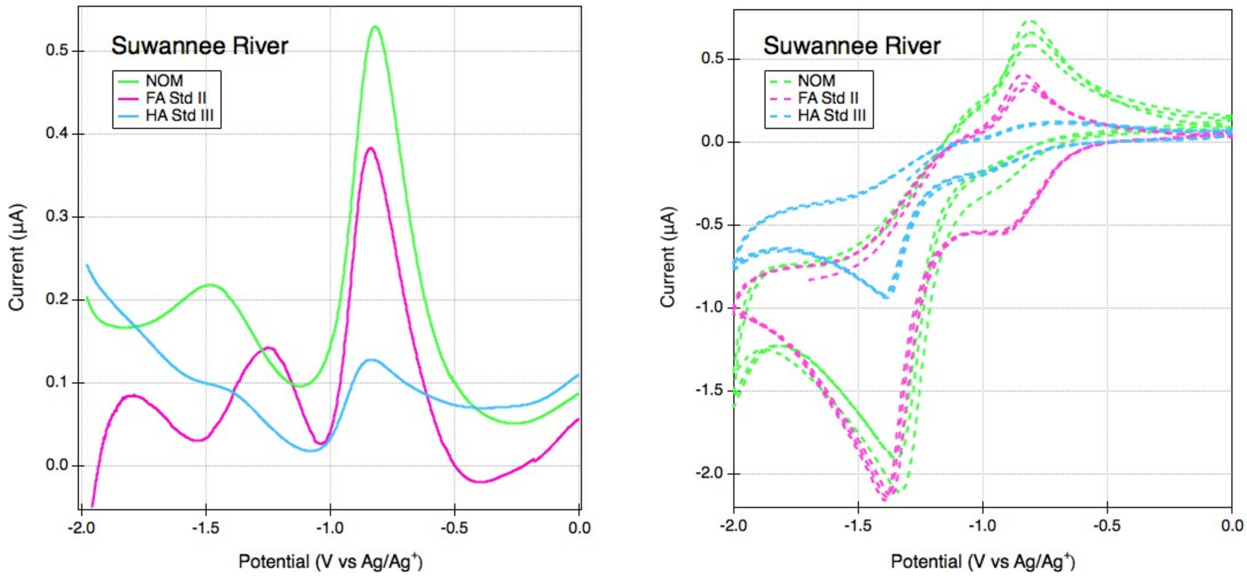

Figure B.13. Comparison of SWVi (A) and SCVi (B) of Suwannee River NOM (green), FA (pink) and HA (blue). Primary data Figures **B.4.48, 4.46, 4.47.**

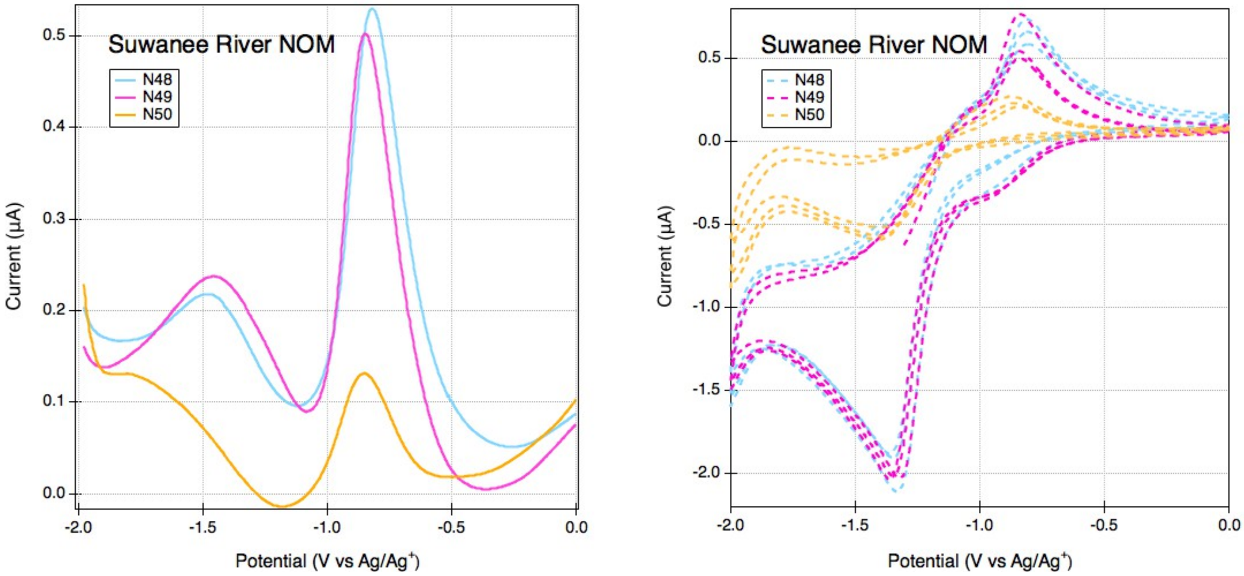

Figure B.14. Comparison of SWVi (A) and SCVi (B) of Suwannee River NOM obtained from different suppliers: J. Needoba, N48 (blue), IHSS, N49 (pink) and D. Macalady, N50 (yellow). Primary data **Figures B.4.48, 4.49, 4.50.**

B.8. Control Experiments (Aging)

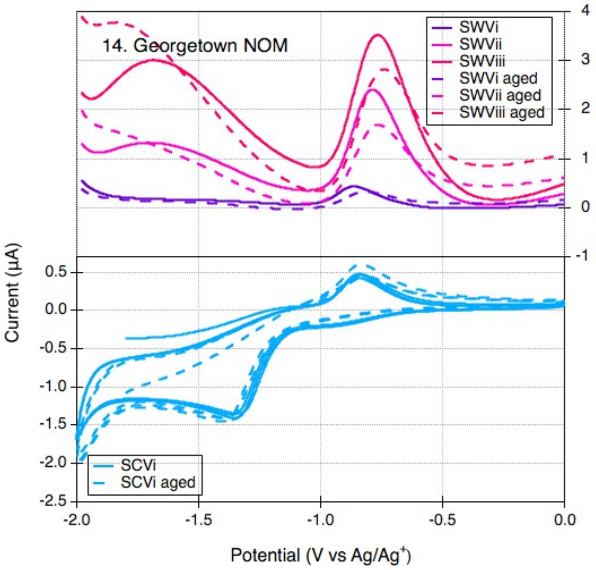

Figure B.15. The effects of aging on Georgetown NOM. Aged samples were left in an amber bottle in DMSO for ~6 days.

B.9. SWVs of Extracted Samples

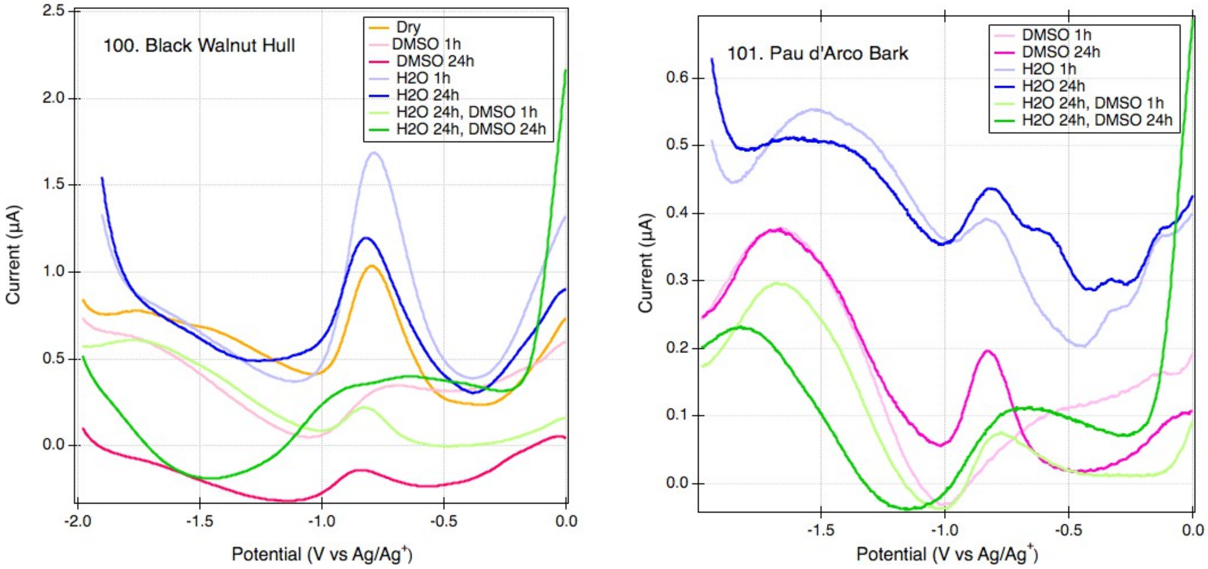

Figure B.16. SWVi of black walnut hull and pau d'arco bark extracted using H2O and DMSO. Conditions: 2.0 mg/mL of sample in 0.1 M TBAFP in DMSO, 1.6 mm Pt working electrode, Pt coil counter electrode and a Ag/Ag+ reference electrode filled with 0.1 M TBAFP and 0.005 M AgNO3 in DMSO. Scan rate: 25 mV s−1.

B.10. References (Appendix B Only)

1. P. G. Tratnyek, M. M. Scherer, B. Deng, S. Hu, Effects of natural organic matter, anthropogenic surfactants, and model quinones on the reduction of contaminants by zero-valent iron. *Water Res.* **35**, 4435-4443 (2001).

2. R. T. Anderson, J. N. Rooney-Varga, C. V. Gaw, D. R. Lovley, Anaerobic benzene oxidation in the Fe(III) reduction zone of petroleum-contaminated aquifers. *Environ. Sci. Technol.* **32**, 1222-1229 (1998).

3. D. L. Macalady, K. Walton-Day, New light on a dark subject: On the use of fluorescence data to deduce redox states of natural organic matter (NOM). *Aquat. Sci.* **71**, 135-143 (2009).

4. G. Aiken, E. Cotsaris, Soil and hydrology: their effect on NOM. *J. Am. Water Works Assoc.* **87**, 36-45 (1995).

5. Y.-P. Chin, G. Aiken, E. O'Loughlin, Molecular weight, polydispersity, and spectroscopic properties of aquatic humic substances. *Environ. Sci. Technol.* **28**, 1853-1858 (1994).

6. J. S. Waples, K. L. Nagy, G. R. Aiken, J. N. Ryan, Dissolution of cinnabar (HgS) in the presence of natural organic matter. *Geochim. Cosmochim. Acta* **69**, 1575-1588 (2005).

7. J. L. Weishaar *et al.*, Evaluation of specific ultraviolet absorbance as an indicator of the chemical composition and reactivity of dissolved organic carbon. *Environ. Sci. Technol.* **37**, 4702-4708 (2003).

8. K. A. Thorn, L. G. Cox, N-15 NMR spectra of naturally abundant nitrogen in soil and aquatic natural organic matter samples of the International Humic Substances Society. *Org. Geochem.* **40**, 484-499 (2009).

9. M. Aeschbacher, M. Sander, R. P. Schwarzenbach, Novel electrochemical approach to assess the redox properties of humic substances. *Environ. Sci. Technol.* **44**, 87-93 (2010).

10. M. Aeschbacher, C. Graf, R. P. Schwarzenbach, M. Sander, Antioxidant properties of humic substances. *Environ. Sci. Technol.* **46**, 4916-4925 (2012).

11. L. Klupfel, A. Piepenbrock, A. Kappler, M. Sander, Humic substances as fully regenerable electron acceptors in recurrently anoxic environments. *Nature Geosci.* **7**, 195-200 (2014).

12. Y. Yuan, X. Cai, Y. Wang, S. Zhou, Electron transfer at microbe-humic substances interfaces: Electrochemical, microscopic and bacterial community characterizations. *Chem. Geol.* **456**, 1-9 (2017).

13. N. Walpen, M. H. Schroth, M. Sander, Quantification of phenolic antioxidant moieties in dissolved organic matter by flow-injection analysis with electrochemical detection. *Environ. Sci. Technol.* **50**, 6423-6432 (2016).

14. B. A. Poulin *et al.*, Effects of sulfide concentration and dissolved organic matter characteristics on the structure of nanocolloidal metacinnabar. *Environ. Sci. Technol.* **51**, 13133-13142 (2017).

15. A. M. Graham, G. R. Aiken, C. C. Gilmour, Effect of dissolved organic matter source and character on microbial Hg methylation in Hg-S-DOM solutions. *Environ. Sci. Technol.* **47**, 5746-5754 (2013).

16. B. A. Poulin, J. N. Ryan, G. R. Aiken, Effects of Iron on Optical Properties of Dissolved Organic Matter. *Environ. Sci. Technol.* **48**, 10098-10106 (2014).

17. B. A. Poulin *et al.*, Spatial dependence of reduced sulfur in Everglades dissolved organic matter controlled by sulfate enrichment. *Environ. Sci. Technol.*, Ahead of Print (2017).

18. J. T. Nurmi, P. G. Tratnyek, Electrochemical properties of natural organic matter (NOM), fractions of NOM, and model biogeochemical electron shuttles. *Environ. Sci. Technol.* **36**, 617-624 (2002).

19. J. Chen, B. Gu, E. J. LeBoeuf, H. Pan, S. Dai, Spectroscopic characterization of structural and functional properties of natural organic matter fractions. *Chemosphere* **48**, 59-68 (2002).

20. J. Chen, B. Gu, R. A. Royer, W. D. Burgos, The roles of natural organic matter in chemical and microbial reduction of ferric iron. *Sci. Total Environ.* **307**, 167-178 (2003).

21. R. L. Fimmen, R. M. Cory, Y.-P. Chin, T. D. Trouts, D. M. McKnight, Probing the oxidation-reduction properties of terrestrially and microbially derived dissolved organic matter. *Geochim. Cosmochim. Acta* **71**, 3003-3015 (2007).

22. F. M. Dunnivant, R. P. Schwarzenbach, D. L. Macalady, Reduction of substituted nitrobenzenes in aqueous solutions containing natural organic matter. *Environ. Sci. Technol.* **26**, 2133-2141 (1992).

23. A. D. Redman, L. Macalady Donald, D. Ahmann, Natural organic matter affects aresnic speciation and sorption onto hematite. *Environ. Sci. Technol.* **36**, 2889-2896 (2002).

24. K. P. Nevin, D. R. Lovley, Mechanisms for Fe(III) oxide reduction in sedimentary environments. *Geomicrobiol. J.* **19**, 141-159 (2002).

25. T. Leefmann, S. Frickenhaus, B. P. Koch, UltraMassExplorer: a browser-based application for the evaluation of high-resolution mass spectrometric data. *Rapid Commun. Mass Spectrom.* **33**, 193-202 (2019).

26. G. C. Wallace, M. Sander, Y.-P. Chin, W. A. Arnold, Quantifying the electron donating capacities of sulfide and dissolved organic matter in sediment pore waters of wetlands. *Environ. Sci. Proc. Impacts*, (2017).

27. A. Kappler, S. B. Haderlein, Natural organic matter as reductant for chlorinated aliphatic pollutants. *Environ. Sci. Technol.* **37**, 2714-2719 (2003).

Appendix C: Supporting Information to Chapter 4[6]

C.1. Properties of the Oxides Studied

Table C.1. Properties of iron oxides used in this study

No.	**Name (Abbrev)**	**Formula Nominal**	**Source (Purity %)**	**D_{50} um**	**SSA m^2/g**	**Key Lit**
1	Goethite (GT)	α-FeOOH	Bayferrox (99.4)	0.1x0.6	15.04	(*1, 2*)
2	Hematite (HT)	α-Fe_2O_3	Bayferrox (99.1)	0.09	14.2	(*1, 3*)
3	Lepidocrocite (LC)	γ-FeO(OH)	Bayferrox (99.4)	0.05x0.3	16.24	(*1, 4*)
4	Magnetite (MT)	Fe_3O_4	Bayferrox (96.5)	0.2	11.76	(*1, 5*)
5	Siderite (ST)	$FeCO_3$	WT Strem (Tech.)			(*6, 7*)
6	Wustite (WT)	FeO	Alfa Aesar (99.5)			(*8, 9*)

C.2. Properties of the Mediators Tested

Table C.2. Mediators used in method development.

No.	**Name (Abbrev)**	**Source (Purity %)**	**E_h Exp/Lit[1,2]**	**Ref**
1	Anthraquinone-2,6-disulfonic acid (AQDS)	Combi-Blocks (98)	−0.540/−0.389	(*1*)
2	2,6-dichloroindophenol (DCIP)	Sigma-Aldrich (97)	−0.060/0.023	(*10*)
3	7-hydroxy-3H-phenoxazin-3-one (Resorufin)	Sigma-Aldrich	−0.340/−0.256	(*10*)
No.	**Name**	**Color (R,O)**	**λ_{max} Exp/Lit (R,O)[2]**	**Ref**
1	AQDS	leuco, yellow	327 (O)/328,386	(*1*)
2	DCIP	blue, leuco	609 (R)/601,256	(*1*)
3	Resorufin	pink, leuco	571 (R)/569,293	(*1*)

[1]Eh values are vs Ag/AgCl. [2]Experimental values (pH 8)/ followed by literature values (pH 7).

---

[6] Reproduction of the Supporting Information to A. S. Pavitt and P. G. Tratnyek, Electrochemical Characterization of Reactive Mineral Intermediates (RMIs) from Fe(II) Amended Iron Oxides, *In prep*.

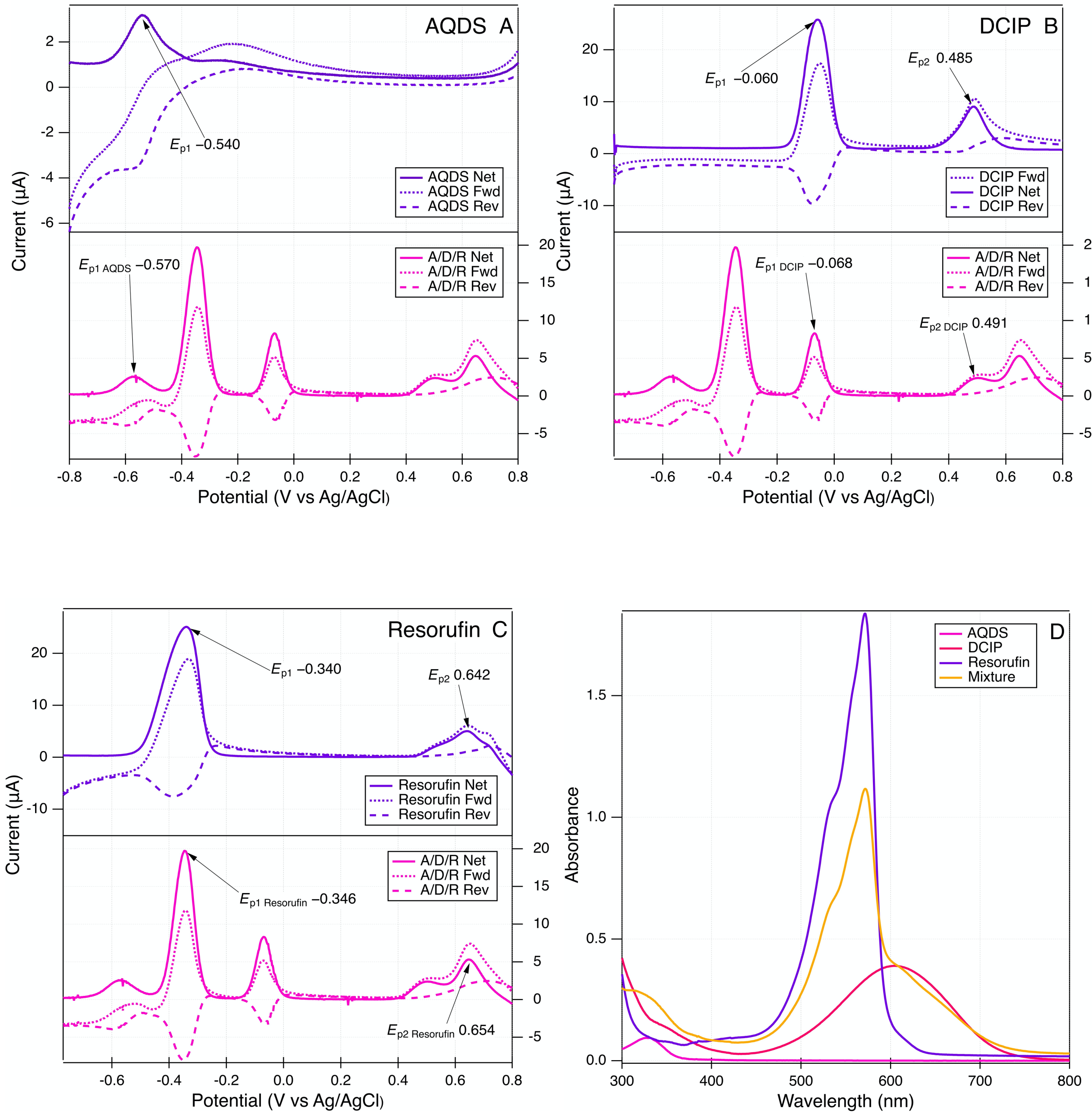

Figure C.1. SWV (A,B,C) and UV-Vis (D) of the three organic mediators: purple (top) is single mediator, pink (bottom) is all three mediators in solution. The solid line is the net response, the dotted lines indicate forward and reverse responses. Conditions: 10 mM NaCl, 10 mM HEPES, 1 mM mediator, 3 mm glassy carbon working electrode, 3.0 M KCl Ag/AgCl reference electrode encased in a fritted bridge tube filled with 10 mM NaCl and 10 mM HEPES, Pt coil reference electrode, scan rate 25 mV s-1, step size 2 mV, amplitude 25 mV. UV-Vis was performed using Perkin Elmer Lambda 20, scanned from 300-800 nm using a Starna quartz cuvette (1 cm path length).

For the electrochemical measurements of the mediators **Figure C.1,** we expanded on the methods developed in our previous work(Pavitt, 2019 #64836) by combining the mediators together in the cell, in addition to performing voltammetry on the singular compounds. The reason for this was two-fold, to ensure that we included a wide range of potentials as mediators only mediate +/- 120 mV (for a one electron reaction) within their standard potentials as per the Nernst equation, and that the mediators were not interfering with each other. If there was interference between the mediators then the potentials and/or current for the group of mediators would differ from the singular mediator response.

C.3. Control Experiments (Oxygen Intrusion)

Figure C.2. O_2 intrusion test. (Left) 5,5-indigodisulfonic acid sodium salt, reduced using sodium borohydride and (right) after 20-hr showing the color change indicative of oxidation. You can see in the picture on the right how the color change is darker closer to the working electrode and over time it is diffusing into the lighter colored, not yet fully oxidized solution. Conditions: 10 mM NaCl, 10 mM HEPES (pH 8), The usual purging of the cell headspace with N_2 was off during the intrusion test.

C.4. Suspension Effect

The suspension effect (SE) is not insignificant and has entire papers devoted to the subject (*11-14*). There are two components to the SE, one is the difference in potential between the sediment and its equilibrium solution (sediment will have overlapping double layers of the charged particles, even though the two components have different potentials, the whole mixture is in equilibrium (Oman, 2004 #34268), and the other is the liquid junction potential. The latter can be minimized by placing the reference and working electrode as close together as possible (*15*), which can be accomplished by using a Luggin-Haber capillary. In our study, we used a double junction for the reference electrode to minimize the junction potential effects and to test the suspension effects in our system. This will be described in the selection of method conditions section, along with our decision to forgo a buffered system and the use of electron transfer mediators.

C.5. EOC and pH of Buffered vs. Unbuffered Solutions and Mediated Response

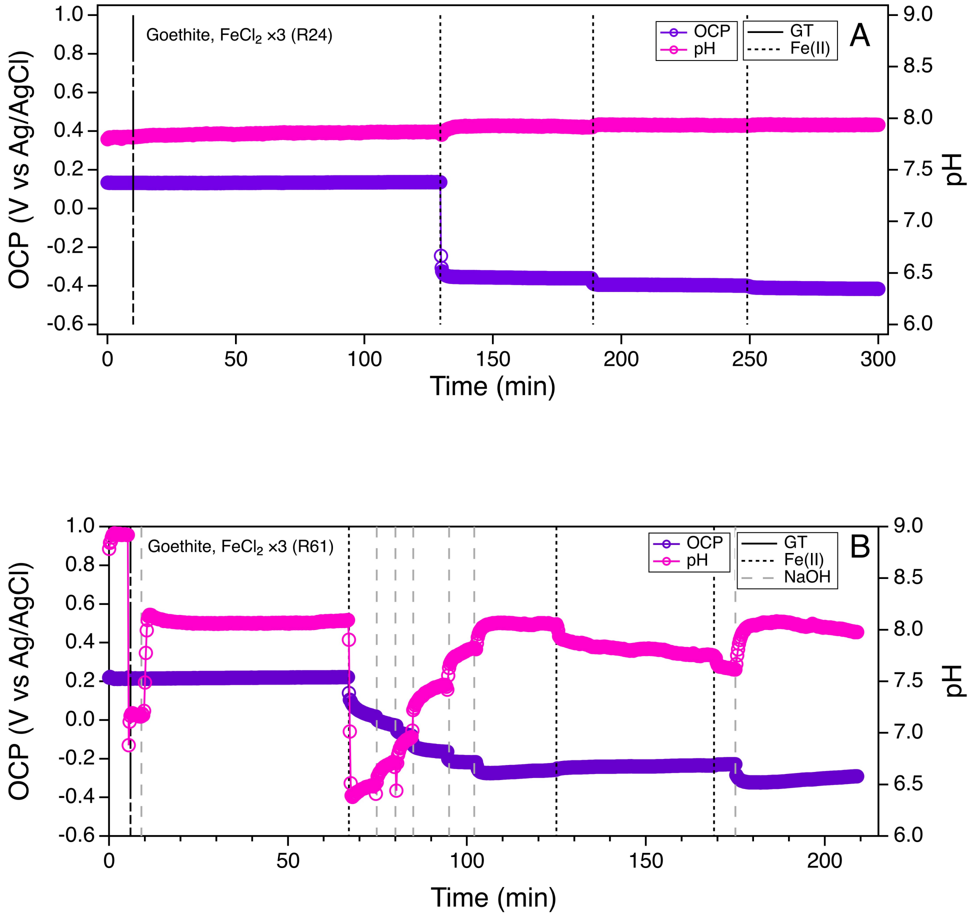

Figure C.3. Open circuit potential (purple) and pH (pink) vs. time for Goethite and Fe(II) (A) buffered, and (B) unbuffered. Conditions: 10 mM NaCl, 10 mM HEPES (for buffered), 0.5 g/L iron oxide, 0.25 mM doses of Fe(II), usually 3 (see legend), 3 mm glassy carbon rotating disk electrode at 2000 rpm, 3.0 M KCl Ag/AgCl reference electrode encased in a fritted bridge tube filled with 10 mM NaCl (and 10 mM HEPES for buffered), pH adjusted with NaOH.

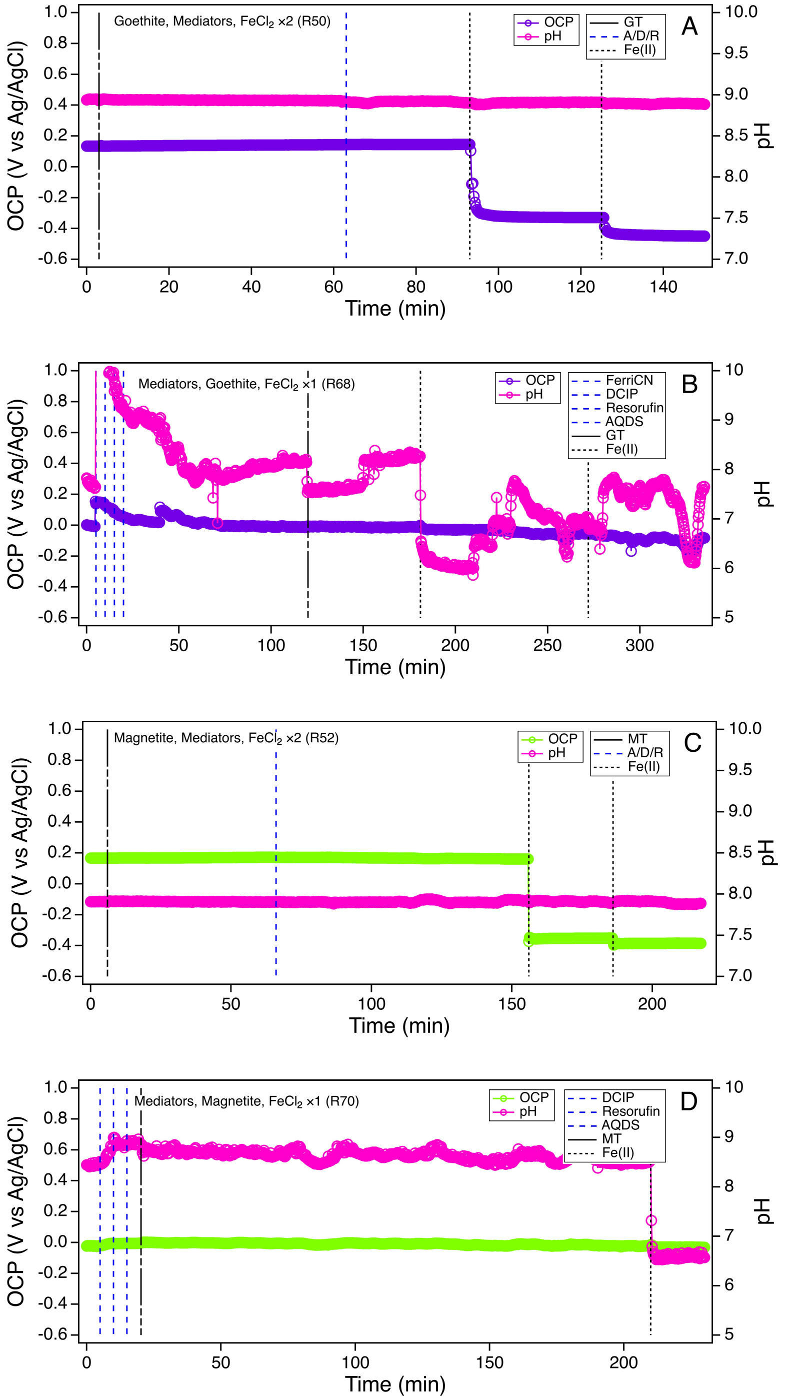

Figure C.4. OCP and pH vs. time of mediated GT (A) buffered and (B) unbuffered and, MT (C) buffered and (D) unbuffered. Conditions: 10 mM NaCl, 10 mM HEPES (for buffered), 0.5 g/L iron oxide, 0.25 mM doses of Fe(II), usually 3 (see legend), 3 mm glassy carbon rotating disk electrode at 2000 rpm, 3.0 M KCl Ag/AgCl reference electrode encased in a fritted bridge tube filled with 10 mM NaCl (and 10 mM HEPES for buffered), pH adjusted with NaOH.

C.6. Control Experiments (Aging, Light, and Double Junction Effects)

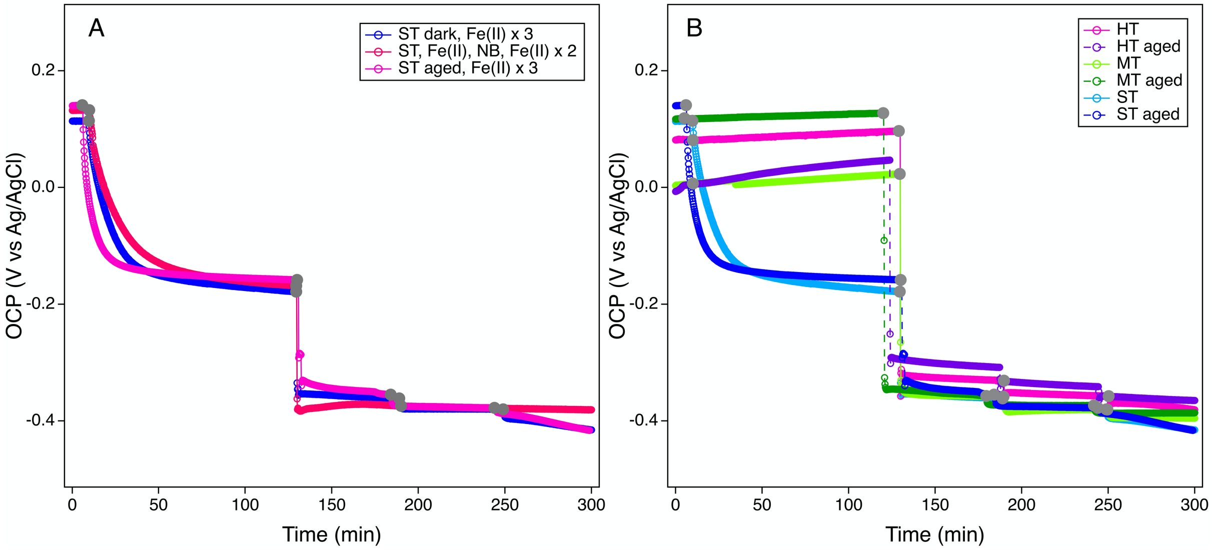

Figure C.5. OCP vs. time for (A) dark and aged ST and (B) aged vs non-aged for HT, MT, ST. Conditions: 10 mM NaCl, 10 mM HEPES, 0.5 g/L iron oxide, 0.25 mM doses of Fe(II), usually 3 (see legend), 3 mm glassy carbon rotating disk electrode at 2000 rpm, 3.0 M KCl Ag/AgCl reference electrode encased in a fritted bridge tube filled with 10 mM NaCl and 10 mM HEPES.

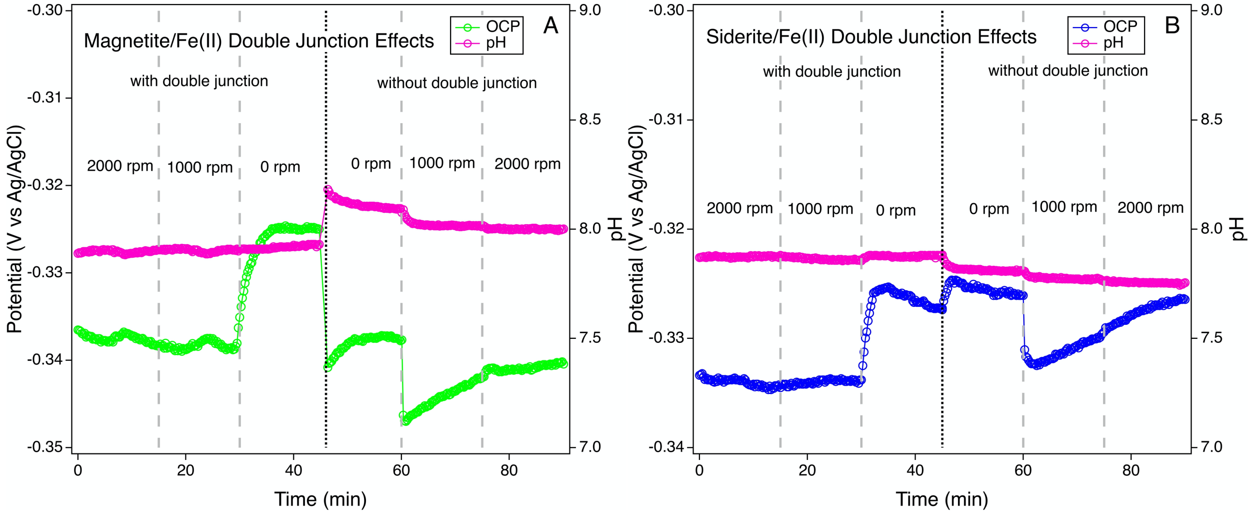

Figure C.6. Effects of stirring and the use of a double junction for the reference electrode on OCP and pH for (A) MT and (B) ST. Conditions: 10 mM NaCl, 10 mM HEPES, 0.5 g/L iron oxide, 0.25 mM Fe(II), 3 mm glassy carbon rotating disk electrode at 2000, 1000 and 0 rpm, 3.0 M KCl Ag/AgCl reference electrode encased (with double junction) or not (without double junction) in a fritted bridge tube filled with 10 mM NaCl and 10 mM HEPES.

C.7. E_{OC} vs. Time and vs. Concentration of Fe(II), Mediators, and Iron Oxides

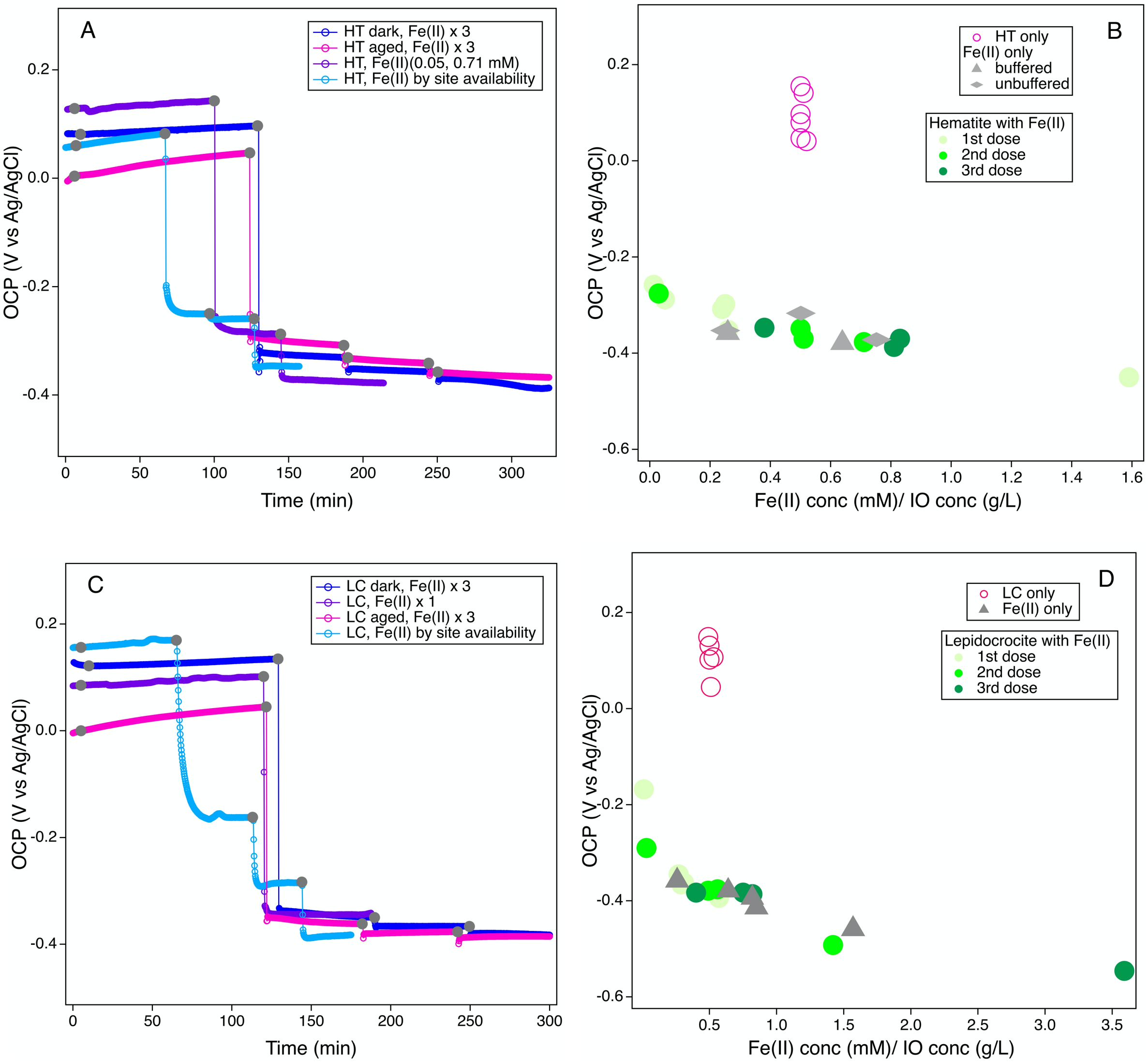

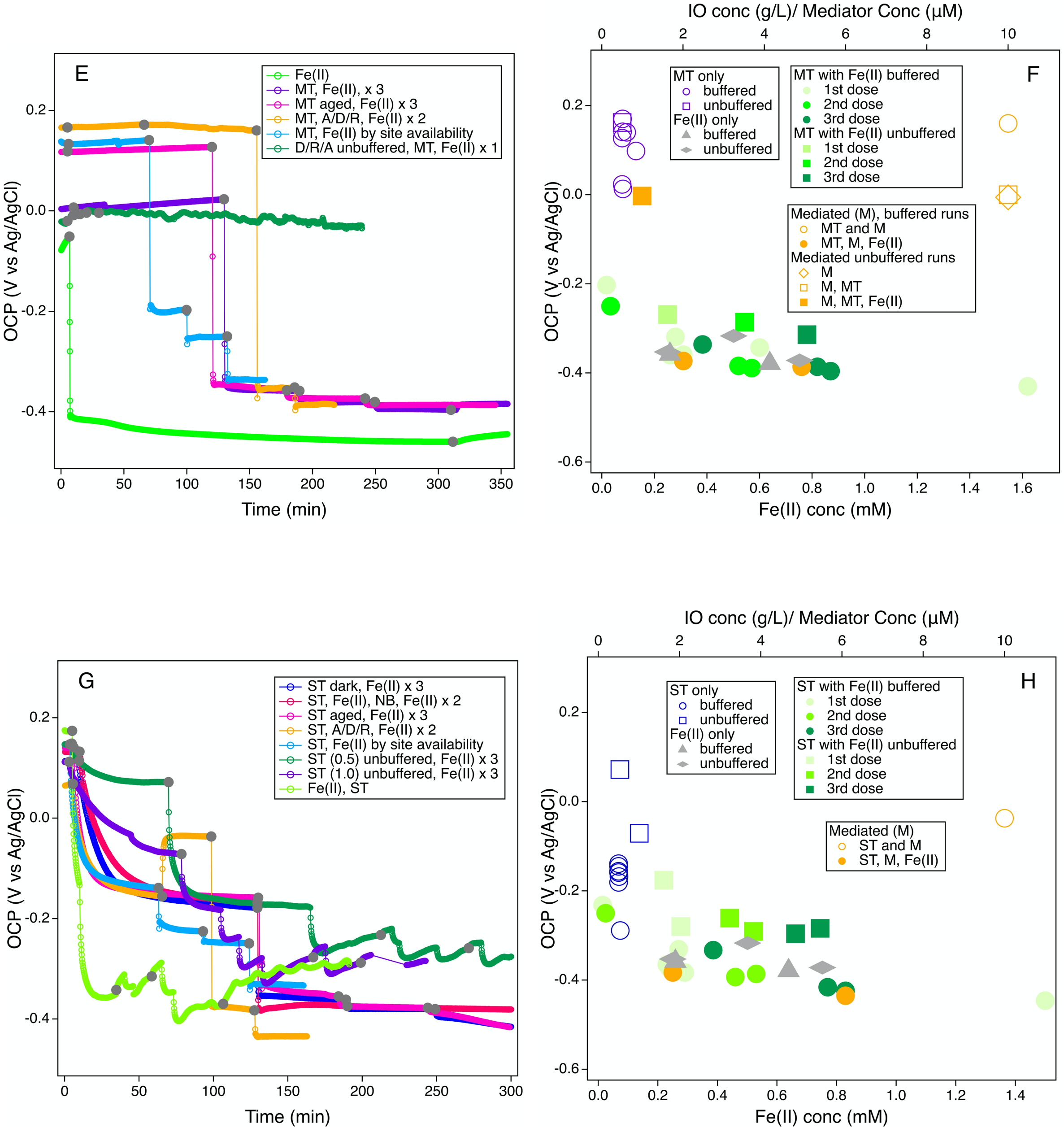
E
Fe(II)
MT, Fe(II), x 3
MT aged, Fe(II) x 3
MT, A/D/R, Fe(II) x 2
MT, Fe(II) by site availability
D/R/A unbuffered, MT, Fe(II) x 1
OCP (V vs Ag/AgCl)
Time (min)
0.2
0.0
-0.2
-0.4
0
50
100
150
200
250
300
350
F
IO conc (g/L)/ Mediator Conc (µM)
Fe(II) conc (mM)
MT only
○ buffered
□ unbuffered
Fe(II) only
▲ buffered
◆ unbuffered
MT with Fe(II) buffered
● 1st dose
● 2nd dose
● 3rd dose
MT with Fe(II) unbuffered
■ 1st dose
■ 2nd dose
■ 3rd dose
Mediated (M), buffered runs
○ MT and M
● MT, M, Fe(II)
Mediated unbuffered runs
◇ M
□ M, MT
■ M, MT, Fe(II)
0
2
4
6
8
10
0.0
0.2
0.4
0.6
0.8
1.0
1.2
1.4
1.6
-0.6
G
ST dark, Fe(II) x 3
ST, Fe(II), NB, Fe(II) x 2
ST aged, Fe(II) x 3
ST, A/D/R, Fe(II) x 2
ST, Fe(II) by site availability
ST (0.5) unbuffered, Fe(II) x 3
ST (1.0) unbuffered, Fe(II) x 3
Fe(II), ST
OCP (V vs Ag/AgCl)
Time (min)
H
ST only
○ buffered
□ unbuffered
Fe(II) only
▲ buffered
◆ unbuffered
ST with Fe(II) buffered
● 1st dose
● 2nd dose
● 3rd dose
ST with Fe(II) unbuffered
■ 1st dose
■ 2nd dose
■ 3rd dose
Mediated (M)
○ ST and M
● ST, M, Fe(II)
IO conc (g/L)/ Mediator Conc (µM)
Fe(II) conc (mM)

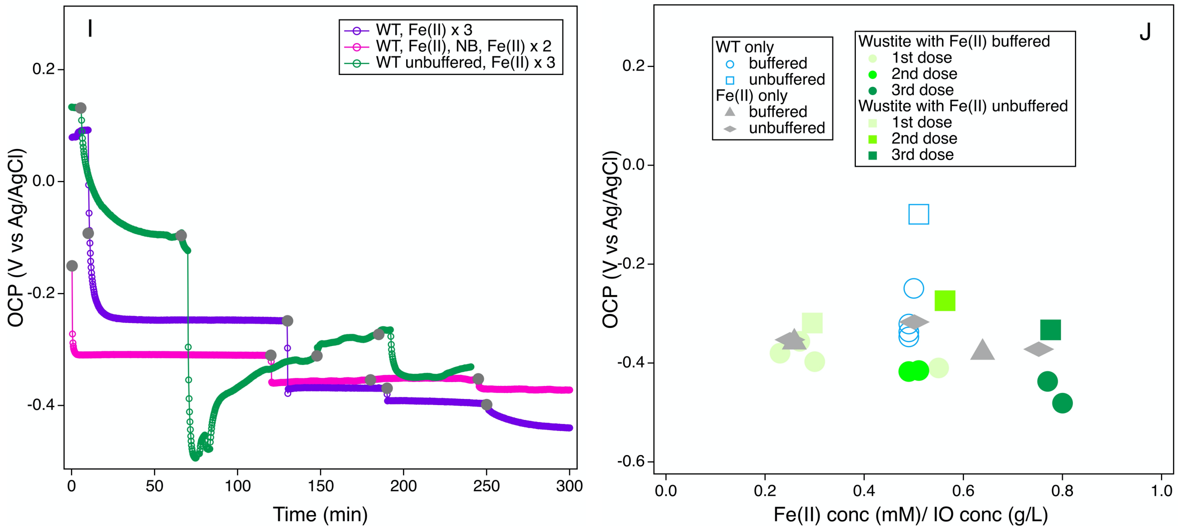

Figure C.7. (A, C, E, G, I) Open circuit potential vs. time and (B, D, F, H, J) vs. Fe(II), iron oxide, mediator concentration of select (left) or all (right) runs for six iron oxides (GT Figure 3A, B). Left grey dots indicate addition of iron oxide, Fe(II), or mediator (G, E). Conditions: 10 mM NaCl, 10 mM HEPES (for buffered runs), 0.5 g/L iron oxide, 0.25 mM doses of Fe(II), usually 3 (see legend), significantly less for the Fe(II) by site availability runs, when used mediator concentrations were 10 μM, 3 mm glassy carbon rotating disk electrode at 2000 rpm, 3.0 M KCl Ag/AgCl reference electrode encased in a fritted bridge tube filled with 10 mM NaCl (and 10 mM HEPES for buffered runs).

C.8. Calculating available surface sites on iron oxides

We previously obtained sizes of the iron oxides 1-4 in our lab using BET (**Table C.1**). We took these number and multiplied them by literature values (*16, 17*), or sites/area low (2 sites m^{-2}) and sites/area high (22 sites m^{-2}) obtaining sites/g of iron oxide low and high. Then based on how much iron oxide was in the electrochemical cell (0.1100 g) we calculated the sites available low and high values. The low sites ranged from $3.57 \cdot 10^{18}$ (LC) to $2.59 \cdot 10^{18}$ (MT), and the high sites from $3.93 \cdot 10^{19}$ (LC) to $2.85 \cdot 10^{19}$ (MT). FeII particles were calculated using molarity in the cell and Avogadro's number ($6.022 \cdot 10^{23}$ mol^{-1}). The first addition of FeII for GT, HT, LC and MT were 55, 57, 40, and 90 %. We did not have calculations for ST or WT. We did not run WT but for ST we used 15 μM FeII, which was an approximate average of the other minerals.

C.9. Thermodynamic Values Used in Calculations

Table C.3. Thermodynamic values and equations used to construct Eh/pH diagrams in Figure 4.

Redox Couple [1]	Log K at 25°C [2]	Equilibrium equations [3]
Fe++/FeOH++	−15.2020	–log[Fe++] – 16.9 Eh – pH + log[FeOH++]
Fe++/Fe(OH)3	−25.0307	–log[Fe++] – 16.9 Eh – 3 pH + log[Fe(OH)3]
Fe++/Fe(OH)3(ppd)	−17.9017	–log[Fe++] – 16.9 Eh – 3 pH
Fe++/GT	−13.5126	–log[Fe++] – 16.9 Eh – 3 pH
Fe++/HT	−13.0343	–log[Fe++] – 16.9 Eh – 3 pH
Fe++/MT	−12.1064	–log[Fe++] – 11.27 Eh – 2.667 pH
GT/Fe++	13.5126	log[Fe++] + 16.9 Eh + 3 pH
GT/FeOH+	3.3336	log[FeOH+] + 16.9 Eh + 2 pH
GT/Fe(OH)2	−7.9096	log[Fe(OH)2] + 16.9 Eh + pH
GT/FeCl+	13.8923	log[FeCl+] – log[Cl-] + 16.9 Eh + 3pH
GT/FeCl2(aq)	13.6123	log[FeCl2] – 2 log[Cl-] + 16.9 Eh + 3 pH
GT/Fe(OH)2(ppd)	0.6641	16.9 Eh + pH
GT/FeO(c)	2.1528	16.9 Eh + pH
GT/MT	1.4061	5.63 Eh + 0.33 pH
GT/WT	−1.0148	15.01 Eh + 0.88 pH
MT/Fe++	36.3193	3 log[Fe++] + 33.8 Eh + 8 pH
MT/Fe+++	−2.7187	3 log[Fe+++] – 16.9 Eh + 8 pH
MT/FeCl+	37.4584	3 log[FeCl+] – 3 log[Cl-] + 33.8 Eh + 8 pH
MT/FeCl2(aq)	36.6184	3 log[FeCl2(aq)] – 6 log[Cl-] + 33.8 Eh + 8 pH
MT/Fe(OH)2(ppd)	−2.2262	33.8 Eh + 2 pH
MT/FeO(c)	2.2399	33.8 Eh + 2 pH
MT/GT	−4.2183	−16.9 Eh – pH
MT/HT	−2.7836	−16.9 Eh – pH
ST/Fe(OH)3(ppd)	−18.1231	log[HCO3-] – 16.9 Eh – 2 pH
ST/NaFeO2(c)	−33.1125	log[HCO3-] – log[Na+] – 16.9 Eh – 3 pH
ST/GT	−13.7339	log[HCO3-] – 16.9 Eh – 2 pH
ST/HT	−13.2557	log[HCO3-] – 16.9 Eh – 2 pH
ST/MT	−12.3278	log[HCO3-] – 11.3 Eh – 1.7 pH

[1] Written as added species / possibly formed species, not as standard reduction couples. [2] Values obtained from the Rxn module of Geochemist's Workbench 12, at 25°C. [3] Log K data are from the default database of thermodynamic properties in GWB 12 (V8.R6+). [] indicate activities. All activities for solids were assumed to be 1 and so are not shown in the equations.

C.10. References (Appendix C Only)

1. D. Fan, M. Bradley, A. W. Hinkle, R. L. Johnson, P. G. Tratnyek, Chemical reactivity probes for assessing abiotic natural attenuation by reducing iron minerals. *Environ. Sci. Technol.* **50**, 1868-1876 (2016).

2. S. D. Taylor *et al.*, Visualizing the iron atom exchange front in the Fe(II)-catalyzed recrystallization of goethite by atom probe tomography. *Proc. Natl. Acad. Sci. USA* **116**, 2866 (2019).

3. K. M. Rosso, S. V. Yanina, C. A. Gorski, P. Larese-Casanova, M. M. Scherer, Connecting observations of hematite (α-Fe_2O_3) growth catalyzed by Fe(II). *Environ. Sci. Technol.* **44**, 61-67 (2010).

4. M. M. Scherer, B. A. Balko, P. G. Tratnyek, in *Mineral-Water Interfacial Reactions: Kinetics and Mechanisms,* D. L. Sparks, T. J. Grundl, Eds. (American Chemical Society, Washington, DC, 1998), vol. 715, pp. 301-322.

5. C. A. Gorski, M. M. Scherer, Influence of magnetite stoichiometry on Fe^{II} uptake and nitrobenzene reduction. *Environ. Sci. Technol.* **43**, 3675-3680 (2009).

6. M. Elsner, R. P. Schwarzenbach, S. B. Haderlein, Reactivity of Fe(II)-bearing minerals toward reductive transformation of organic contaminants. *Environ. Sci. Technol.* **38**, 799-807 (2003).

7. S. Peulon, H. Antony, L. Legrand, A. Chausse, Thin layers of iron corrosion products electrochemically deposited on inert substrates: synthesis and behaviour. *Electrochim. Acta* **49**, 2891-2899 (2004).

8. H. F. Rizzo, R. S. Gordon, I. B. Cutler, The Determination of Phase Boundaries and Thermodynamic Functions in the Iron-Oxygen System by EMF Measurements. *J. Electrochem. Soc.* **116**, 266 (1969).

9. R. M. Cornell, U. Schwertmann, *The Iron Oxides: Structure, Properties, Reactions, Occurrences And Uses*. (John Wiley & Sons, 2003).

10. P. G. Tratnyek *et al.*, Visualizing redox chemistry: Probing environmental oxidation-reduction reactions with indicator dyes. *The Chemical Educator* **6**, 172-179 (2001).

11. S. F. Oman, Electrode potentials in suspensions interpreted as a mixed potential. *Acta Chim. Slov.* **51**, 189-201 (2004).

12. D. P. Brezinski, Influence of colloidal charge on response of pH and reference electrodes: the suspension effect. *Talanta* **30**, 347-354 (1983).

13. A. Al-Busaidi, P. Cookson, T. Yamamoto, Methods of pH determination in calcareous soils: use of electrolytes and suspension effect. *Soil Research* **43**, 541-545 (2005).

14. M. P. S. Mousavi, S. A. Saba, E. L. Anderson, M. A. Hillmyer, P. Buhlmann, Avoiding errors in electrochemical measurements: Effect of frit material on the performance of reference electrodes with porous frit junctions. *Anal. Chem. (Washington, DC, U. S.)* **88**, 8706-8713 (2016).

15. A. J. Bard, L. R. Faulkner, *Electrochemical Methods. Fundamentals and Applications*. (Wiley, New York, 2001), pp. 833.

16. G. Sposito. (American Chemical Society, 2010), pp. ENVR-113.

17. A. D. James, F. H. Kim, in *Geochemical Processes at Mineral Surfaces*. (American Chemical Society, 1987), vol. 323, chap. 1, pp. 2-18.